Summer 2003

Hypersonic Boundary-Layer Stability Across a Compression Corner

Hongwu Zhao
Old Dominion University

HYPERSONIC BOUNDARY-LAYER STABILITY ACROSS A COMPRESSION CORNER

by

Hongwu Zhao
B.S. July 1994, Beijing University of Aeronautics and Astronautics
M.S. March 1997, Beijing University of Aeronautics and Astronautics

A Dissertation Submitted to the Faculty of
Old Dominion University in Partial Fulfillment of
the Requirement for the Degree of

DOCTOR OF PHILOSOPHY

AEROSPACE ENGINEERING

OLD DOMINION UNIVERSITY

August 2003

Approved by:

_____
(Director) Osama A. Kandil

_____
(Co-Director) Ponnampalam Balakumar

_____
(Member) Robert L. Ash

_____
(Member) Chuh Mei

ABSTRACT

HYPERSONIC BOUNDARY-LAYER STABILITY
ACROSS A COMPRESSION CORNER

Hongwu Zhao
Old Dominion University, 2003
Director: Dr. Osama A. Kandil
Co-Director: Dr. Ponnampalam Balakumar

Stability of a hypersonic boundary-layer over a compression corner was investigated numerically. The three-dimensional compressible Navier-Stokes equations were solved using a fifth-order weighted essentially non-oscillating (WENO) shock capturing scheme to study the shock wave and boundary-layer interactions. The boundary-layer stability was studied in three distinct regions: upstream of the separation region, inside the separation region and downstream of the separation region. After the mean flow field was computed, linear stability theory was employed to predict the unstable disturbance modes in different flow regions and also to find the most amplified disturbance frequency across the compression corner. Gortler instability computations were performed to study the influence of the streamline curvatures on boundary-layer stability, and PSE(parabolized stability equation) method was employed to obtain the initial disturbances for direct numerical simulation.

To study the boundary-layer stability by direct numerical simulation, two- or three-dimensional initial disturbances were introduced at the initial streamwise location of the computational domain. Two-dimensional disturbance evolution simulation shows that two-dimensional high frequency linear disturbances grow exponentially upstream and downstream of the separation region and remain neutral in the separation region, but two-dimensional low frequency linear disturbances only grow in a narrow area inside the separation region and remain neutral upstream and downstream of the separation region.

Two-dimensional nonlinear disturbances will saturate downstream of the separation region when their amplitudes reach quit large amplitude.

The three-dimensional disturbance evolution simulations show that three-dimensional linear mono-frequency disturbances are less amplified than its two-dimensional counterpart across the compression corner. The three-dimensional nonlinear mono-frequency disturbance evolution indicates that mode (0,2) is responsible for the oblique breakdown. Three-dimensional disturbances are much more amplified with the presence of two-dimensional primary disturbance due to the secondary instability. Finally, the simulations of three-dimensional random frequency disturbance evolution with the presence of a two-dimensional primary disturbance show that the secondary instability first occurs downstream of the separation region and a fundamental or K-type breakdown will be triggered by this secondary instability.

ACKNOWLEDGMENTS

First I want to express my great thanks for my dissertation director, Dr. Osama A. Kandil. I appreciated his time and efforts in the arrangement and coordination of my comprehensive examinations and dissertation defense. He also provided me with invaluable advice in my dissertation research and much help in my course work study.

Next, I would like to express my most sincere respect and appreciation to my dissertation co-director, Dr. Ponnampalam Balakumar, at NASA Langley Research Center. He always showed his great enthusiasm in my dissertation supervision whether he was at ODU or NASA. I am indebted to him for his unreserved guidance during the course of this dissertation research. Most of the background material has been derived from the lectures and works of Dr. Balakumar.

Special thanks should also be given to my dissertation committee members, Dr. Robert L. Ash and Dr. Chuh Mei, for their time and valuable comments in reviewing this dissertation.

Finally, I want to convey my deepest thanks to my wife, Hong Yao. She helped me during my most difficult times. Without her support and encouragement, it's unlikely that I would have finished this dissertation in such a short time.

NOMENCLATURE

English Symbols

A_0	Coefficient matrix of linear stability theory
A,B,C,D	Coefficient matrices of PSE
A_2,B_2,C_2	Coefficient matrices of Gortler instability
c	Phase velocity
C_v	Specific heat at constant volume
E,F,G	Inviscid fluxes
E_v,F_v,G_v	Viscous fluxes
e_t	Total energy
f	Disturbance frequency
F_0	Non-dimensional disturbance frequency
G_r	Gortler number
J	Jacobian matrix
k_T	Heat conductivity coefficient
L	Reference length
M	Mach number
N	N factor
p	Pressure
p_r	Prandtl number
Q	Conservative variable vector
R	Gas constant
Re	Reynolds number
r, θ	Cylindrical coordinates
T	Temperature
t	Time

u_1,u_2,u_3	Velocity in streamwise, wall normal, and spanwise directions
u,v,w	Velocity in streamwise, wall normal, and spanwise directions
W	Complex potential
x,y,z	Cartesian coordinates
x_1, x_2, x_3	Cartesian coordinates
Z	Complex variable

Greek Symbols

α	Streamwise wave number
β	Spanwise wave number
ε	Initial disturbance amplitude
ρ	Density
Π	Stress tensor
μ	Viscosity coefficient
ν	Kinematic viscosity
γ	Specific heat constant
δ	Boundary-layer thickness
δ_d	Displacement thickness
δ_0	Boundary-layer thickness at the initial streamwise location
ξ,η,ζ	Curvilinear coordinates
ω	Disturbance frequency
φ	Disturbance velocity potential
λ	Second viscosity coefficient
λ_x	Wave length in streamwise direction
λ_z	Wave length in spanwise direction
κ	Curvature radius
θ_0	The corner angle
θ_w	The oblique shock deflection angle

Subscripts

∞	Upstream infinity flow variables
inf	Upstream infinity flow variables
ref	Reference variables
dis	Disturbance quantities
max	Maximal value

Superscripts

*	Dimensional variables
–	Mean flow variables
′	Disturbance variables
^	Normal mode variables
~	The variables in curvilinear coordinate system

TABLE OF CONTENTS

LIST OF FIGURES

CHAPTER I

INTRODUCTION*

1.1 The background of current research

The transition of boundary-layers from a laminar to a turbulent state play an important role in many fluid mechanics problems since it ultimately affects basic quantities such as heat transfer and skin friction. In general, the transition can have either positive or negative effects. In some situations it is harmful, but it is desirable in other situations. For example, the low skin-friction coefficient of laminar boundary-layer flow is very attractive to those who design engines or pay the fuel for high-speed vehicles such as airplanes. However, the low mixing of fluid quantities such as chemical species, heat or momentum may be problematic for others who design these engines or cope with the danger of separation in adverse pressure gradients. They may clearly prefer a turbulent state of flow. This summarizes the situation at the inlet of the NASA Hyper-X propulsion system.

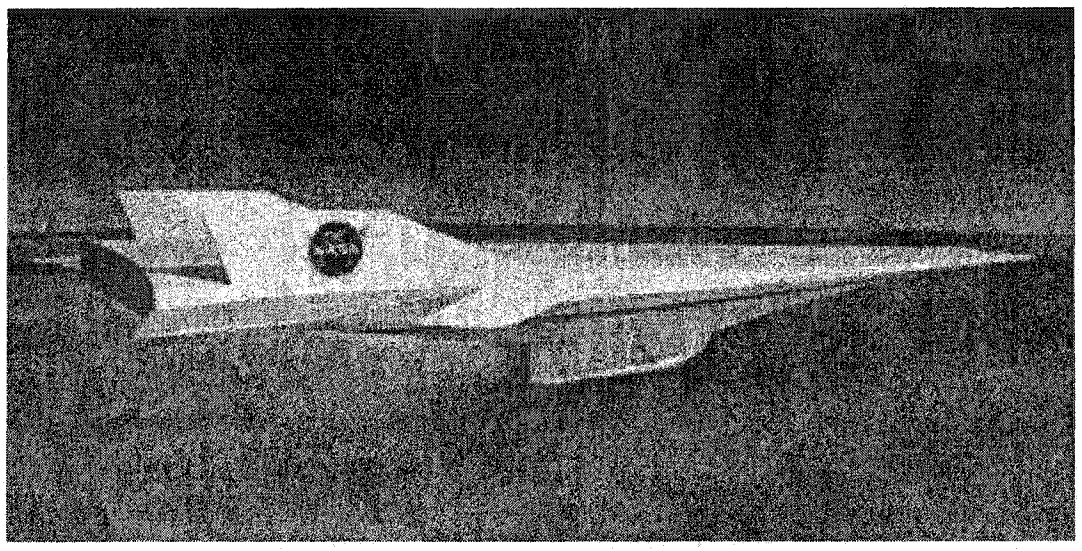

Figure 1.1 The hyper-X flight vehicle.

* The reference model of this work is *IEEE Journals and Transactions*

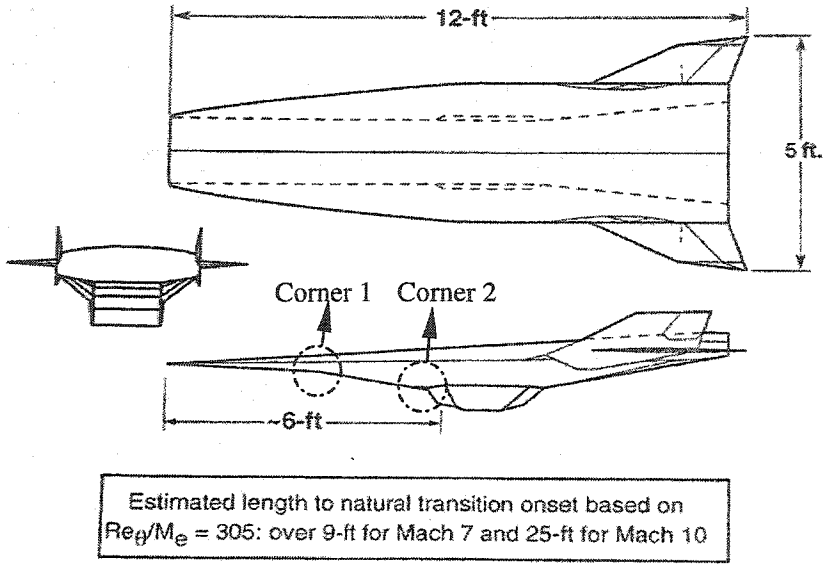

Figure 1.2 The geometry configuration of the Hyper-X model.

Figure 1.1 shows a Hyper-X vehicle and associated operation conditions. In order to provide the most robust scramjet propulsion system, a turbulent boundary-layer at the inlet interface is required. Ingestion of a turbulent boundary-layer into the inlet enhances the performance and operability of the engine through improved fuel air mixing and reduced susceptibility to drag-enhancing internal flow separations. However, based on the current knowledge of boundary-layer transition at hypersonic flight conditions, an estimation of the location of natural transition on the Hyper-X forebody suggests that boundary-layer trip devices are necessary to ensure a turbulent boundary at the inlet. An experimental investigation of boundary-layer trip effectiveness and the effect of the trips on the aeroheating characteristics for a 33% scale Hyper-X forebody model has been conducted in the LaRC 20-inch Mach 6 air tunnel by Berry, DiFulvio, and Kowalkowski[1], and Berry, Auslender and Dilley[2]. They investigated the effects of discrete roughness elements on forebody boundary-layer transition, which included variations in trip configuration and height. But for a more effective and economical study of hypersonic boundary-layer transition tripping, numerical simulation of transition at the inlet of the engine is a good solution. By numerical simulation, the most effective configuration for the boundary-layer trip can be determined. In addition, the hypersonic

transition mechanism across a compression corner can also be disclosed by numerical simulation.

1.2 The phenomena of shock wave/boundary-layer interaction

It is observed from the geometric configuration of the Hyper-X model shown in Figure 1.2 that two compression corners exist on its forebody. Under hypersonic flight conditions, the shocks will form and a large adverse pressure gradient will be produced across the compression corners. It is well known that when a large adverse pressure gradient exists in the inviscid pressure distribution, viscous effects become important. The interaction of the boundary-layer with the adverse pressure gradient modifies the pressure distribution and the flow field is drastically modified, including the appearance of multiple shocks, flow separation, transition to turbulence, unsteadiness and three-dimensionality. This phenomenon is observed in transonic flow over airfoils, supersonic flows over compression corners, curved surfaces and steps etc.

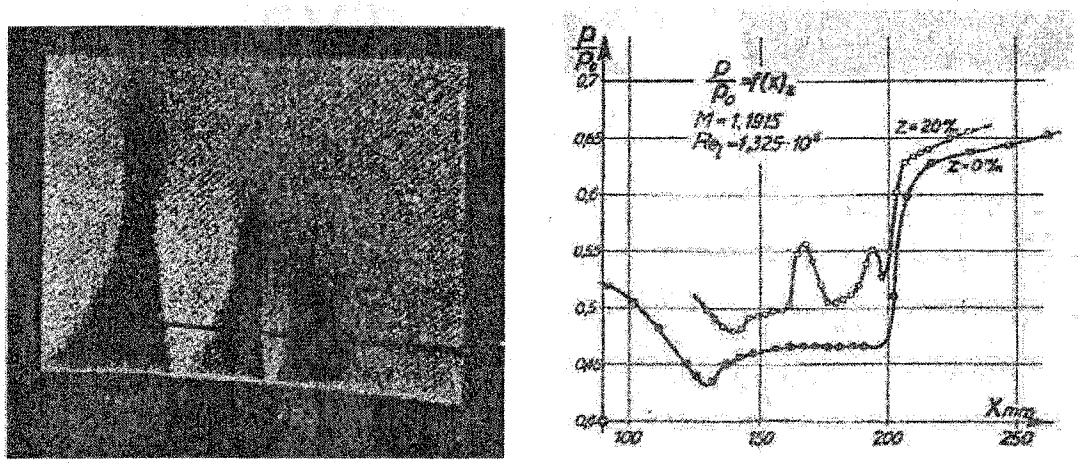

Figure 1.3a The shock formation and pressure distribution on an airfoil with laminar flow M=1.191.

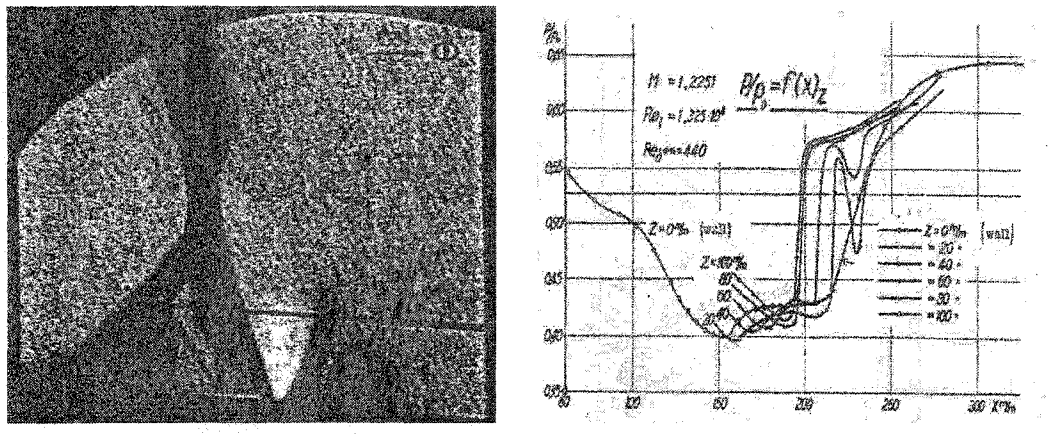

Figure 1.3b The shock formation and pressure distribution on the same airfoil with laminar flow M=1.225.

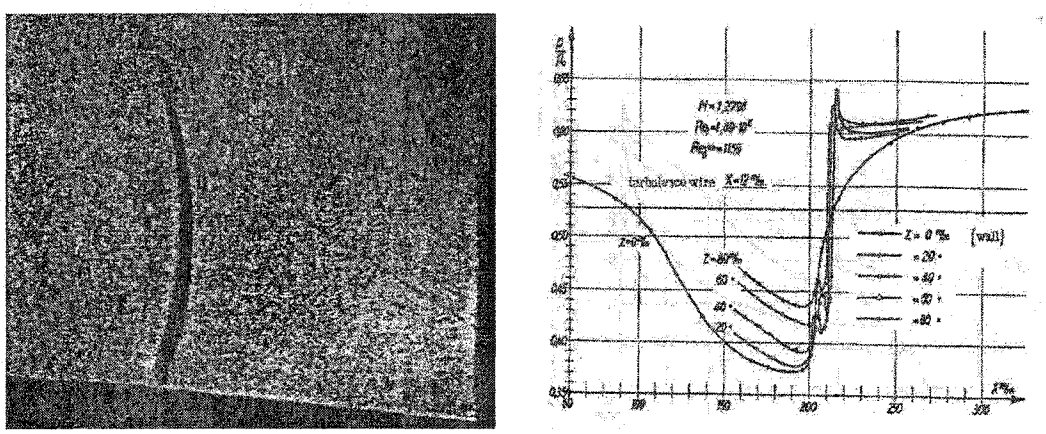

Figure 1.3c The shock formation and pressure distribution on the same airfoil with turbulent flow M=1.280.

Ackert, Feldmann and Rott[3] investigated experimentally the mutual influences of compression shocks and boundary-layers in transonic and at low supersonic Mach numbers in laminar and turbulent flow regimes. The results are shown in Figures 1.3a-1.3c. The measurements and the observations showed the formation of λ-shock for laminar boundary-layers at Mach numbers close to 1.2 and multiple shocks were observed with decreasing Mach numbers. The λ shocks consist of a main shock with a preceding oblique compression wave. The flow in front of the main shock is separated and there is a gradual increase of pressure starting upstream of the separation point. This gradual increase in pressure ends with a sharp increase near the main shock and the flow becomes turbulent behind the shock. For turbulent flows only normal shocks are observed.

In both cases the boundary-layer thickness increases considerably by a factor of ten in laminar flow and by a factor of four in turbulent flows.

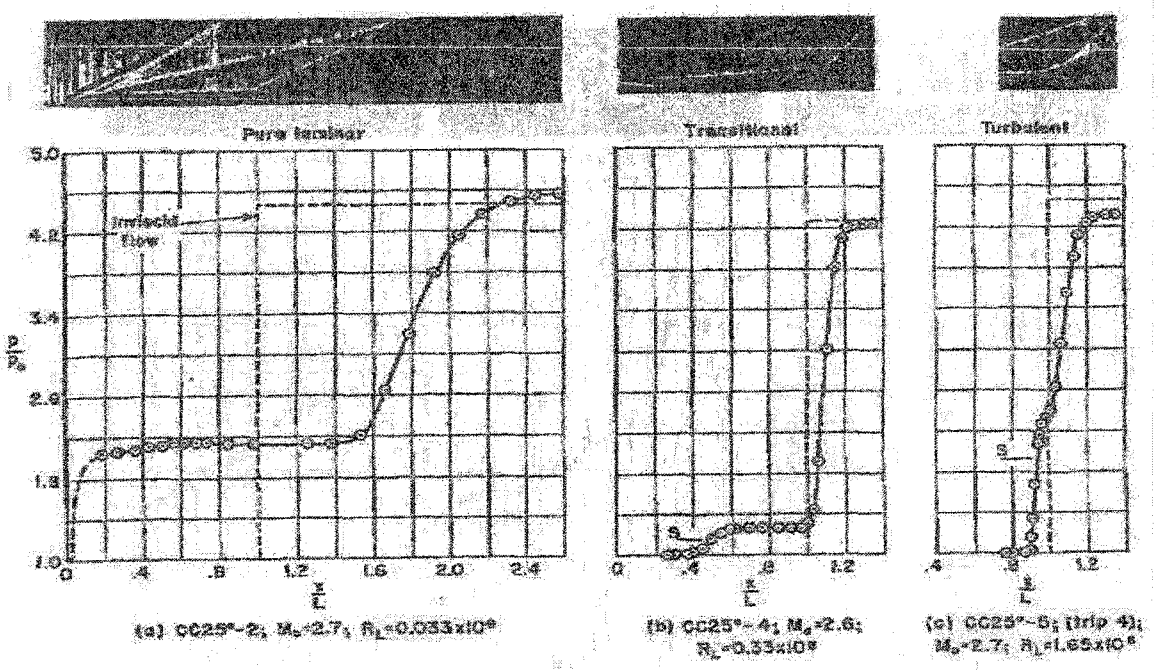

Figure 1.4 The three flow regimes for a supersonic flow going through a compression corner.

Chapman, Kuehn and Larson[4] conducted an extensive investigation on flow separation for steps, bases, compression corners, and curved surfaces at different Mach numbers ranging from 0.4 to 3.6 and at different Reynolds numbers. Figure 1.4 shows the three flow regimes for the supersonic flow with Mach number 2.7 going through a compression corner. It was observed that the pressure distribution in separated flow depends on the location of the transition point relative to the reattachment and separation points. In laminar separation, the pressure rises smoothly and reaches a plateau. Depending on the downstream condition, the pressure rises smoothly to the final pressure. In transitional separation where the flow starts to become turbulent between the separation and reattachment points, the pressure initially rises smoothly, as in laminar flows, and then increases sharply near the transition region and the pressure distribution becomes unsteady. In turbulent separated flows, the pressure increases rapidly from start to finish. It is also observed that the mixing layer above the separation bubble is stable in

supersonic flows and the stability increases with increasing Mach numbers. Therefore laminar separated flows become very important in hypersonic boundary-layers.

From these two experiments we see that the most spectacular feature of the phenomena is that the boundary-layer separates some distance ahead of the incident shock, generating compression waves in the main stream which can coalesce to form a secondary shock. The upstream influence observed in these experiments was perplexing at that time since: 1) the boundary-layer equations are parabolic and, therefore, do not permit upstream propagation of disturbances; 2) The supersonic external flow can only transmit disturbances downstream.

The mechanism for upstream disturbance propagation was first explained by Lighthill[5][6] using self-induced separation theory and later using asymptotic triple-deck theory by Stewartson and Williams[7], Brown, Stewartson and Williams[8], Rizzetta, Burggraf and Jenson[9], and Brown, Cheng and Lee[10]. In fact, from the physical point of view, this separation is due to the interaction between the shock wave and boundary-layer. Figures 1.5a-d give a graphic representation of how the shock induced separation occurs. We know when an inviscid supersonic flow goes through a compression corner, an oblique shock will form at the vertex and an inviscid pressure discontinuity will appear across the shock. But if this supersonic flow is viscous, a boundary-layer exists along the wall of the compression corner. When this boundary-layer interacts with the oblique shock, due to the adverse pressure gradient, the boundary-layer thickness close to the vertex increases. This part of the boundary-layer whose thickness is increased will alter the pressure distribution at the outer part of the boundary-layer. This altered pressure distribution induces further growth of the boundary-layer thickness upstream of the original discontinuity. This process continues until the flow reaches a kind of equilibrium at one specific location some distance upstream of the shock impingement point. Then a steady separation bubble is formed in the area close to the corner vertex point. The boundary-layer thickness increases

significantly in the separation bubble region. Some compression waves appear along the edge of the boundary-layer. These compression waves merge together far away to form an oblique shock.

The shock wave/boundary-layer interaction attracted a lot of research interests in the last few decades[11]-[22]. But most experimental and numerical work mainly focused on the steady flow boundary-layer, including both laminar and turbulent boundary-layers. The main objectives of these research were to 1) predict the separation, including the separation area length, the location of the separation and reattachment points; 2) predict the pressure distribution and drag force along the surface; 3) study the influences of Mach number and Reynolds number as well as wall temperature on the separation. As to the boundary-layer instability and transition with the existence of shock wave/boundary-layer interaction, little work had been previously done.

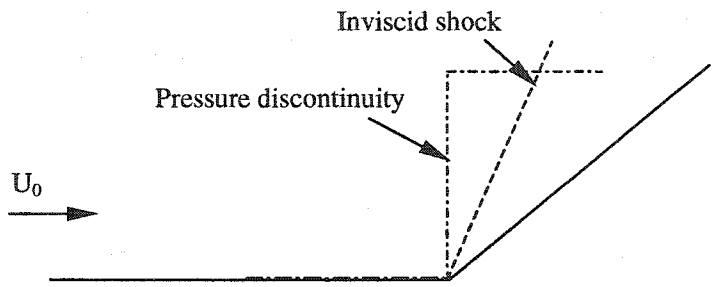

Figure 1.5a The shock produced by inviscid supersonic flow.

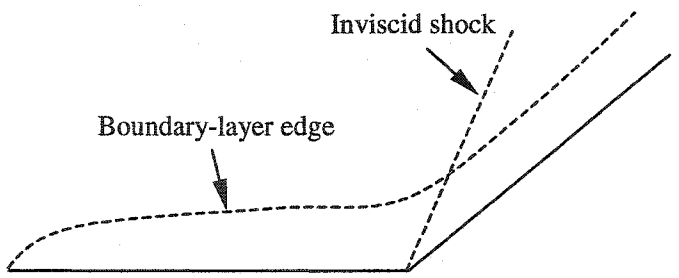

Figure 1.5b The boundary-layer encountering the inviscid shock.

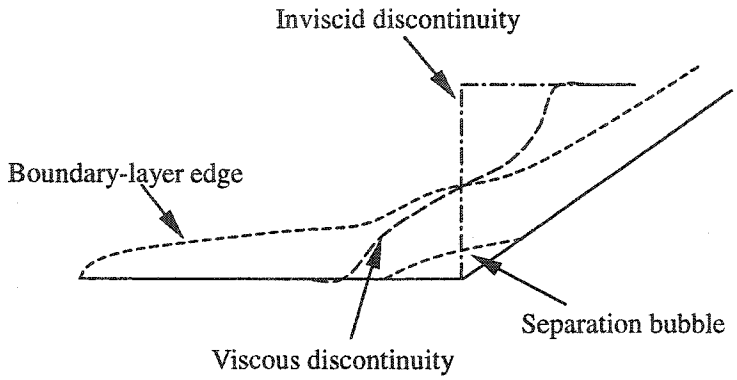

Figure 1.5c Alteration of the boundary-layer thickness under the adverse pressure gradient.

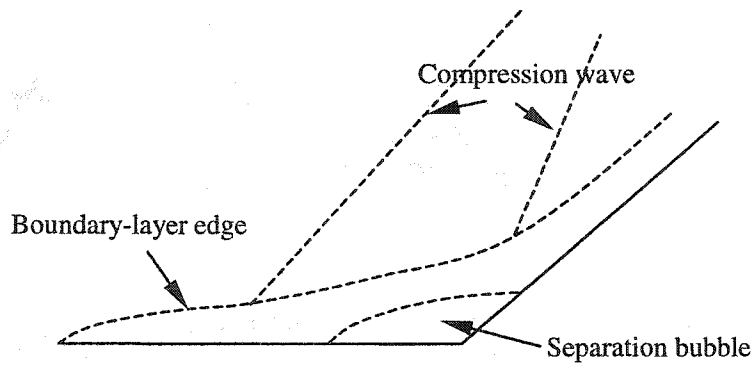

Figure 1.5d Representation of shock induced flow separation.

1.3 The stability and transition problems with the existence of shock wave and boundary-layer interaction

Compared with the boundary-layer transition along a flat plate, the transition with the existence of a shock wave and boundary-layer interaction will be more complex. The boundary-layer of hypersonic flow across a compression corner exhibits four distinct regions, as shown in Figure 1.6: (I) the boundary-layer prior to separation; (II) the mixing layer above the separation bubble in the corner; (III) the separation bubble in the corner

and (IV) the boundary-layer downstream of the separation bubble. Hence, the transition to turbulence can occur due to different instabilities which may exist in these regions. In hypersonic boundary-layers the transition is dominated by the high frequency two-dimensional second mode type disturbances[23]. Hence, upstream and downstream of the separation region, transition might occur due to this instability. But in the separation region and the mixing layer region above separation bubble, the transition mechanism is unknown. So the main objective of the current research is to investigate the boundary-layer instability and transition across these four regions by direct numerical simulations.

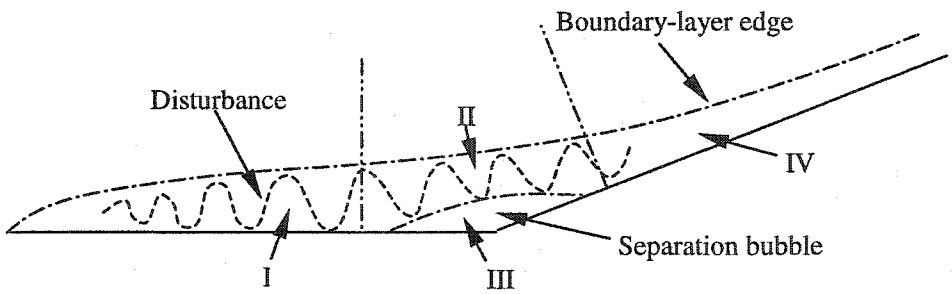

Figure 1.6 The partitions of flow regions across the compression corner.

1.4 The physical mechanism of the boundary-layer transition

The physical mechanism of transition has long been a mystery since Reynolds' milestone transition experiment in 1883. But the mechanism is becoming more and more clear, due to a large amount of experimental, theoretical and numerical work in the last few decades. A systematic description had been given by Kachanov[24][25] about the physical mechanism of laminar boundary-layer transition. In general, the transition is a result of the nonlinear response of the laminar boundary-layers to forcing disturbances. The transition process is illustrated in Figure 1.7 and follows the following five stages:

1) Receptivity.

2) Linear instability.

3) Nonlinear stability and saturation.

4) Secondary instability.

5) Breakdown to turbulence.

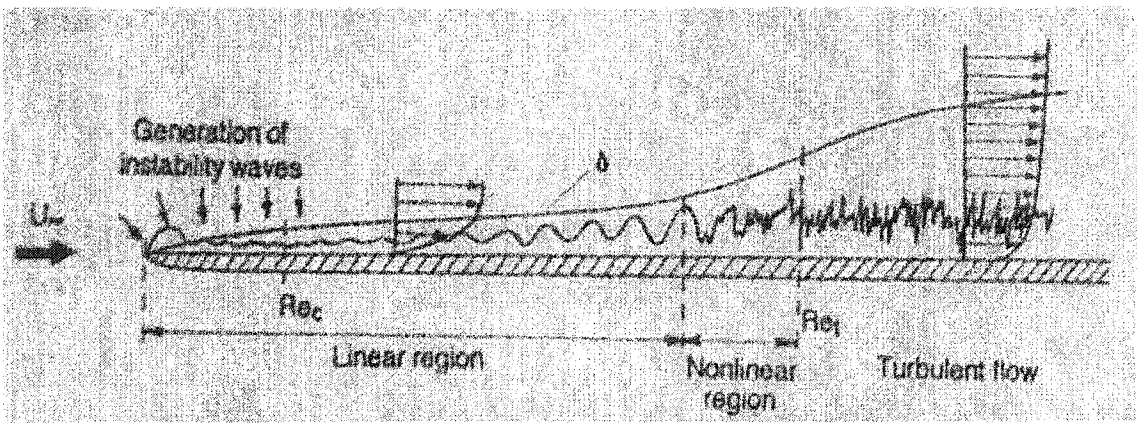

Figure 1.7 Illustration of the transition process[24].

The receptivity of boundary-layers to external disturbances is the process of converting environmental disturbances into unstable waves called Tollmien-Schlicting waves in the boundary-layers. In quiescent environments, the initial amplitudes of these unstable waves are small compared to any characteristic velocity and length scale in the flow. The receptivity mechanism provides important initial conditions in terms of amplitude, frequency and phase for these unstable waves in the boundary-layers. Goldstein[26][27] used asymptotic methods to explain theoretically how Tollmien-Schlicting waves were generated near the leading edge of a flat plate by long wavelength acoustic disturbances and he also showed the development of these waves in the boundary-layer at their initial stage. In the second stage, the amplitudes of these instability waves grow exponentially downstream and this process is governed by the linearized Navier-Stokes equations. Further downstream, the amplitude of the disturbances become so large that nonlinear effects inhibit the exponential growth and the amplitudes of the disturbance eventually saturate or attain singular values. Induced by these finite amplitude saturated disturbances, the three-dimensional disturbances begin to

grow rapidly. This is called secondary instability and can be analyzed using Floquet theory[28]. When the amplitudes of the three-dimensional disturbances reach the same order as that of the two-dimensional disturbances, the spectrum broadens due to complex nonlinear interactions and further instabilities, and the flow becomes turbulent in a short distance downstream.

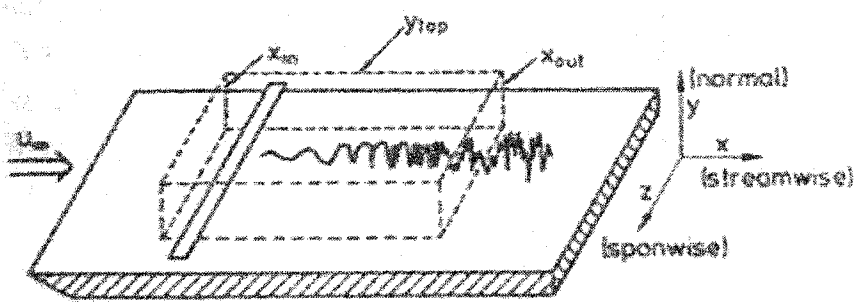

Figure 1.8 Sketch of the vibrating-ribbon transition experiment[29].

In general, transition under natural conditions is influenced by a variety of factors. Different routes to turbulence have been discovered. The classical experiment of Klebanoff *et al*[29] on forced transition in incompressible flow over a flat plat were the focal points of theoretical attempts to describe the transition process. The experiment utilized the vibrating-ribbon technique as illustrated in Figure 1.8 to force artificially finite-amplitude, monochromatic Tollmien-Schlichting(T-S) waves under carefully controlled conditions. The ribbon induces a predominantly two-dimensional disturbance, in which the least stable linear mode rapidly dominates the flow downstream of the ribbon. The resulting T-S wave evolves linearly for several wavelengths downstream. When the two-dimensional wave amplitude exceeds some critical threshold, three-dimensional disturbances are amplified as a result of the secondary instability. The fluctuations grow rapidly at the spanwise "peak" positions whereas, in between at the "valley" positions, this growth occurs only further downstream. After the three-dimensional disturbance amplitudes have attained the order of magnitude of the two-dimensional wave, the Λ-structure (lambda vortex) appears, with the tip at the peak

position. On top of the lambda vortex is induced a detached high-shear layer of the streamwise velocity, which intensifies, elongates, and eventually rolls up. An increasing number of sharp low-velocity pulses, the so-called "spikes", are then observed during each cycle in the instantaneous-velocity signals at the peak position. Later in the process, the high-shear layer breaks down, forming new smaller structures. Then, local regions of turbulence appear periodically in the streamwise and spanwise directions, and they spread as they travel downstream until a fully turbulent flow is attained.

With much credit to Mack[23], the instability and transition of compressible flow had also been well understood. He first predicted that multiple instability modes coexist in high speed flow, where the first instability mode is similar to the T-S wave in incompressible flow, and all other modes are higher acoustic modes. The first of all these acoustic modes is called the second mode. It is the second mode that is the most dangerous mode in high speed flow. It attains its peak amplification rate at a Mach number of about 4.5. It is characterized by high frequencies, is predominantly inviscid in nature, travels with a phase velocity nearly that of the mean streamwise velocity at the boundary-layer edge, and is most unstable when two-dimensional. So for the study of hypersonic flow instability and transition, the second mode instability should be a main concern.

1.5 The theories for studying the boundary-layer transition

For studying boundary-layer transition phenomena, a variety of theoretical and computational tools have been developed in the last few decades. These tools include the following: linear stability theory[23], secondary instability theory(SIT)[28], parabolized stability equations(PSE)[30], large eddy simulation(LES)[31][32], and direct numerical simulation(DNS)[33]-[46]. They are listed in order of increasing computational requirements, and the fourth and the fifth of these methods are still in the early stages of development. For an economical and revealing study of each stage in a comprehensive investigation of a complete transition process from laminar to turbulence, we see the

appropriate role for these approaches to be as follows: LST should be used to select the most important primary instability waves and, thereby, to determine the relevant streamwise scales of the instability waves. SIT disclosed the most important secondary instabilities and serves largely to determine the relevant scales in the spanwise direction. The PSE approach uses LST and SIT as a guide and provides a tool for conducting relatively inexpensive spatial simulations of the primary, secondary, and early nonlinear stages of transition. DNS builds upon the results of SIT and the PSE approach and is most appropriate for simulations of the strongly nonlinear stages of transition.

In the last few decades, linear stability theory and PSE methods have been used extensively to analyze the transition process in incompressible and compressible flat-plate and axis-symmetric boundary-layers[47]-[58]. The transition onset point can be predicted using the N-factor method. However, linear theory is applicable only to some specific transition problems, and even then it describes just the first stage of transition; that is, the slow growth of the primary instability. Subsequent stages are due to nonlinear interactions. Due to the existence of interactions between the shock wave and instability wave, the evolution of disturbance in the boundary-layer become more complex especially for boundary-layer flows with discontinuities. The linear stability theory and the PSE method cease to be valid. Direct numerical simulation is necessary for the present investigation of boundary-layer transition with the existence of shock wave and boundary-layer interaction.

1.6 Direct numerical simulation of boundary-layer transition

By direct numerical simulation, we refer to the numerical simulation of the full nonlinear, time-dependent Navier-Stokes equations without any empirical closure assumptions. This approach can provide a complete space-time history of the flow field and permit precise parametric study. It is the most accurate and appropriate method for transition and turbulence study. But the DNS are, in practice, still strongly constrained by computer resources and algorithmic limitations. Most current DNS studies are only

conducted for very simple geometries, such as the flat plates and the axisymmetric bodies. Even so, most transition investigations can only reach the early nonlinear stage. Only in a few highly idealized instances can they be conducted reliably all the way to a fully turbulent stage. Despite these limitations, direct numerical simulations of transition have played an active role in theoretical transition research since the 1980s and have formed an increasingly important complement to traditional experimental and theoretical investigations.

Direct numerical simulation includes spatial simulation and temporal simulation. From most of the transition experiments, we know that in spatial evolution of the transition, the primary and secondary instability processes take between 5 and 20 wavelengths. The laminar breakdown stage occurs roughly over two wavelengths, and the final transition to turbulence takes perhaps four more. The breakdown process involves length scales between one and two orders of magnitude smaller than the T-S scale. As a result, significantly more grid points are necessary to simulate the breakdown process. It is a daunting task to provide enough grid points to simulate the full transition process for most currently available super computers. In addition, sometimes it is difficult to provide the proper outflow boundary conditions in spatial simulations. Due to these two reasons, much current numerical simulation work has been performed in the temporal rather than the spatial setting. Here, the spatial evolution of the disturbances, resulting from time-dependent, periodic forcing, is replaced by the temporal evolution resulting from a spatially periodic initial condition. The spatial evolution of the disturbances can be appropriately obtained from the temporal evolution by the Gaster[59] transformation. Owing to the assumption of streamwise periodicity, only one wavelength need be resolved in the temporal approximation. This provides a big advantage, which saves computation time. In addition, the outflow boundary condition dilemma is circumvented.

Even though temporal simulation is more economical in computation time, it involves an intrinsic parallel flow assumption. That is, the mean flow is taken to be

constant in the streamwise direction, and the unperturbed velocity normal to the wall is neglected. The effects of boundary-layer growth can only be partially included by permitting the boundary-layer to thicken with time. So the temporal simulation is only suitable for the flat plate boundary-layer transition. For the present hypersonic boundary-layer transition across a compression corner, the mean flow will show a significant change in the streamwise direction due to the existence of the pressure discontinuity. So the temporal simulation ceased to be valid in the present study. In addition, as transition in the boundary-layer flow evolves in the streamwise direction, it is natural to simulate this process with a spatial approach.

1.7 Literatures review

As discussed above, due to a large amount of computation, accurate direct numerical simulation(DNS) are a major challenge for the complete laminar-turbulent transition process. This was a daunting task until the late 1980s, particularly for high-speed boundary-layer flow. The first tentative steps were taken by Bayliss *et al*[60] in the use of DNS to investigate transition to turbulence in supersonic, wall-bounded flows. They presented the first DNS result for supersonic boundary-layer flow along a flat plate. These results were for spatially evolving, but two-dimensional flow. The first three-dimensional DNS of a perturbed high-speed(Mach 4.5) flat-plate boundary-layer flow was accomplished by Erlebacher and Hussaini[61]. This numerical experiment used temporal DNS to examine boundary-layer stability, but stopped far short of attaining a transitional state.

Due partly to increased supercomputer capacity, there have been many recent noteworthy three-dimensional simulations of compressible wall-bounded flows. Among these are temporal simulation by Normand and Lesieur[32], Pruett and Zang[36], Adams and Kleiser[38]; and spatial simulations by Maestrello *et al.*[62], Normand and Lesieur[32], Eissler and Bestek[63], Ng and Zang[64], and Pruett and Chang[33][35].

From this literature we note that most DNS of boundary-layer transition are

performed for the flat plate and axisymmetric boundary-layers. As to the DNS of boundary-layer transition with the existence of an adverse pressure gradient and flow separation, little work has thus for been done. However, transition arising from a separated region of flow is quite common and plays an important role in engineering. It is difficult to predict using conventional models and the transition mechanism is still not fully understood. The transition mechanism in the separation bubble was studied by Spalart & Strelets[65] using large-eddy simulation, and also by Yang and Voke[66] using direct numerical simulation in incompressible flow. Their results show that the instability mechanism in the separation bubble for incompressible flow is dominated by Kelvin-Helmholtz instability. However, for the high-speed flow going through a compression corner, the flow separates due to shock wave/boundary-layer interaction. The boundary-layer transition mechanism will be different from that of the incompressible flow in the separation bubble. And so far, no literature has been found that deals with boundary-layer instability and transition including shock wave/boundary-layer interactions.

1.8 Outline of the present research

The main objective of present research is to study the boundary-layer instability and transition across a compression corner under hypersonic flow conditions by direct numerical simulation. But the linear stability theory, PSE method, as well as Gortler instability theory will also be used in the present investigation. According to the content of the present research, the thesis will include the following chapters.

In chapter 2, the governing equations and the solution algorithm for LST, PSE, Gortler instability and DNS will be presented.

In chapter 3, the two-dimensional mean flow across the compression corner will be obtained by two-dimensional steady computation.

In chapter 4, the LST will be used to perform the parametric study for two- and three-dimensional disturbance evolution across the compression corner. The Gortler

instability computation will also be performed in this chapter.

In chapter 5, the DNS is used to study the two-dimensional linear and nonlinear disturbance evolution across the compression corner.

In chapter 6, the DNS is used to study the three-dimensional linear and nonlinear disturbance evolution across the compression corner. Random frequency disturbances evolution will also be simulated in this chapter.

In chapter 7, conclusions of the present research and the recommendations for future research will be presented.

CHAPTER II

GOVERNING EQUATIONS AND SOLUTION ALGORITHM

In the present investigation, the main objective is to use DNS to simulate the two-dimensional and oblique disturbance evolution across the compression corner, we will focus on the numerical scheme required to solve two- and three-dimensional compressible Navier-Stokes equation. On the other hand, in order to perform the parametric study and validate the DNS codes, as well as provide the initial disturbance for DNS, we need to solve linearized Navier-Stokes equations such as LST and PSE. In addition, Gortler instability computations should also be performed to study the influence of streamline curvature. In this chapter, we will first present the full three-dimensional compressible Navier-Stokes equations. Then we will give a derivation for LST, PSE and Gortler instability theory, as well as the numerical schemes to solve these linearized Navier-Stokes equations. Finally, we will focus on the numerical schemes of DNS.

2.1 Three-dimensional compressible Navier-Stokes equations

The vector forms of the three-dimensional compressible Navier-Stokes equations in a Cartesion coordinate system can be expressed as equations (2.1)-(2.4). Where the superscript ' * ' stands for the dimensional variables.

Continuity equation

$$\frac{\partial \rho^*}{\partial t^*} + \nabla \cdot \rho^* \mathbf{V}^* = \mathbf{0} \tag{2.1}$$

Momentum equations

$$\rho^* \left(\frac{\partial \mathbf{V}^*}{\partial t^*} + \mathbf{V}^* \cdot \nabla \mathbf{V}^*\right) = \nabla \cdot \Pi \tag{2.2}$$

Energy equation

$$\rho^* C_V \left(\frac{\partial T^*}{\partial t^*} + \mathbf{V}^* \cdot \nabla T^*\right) = \nabla \cdot k_T^* \nabla T^* + \Phi \tag{2.3}$$

Equation of state

$$p^* = R\rho^* T^* \tag{2.4}$$

The gas is assumed to be thermally and calorically perfect. Π represents the stress tensor, which consists of normal and shearing stresses. Its components τ_{ij}^* can be expressed as equation (2.5), where the Stokes hypothesis $\lambda^*=-2/3\mu^*$ is enforced.

$$\tau_{ij}^* = -p^* \delta_{ij} + \mu^* \left[\frac{\partial u_i^*}{\partial x_j^*} + \frac{\partial u_j^*}{\partial x_i^*} - \frac{2}{3}\delta_{ij}\frac{\partial u_k^*}{\partial x_k^*}\right];\ i, j, k = 1,2\,or\,3 \tag{2.5}$$

And Φ is the dissipation term in the energy equation. It can be expressed as

$$\Phi = \tau_{ij}^* e_{ij}^*;\ i, j = 1,2,3 \tag{2.6}$$

where

$$e_{ij}^* = \frac{1}{2}\left(\frac{\partial u_i^*}{\partial x_j^*} + \frac{\partial u_j^*}{\partial x_i^*}\right) \tag{2.7}$$

The viscousity coefficient μ^* and thermal conductivity, k_T^*, are calculated using Sutherland's law together with a constant Prandtl number p_r.

$$\mu^* = \frac{c_1 T^{*\frac{3}{2}}}{T^* + c_2} \tag{2.8}$$

where c_1=7.30246×10^{-7}, c_2=198.7°R

$$k_T^* = \frac{\gamma}{\gamma - 1}\frac{1}{p_r}\mu^* \tag{2.9}$$

where γ is the specific heat coefficient, $\gamma = 1.4$ and $p_r = 0.7$.

2.2 Non-dimensionalization of the governing equations

As is customary and convenient, the governing equations must be

non-dimensionalized using some characteristic quantities. The density, ρ^*, temperature, T^*, velocity, u_i^*, and viscousity coefficient, μ^*, are non-dimensionalized by their corresponding upstream reference values, ρ_∞^*, T_∞^*, U_∞^* and μ_∞^*, respectively. The pressure is non-dimensionalized by the quantity $\rho_\infty^* U_\infty^{*2}$. The reference value for length is computed by

$$L^* = \sqrt{\frac{\nu_\infty^* x_0^*}{U_\infty^*}} \tag{2.10}$$

where x_0^* is the location of the beginning of computational domain in the streamwise direction.

So using the above characteristic quantities, we can get the non-dimensional variables as follows:

$$x_i = \frac{x_i^*}{L^*}; \qquad t = \frac{t^*}{L^*/U_\infty^*}; \qquad u_i = \frac{u_i^*}{U_\infty^*}; \qquad \mu = \frac{\mu^*}{\mu_\infty^*}$$

$$\rho = \frac{\rho^*}{\rho_\infty^*}; \qquad p = \frac{p^*}{\rho_\infty^* U_\infty^{*2}}; \qquad T = \frac{T^*}{T_\infty^*}; \qquad \mathrm{Re} = \frac{\rho_\infty^* U_\infty^* L^*}{\mu_\infty^*}$$

The non-dimensionalized Navier-Stokes equations are given in equations (2.11)-(2.16). Where x_1, x_2, x_3 stand for the coordinates in the streamwise direction, the wall normal direction, and the spanwise direction respectively, and u_1, u_2, u_3 stand for the corresponding velocity components in these three directions.

Continuity equation

$$\frac{\partial \rho}{\partial t} + \frac{\partial}{\partial x_1}(\rho u_1) + \frac{\partial}{\partial x_2}(\rho u_2) + \frac{\partial}{\partial x_3}(\rho u_3) = 0 \tag{2.11}$$

Momentum equations

$$\rho\left(\frac{\partial u_1}{\partial t}+u_1\frac{\partial u_1}{\partial x_1}+u_2\frac{\partial u_1}{\partial x_2}+u_3\frac{\partial u_1}{\partial x_3}\right)$$

$$=-\frac{\partial p}{\partial x_1}+\frac{1}{\mathrm{Re}}\left\{\frac{2}{3}\frac{\partial}{\partial x_1}\left[\mu\left(2\frac{\partial u_1}{\partial x_1}-\frac{\partial u_2}{\partial x_2}-\frac{\partial u_3}{\partial x_3}\right)\right]\right. \tag{2.12}$$

$$\left.+\frac{\partial}{\partial x_2}\left[\mu\left(\frac{\partial u_1}{\partial x_2}+\frac{\partial u_2}{\partial x_1}\right)\right]+\frac{\partial}{\partial x_3}\left[\mu\left(\frac{\partial u_1}{\partial x_3}+\frac{\partial u_3}{\partial x_1}\right)\right]\right\}$$

$$\rho\left(\frac{\partial u_2}{\partial t}+u_1\frac{\partial u_2}{\partial x_1}+u_2\frac{\partial u_2}{\partial x_2}+u_3\frac{\partial u_2}{\partial x_3}\right)$$

$$=-\frac{\partial p}{\partial x_2}+\frac{1}{\mathrm{Re}}\left\{\frac{2}{3}\frac{\partial}{\partial x_2}\left[\mu\left(2\frac{\partial u_2}{\partial x_2}-\frac{\partial u_1}{\partial x_1}-\frac{\partial u_3}{\partial x_3}\right)\right]\right. \tag{2.13}$$

$$\left.+\frac{\partial}{\partial x_1}\left[\mu\left(\frac{\partial u_1}{\partial x_2}+\frac{\partial u_2}{\partial x_1}\right)\right]+\frac{\partial}{\partial x_3}\left[\mu\left(\frac{\partial u_2}{\partial x_3}+\frac{\partial u_3}{\partial x_2}\right)\right]\right\}$$

$$\rho\left(\frac{\partial u_3}{\partial t}+u_1\frac{\partial u_3}{\partial x_1}+u_2\frac{\partial u_3}{\partial x_2}+u_3\frac{\partial u_3}{\partial x_3}\right)$$

$$=-\frac{\partial p}{\partial x_3}+\frac{1}{\mathrm{Re}}\left\{\frac{2}{3}\frac{\partial}{\partial x_3}\left[\mu\left(2\frac{\partial u_3}{\partial x_3}-\frac{\partial u_2}{\partial x_2}-\frac{\partial u_1}{\partial x_1}\right)\right]\right. \tag{2.14}$$

$$\left.+\frac{\partial}{\partial x_2}\left[\mu\left(\frac{\partial u_3}{\partial x_2}+\frac{\partial u_2}{\partial x_3}\right)\right]+\frac{\partial}{\partial x_1}\left[\mu\left(\frac{\partial u_1}{\partial x_3}+\frac{\partial u_3}{\partial x_1}\right)\right]\right\}$$

Energy equation

$$\rho\left(\frac{\partial T}{\partial t}+u_1\frac{\partial T}{\partial x_1}+u_2\frac{\partial T}{\partial x_2}+u_3\frac{\partial T}{\partial x_3}\right)$$

$$=\frac{\gamma}{P_r\,\mathrm{Re}}\left[\frac{\partial}{\partial x_1}\left(\mu\frac{\partial T}{\partial x_1}\right)+\frac{\partial}{\partial x_2}\left(\mu\frac{\partial T}{\partial x_2}\right)+\frac{\partial}{\partial x_3}\left(\mu\frac{\partial T}{\partial x_3}\right)\right]$$

$$+\gamma(\gamma-1)\frac{M_\infty^2}{\mathrm{Re}}\left\{2\mu\left[\left(\frac{\partial u_1}{\partial x_1}\right)^2+\left(\frac{\partial u_2}{\partial x_2}\right)^2+\left(\frac{\partial u_3}{\partial x_3}\right)^2\right]\right.$$
$$-\frac{2}{3}\mu\left(\frac{\partial u_1}{\partial x_1}+\frac{\partial u_2}{\partial x_2}+\frac{\partial u_3}{\partial x_3}\right)^2+\mu\left[\left(\frac{\partial u_1}{\partial x_2}+\frac{\partial u_2}{\partial x_1}\right)^2+\left(\frac{\partial u_1}{\partial x_3}+\frac{\partial u_3}{\partial x_1}\right)^2\right. \tag{2.15}$$
$$\left.\left.+\left(\frac{\partial u_3}{\partial x_2}+\frac{\partial u_2}{\partial x_3}\right)^2\right]\right\}-\gamma(\gamma-1)M_\infty^2 p\left(\frac{\partial u_1}{\partial x_1}+\frac{\partial u_2}{\partial x_2}+\frac{\partial u_3}{\partial x_3}\right)$$

State equation

$$p=\frac{\rho T}{\gamma M_\infty^2} \tag{2.16}$$

2.3 Linearization of the governing equations

The principle of classical stability theory evolves around the concept of determining whether a small disturbance introduced into a laminar boundary-layer will amplify or decay. If the disturbance decays, the boundary-layer is stable and if the disturbance grows, the boundary-layer is unstable. In stability theory, the first step in the methodology of analyzing the evolution of small disturbance is to assume the total flow as composed of mean quantities and small disturbance quantities. That is

$$u_1=\overline{U}_1+u_1' \tag{2.17}$$

$$u_2=\overline{U}_2+u_2' \tag{2.18}$$

$$u_3=\overline{U}_3+u_3' \tag{2.19}$$

$$\rho=\overline{\rho}+\rho' \tag{2.20}$$

$$p=\overline{p}+p' \tag{2.21}$$

$$T=\overline{T}+T' \tag{2.22}$$

$$\mu=\overline{\mu}+\mu' \tag{2.23}$$

where the symbol "–" stands for the mean flow quantities and the symbol " ' " stands for

the disturbance quantities.

Now we substitute the above total quantities into the dimensionless Navier-Stokes equations which are given in equations (2.11)-(2.16). Compared with the mean quantities, the disturbance quantities are very small. So the higher order nonlinear terms can be neglected. In addition, the present research analyzes the instability of two-dimensional boundary-layers. The mean flow is two-dimensional. And the mean flow velocity in the spanwise direction is zero, that is $\overline{U}_3 = 0$. So we can neglect the linear terms concerned with $\overline{U}_3$. Finally, because the viscosity is a function only of temperature, we have the following equations

$$\mu' = \frac{\partial \overline{\mu}}{\partial \overline{T}} T' \tag{2.24}$$

$$\frac{\partial \mu'}{\partial x_i} = \frac{\partial^2 \overline{\mu}}{\partial \overline{T}^2} \frac{\partial \overline{T}}{\partial x_i} T' + \frac{\partial \overline{\mu}}{\partial \overline{T}} \frac{\partial T'}{\partial x_i} \tag{2.25}$$

$$\frac{\partial \overline{\mu}}{\partial x_i} = \frac{\partial \overline{\mu}}{\partial \overline{T}} \frac{\partial \overline{T}}{\partial x_i} \tag{2.26}$$

Then after some manipulations of the equations, we can write the linearized Navier-Stokes equation as

Continuity equation

$$\begin{aligned} &\frac{\partial \rho'}{\partial t} + \overline{\rho} \frac{\partial u_1'}{\partial x_1} + u_1' \frac{\partial \overline{\rho}}{\partial x_1} + \overline{U}_1 \frac{\partial \rho'}{\partial x_1} + \rho' \frac{\partial \overline{U}_1}{\partial x_1} + \overline{\rho} \frac{\partial u_2'}{\partial x_2} \\ &+ u_2' \frac{\partial \overline{\rho}}{\partial x_2} + \overline{U}_2 \frac{\partial \rho'}{\partial x_2} + \rho' \frac{\partial \overline{U}_2}{\partial x_2} + \overline{\rho} \frac{\partial u_3'}{\partial x_3} = 0 \end{aligned} \tag{2.27}$$

Momentum equations

$$\overline{\rho}\left(\frac{\partial u_1'}{\partial t} + \overline{U}_1 \frac{\partial u_1'}{\partial x_1} + \overline{U}_2 \frac{\partial u_1'}{\partial x_2} + \frac{\partial \overline{U}_1}{\partial x_1} u_1' + \frac{\partial \overline{U}_1}{\partial x_2} u_2' \right) + \left(\overline{U}_1 \frac{\partial \overline{U}_1}{\partial x_1} + \overline{U}_2 \frac{\partial \overline{U}_1}{\partial x_2} \right) \rho'$$

$$= -\frac{\partial p'}{\partial x_1} + \frac{1}{\mathrm{Re}}\left[\frac{2}{3}\frac{\partial \overline{\mu}}{\partial \overline{T}}\frac{\partial \overline{T}}{\partial x_1}\left(2\frac{\partial u_1'}{\partial x_1} - \frac{\partial u_2'}{\partial x_2} - \frac{\partial u_3'}{\partial x_3}\right)\right.$$

$$+\overline{\mu}\left(\frac{4}{3}\frac{\partial^2 u_1'}{\partial x_1^2} + \frac{\partial^2 u_1'}{\partial x_2^2} + \frac{\partial^2 u_1'}{\partial x_3^2}\right) + \frac{\partial \overline{\mu}}{\partial \overline{T}}\frac{\partial \overline{T}}{\partial x_2}\left(\frac{\partial u_1'}{\partial x_2} + \frac{\partial u_2'}{\partial x_1}\right)$$

$$+\frac{1}{3}\overline{\mu}\left(\frac{\partial^2 u_2'}{\partial x_1 \partial x_2} + \frac{\partial^2 u_3'}{\partial x_1 \partial x_3}\right) + \left(\frac{4}{3}\frac{\partial^2 \overline{U}_1}{\partial x_1^2} + \frac{\partial^2 \overline{U}_1}{\partial x_2^2} + \frac{1}{3}\frac{\partial^2 \overline{U}_2}{\partial x_1 \partial x_2}\right)\frac{\partial \overline{\mu}}{\partial \overline{T}}T' \qquad (2.28)$$

$$+\left(\frac{4}{3}\frac{\partial \overline{U}_1}{\partial x_1} - \frac{2}{3}\frac{\partial \overline{U}_2}{\partial x_2}\right)\cdot\left(\frac{\partial^2 \overline{\mu}}{\partial \overline{T}^2}\frac{\partial \overline{T}}{\partial x_1}T' + \frac{\partial \overline{\mu}}{\partial \overline{T}}\frac{\partial T'}{\partial x_1}\right)$$

$$\left.+\left(\frac{\partial \overline{U}_1}{\partial x_2} + \frac{\partial \overline{U}_2}{\partial x_1}\right)\cdot\left(\frac{\partial^2 \overline{\mu}}{\partial \overline{T}^2}\frac{\partial \overline{T}}{\partial x_2}T' + \frac{\partial \overline{\mu}}{\partial \overline{T}}\frac{\partial T'}{\partial x_2}\right)\right]$$

$$\overline{\rho}\left(\frac{\partial u_2'}{\partial t} + \overline{U}_1\frac{\partial u_2'}{\partial x_1} + \overline{U}_2\frac{\partial u_2'}{\partial x_2} + \frac{\partial \overline{U}_2}{\partial x_1}u_1' + \frac{\partial \overline{U}_2}{\partial x_2}u_2'\right) + \left(\overline{U}_1\frac{\partial \overline{U}_2}{\partial x_1} + \overline{U}_2\frac{\partial \overline{U}_2}{\partial x_2}\right)\rho'$$

$$= -\frac{\partial p'}{\partial x_2} + \frac{1}{\mathrm{Re}}\left[\frac{2}{3}\frac{\partial \overline{\mu}}{\partial \overline{T}}\frac{\partial \overline{T}}{\partial x_2}\left(2\frac{\partial u_2'}{\partial x_2} - \frac{\partial u_1'}{\partial x_1} - \frac{\partial u_3'}{\partial x_3}\right)\right.$$

$$+\overline{\mu}\left(\frac{4}{3}\frac{\partial^2 u_2'}{\partial x_2^2} + \frac{\partial^2 u_2'}{\partial x_1^2} + \frac{\partial^2 u_2'}{\partial x_3^2}\right) + \frac{\partial \overline{\mu}}{\partial \overline{T}}\frac{\partial \overline{T}}{\partial x_1}\left(\frac{\partial u_2'}{\partial x_1} + \frac{\partial u_1'}{\partial x_2}\right)$$

$$+\frac{1}{3}\overline{\mu}\left(\frac{\partial^2 u_1'}{\partial x_1 \partial x_2} + \frac{\partial^2 u_3'}{\partial x_2 \partial x_3}\right) + \left(\frac{4}{3}\frac{\partial^2 \overline{U}_2}{\partial x_2^2} + \frac{\partial^2 \overline{U}_2}{\partial x_1^2} + \frac{1}{3}\frac{\partial^2 \overline{U}_1}{\partial x_1 \partial x_2}\right)\frac{\partial \overline{\mu}}{\partial \overline{T}}T'$$

$$+\left(\frac{4}{3}\frac{\partial \overline{U}_2}{\partial x_2} - \frac{2}{3}\frac{\partial \overline{U}_1}{\partial x_1}\right)\cdot\left(\frac{\partial^2 \overline{\mu}}{\partial \overline{T}^2}\frac{\partial \overline{T}}{\partial x_2}T' + \frac{\partial \overline{\mu}}{\partial \overline{T}}\frac{\partial T'}{\partial x_2}\right)$$

$$\left.+\left(\frac{\partial \overline{U}_1}{\partial x_2} + \frac{\partial \overline{U}_2}{\partial x_1}\right)\cdot\left(\frac{\partial^2 \overline{\mu}}{\partial \overline{T}^2}\frac{\partial \overline{T}}{\partial x_1}T' + \frac{\partial \overline{\mu}}{\partial \overline{T}}\frac{\partial T'}{\partial x_1}\right)\right] \qquad (2.29)$$

$$\overline{\rho}\left(\frac{\partial u_3'}{\partial t} + \overline{U}_1\frac{\partial u_3'}{\partial x_1} + \overline{U}_2\frac{\partial u_3'}{\partial x_2}\right)$$

$$= -\frac{\partial p'}{\partial x_3} + \frac{1}{\mathrm{Re}}\left[\overline{\mu}\left(\frac{4}{3}\frac{\partial^2 u_3'}{\partial x_3^2} + \frac{\partial^2 u_3'}{\partial x_1^2} + \frac{\partial^2 u_3'}{\partial x_2^2}\right)\right.$$

$$+ \frac{\partial \overline{\mu}}{\partial \overline{T}}\frac{\partial \overline{T}}{\partial x_1}\left(\frac{\partial u_3'}{\partial x_1} + \frac{\partial u_1'}{\partial x_3}\right) + \frac{\partial \overline{\mu}}{\partial \overline{T}}\frac{\partial \overline{T}}{\partial x_2}\left(\frac{\partial u_3'}{\partial x_2} + \frac{\partial u_2'}{\partial x_3}\right) \tag{2.30}$$

$$\left. + \frac{1}{3}\overline{\mu}\left(\frac{\partial^2 u_1'}{\partial x_1 \partial x_3} + \frac{\partial^2 u_2'}{\partial x_2 \partial x_3}\right) - \frac{2}{3}\left(\frac{\partial \overline{U}_1}{\partial x_1} + \frac{\partial \overline{U}_2}{\partial x_2}\right)\cdot\frac{\partial \overline{\mu}}{\partial \overline{T}}\frac{\partial T'}{\partial x_3}\right]$$

Energy equation

$$\overline{\rho}\left(\frac{\partial T'}{\partial t} + \overline{U}_1\frac{\partial T'}{\partial x_1} + \overline{U}_2\frac{\partial T'}{\partial x_2} + \frac{\partial \overline{T}}{\partial x_1}u_1' + \frac{\partial \overline{T}}{\partial x_2}u_2'\right) + \left(\overline{U}_1\frac{\partial \overline{T}}{\partial x_1} + \overline{U}_2\frac{\partial \overline{T}}{\partial x_2}\right)\rho'$$

$$= \frac{\gamma}{P_r\,\mathrm{Re}}\left[\frac{\partial \overline{\mu}}{\partial \overline{T}}\left(\frac{\partial \overline{T}}{\partial x_1}\frac{\partial T'}{\partial x_1} + \frac{\partial \overline{T}}{\partial x_2}\frac{\partial T'}{\partial x_2}\right) + \overline{\mu}\left(\frac{\partial^2 T'}{\partial x_1^2} + \frac{\partial^2 T'}{\partial x_2^2} + \frac{\partial^2 T'}{\partial x_3^2}\right)\right.$$

$$+ \frac{\partial \overline{T}}{\partial x_1}\left(\frac{\partial^2 \overline{\mu}}{\partial \overline{T}^2}\frac{\partial \overline{T}}{\partial x_1}T' + \frac{\partial \overline{\mu}}{\partial \overline{T}}\frac{\partial T'}{\partial x_1}\right) + \frac{\partial \overline{T}}{\partial x_2}\left(\frac{\partial^2 \overline{\mu}}{\partial \overline{T}^2}\frac{\partial \overline{T}}{\partial x_2}T' + \frac{\partial \overline{\mu}}{\partial \overline{T}}\frac{\partial T'}{\partial x_2}\right)$$

$$\left. + \left(\frac{\partial^2 \overline{T}}{\partial x_1^2} + \frac{\partial^2 \overline{T}}{\partial x_2^2}\right)\frac{\partial \overline{\mu}}{\partial \overline{T}}T'\right] + \gamma(\gamma-1)\frac{M_\infty^2}{\mathrm{Re}}\left\{\left[2\left(\frac{\partial \overline{U}_1}{\partial x_1}\right)^2 + 2\left(\frac{\partial \overline{U}_2}{\partial x_2}\right)^2\right.\right.$$

$$+ \frac{2}{3}\left(\frac{\partial \overline{U}_1}{\partial x_1} + \frac{\partial \overline{U}_2}{\partial x_2}\right)^2 + \left.\left(\frac{\partial \overline{U}_1}{\partial x_2} + \frac{\partial \overline{U}_2}{\partial x_1}\right)^2\right]\frac{\partial \overline{\mu}}{\partial \overline{T}}T' + \frac{4}{3}\overline{\mu}\left(4\frac{\partial \overline{U}_1}{\partial x_1} + \frac{\partial \overline{U}_2}{\partial x_2}\right)\frac{\partial u_1'}{\partial x_1}$$

$$+ \frac{4}{3}\overline{\mu}\left(\frac{\partial \overline{U}_1}{\partial x_1} + 4\frac{\partial \overline{U}_2}{\partial x_2}\right)\frac{\partial u_2'}{\partial x_2} + \frac{4}{3}\overline{\mu}\left(\frac{\partial \overline{U}_1}{\partial x_1} + \frac{\partial \overline{U}_2}{\partial x_2}\right)\frac{\partial u_3'}{\partial x_3} + 2\overline{\mu}\left(\frac{\partial \overline{U}_1}{\partial x_2} + \frac{\partial \overline{U}_2}{\partial x_1}\right) \tag{2.31}$$

$$\left.\left.\cdot\left(\frac{\partial u_2'}{\partial x_1} + \frac{\partial u_1'}{\partial x_2}\right)\right]\right\} - \gamma(\gamma-1)M_\infty^2\left[\overline{p}\left(\frac{\partial u_1'}{\partial x_1} + \frac{\partial u_2'}{\partial x_2} + \frac{\partial u_3'}{\partial x_3}\right) + \left(\frac{\partial \overline{U}_1}{\partial x_1} + \frac{\partial \overline{U}_2}{\partial x_2}\right)p'\right]$$

State equation

$$p' = \frac{1}{\gamma M_\infty^2}(\overline{T}\rho' + \overline{\rho}T') \tag{2.32}$$

2.4 Linear stability theory(LST)

Despite its limitations, the linear stability theory is still of great interest as a tool for the semi-empirical prediction of transition to turbulence. Currently, the preferred linear stability predictive method in industry for transition in incompressible flow over complex geometries rests on the Orr-Sommerfeld equation given as equation (2.33).

$$(\overline{U}_1 - c)(\varphi'' - \alpha^2\varphi) - \overline{U}_1''\varphi = -\frac{i}{\alpha \,\mathrm{Re}}(\varphi'''' - 2\alpha^2\varphi'' + \alpha^4) \tag{2.33}$$

The compressible analogue of the Orr-Sommerfeld equation is a coupled set of five ordinary differential equations. These include three second-order momentum equations, one second-order energy equation, and one first-order continuity equation. So the derivation and numerical solution of LST in compressible flow is much more complicated.

2.4.1 The derivation of LST

Following the formulation of the stability theory given by Mack[23] in 1969, the linear stability theory for a three-dimensional compressible boundary-layer is derived in this section. To derive the linear stability theory, the flow is assumed to be locally parallel. Since variations of the mean flow in the streamwise directions are much slower than in the normal direction, one assumes that the mean flow quantities only depend on the wall-normal coordinate and the normal mean flow component is zero. That is

$$\overline{U}_2 = 0; \quad \frac{\partial \overline{U}_1}{\partial x_1} = 0 \tag{2.34}$$

A normal mode formulation is employed for the disturbance quantities. The disturbance quantities as written in equation (2.35) consist of a complex amplitude vector that depends only on the wall-normal coordinate, and a complex phase that allows for periodic variations in the wall-parallel directions and in time.

$$\begin{bmatrix} u_1'(x_1,x_2,x_3,t) \\ u_2'(x_1,x_2,x_3,t) \\ u_3'(x_1,x_2,x_3,t) \\ \rho'(x_1,x_2,x_3,t) \\ p'(x_1,x_2,x_3,t) \\ T'(x_1,x_2,x_3,t) \end{bmatrix} = \begin{bmatrix} \hat{u}_1(x_2) \\ \hat{u}_2(x_2) \\ \hat{u}_3(x_2) \\ \hat{\rho}(x_2) \\ \hat{p}(x_2) \\ \hat{T}(x_2) \end{bmatrix} e^{i(\alpha x_1+\beta x_3-\omega t)} \tag{2.35}$$

where $\hat{u}_1,\hat{u}_2,\hat{u}_3,\hat{\rho},\hat{p},\hat{T}$ are the complex amplitude functions of the flow variables $u_1',u_2',u_3',\rho',p',T'$ respectively. α and β are the dimensionless wave numbers $2\pi L^*/\lambda_x^*$ and $2\pi L^*/\lambda_z^*$, where λ_x^* and λ_z^* are the wavelengths in streamwise and spanwise directions respectively; and ω is the dimensionless frequency $\omega^* L^*/U_\infty^*$.

Now we substitute the above disturbance quantities into the linearized Navier-Stoke equations given in equations (2.27-2.32) and rearrange. After collecting the coefficients, we can get eight first order differential equations written in matrix form as following

$$\frac{d\hat{\mathbf{q}}}{dx_2} = A_0\hat{\mathbf{q}} \tag{2.36}$$

where A_0 is an 8×8 coefficient matrix and the elements a_{ij} of this matrix are given in Appendix I.

$$\hat{\mathbf{q}} = [\hat{u}_1, \frac{d\hat{u}_1}{dx_2}, \hat{u}_2, \frac{d\hat{u}_2}{dx_2}, \hat{T}, \frac{d\hat{T}}{dx_2}, \hat{u}_3, \hat{p}]^T \tag{2.37}$$

The boundary conditions are

$$\hat{u}_1 = \hat{u}_2 = \hat{u}_3 = \hat{T} = 0, \text{ at } x_2 = 0 \tag{2.38}$$

and

$$\hat{u}_1,\hat{u}_2,\hat{u}_3,\hat{T} \to 0, \text{ as } x_2 \to \infty \tag{2.39}$$

2.4.2 The temporal and spatial amplification theory

The first order differential equations derived above along with the homogenous

boundary conditions are actually an eigenvalue problem that can be simply written as:

$$F(\alpha, \beta, \omega, \mathrm{Re}) = 0 \tag{2.40}$$

For a given Reynolds number, if any pair of the three variables α, β, ω are known, we can obtain the third variable from the above equation. If α or β are complex, the disturbance amplitude will change in either the streamwise or spanwise direction. If ω is complex, then the disturbance amplitude will change in time. The former case is referred to as spatial amplification theory, the latter as the temporal amplification theory. If all three quantities are complex, the disturbance amplitude will change in both space and time. In temporal theory, we can express ω as $\omega = \alpha c$, where $c = c_r + ic_i$, c_r is the phase velocity and c_i is the temporal amplification rate.

For temporal amplification theory, there are three possible cases:

$c_i < 0$, damped disturbance

$c_i = 0$, neutral disturbance

$c_i > 0$, amplified disturbance

And for spatial amplification theory, there are also three possible cases:

$\alpha_i > 0$, damped disturbance

$\alpha_i = 0$, neutral disturbance

$\alpha_i < 0$, amplified disturbance

2.4.3 The numerical scheme to solve LST

The numerical methods for solving the relevant eigenvalue problem can be broadly classified into initial value methods and boundary value methods. The initial value methods(IVM) consist of constructing independent initial value problems whose solutions satisfy the eighth-order set of differential equations and conditions at the

free-stream boundary. The solution is integrated towards the solid boundary by using Runge-Kutta integration and it is required that a linear combination of the solutions satisfies the boundary conditions at the wall. In other words, the relevant characteristic determinant is made to vanish, thus yielding the eigenvalue of the differential system. The main advantage of IVM is the minimal computer memory requirement and their capacity to adjust the integration to local conditions. The disadvantage is that they require a good guess of the eigenvalue. For spatial stability of high Mach number flows, this may require that the eigenvalue be known to be accurate to three or four decimal places for the method to converge. This also means that there is always a risk of missing some modes.

In the boundary value methods(BVM), the differential equations are reduced to linear algebraic equations using either a finite-difference discretization or a spectral representation. The global eigenvalues can be obtained by solving the characteristic determinant of a generalized eigenvlue problem. The number of eigenvalues thus obtained is proportional to the number of grid points used. If a guess of the eigenvalue is available, then the eigenvalue may be purified by a local eigenvalue search procedure involving matrix inversion and Newton iteration. The main advantage of BVM is its ability to yield eigenvalues when no prior knowledge of the instability is available for the problem of interest.

Based on BVM, a fourth order accurate two-point compact scheme was derived by Malik, Chuang and Hussaini[51] using the Euler-Maclaurin formula:

$$\Psi^k - \Psi^{k-1} = \frac{h_k}{2}\left(\frac{d\Psi^k}{dx_2} + \frac{d\Psi^{k-1}}{dx_2}\right) - \frac{h_k^2}{12}\left(\frac{d^2\Psi^k}{dx_2^2} + \frac{d^2\Psi^{k-1}}{dx_2^2}\right) + O(h_k^5) \qquad (2.41)$$

where $h_k = x_2(k) - x_2(k-1)$, $k = 1,2,\cdots N$

In order to apply this scheme to the first order equations (2.36), we set

$$\Psi = \{\hat{q}_i\}; \quad \frac{d\Psi}{dx_2} = \left\{\sum_{j=1}^{8} a_{ij}\hat{q}_j\right\}; \quad \frac{d^2\Psi}{dx_2^2} = \left\{\sum_{j=1}^{8} b_{ij}\hat{q}_j\right\} \qquad (2.42)$$

where

$$b_{ij} = \frac{da_{ij}}{dx_2} + \sum_{l}^{8} a_{il} a_{lj} \tag{2.43}$$

Substituting the above equations into equation (2.41), we get,

$$\hat{q}_i^k - \frac{h_k}{2}\sum_{j=1}^{8} a_{ij}^k \hat{q}_j^k + \frac{h_k^2}{12}\sum_{j=1}^{8} b_{ij}^k \hat{q}_j^k - \left[\hat{q}_i^{k-1} + \frac{h_k}{2}\sum_{j=1}^{8} a_{ij}^{k-1}\hat{q}_j^{k-1} - \frac{h_k^2}{12}\sum_{j=1}^{8} b_{ij}^{k-1}\hat{q}_j^{k-1}\right] = 0 \tag{2.44}$$

This equation along with the boundary conditions given in equations (2.38) and (2.39), can be written in block tridiagonal form as

$$A_k \hat{\mathbf{q}}^{k-1} + B_k \hat{\mathbf{q}}^k + C_k \hat{\mathbf{q}}^{k+1} = \mathbf{H}, \quad k = 1,2,\cdots N \tag{2.45}$$

where A_k, B_k, and C_k are 8×8 matrices and $\mathbf{H}$ is an 8×1 null matrix.

To avoid a trivial solution, nonhomogenous boundary conditions are imposed at the wall. Specifically, the boundary condition $\hat{q}_1^1 = 0$ is replaced by $\hat{q}_8^1 = 1$. This is equivalent to normalizing the eigenfunction by the value of the pressure perturbations at the wall. Now equation (2.45) is nonhomogenous and a nontrivial solution can be obtained for the guessed eigenvalue, for example, $\omega = \omega_0$ if α and β are given. Newton's method is used to iterate on ω such that the missing boundary condition $\hat{q}_1^1 = 0$ is satisfied. Thus, when a solution, $\hat{\mathbf{q}}$, is obtained for ω_0, the correction, $\Delta\omega$, is determined from the equation

$$\hat{q}_1^1 + \frac{\partial \hat{q}_1^1}{\partial \omega}\Delta\omega = 0 \tag{2.46}$$

where $\hat{q}_1^1$ is known from the solution $\hat{\mathbf{q}}$ just obtained; $\partial\hat{q}_1^1/\partial\omega$ is obtained from the forward Euler formulas

$$\frac{\partial \hat{q}_1^1}{\partial \omega} = \frac{\hat{q}_1^1\big|_{\omega+\delta\omega} - \hat{q}_1^1\big|_{\omega}}{\delta\omega} \tag{2.47}$$

and we can use the same program to obtain $\hat{q}_1^1\big|_{\omega+\delta\omega}$.

We can also obtain α or β based on the same method described above if the other two variables are known.

2.5 Parabolized stability equation(PSE)

In spite of the qualitative success of the parallel flow assumption in linear stability theory, the linear stability computation does not explain some important phenomena, and experiments have shown systematic differences with the theory. Apart from exhibiting a minimum critical Reynolds number that is lower than that given by the linear stability theory, evidence from experiments shows that the growth rate of the disturbance is not only a function of the coordinate normal to the wall, but also varies for different flow quantities. These phenomena occur due to the increase in the boundary-layer thickness. In cases where the mean boundary-layer thickness and flow changes rapidly due to localized adjustments, the parallel flow assumption is expected to fail, and the stability characteristics may not be accurately predicted. Also at the early stages of the nonlinear interactions, El-Haddy[67] has shown that nonparallel flow effects may control the initial development of the triad components in a triad resonant interaction model.

The problem of disturbances in a nonparallel boundary-layer is difficult to model and has attracted much attention. Various nonparallel stability theories have been developed. A multiple scales method was employed by Gaster[68] and Saric & Nayfeh[69] to account for the non-parallel effect for 2D waves in Blasius flow. From their numerical results, this method yields results which are much closer to experimental results than the LST method. More recently, the concept of the parabolized stability equation was introduced by Herbert and Bertolotti[30] in 1987 and has now been well developed and applied to a variety of linear and nonlinear stability problems for two and three-dimensional, incompressible and compressible boundary-layer flows. In order to evaluate these nonparallel theories, Fasel and Konzelmann[70] studied the nonparallel

stability over a flat-plate by solving the complete Navier-Stokes equations and compared the results with those of various non-parallel theories. Good agreement was obtained between these nonparallel theories and the direct numerical simulations.

2.5.1 The derivation of PSE

In general, if the boundary-layers are not parallel, the mean flow velocity components $\overline{U}_1$ exhibit small variations in the streamwise direction, and the component $\overline{U}_2$ normal to the wall surface is non-zero to provide the mass balance as the displacement thickness changes. That is

$$\overline{U}_2 \neq 0;\ \frac{\partial \overline{U}_1}{\partial x_1} \neq 0 \tag{2.48}$$

Now the eigenfunction will change in both the streamwise and wall normal directions. And the streamwise wave number is not constant any more, changing in the streamwise direction. So the disturbances are assumed to have the following form:

$$\begin{bmatrix} u_1'(x_1,x_2,x_3,t) \\ u_2'(x_1,x_2,x_3,t) \\ u_3'(x_1,x_2,x_3,t) \\ \rho'(x_1,x_2,x_3,t) \\ p'(x_1,x_2,x_3,t) \\ T'(x_1,x_2,x_3,t) \end{bmatrix} = \begin{bmatrix} \hat{u}_1(x_1,x_2) \\ \hat{u}_2(x_1,x_2) \\ \hat{u}_3(x_1,x_2) \\ \hat{\rho}(x_1,x_2) \\ \hat{p}(x_1,x_2) \\ \hat{T}(x_1,x_2) \end{bmatrix} e^{i\left[\int \alpha(x_1)dx_1 + \beta x_3 - \omega t\right]} \tag{2.49}$$

Substituting these disturbance forms into the linearized Navier-Stokes equations (2.27)-(2.32) and collecting the coefficients, we get the second order differential equations written in matrix form as

$$A_1 \frac{\partial^2 \hat{\mathbf{q}}}{\partial x_1^2} + A_2 \frac{\partial^2 \hat{\mathbf{q}}}{\partial x_2^2} + B_1 \frac{\partial^2 \hat{\mathbf{q}}}{\partial x_1 \partial x_2} + C_1 \frac{\partial \hat{\mathbf{q}}}{\partial x_1} + C_2 \frac{\partial \hat{\mathbf{q}}}{\partial x_2} + D_1 \hat{\mathbf{q}} = 0 \tag{2.50}$$

With very slow changes of the disturbance along the streamwise direction compared with the relatively faster change in the wall normal direction, the second derivative of the eigenfunction with respective to x_1 can be neglected. Then we can obtain a parabolized

stability equation in the streamwise direction as following

$$A\frac{\partial^2 \hat{\mathbf{q}}}{\partial x_2^2} + B\frac{\partial \hat{\mathbf{q}}}{\partial x_1} + C\frac{\partial \hat{\mathbf{q}}}{\partial x_2} + D\hat{\mathbf{q}} = 0 \tag{2.51}$$

where $\hat{\mathbf{q}} = [\hat{u}_1, \hat{u}_2, \hat{u}_3, \hat{\rho}, \hat{T}]^T$

and A, B, C, D are 5×5 coefficient matrices; their elements are given in Appendix II.

The boundary conditions are expressed as

$$\hat{u}_1 = \hat{u}_2 = \hat{u}_3 = \hat{T} = 0, \text{ at } x_2 = 0 \tag{2.52}$$

and

$$\hat{u}_1, \hat{u}_2, \hat{u}_3, \hat{T} \to 0, \text{ as } x_2 \to \infty \tag{2.53}$$

2.5.2 The numerical scheme to solve PSE

The PSE derived above can be discretized using a fourth-order central finite difference scheme in the wall normal direction. That is

$$\frac{\partial \hat{\mathbf{q}}}{\partial x_2} = \frac{-\hat{\mathbf{q}}^i_{j+2} + 8\hat{\mathbf{q}}^i_{j+1} - 8\hat{\mathbf{q}}^i_{j-1} + \hat{\mathbf{q}}^i_{j-2}}{12\Delta x_2} + O(\Delta x_2^4) \tag{2.54}$$

$$\frac{\partial^2 \hat{\mathbf{q}}}{\partial x_2^2} = \frac{-\hat{\mathbf{q}}^i_{j+2} + 16\hat{\mathbf{q}}^i_{j+1} - 30\hat{\mathbf{q}}^i_{j} + 16\hat{\mathbf{q}}^i_{j-1} - \hat{\mathbf{q}}^i_{j-2}}{12(\Delta x_2)^2} + O(\Delta x_2^4) \tag{2.55}$$

Because the PSE is parabolic in the streamwise direction, it can be discretized using a first order backward differencing scheme in this direction. That is

$$\frac{\partial \hat{\mathbf{q}}}{\partial x_1} = \frac{\hat{\mathbf{q}}^i_j - \hat{\mathbf{q}}^{i-1}_j}{\Delta x_1} + O(\Delta x_1) \tag{2.56}$$

Using the above differencing schemes, the PSE can be discretized and written in block penta-diagonal matrix form as:

$$AL_2^j\hat{\mathbf{q}}^i_{j-2} + AL_1^j\hat{\mathbf{q}}^i_{j-1} + AD^j\hat{\mathbf{q}}^i_j + AU_1^j\hat{\mathbf{q}}^i_{j+1} + AU_2^j\hat{\mathbf{q}}^i_{j+2} = B^j\hat{\mathbf{q}}^{i-1}_j \tag{2.57}$$

where $j = 1,2,\cdots N$ and AL_2, AL_1, AD, AU_1, AU_2 refer to the lower subdiag- onal, subdiagonal, diagonal, superdiagonal and upper superdiagonal matrices of size 5×5,

respectively.

The major advantage of the PSE is that despite a small elliptic remainder consisting of the streamwise pressure gradient, the system of PDE is parabolic and its solution can be obtained by a marching-type method. But since both the shape functions and the phase of the disturbance quantities depend on the streamwise coordinate, it is more difficult to determine the complex streamwise wave number. In a non-parallel mean flow, the different physical quantities grow at different rates, and, thus, one can only determine the growth rate from the computed wave number, α, based on some quantities (e.g., velocity, pressure, or energy). Usually, the wave number, α, is computed at the location in the boundary-layer where the disturbance quantities, or the disturbance energy become maximal. This location varies slowly in the marching direction.

The procedure to compute α at a streamwise station is described as follows. Starting with an initial solution found from solving the local eigenvalue problem at $x_1 = x_0$, one marches to the next station $x_1 = x_0 + \Delta x_1$ and solves for the shape functions $\hat{\mathbf{q}}$ assuming that $\alpha(x_1 = x_0 + \Delta x_1) = \alpha(x_0)$. Approximating the change in the shape functions with a Taylor series at $x_1 = x_0 + \Delta x_1$, one can derive an equation to update α at $x_1 = x_0 + \Delta x_1$, where $\hat{\rho}_{\max}$ represents for the normal maximal value of the density shape function.

$$\alpha_{new} = \alpha_{old} + \frac{1}{|\hat{\rho}_{\max}|}\left(\frac{\partial \hat{\rho}_{\max}}{\partial x_1}\right) \tag{2.58}$$

Updating the shape functions and iterating until the change in α is less than some defined tolerance, the solution at this station is obtained and the procedure repeated at the next streamwise station. The PSE method is very efficient since it takes only a few iterations on α to obtain an accurate solution, provided that the gradients in the flow field are moderate.

2.6 Gortler instability theory

Counter rotating vortices whose rotating axes are in the streamwise direction appear in boundary-layer flows along concave surfaces due to the imbalance between pressure forces and centrifugal forces. These vortices are called Gortler vortices and they play an important role in stability problems along concave walls. The existence of this stationary vortex instability in a boundary-layer over a concave wall was first predicted theoretically by Gortler. Since this pioneering work, Gortler vortices have been the subject of numerous theoretical and experimental studies. Spall and Malik[71] studied the Gortler vortices in supersonic and hypersonic boundary-layers. They found that compressibility has a stabilizing effect on the Gortler instability, while the effect of an adverse pressure gradient is found to be destabilizing. Winoto and Low[72] conducted an experimental investigation on the transition of boundary-layer flows in the presence of Gortler vortices and found the relation between the onset of transition and the Gortler number with the flow conditions under investigation. Benmalek and Saric[73] investigated the effects of curvature variation on the nonlinear evolution of Gortler vortices. Whang and Zhong[74][75] conducted a direct numerical simulation of Gortler instability in an hypersonic boundary-layer and studied the interactions of the Gortler vortex with a second shear mode. Other studies are performed by Gouplie, Klingmann and Bottaro[76], and Cunff and Zebib[77].

The theory of the Gortler instability has been discussed in detail by Saric[78]. In this section, we will give a brief description of the governing equations of this instability and the solution algorithm. Consider the linearized Navier-Stokes equations (2.27)-(2.32). Coordinate transformations are applied to transform the Cartesian coordinates (x_1, x_2, x_3) into a curvilinear system (ξ, η, ζ), as shown geometrically in Figure 2.1.

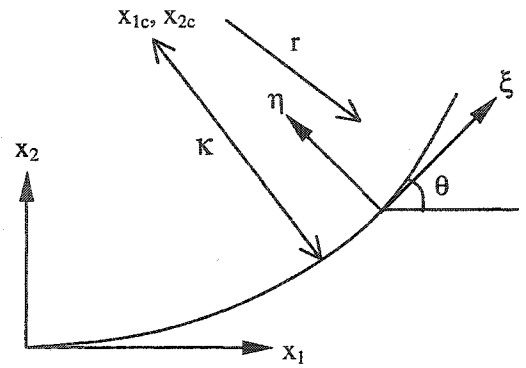

Figure 2.1 Schematic of the curvilinear coordinate system.

According to the geometry shown in Figure 2.1, we get the following relations

$$d\xi = \kappa d\theta \tag{2.59}$$

$$\eta = \kappa - r \tag{2.60}$$

$$\varsigma = x_3 \tag{2.61}$$

where κ is the radius of curvature of the wall, x_{1c}, x_{2c} are the center of the curvature.

$$r = \sqrt{(x_1 - x_{1c})^2 + (x_2 - x_{2c})^2} \tag{2.62}$$

$$\tan\theta = (x_2 - x_{2c})/(x_1 - x_{1c}) \tag{2.63}$$

For normal mode analysis, the disturbance form is

$$\begin{bmatrix} u_1'(\xi,\eta,\varsigma,t) \\ u_2'(\xi,\eta,\varsigma,t) \\ u_3'(\xi,\eta,\varsigma,t) \\ \rho'(\xi,\eta,\varsigma,t) \\ p'(\xi,\eta,\varsigma,t) \\ T'(\xi,\eta,\varsigma,t) \end{bmatrix} = \begin{bmatrix} \hat{u}_1(\eta) \\ \hat{u}_2(\eta) \\ \hat{u}_3(\eta) \\ \hat{\rho}(\eta) \\ \hat{p}(\eta) \\ \hat{T}(\eta) \end{bmatrix} e^{i(\alpha\xi + \beta\varsigma - \omega t)} \tag{2.64}$$

Because the Gortler vortices are stationary, we have $\omega = 0$. Now if we use equations (2.59)-(2.63) to perform the coordinate transformation and substitute the disturbance equations (2.64), we can get the following homogenous system of ordinary differential equations

$$A_2 \frac{d^2\hat{\mathbf{q}}}{d\eta^2} + B_2 \frac{d\hat{\mathbf{q}}}{d\eta} + C_2 = 0 \tag{2.65}$$

where

$$\hat{\mathbf{q}} = \left[\hat{u}_1, \hat{u}_2, \hat{p}, \hat{T}, \hat{u}_3\right]^T \tag{2.66}$$

and A_2, B_2, C_2 are 5×5 matrices

The boundary conditions are

$$\hat{u}_1 = \hat{u}_2 = \hat{u}_3 = \hat{T} = 0 \quad at \quad \eta = 0 \tag{2.67}$$

and

$$\hat{u}_1,\ \hat{u}_2,\ \hat{u}_3,\ \hat{T} \to 0 \ \ as \ \ \eta \to \infty \tag{2.68}$$

In equation (2.65), the Gortler number is implicitly included in the coordinate transformation procedure. The Gortler number can be expressed in the following form:

$$G_r = \frac{U_\infty \delta_d}{\nu} (\delta_d \kappa)^{\frac{1}{2}} \tag{2.69}$$

where δ_d is the displacement thickness of the boundary-layer.

Equations (2.65) together with the boundary conditions (2.67) and (2.68) form the following eigenvalue problem

$$F(\alpha,\ \beta,\ G_r,\ \mathrm{Re}) = 0 \tag{2.70}$$

By this equation, we can study the instability of the Gortler vortices at the specific Gortler number. The numerical scheme to solve this eigenvalue problem is the same as used for linear stability theory.

2.7 The algorithm for direct numerical simulation

For direct numerical simulation of instability and transition of boundary-layers, two methods have been used extensively for spatial discretization of the Navier-Stokes equations: finite difference and spectral methods. In general, the spectral methods run much faster than the finite difference methods. But there are many problems of interest

for which spectral methods are difficult to apply. Among these are the compressible flows in which discontinuities are expected and also flows with complex geometries. In contrast, finite-difference methods can treat discontinuities and complex geometries easily. Sometimes a combination of these two methods is used for three-dimensional simulation of transition. That is, finite difference methods are applied in the wall normal direction and spectral methods are applied in all other two directions using a periodic flow assumption in these two directions. This method was used by Pruett & Zang[36] and Pruett & Chang[34] to simulate the transition in a high speed axisymmetric boundary-layer. For our present study of transition over a compression corner under hypersonic conditions, due to the existence of a discontinuity, finite difference methods must be applied in all three directions.

Due to its nature, transition simulations must be far more accurate over a broad range of frequencies and amplitudes than is customary in conventional steady-state computational fluid dynamics. The fundamental physics of a flow may be sensitive to a small amount of energy in some specific portion of the spectrum. Indeed, truncation errors of less than one percent(and often less than even 0.1%) are sought. For this reason most practitioners have preferred schemes with at least fourth-order accuracy in space. Most of the present high-order schemes are linear schemes, such as fourth-order MacCormack[79] and compact schemes of Lele[80]. Owing to their linear nature, these schemes lack a robust shock-capturing capability. However, some nonlinear schemes, such as essentially non-oscillatory(ENO) scheme, allow for the formal high-order accuracy for smooth flows while providing a shock capturing capability. In the present study, we will adopt a fifth order accurate weighted essentially non-oscillatory(WENO) scheme for spatial discretization.

For time discretization, transition simulations traditionally have used second, third, or fourth order accurate methods. Computer-memory constraints have inhibited the use of higher-order methods. In the present study, a third order total variation diminishing(TVD)

Runge-Kutta scheme for time integration has been used. We will explain these schemes in detail.

2.7.1 The conservative form of the Navier-Stokes equations

For the convenience of programming, the following non-dimensional quantities are used for the direct numerical simulation in the present study. The reference length is still the similarity variable $L^* = \sqrt{\frac{V_\infty^* x_0^*}{U_\infty^*}}$, but the reference velocity is now written as $U_{ref}^* = \sqrt{RT_\infty^*}$. So we obtain the following non-dimensional quantities:

$$x_i = \frac{x_i^*}{L^*}; \qquad t = \frac{t^*}{L^*/U_{ref}^*}; \qquad u_i = \frac{u_i^*}{U_{ref}^*}; \qquad \mu = \frac{\mu^*}{\mu_\infty^*}$$

$$\rho = \frac{\rho^*}{\rho_\infty^*}; \qquad p = \frac{p^*}{p_\infty^*}; \qquad T = \frac{T^*}{T_\infty^*}; \qquad \mathrm{Re} = \frac{\rho_\infty^* U_{ref}^* L^*}{\mu_\infty^*}$$

After non-dimensionalization using the above reference quantities, the three-dimensional compressible Navier-Stokes equations (2.1)-(2.4) can be written in conservative form as equation (2.71). For convenience, we now use (x, y, z) to represent the coordinates in the streamwise, wall normal and spanwise direction, and (u, v, w) to represent the corresponding velocity components.

$$\frac{\partial Q}{\partial t} + \frac{\partial E}{\partial x} + \frac{\partial F}{\partial y} + \frac{\partial G}{\partial z} = \frac{\partial E_v}{\partial x} + \frac{\partial F_v}{\partial y} + \frac{\partial G_v}{\partial z} \tag{2.71}$$

$$Q = [\rho,\ \rho u,\ \rho v,\ \rho w,\ \rho e_t]^T \tag{2.72}$$

$$E = [\rho u,\ \rho u^2 + p,\ \rho uv,\ \rho uw,\ (\rho e_t + p)u]^T \tag{2.73}$$

$$F = [\rho v,\ \rho vu,\ \rho v^2 + p,\ \rho vw,\ (\rho e_t + p)v]^T \tag{2.74}$$

$$G = [\rho w,\ \rho wu,\ \rho wv,\ \rho w^2 + p,\ (\rho e_t + p)w]^T \tag{2.75}$$

$$E_v = \begin{bmatrix} 0 \\ \tau_{xx} \\ \tau_{xy} \\ \tau_{xz} \\ u\tau_{xx} + v\tau_{xy} + w\tau_{xz} - q_1 \end{bmatrix} \tag{2.76}$$

$$F_v = \begin{bmatrix} 0 \\ \tau_{yx} \\ \tau_{yy} \\ \tau_{yz} \\ u\tau_{yx} + v\tau_{yy} + w\tau_{yz} - q_2 \end{bmatrix} \tag{2.77}$$

$$G_v = \begin{bmatrix} 0 \\ \tau_{zx} \\ \tau_{zy} \\ \tau_{zz} \\ u\tau_{zx} + v\tau_{zy} + w\tau_{zz} - q_3 \end{bmatrix} \tag{2.78}$$

where

$$q_j = \frac{-\gamma\mu}{(\gamma-1)P_r \,\mathrm{Re}} \frac{\partial T}{\partial x_j} \tag{2.79}$$

$$\tau_{ij} = \frac{\mu}{\mathrm{Re}}\left[\frac{\partial u_i}{\partial x_j} + \frac{\partial u_j}{\partial x_i} - \frac{2}{3}\delta_{ij}\frac{\partial u_k}{\partial x_k}\right] \tag{2.80}$$

$$e_t = e + \frac{u^2+v^2+w^2}{2}, \quad e = c_v T \tag{2.81}$$

For the convenience of computation, the equations are transformed from physical coordinates (x, y, z) to the computational coordinate system (ξ, η, ς) in a conservative manner such that the general form of the equations is unchanged.

$$\frac{\partial \tilde{Q}}{\partial t}+\frac{\partial \tilde{E}}{\partial \xi}+\frac{\partial \tilde{F}}{\partial \eta}+\frac{\partial \tilde{G}}{\partial \varsigma}=\frac{\partial \tilde{E}_v}{\partial \xi}+\frac{\partial \tilde{F}_v}{\partial \eta}+\frac{\partial \tilde{G}_v}{\partial \varsigma} \tag{2.82}$$

where

$$\xi=\xi(x,y,z); \quad \eta=\eta(x,y,z); \quad \varsigma=\varsigma(x,y,z); \tag{2.83}$$

The metrics can be expressed as following

$$\xi_x=|J|\cdot(y_\eta z_\varsigma-y_\varsigma z_\eta) \tag{2.84}$$

$$\xi_y=-|J|\cdot(x_\eta z_\varsigma-x_\varsigma z_\eta) \tag{2.85}$$

$$\xi_z=|J|\cdot(x_\eta y_\varsigma-x_\varsigma y_\eta) \tag{2.86}$$

$$\eta_x=-|J|\cdot(y_\xi z_\varsigma-y_\varsigma z_\xi) \tag{2.87}$$

$$\eta_y=|J|\cdot(x_\xi z_\varsigma-x_\varsigma z_\xi) \tag{2.88}$$

$$\eta_z=-|J|\cdot(x_\xi y_\varsigma-x_\varsigma y_\xi) \tag{2.89}$$

$$\varsigma_x=|J|\cdot(y_\xi z_\eta-y_\eta z_\xi) \tag{2.90}$$

$$\varsigma_y=-|J|\cdot(x_\xi z_\eta-x_\eta z_\xi) \tag{2.91}$$

$$\varsigma_z=|J|\cdot(x_\xi z_\eta-x_\eta z_\xi) \tag{2.92}$$

where J is the Jacobian, given by:

$$J=\left[\frac{\partial(\xi,\eta,\varsigma)}{\partial(x,y,z)}\right]=\begin{bmatrix}\xi_x & \xi_y & \xi_z\\ \eta_x & \eta_y & \eta_z\\ \varsigma_x & \varsigma_y & \varsigma_z\end{bmatrix} \tag{2.93}$$

The components of the flux in the computational domain are related to the flux in the Cartesian domain by

$$[\tilde{Q}]=\frac{[Q]}{|J|} \tag{2.94}$$

$$\begin{bmatrix}\tilde{E}\\ \tilde{F}\\ \tilde{G}\end{bmatrix}=\frac{J}{|J|}\begin{bmatrix}E\\ F\\ G\end{bmatrix} \tag{2.95}$$

$$\begin{bmatrix} \tilde{E}_v \\ \tilde{F}_v \\ \tilde{G}_v \end{bmatrix} = \frac{J}{|J|} \begin{bmatrix} E_v \\ F_v \\ G_v \end{bmatrix} \tag{2.96}$$

The governing equations are solved using a 5th order accurate weighted essentially non-oscillatory(WENO) scheme for spatial discretization and a 3rd order total variation diminishing(TVD) Runge-Kutta scheme for time integration. The WENO scheme and TVD methods are described in Shu[81] and application of the ENO method to the N-S equations is given in Atkins[82].

ENO schemes are the finite difference schemes designed for problems with piecewise smooth solutions containing discontinuities. The key idea lies at the approximation level, where a nonlinear adaptive procedure is used to automatically choose the locally smoothest stencil, hence avoiding crossing discontinuities in the interpolation procedure as much as possible. The WENO scheme has been developed to improve the ENO scheme. The ENO and WENO schemes have been quite successful in applications, especially for problems containing both shocks and complicated smooth solution structures, such as compressible turbulence simulations and aeroacoustics. We will give a brief discussion for these two kinds of schemes in the following sections.

2.7.2 ENO scheme

In the ENO approach, the spatial derivatives are approximated to high order at the nodes allowing the equations at each point to be integrated in time and the spatial derivatives with respect to a given direction are approximated by expansions in that direction only. Hence, a one-dimensional description is trivially extended to any number of spatial dimensions. Consider the one-dimensional equation

$$\frac{\partial \tilde{Q}}{\partial t} + \frac{\partial \tilde{E}}{\partial \xi} = 0 \tag{2.97}$$

The spatial derivative at a point is approximated by a difference of numerical fluxes, much like the approach of traditional finite-volume methods. The numerical flux is

defined in terms of nearby point values of the physical flux such that 1) the difference of the numerical flux values approximates the derivative of the physical flux to the desired order of accuracy, and 2) the consistency condition required for flux-conservation is satisfied. That is

$$\frac{\partial \tilde{E}}{\partial \xi}(\xi_i) = \frac{\hat{E}(\xi_{i+1/2}) - \hat{E}(\xi_{i-1/2})}{\Delta \xi} + O(\Delta \xi^k), \quad i = 0,1,...,N \tag{2.98}$$

where ξ_i stands for the coordinate at the i^{th} grid point. N stands for the total number of grid points, and k represents the order of the differencing accuracy.

Here $\hat{E}$ can be defined by either a Lagrangian or Newton interpolation polynomial with the physical flux in some neighborhood of ξ_i. The neighborhood is allowed to shift left or right to form different interpolation stencils. That is

$$\hat{E}^{(r)}(\xi_{i+1/2}) = \sum_{j=0}^{k-1} c_{rj} \tilde{E}(\xi_{i-r+j}), \quad r = 0,1,...,k-1 \tag{2.99}$$

where c_{rj} is the interpolation coefficient for the r^{th} interpolation stencil.

Among all these interpolation stencils, the ENO scheme uses an adaptive procedure which is essentially a searching algorithm to find the smoothest stencil relative to the specified reference point so that a good resolution at the discontinuity can be achieved. The basic idea is to avoid including the discontinuous cell in the stencil. For example, if we want to construct a third order interpolation function at point $\xi_{i+1/2}$, three candidate stencils can be used: $\{\xi_i, \xi_{i+1}, \xi_{i+2}\}$, $\{\xi_{i-1}, \xi_i, \xi_{i+1}\}$ and $\{\xi_{i-2}, \xi_{i-1}, \xi_i\}$. Among these stencils, some may include the discontinuous cell. So these stencils are not good for primitive value reconstruction. They should be discarded. The selection of the interpolation stencil has been described as the following a few steps in Shu[81].

1) Compute the divided differences of the primitive function $\tilde{E}(\xi)$, for degrees 1 to k, according to the equation

$$\tilde{E}[\xi_i,\cdots,\xi_{i+j}] \equiv \frac{\tilde{E}[\xi_{i+1},\cdots,\xi_{i+j}] - \tilde{E}[\xi_i,\cdots,\xi_{i+j-1}]}{\xi_{i+j} - \xi_i},\ j = 1\cdots k \tag{2.100}$$

2) Start with a two-point stencil $S_2(i) = \{\xi_i, \xi_{i+1}\}$ to reconstruct $\tilde{E}(\xi)$ at $\xi_{i+1/2}$.

3) For l=2, …, k, assuming the stencil $S_l(i) = \{\xi_{i+1},\cdots,\xi_{i+l-1}\}$ is known, add one of the two neighboring points ξ_{i-1} or ξ_{i+l} to the stencil, following the ENO procedure:

if $\left|\tilde{E}[\xi_{i-1},\cdots,\xi_{i+l-1}]\right| < \left|\tilde{E}[\xi_{i+1},\cdots,\xi_{i+l}]\right|$, then add ξ_{i-1} to stencil $S_l(i)$ to obtain the new stencil

$$S_{l+1}(i) = \{\xi_{i-1},\cdots,\xi_{i+l-1}\} \tag{2.101}$$

otherwise add ξ_{i+l} to the stencil $S_l(i)$ to obtain the new stencil

$$S_{l+1}(i) = \{\xi_i,\cdots,\xi_{i+l}\} \tag{2.102}$$

By this procedure, we can get an interpolation stencil of k^{th} order, which is the smoothest one among all other stencils at the interpolation point. Figure 2.2 shows the comparison of two interpolation results for the step function, one with fixed central stencil cubic interpolation and another with ENO cubic interpolation. It can be seen that ENO interpolation gets a much smoother result than the central interpolation.

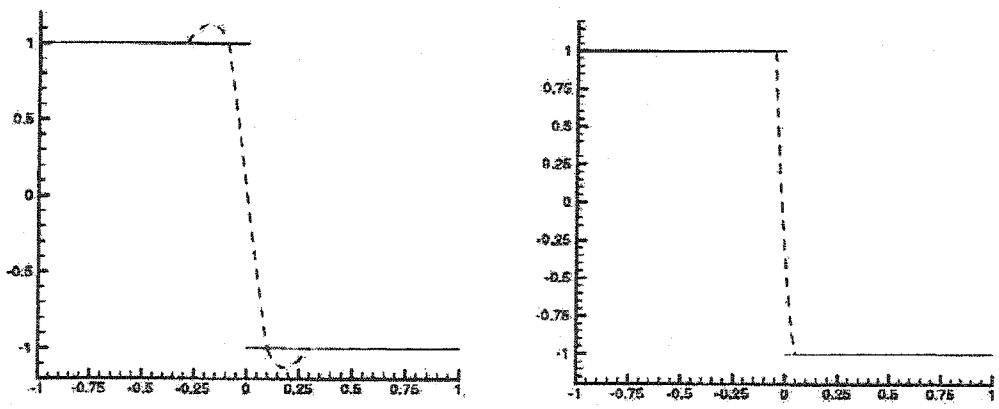

Figure 2.2 Fixed central stencil cubic interpolation(left) and ENO cubic interpolation(right) for the step function. Solid: exact function; Dashed: interpolant piecewise cubic polynomials(Shu[81]).

2.7.3 WENO scheme

In the stencil selection process of the ENO scheme, k candidate stencils are considered, covering *2k-1* cells, but only one of the stencils is actually used in forming the flux, resulting in k^{th} order accuracy. If all of the *2k-1* cells in the potential stencils are used, one could get $(2k\text{-}1)^{th}$ order accuracy in smooth regions. Based on this idea, the WENO scheme is developed to attempt to improve upon the ENO scheme. The basic idea of the WENO scheme is that instead of using only one of the candidate stencils to form the reconstruction, one uses a convex combination of all of them. Suppose the k candidate stencils

$$S_r(i) = \{\xi_{i-r}, \cdots, \xi_{i-r+k-1}\}, \quad r = 0, \cdots, k-1 \tag{2.103}$$

produce k different reconstructions to the value $\xi_{i+1/2}$ according to the equation

$$\hat{E}^{(r)}(\xi_{i+1/2}) = \sum_{j=0}^{k-1} c_{rj} \tilde{E}(\xi_{i-r+j}), \quad r = 0,1,\ldots,k-1 \tag{2.104}$$

WENO reconstruction would take a convex combination of all $\hat{E}^{(r)}(\xi_{i+1/2})$ as a new approximation to the cell boundary value $\tilde{E}(\xi_{i+1/2})$. That is

$$\hat{E}(\xi_{i+1/2}) = \sum_{r=0}^{k-1} \omega_r \hat{E}^{(r)}(\xi_{i+1/2}) = \tilde{E}(\xi_{i+1/2}) + O(\Delta\xi^{2k-1}) \tag{2.105}$$

Apparently, the key to the success of WENO is the choice of weights ω_r. We require

$$\omega_r \geq 0 \qquad \sum_{r=0}^{k-1} \omega_r = 1 \tag{2.106}$$

for stability and consistency.

When the function $\tilde{E}(\xi)$ has a discontinuity in one or more of the stencils, we desire that the corresponding weights, ω_r, be essentially zero, to emulate the successful ENO ideas. Another consideration is that the weights should be smooth functions of the

cell averages involved. Finally, we would like to have weights which are computationally efficient. All these considerations lead to the following form of weights:

$$\omega_r = \frac{\alpha_r}{\sum_{s=0}^{k-1}\alpha_s}, \quad r = 0,\ldots,k-1 \tag{2.107}$$

with

$$\alpha_r = \frac{d_r}{(\varepsilon_1 + \beta_r)^2} \tag{2.108}$$

Here $\varepsilon_1 > 0$ is introduced to prevent the denominator from becoming zero. We take $\varepsilon_1 = 10^{-6}$ in our numerical computation. d_r is the weight coefficient for r^{th} interpolation stencil when $\tilde{E}(\xi)$ is smooth in all of the candidate stencils. We can see d_r is always positive and must satisfy

$$\sum_{r=0}^{k-1} d_r = 1 \tag{2.109}$$

For the 5th order WENO scheme, k=3, we have

$$d_0 = \frac{3}{10}, \quad d_1 = \frac{3}{5}, \quad d_2 = \frac{1}{10} \tag{2.110}$$

And β_r is the smooth indicator for the r^{th} interpolation stencil. It was determined by the following equation

$$\beta_r = \sum_{l=1}^{k-1} \int_{\xi_{i-1/2}}^{\xi_{i+1/2}} \Delta\xi^{2l-1} \left(\frac{\partial^l p_r(\xi)}{\partial^l \xi} \right)^2 d\xi \tag{2.111}$$

where $p_r(\xi)$ represents the reconstruction polynomial on the stencil $S_r(i)$ and can be expressed in density variables. For k=3, the above equation gives the following smoothness measurement.

$$\beta_0 = \frac{13}{12}(\rho_i - 2\rho_{i+1} + \rho_{i+2})^2 + \frac{1}{4}(3\rho_i - 4\rho_{i+1} + \rho_{i+2})^2 \tag{2.112}$$

$$\beta_1 = \frac{13}{12}(\rho_{i-1} - 2\rho_i + \rho_{i+1})^2 + \frac{1}{4}(\rho_{i-1} - \rho_{i+1})^2 \tag{2.113}$$

$$\beta_2 = \frac{13}{12}(\rho_{i-2} - 2\rho_{i-1} + \rho_i)^2 + \frac{1}{4}(\rho_{i-2} - 4\rho_{i-1} + 3\rho_i)^2 \tag{2.114}$$

2.7.4 Flux splitting approach

When we apply the WENO algorithm to the Navier-Stokes equations, the inviscid and viscous terms require different numerical treatments to reflect their fundamentally different properties. The inviscid terms characteristically describe wave phenomena. The ideal approach would be to decompose the inviscid flux vector into characteristic components and treat each wave with an appropriate scalar operator. However, within the ENO framework, such an approach requires the creation of a characteristic subset at each grid point, which greatly increases the computational effort and storage requirements. A computationally-efficient alternative is a local flux-splitting approach. For each coordinate direction *k*, the inviscid flux is split into two components: one with all positive eigenvalues, and the other with all negative eigenvalues.

$$\tilde{E}_k = \tilde{E}_k^+ + \tilde{E}_k^- \tag{2.115}$$

$$\tilde{E}_k^{\mp} = \tilde{E}_k \mp \sigma_k \tilde{Q} \tag{2.116}$$

$$\sigma_k = \sigma(\lambda_k) \geq |\lambda_k| \tag{2.117}$$

here λ_k = maximum eigenvalue of $\left|\frac{\partial \tilde{E}_k}{\partial \tilde{Q}}\right|$

More elaborate means of flux splitting exist, but this simple approach is inexpensive and works well. The only formal restriction on the splitting is that split fluxes must be smooth functions of $\tilde{Q}$. This is necessary to ensure that higher derivatives exist when evaluating the numerical flux, in addition to the usual need to prohibit expansion shocks. For the present splitting technique, the splitting flux will be smooth if the function σ is smooth. In the present implementation, we select

$$\sigma(\lambda) = \sqrt{\varepsilon_2^2 + \lambda^2} \tag{2.118}$$

where ε_2 is a small number taken as 0.05.

After the inviscid flux splitting, we simply divide the viscous flux into two parts equally and add each part to the positive and negative component of the inviscid flux respectively. The WENO scheme is then applied to each component of the combined flux according to the wave propagating direction.

2.7.5 TVD Runge-Kutta integration

Using total variation diminishing(TVD) Runge-Kutta method for time integration can eliminate numerical oscillation. Figure 2.3 shows a comparison of two numerical results, one with TVD time discretization and the other with non-TVD time discretization. It can be seen that the non-TVD result is oscillatory.

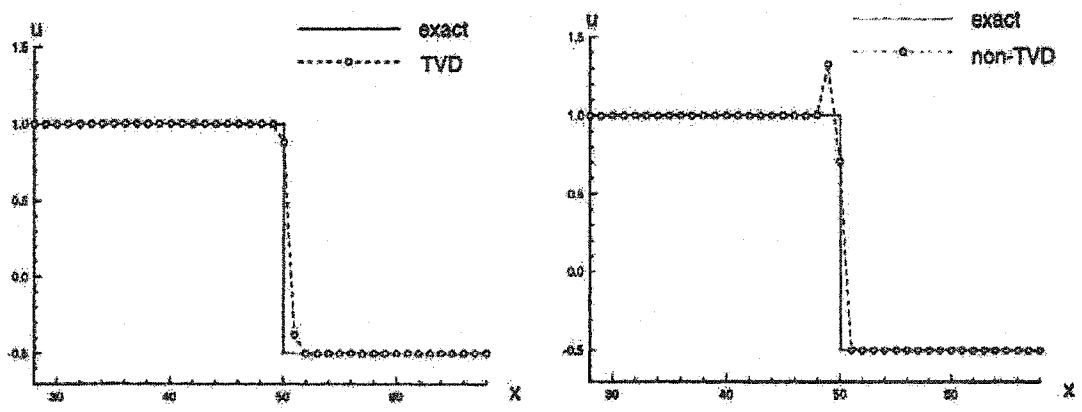

Figure 2.3 Comparison of second order TVD and non-TVD spatial discretization results(Shu[81]).

A three stage TVD Runge-Kutta method was adopted in present simulation, given by:

$$\tilde{Q}^{(1)} = \tilde{Q}^n + \Delta t L(\tilde{Q}^n) \tag{2.119}$$

$$\tilde{Q}^{(2)} = \frac{3}{4}\tilde{Q}^n + \frac{1}{4}\tilde{Q}^{(1)} + \frac{1}{4}\Delta t L(\tilde{Q}^{(1)}) \tag{2.120}$$

$$\tilde{Q}^{n+1} = \frac{1}{3}\tilde{Q}^n + \frac{2}{3}\tilde{Q}^{(2)} + \frac{2}{3}\Delta t L(\tilde{Q}^{(2)}) \tag{2.121}$$

where $L(\tilde{Q})$ is the WENO approximation to the spatial derivative of flux vectors. And the time step is determined on the basis of an inviscid CFL number,

$$CFL = \frac{\Delta t}{|J|}\sum_{k=1}^{3}|\lambda_k| \tag{2.122}$$

2.7.6 Parallel computation algorithm

With the development of computational fluid dynamics, the requirement of high-speed computers with large memories has become more and more urgent, especially for the direct numerical simulation of turbulence. It still remains a daunting task for even the fastest single processor computers, even though new processors are manufactured with double or even triple the computational speed each year. As the best solution to this problem, parallel computation now attracts more and more interest among researchers in the area of CFD. The so-called parallel computation means to run the same job on multi-processors simultaneously using algorithms that allow each processor to run different parts of the job. Then a big job can be divided into several small jobs which can run on different processors simultaneously. As a result, the clock time to run big jobs will be significantly decreased.

In general, two kinds of algorithms have been widely used for parallel computation that depend on the structure of the parallel machine: a shared-memory algorithm for vector machines and a message passing interface (MPI) algorithm for cluster machines. For the shared-memory parallel algorithm, all of the CPUs of the parallel machine must share the same memory. So each CPU can manipulate the same variables. This kind of algorithm is easy for parallel programming. The shared-memory parallel codes can be developed only by adding some parallel directives into the ordinary codes which usually run on single-CPU computers. Because no data exchange exists between the different CPUs, the computation efficiency of this algorithm can reach very high levels. But this kind of vector parallel machine is too expensive and is not easy to access. On the other hand, for the MPI parallel algorithm, each CPU of the parallel machine possesses its own memory, and each CPU can only manipulate its own memory. So the same variables will stand for the different values for different CPUs. Then for those codes in which the variables at the different parts running on different CPUs are related to each other, data exchanges of these variables between different CPUs are necessary. The code

development for this kind of parallel machine is much more complicated than the shared-memory machines. Some communicating codes should be developed for data exchange. In addition, data exchange among CPUs takes up part of each CPU's time, so the parallel computation efficiency cannot reach very high levels, but the big advantage is that this kind of cluster parallel machine is relatively cheap compared with vector machines. Any number and any type of independent computers can be assembled into a cluster parallel machine by the network. There are no limitations to the number of machines and the memory of the CPUs. It is very economical especially for small companies. In present numerical simulation, we developed a parallel code based on an MPI parallel computation algorithm. The code runs on a 64-CPU cluster machine. First, we will give a brief introduction to MPI.

The MPI is a library of functions and macros that can be used in C, FORTRAN, and C++ programs. A detailed description of all these functions and macros are given in William[83][84]. As its name implies, MPI is intended for use in programs that exploit the existence of multiple processors by message-passing. It was developed in 1993-1994 by a group of researchers from industry, government, and academia. As such, it is one of the first standards for programming parallel processors, and it is the first that is based on message-passing.

MPI includes point-to-point message passing and collective (global) operations, all scoped to a user-specified group of processes. Furthermore, MPI provides abstractions for processes at two levels. First, processes are named according to the rank of the group in which the communication is being performed. Second, virtual topologies allow for graph or Cartesian naming of processes that help relate the application semantics to the message passing semantics in a convenient, efficient way. Communicators, which house groups and communication context (scoping) information, provide an important measure of safety that is necessary and useful for building up library-oriented parallel code.

MPI provides a set of send and receive functions that allow the communication of

typed data with an associated tag. Typing of the message contents is necessary for heterogeneous support - the type information is needed so that correct data representation conversions can be performed as data are sent from one architecture to another. The tag allows selectivity of messages at the receiving end: one can receive on a particular tag, or one can wild-card this quantity, allowing reception of messages with any tag. Message selectivity on the source process of the message is also provided. A fragment of code appears in the following and shows an example of process 0 sending a message to process 1.

```
program greetings
include 'mpif.h'
integer my_rank
integer source
integer dest
integer tag
character*100 message
integer status(MPI_STATUS_SIZE)
integer ierr
call MPI_Init(ierr)
call MPI_Comm_rank(MPI_COMM_WORLD, my_rank, ierr)
if (my_rank.eq.0) then
message='Greetings from process 0'
      dest=1
      tag=0
      call MPI_Send(message, 25,
&   MPI_CHAR, dest, tag, MPI_COMM_WORLD, ierr)
      else
      source=0
       tag=0
       call MPI_Recv(message,100, MPI_CHAR,
&   source,tag, MPI_COMM_WORLD, status, ierr)
       write(6,*) message
       endif
       call MPI_Finalize(ierr)
       end
```

This code executes on both process 0 and process 1. The example sends a character string. MPI_COMM_WORLD is a default communicator provided upon start-up. Among

other things, a communicator serves to define the allowed set of processes involved in a communication operation. Process ranks are integers, serve to label processes, and are discovered by inquiry to a communicator (see the call to MPI_Comm_rank()). The typing of the communication is evident by the specification of MPI_CHAR. The sending and receiving process specified that the sending and incoming data were to be placed in 'message' and that it had a maximum size of 100 elements, of type MPI_CHAR. The variable status, set by MPI_Send() and MPI_Recv(), gives information on the destination, source as well as tag of the message and how many elements were actually sent and received. For example, the receiver can examine this variable to find out the actual length of the character string received. This example program shows the basic idea how message-passing algorithm works.

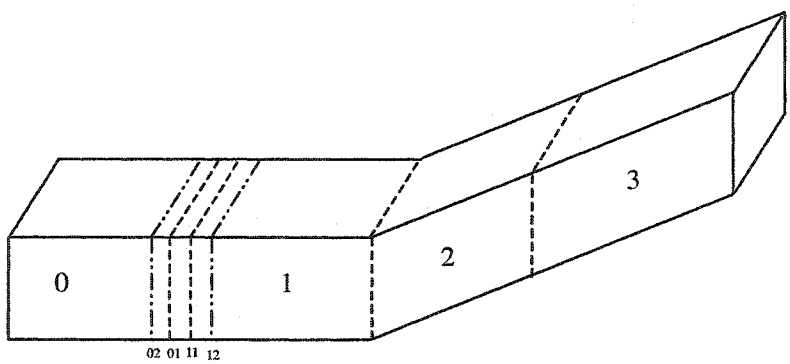

Figure 2.4 The streamwise partition of the grid for MPI.

Now we turn our attention to the parallel algorithm of our present computational case. The computation was performed in a three-dimensional space which was discretized by a three-dimensional grid. The basic idea for parallel computation is to divide this three-dimensional space into a number of small spaces. Then the computation was performed in each of these smaller spaces simultaneously with one CPU for each. For convenience of programming, the space was divided in only one direction. Figure 2.4 illustrates the spatial partition in the streamwise direction.

In this figure, the grid was divided into four smaller domains, and the computations were performed in each of these domains simultaneously. From the WENO scheme, we

know that in order to perform the streamwise differencing at each grid point, its four streamwise neighboring grid points is required, including two points to the left and two point to the right. If a point is located in the middle of its own grid domain, there should not be any problem, but if the point is a boundary point or a point adjacent to the boundary points of the domain, the problem appears when we perform the differencing operation at this point. The differencing at this point needs the values from the one or two other points which belong to the other computational domains manipulated by other CPUs. For example, at the interface of domain "0" and domain "1", four streamwise boundary sections exist, where sections "02" and "01" are the last two sections in domain "0", and the sections "11" and "12" are the first two sections in domain "1". Streamwise differencing at the points on section "02" requires the values of the points on section "11", and the streamwise difference at the points on section "01" requires the values of points on both sections "11" and "12". The converse is true for streamwise differencing at the points on sections "12" and "11". So if the computations in domain "0" and domain "1" are performed on two different CPUs with rank "0" and rank "1" respectively, the CPU with rank "0" needs to send the data on the sections "01" and "02" to the CPU with rank "1" and receive the data on the sections "11" and "12", which is sent by the CPU with rank "1". At the same time, the CPU with rank "1" needs to send the data on sections "11" and "12" to the CPU with rank "0" and receive the data on sections "01" and "02", which is sent by the CPU with rank "0". The following fragment of code shows how these sending and receiving procedures are realized by message-passing programming.

```
if(my_rank.ge.1.and.my_rank.le.numcpus-2) then
call MPI_SEND(us1,ndat,MPI_REAL8,
   1    my_rank-1,1,MPI_COMM_WORLD,ierr)
call MPI_SEND(us2,ndat,MPI_REAL8,
   1    my_rank-1,2,MPI_COMM_WORLD,ierr)
call MPI_SEND(us3,ndat,MPI_REAL8,
   1    my_rank+1,3,MPI_COMM_WORLD,ierr)
call MPI_SEND(us4,ndat,MPI_REAL8,
   1    my_rank+1,4,MPI_COMM_WORLD,ierr)
call MPI_SEND(ts1,ndat1,MPI_REAL8,
```

```
   1    my_rank-1,5,MPI_COMM_WORLD,ierr)
call MPI_SEND(ts2,ndat1,MPI_REAL8,
   1    my_rank-1,6,MPI_COMM_WORLD,ierr)
call MPI_SEND(ts3,ndat1,MPI_REAL8,
   1    my_rank+1,7,MPI_COMM_WORLD,ierr)
call MPI_SEND(ts4,ndat1,MPI_REAL8,
   1    my_rank+1,8,MPI_COMM_WORLD,ierr)
call MPI_RECV(ur1,ndat,MPI_REAL8,
   1    my_rank-1,3,MPI_COMM_WORLD,status,ierr)
call MPI_RECV(ur2,ndat,MPI_REAL8,
   1    my_rank-1,4,MPI_COMM_WORLD,status,ierr)
call MPI_RECV(ur3,ndat,MPI_REAL8,
   1    my_rank+1,1,MPI_COMM_WORLD,status,ierr)
call MPI_RECV(ur4,ndat,MPI_REAL8,
   1    my_rank+1,2,MPI_COMM_WORLD,status,ierr)
call MPI_RECV(tr1,ndat1,MPI_REAL8,
   1    my_rank-1,7,MPI_COMM_WORLD,status,ierr)
call MPI_RECV(tr2,ndat1,MPI_REAL8,
   1    my_rank-1,8,MPI_COMM_WORLD,status,ierr)
call MPI_RECV(tr3,ndat1,MPI_REAL8,
   1    my_rank+1,5,MPI_COMM_WORLD,status,ierr)
call MPI_RECV(tr4,ndat1,MPI_REAL8,
  1    my_rank+1,6,MPI_COMM_WORLD,status,ierr)
 end if

 if(my_rank.eq.0) then
 call MPI_SEND(us3,ndat,MPI_REAL8,
   1    my_rank+1,3,MPI_COMM_WORLD,ierr)
 call MPI_SEND(us4,ndat,MPI_REAL8,
   1    my_rank+1,4,MPI_COMM_WORLD,ierr)
 call MPI_SEND(ts3,ndat1,MPI_REAL8,
   1    my_rank+1,7,MPI_COMM_WORLD,ierr)
 call MPI_SEND(ts4,ndat1,MPI_REAL8,
   1    my_rank+1,8,MPI_COMM_WORLD,ierr)
 call MPI_RECV(ur3,ndat,MPI_REAL8,
   1    my_rank+1,1,MPI_COMM_WORLD,status,ierr)
 call MPI_RECV(ur4,ndat,MPI_REAL8,
   1    my_rank+1,2,MPI_COMM_WORLD,status,ierr)
 call MPI_RECV(tr3,ndat1,MPI_REAL8,
   1    my_rank+1,5,MPI_COMM_WORLD,status,ierr)
  call MPI_RECV(tr4,ndat1,MPI_REAL8,
   1       my_rank+1,6,MPI_COMM_WORLD,status,ierr)
  end if
```

```
if(my_rank.eq.numcpus-1) then
call MPI_SEND(us1,ndat,MPI_REAL8,
  1    my_rank-1,1,MPI_COMM_WORLD,ierr)
call MPI_SEND(us2,ndat,MPI_REAL8,
  1    my_rank-1,2,MPI_COMM_WORLD,ierr)
call MPI_SEND(ts1,ndat1,MPI_REAL8,
  1    my_rank-1,5,MPI_COMM_WORLD,ierr)
call MPI_SEND(ts2,ndat1,MPI_REAL8,
  1    my_rank-1,6,MPI_COMM_WORLD,ierr)
call MPI_RECV(ur1,ndat,MPI_REAL8,
  1    my_rank-1,3,MPI_COMM_WORLD,status,ierr)
call MPI_RECV(ur2,ndat,MPI_REAL8,
  1    my_rank-1,4,MPI_COMM_WORLD,status,ierr)
call MPI_RECV(tr1,ndat1,MPI_REAL8,
  1    my_rank-1,7,MPI_COMM_WORLD,status,ierr)
call MPI_RECV(tr2,ndat1,MPI_REAL8,
    1    my_rank-1,8,MPI_COMM_WORLD,status,ierr)
 end if
```

These sending and receiving functions are executed at each Runge-Kutta time iteration. In order to make sure that all CPUs run synchronously, the following barrier function should be called by each CPU after each sending and receiving operation.

call MPI_BARRIER(MPI_COMM_WORLD,status,ierr)

This function keeps each CPU in a waiting status after it has finished the sending and receiving operations until all of the other CPUs are also finished with the same operation. This makes sure that no CPU can run faster than any other CPUs, and all CPUs send or receive the data which is computed at the same time iteration step. Of course, this function wastes a lot of CPU time, but it is good for computational safety.

In order to estimate the effectiveness of the MPI parallel algorithm in improving the computational speed, we define the parallel computation efficiency as the ratio of the CPU time used for computation to the total CPU time which includes the computation time, data exchange time and waiting time. In general, the larger the number of CPUs used, the lower the parallel computation efficiency. Because more CPUs means more data exchange interfaces, as a result, more CPU time will be spent in data exchange. It is

important to choose a reasonable CPU number so that a high computational speed can be achieved with high computation efficiency. In addition, the amount of data for exchange also influences the computation efficiency. The computational domain should be divided using the principle that the amount of data for exchange at the interface sections should be as small as possible. In the present parallel computation, the computational domain was divided in the streamwise direction because there are fewer grid points in the streamwise sections than in the normal and spanwise sections.

2.8 Summary

In this chapter, we have discussed the governing equations and numerical algorithms for linear stability theory, parabolized stability equation, Gortler instability theory and direct numerical simulation. In the next a few chapters, we will apply these theories and numerical methods to analyze hypersonic boundary-layer stability and transition over a compression corner. First, a two-dimensional steady mean flow was computed by performing unsteady computations at a variable time step until the residual achieved small value ~10^{-5}. Then the LST method was used in an approximate study of two- and three-dimensional disturbance evolution across a compression corner based on the mean flow. Next, Gortler instability theory was used to study the instability of the Grotler vortices in the presence of streamline curvature. Finally, a DNS was performed to study two- and three-dimensional linear and nonlinear disturbance evolution across a compression corner. The LST and PSE methods were used to check the validation of the DNS codes and also to provide the initial disturbances for DNS. Both the single-frequency and multiple-frequency disturbance evolutions were simulated.

CHAPTER III

STEADY MEAN FLOW COMPUTATIONS

To study the hypersonic instability and transition across a compression corner, the steady mean flow across the corner must first be obtained. As we have discussed in Chapter 1, when a large adverse pressure gradient exists in the inviscid pressure distribution, viscous effects become important. The interaction between the adverse pressure gradient and the boundary-layer induces flow separation at the corner. The physical mechanism of shock induced separation has been explained in Chapter 1. Because corner flow occur widely on hypersonic lifting re-entry vehicles, such as body flaps, elevons and rudders, to fully understand the phenomena associated with the shock wave/boundary-layer interaction is very important in order to improve control effectiveness of these vehicles and reduce surface heating.

A great deal of experimental and numerical work has been done to study the hypersonic flow going through a compression corner. Lewis, Kubota, and Lees[11] had conducted an experimental investigation of supersonic laminar, two-dimensional boundary-layer separation in a compression corner with and without cooling. In that experiment, the influences of cooling of the wall on the separation had been investigated. Luca and Cardone[22] investigated the viscous interaction phenomena experimentally in a hypersonic wedge flow at a Mach number of 7.14. The influence of the leading-edge shape, flat plate length, and ramp angle on the separation region, average heat transfer at reattachment, and wavelength of the heat transfer oscillations was analyzed. A combined experimental and computational study of hypersonic shock wave/boundary-layer interactions was reported by Simeonides, Haase & Manna[17] and Simeonides & Haase[18]. They found that the phenomenon of shock wave/boundary-layer interaction at hypersonic Mach numbers was accompanied by the interaction between the separation and reattachment shocks, which can have a profound effect on the ramp pressure

distribution and ramp heating. Other numerical simulations have been performed by Rudy, Thomas, Kumar and Gnoffo[14], and Grasso, Leone and Delery[16]. A comparison of the numerical simulations by different codes such as CFL3D, USA-PG2, LAURA, NASCRLN had been made by Rudy *et al.*

In this chapter, we will perform the steady computation of hypersonic flow going through a compression corner using the WENO scheme which is good for shock capturing. The basic theory was introduced in Chapter 2. We will first present the computational model, grid and computational parameters. Then we will show the steady mean flow results followed by a discussion of the results. Finally, the conclusions on the steady computation will be given.

3.1 Computational model

The computations are performed on a 5.5°compression corner with hypersonic incoming flow. The geometry of the computational model is illustrated in Figure 3.1, and is a Hyper-X forebody model with two corners. The first corner is 5.5° and the second corner is 8.5°. The hypersonic flow goes through the corner from left to right as indicated in the figure. The current numerical simulations are performed in a domain which only includes the first corner.

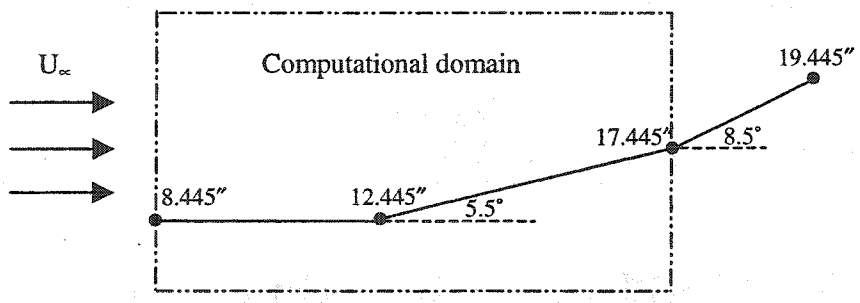

Figure 3.1 The geometry of the computational model.

3.2 Flow parameters

The flow parameters are given in Table 1. These parameters are selected to simulate the Hyper-X wind tunnel model and the experimental conditions.

Table 1: Flow parameters

Freestream Mach number M_∞	=5.373
Freestream Reynolds number Re_∞	=5.464×10^6/ft
Freestream density ρ_∞^*	=6.0891×10^{-3}lbm/ft^3
Freestream pressure p_∞^*	=43.384lbf/ft^2
Freestream velocity U_∞^*	=3043.86ft/s
Reference velocity U_{ref}^*	=478.79ft/s
Freestream Temperture T_∞^*	=133.55°R
Freestream kinematic viscosity ν_∞^*	=5.5707×10^{-4}ft^2/s
Wall temperature T_{wall}^*	=540°R
Prandtl number Pr	=0.70
Ratio of specific heats γ	=1.4
Non-dimensional frequency F_0=1.0×10^{-4}	=264.7kHz

where the non-dimensional frequency F_0 is expressed as $F_0 = \omega / \mathrm{Re} = 2\pi f^* \nu_\infty^* / U_{ref}^{*2}$

3.3 The grid generation and metric computations

The grid for a compression corner can be generated using conformal mapping method. The idea is based on the potential and stream function methods. The complex potential for a steady, irrotational flow going through a compression corner with an angle θ_0 can be expressed as following.

$$W(Z) = \phi(x, y) + i\psi(x, y) = e^{-in\theta_0} Z^n = r^n e^{in(\theta-\theta_0)} \tag{3.1}$$

with

$$n = \frac{\pi}{\pi - \theta_0}; \quad x = r\cos\theta; \quad y = r\sin\theta \tag{3.2}$$

where (x,y) are the Cartesion coordinates and (r,θ) are the polar coordinates.

So the potential and stream functions can be written as

$$\phi(x, y) = r^n \cos(\theta - \theta_0) \tag{3.3}$$

$$\psi(x, y) = r^n \sin(\theta - \theta_0) \tag{3.4}$$

The complex coordinate Z can be expressed by potential and stream functions as follows

$$Z = x + iy = e^{i\theta_0}(\phi + i\psi)^{\frac{\pi-\theta_0}{\pi}} \tag{3.5}$$

From this relation it can be seen that the physical domain can be mapped from a domain constructed by the equal potential lines and the stream lines as shown in Figure 3.2. In this way, a complicated flow domain can be mapped into a simple domain.

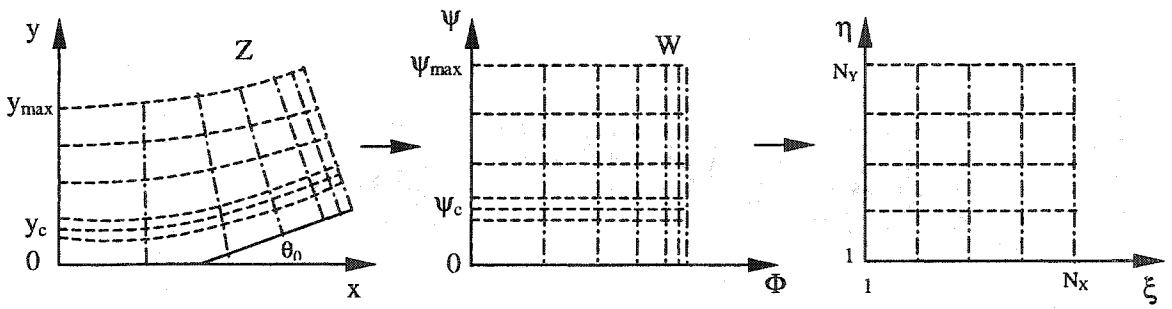

Figure 3.2 Illustration of the conformal mapping method.

For the convenience of discretization of the governing equations, the physical domain (x,y) needs to be mapped into a computational domain (ξ,η) with unit grid steps in both the ξ and η directions. In addition, in order to handle the computations with large gradients in the boundary-layer, the grid lines need to be stretched in the y-direction at the location of critical layer y_c. The following stretching function was used.

$$\psi = \psi_c\left\{1 + \frac{\sinh[\tau((\eta-1)/(N_Y-1) - B)]}{\sinh(\tau B)}\right\} \tag{3.6}$$

where

$$B = \frac{1}{2\tau}\ln\left[\frac{1 + (e^{\tau} - 1)(\psi_c/\psi_{\max})}{1 + (e^{-\tau} - 1)(\psi_c/\psi_{\max})}\right] \qquad 0 < \tau < \infty \tag{3.7}$$

and ψ_c is the location corresponding to y_c where the grid is stretched, while τ is a parameter used to control the grid density in the stretching region.

The same stretching function was also used to stretch the grid lines in the x direction at the end of the computational domain where the nonlinear harmonic interaction occurs for unsteady computation. Then the metrics can be obtained via chain rule differentiation:

$$\xi_x = \frac{\partial \xi}{\partial \phi}\frac{\partial \phi}{\partial x}; \qquad \xi_y = \frac{\partial \xi}{\partial \phi}\frac{\partial \phi}{\partial y} \tag{3.8}$$

$$\eta_x = \frac{\partial \eta}{\partial \psi}\frac{\partial \psi}{\partial x}; \qquad \eta_y = \frac{\partial \eta}{\partial \psi}\frac{\partial \psi}{\partial y} \tag{3.9}$$

From Cauchy theory we have

$$\frac{\partial \phi}{\partial x} = u; \qquad \frac{\partial \phi}{\partial y} = v; \qquad \frac{\partial \psi}{\partial y} = u; \qquad \frac{\partial \psi}{\partial x} = -v \tag{3.10}$$

and

$$u - iv = \frac{dW}{dZ} = \frac{\pi}{\pi - \theta_0} r^{\frac{\theta_0}{\pi-\theta_0}} e^{-i\theta_0 \frac{\pi-\theta}{\pi-\theta_0}} \tag{3.11}$$

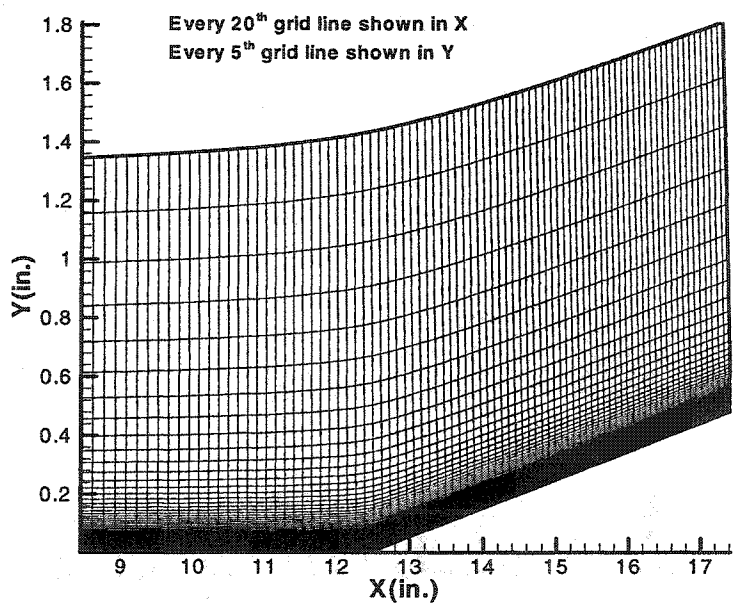

Figure 3.3 The computational grid.

According to this transformation, we can obtain the metrics by analytical methods. The physical grid which was generated by conformal mapping methods is shown as Figure 3.3. The grid size is 1701×301 in streamwise and normal directions, respectively.

3.4 The Euler computations for code validation

Before we begin to perform the steady computation, a code validation check is necessary. This was done by comparing the Euler results obtained by this code with inviscid theoretical results. Figure 3.5 shows the density contours for inviscid hypersonic flow at a Mach number of 5.373, going through a 5.5° compression corner. Figure 3.6 shows the pressure distribution. The density contour in Figure 3.5 shows that the deflection angle of oblique shock is about 14.8°. And in Figure 3.6, the pressure increase across the shock is $p_2/p_1 = 1.98$.

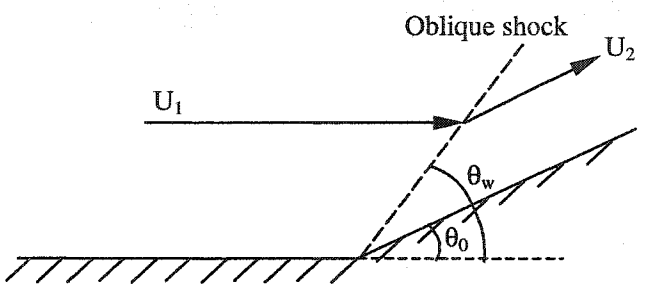

Figure 3.4 The oblique shock across the compression corner.

According to the compressible flow theory, for the supersonic flow along a wedge with a wedge angle θ_0 as shown in Figure 3.4, if we know the flow Mach number, we can obtain the deflection angle θ_w of the oblique shock and the pressure increase across the shock according to following equations

$$\tan\theta_0 = 2\cot\theta_w \frac{M_1^2 \sin^2\theta_w - 1}{M_1^2(\gamma + \cos 2\theta_w) + 2} \tag{3.123}$$

$$\frac{p_2}{p_1} = 1 + \frac{2\gamma}{\gamma+1}(M_1^2 \sin^2\theta_w - 1) \tag{3.124}$$

For the given Mach number and wedge angle, we find that θ_w=14.7° and p_2/p_1=2.00. It is observed from the comparisons that the numerical Euler results agree very well with the inviscid theoretical results. The code is validated with further computations.

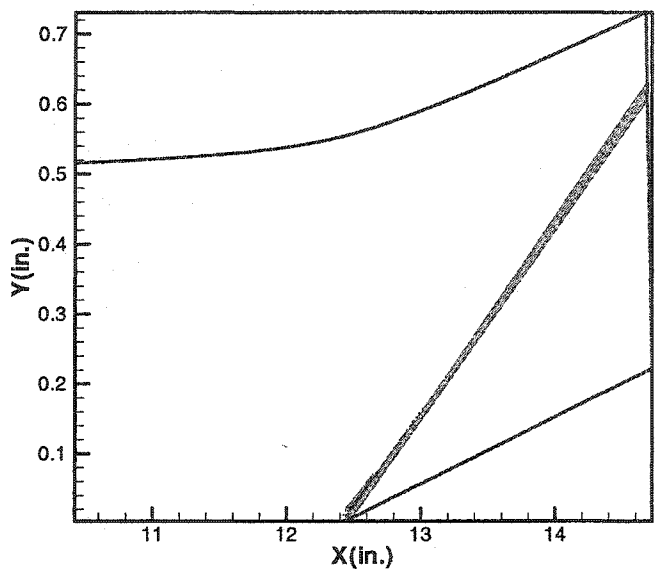

Figure 3.5 The density contour across the compression corner obtained by Euler computation.

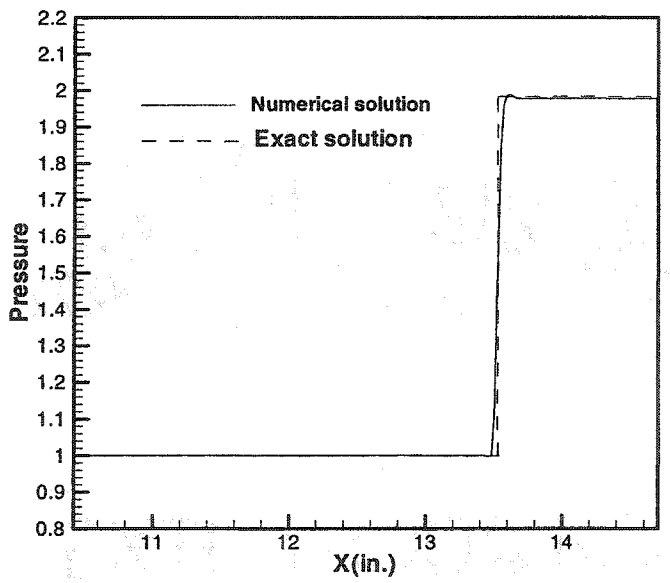

Figure 3.6 The pressure comparison between the numerical result and the exact solution.

3.5 The initial and boundary conditions for the viscous mean flow computation

In the present study, we are mostly concerned with the separation bubble region for both steady and unsteady hypersonic flow. So we begin our computation at a streamwise location which is approximately 3 inches upstream of the separation point. At this streamwise location, similarity boundary-layer results are applied as the inflow boundary conditions. These results are obtained by a similarity transformation of the two-dimensional compressible boundary-layer equation. Consider the following boundary-layer equations

$$\frac{\partial}{\partial x}(\rho u)+\frac{\partial}{\partial x}(\rho v)=0 \tag{3.12}$$

$$\rho\left(u\frac{\partial u}{\partial x}+v\frac{\partial u}{\partial y}\right)=\frac{\partial}{\partial y}\left(\mu\frac{\partial u}{\partial y}\right) \tag{3.13}$$

$$\rho u C_p\frac{\partial T}{\partial x}+\rho v C_p\frac{\partial T}{\partial y}=\frac{\partial}{\partial y}(k_T\frac{\partial T}{\partial y})+\mu\left(\frac{\partial u}{\partial y}\right)^2 \tag{3.14}$$

$$\rho T=\rho_\infty T_\infty \tag{3.15}$$

We can choose the similarity variables as following

$$s=\mu_\infty\rho_\infty U_\infty x \tag{3.16}$$

$$\eta=\frac{U_\infty\rho_\infty}{(2s)^{1/2}}\int_0^y\frac{T_\infty}{T}dy \tag{3.17}$$

where the subscript "∞" stands for the upstream flow parameters.

The stream function, ψ, and temperature, T, can be written as functions of the above similarity variables as follows:

$$\psi=(2s)^{1/2}f(\eta) \tag{3.18}$$

$$T=T_\infty\, g(\eta) \tag{3.19}$$

$$u = \frac{1}{\rho}\frac{\partial \psi}{\partial y} = \frac{\partial \psi}{\partial \eta}\cdot\frac{\partial \eta}{\partial y} = U_\infty f'(\eta) \tag{3.20}$$

$$\begin{aligned} v &= -\frac{1}{\rho}\frac{\partial \psi}{\partial x} = -\frac{1}{\rho}\left(\frac{\partial \psi}{\partial s}\frac{\partial s}{\partial x} + \frac{\partial \psi}{\partial \eta}\frac{\partial \eta}{\partial x}\right) \\ &= -\frac{1}{\rho}\left[\frac{1}{(2s)^{1/2}} f(\eta)\mu_\infty \rho_\infty U_\infty + (2s)^{1/2} f'\frac{\partial \eta}{\partial x}\right] \end{aligned} \tag{3.21}$$

The continuity equation is automatically satisfied by the stream function. If we substitute the stream function into the momentum equation, after simplification and rearrangement, we get the following similarity equation for the boundary layer momentum equation.

$$\frac{d}{d\eta}\left(\frac{\rho\mu}{\rho_\infty \mu_\infty} f''\right) + ff'' = 0 \tag{3.22}$$

If we substitute the stream function and temperature into the energy equation and rearrange, we get the following similarity equation for the energy equation.

$$\frac{d}{d\eta}\left(\frac{\rho\mu}{\rho_\infty \mu_\infty}\cdot\frac{g'}{P_r}\right) + fg' + (\gamma - 1)M_\infty^2\left(\frac{\rho\mu}{\rho_\infty \mu_\infty}\right)\cdot f''^2 = 0 \tag{3.23}$$

The boundary conditions for these similarity equations can be written as following

$$f(0) = 0,\ f'(0) = 0,\ g(0) = \frac{T_{wall}}{T_\infty} \quad at \quad \eta = 0 \tag{3.24}$$

A fourth-order Runge-Kutta method was used to solve the above ordinary differential equations with the given boundary condition. The velocity and temperature distributions are shown in Figure 3.7 and Figure 3.8. All other variables such as ρ, p, v, e_t can be obtained using the state equation and continuity equation. These similarity results can also be used as the initial conditions for time iteration to get the steady mean flow across the compression corner. Because the flow is supersonic in the whole computational domain except in the boundary-layer close to the wall, the extrapolation method can be applied at the outflow boundary condition. At the wall, the non-slip condition and the

wall temperature are specified.

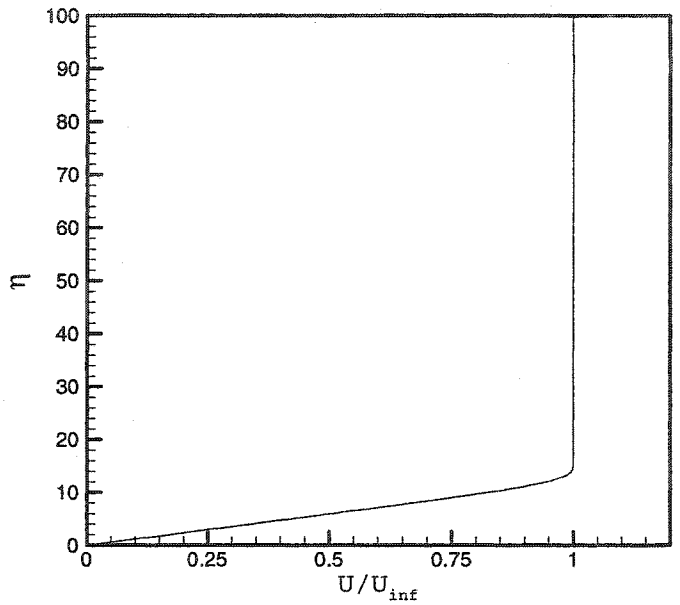

Figure 3.7 The streamwise velocity distribution for the similarity boundary-layer.

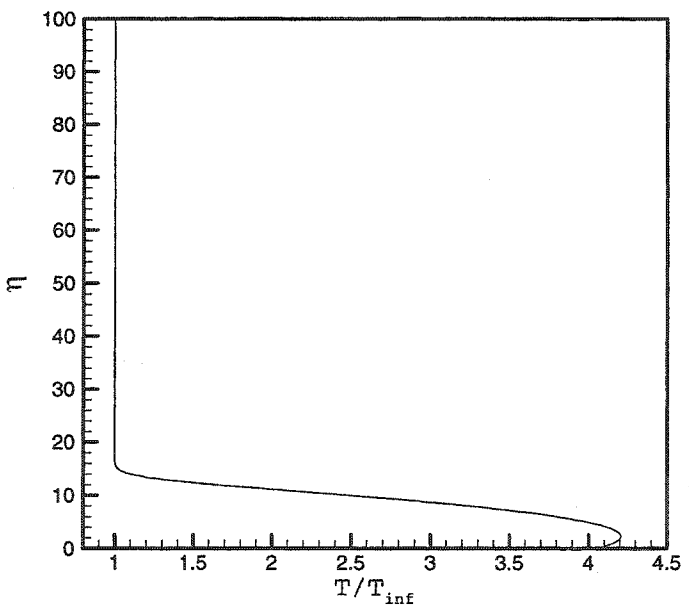

Figure 3.8 The temperature distribution for the similarity boundary-layer.

3.6 Mean flow results

In this section, the mean flow results and discussion will be presented. The results are obtained by unsteady time iteration using local time step in the whole computational domain until the maximal residual is less than ~10^{-5}. Figures 3.9-3.14 show the results for the steady mean flow field. Figure 3.9a and 3.9b show the density contours. Figure 3.10 and Figure 3.11 show Mach contours and normal velocity contours respectively. Figures 3.12a and 3.12b show the streamline patterns. Figures 3.9b and 3.12b depict the expanded view near the corner region. Figure 3.13 shows the streamwise pressure distribution at different distances from the wall with Y=0, 0.08, 0.120, 0.237 inches respectively. Figure 3.14 shows the variation of the boundary-layer thickness and the displacement thickness in the streamwise direction.

As we discussed earlier, due to the interaction of the oblique shock and the boundary-layer, the boundary-layer separates near the corner and a separation bubble is formed. In this case the separation point is located at about 10.8 inches and reattaches at about 14.1 inches (the corner is located at 12.445 inches). The boundary-layer thickness at X=10 inches is about 0.08 inches. Hence the separation and reattachment points are located at about 20 boundary-layer thicknesses from the corner point and the separated region is about 40 boundary-layer thicknesses long. Figure 3.12 show that a separation bubble is formed in the corner region and there is a circulation flow in the separation bubble. The streamlines are concave outside of the separation bubble. Figure 3.12b also shows that the boundary of the separated region is almost a straight line and is inclined at about 3.1° while the main ramp is inclined at 5.5°. Due to this new inclined surface, two compression waves, one close to the separation point and another near the reattachment point, are created as shown in the density contours of Figure 3.9b. From the Mach contours shown in Figure 3.10, we notice that a very thin subsonic layer exists close to the wall. The normal velocity shown in Figure 3.11 exhibits significant changes across the compression waves.

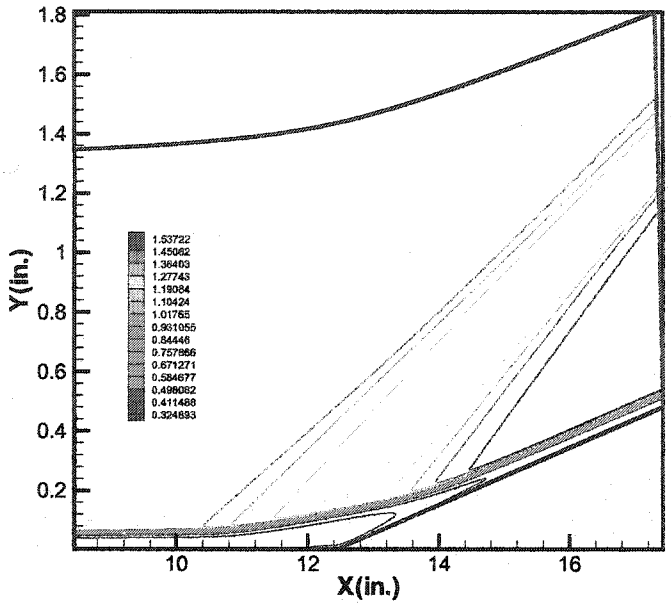

Figure 3.9a Density contour distribution.

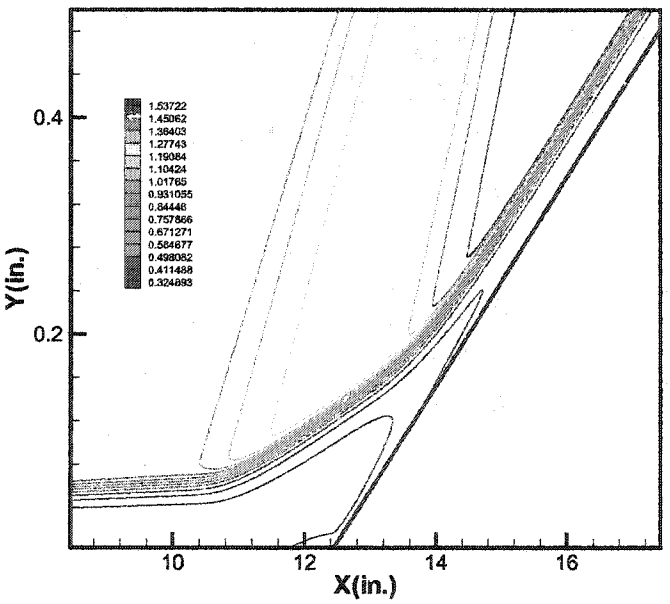

Figure 3.9b Expanded view of the density contours.

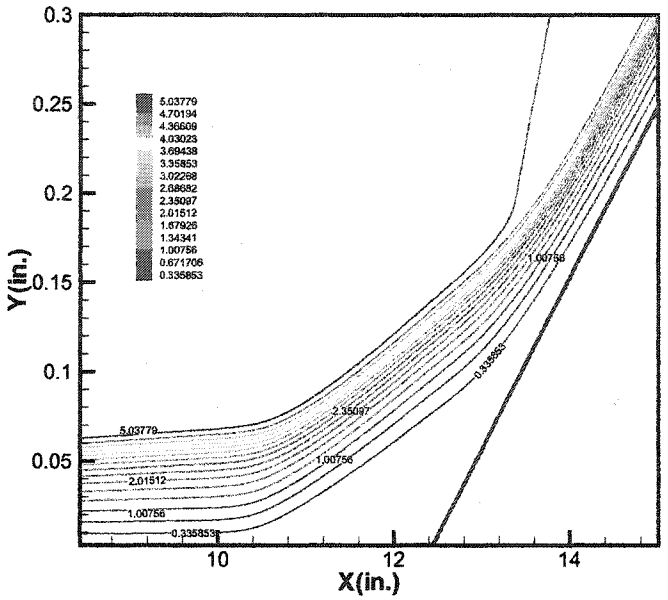

Figure 3.10 The Mach contour distribution.

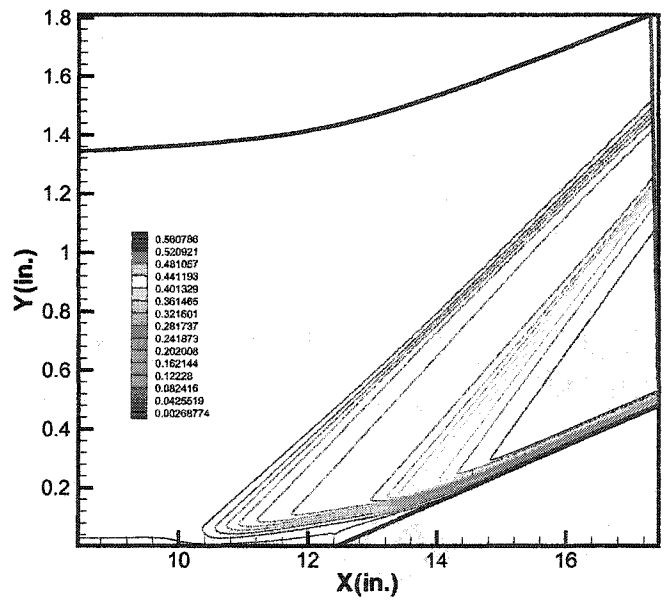

Figure 3.11 Normal velocity contours near the compression corner.

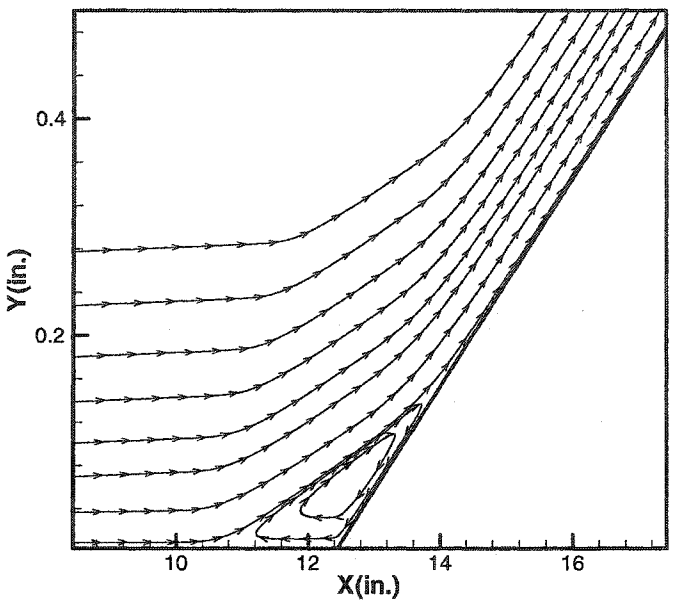

Figure 3.12a The streamline distribution.

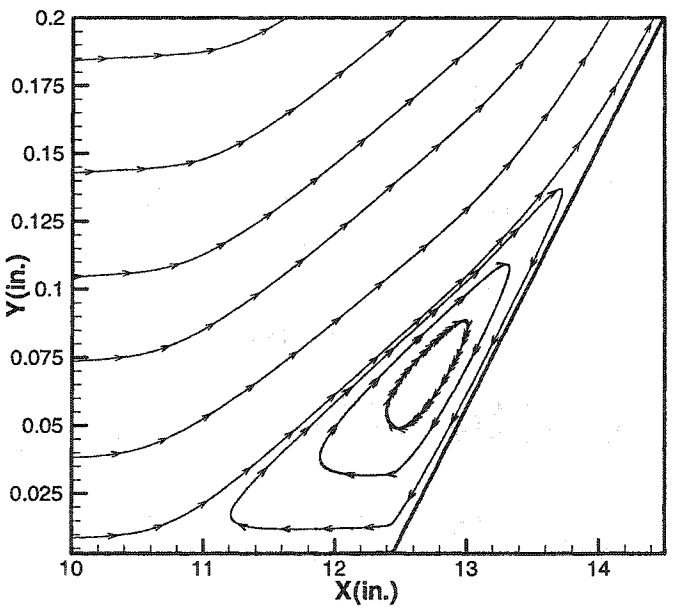

Figure 3.12b Expanded view of streamlines close to the corner.

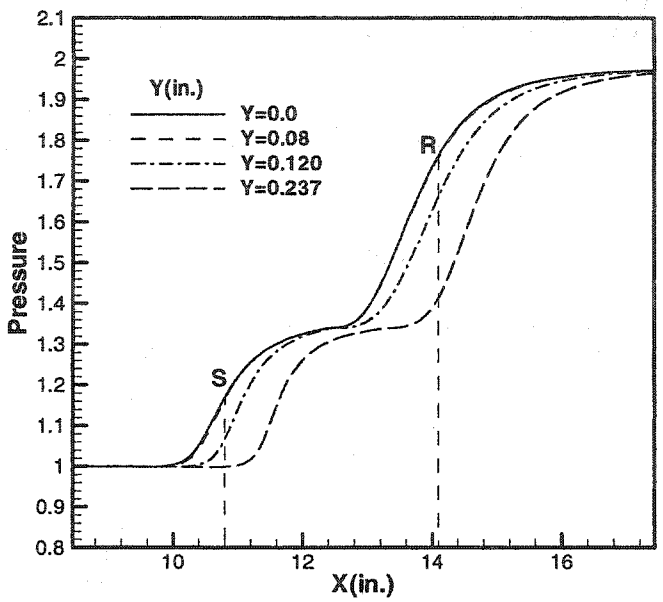

Figure 3.13 The pressure distribution in the streamwise at different normal locations.

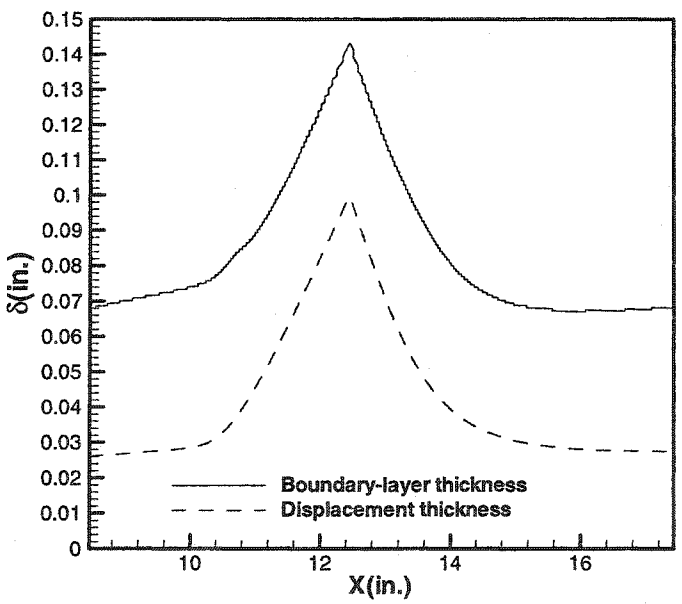

Figure 3.14 The boundary-layer thickness distribution.

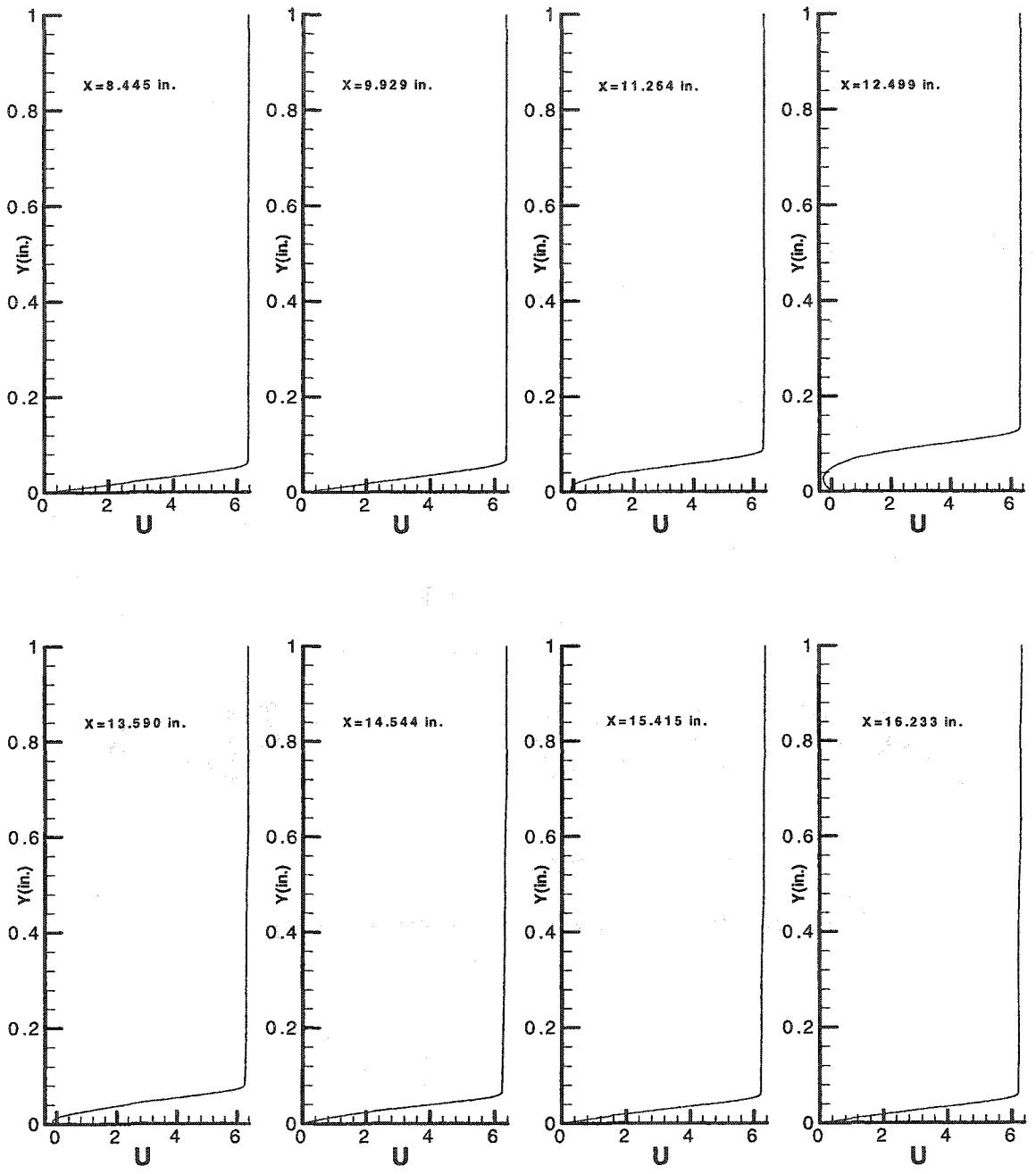

Figure 3.15a The streamwise velocity distributions at different streamwise locations.

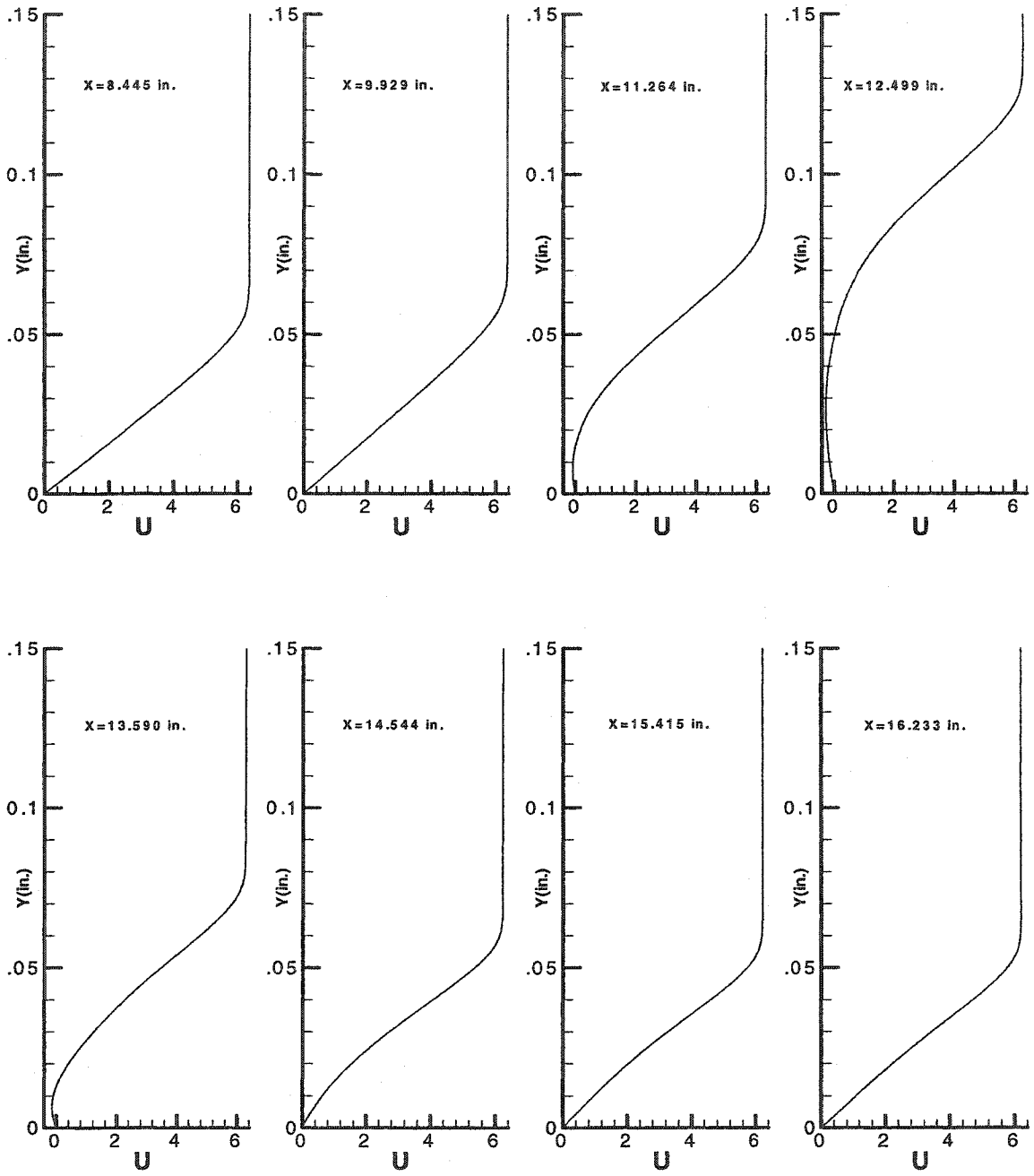

Figure 3.15b Expanded view of the streamwise velocity distributions in the boundary-layer.

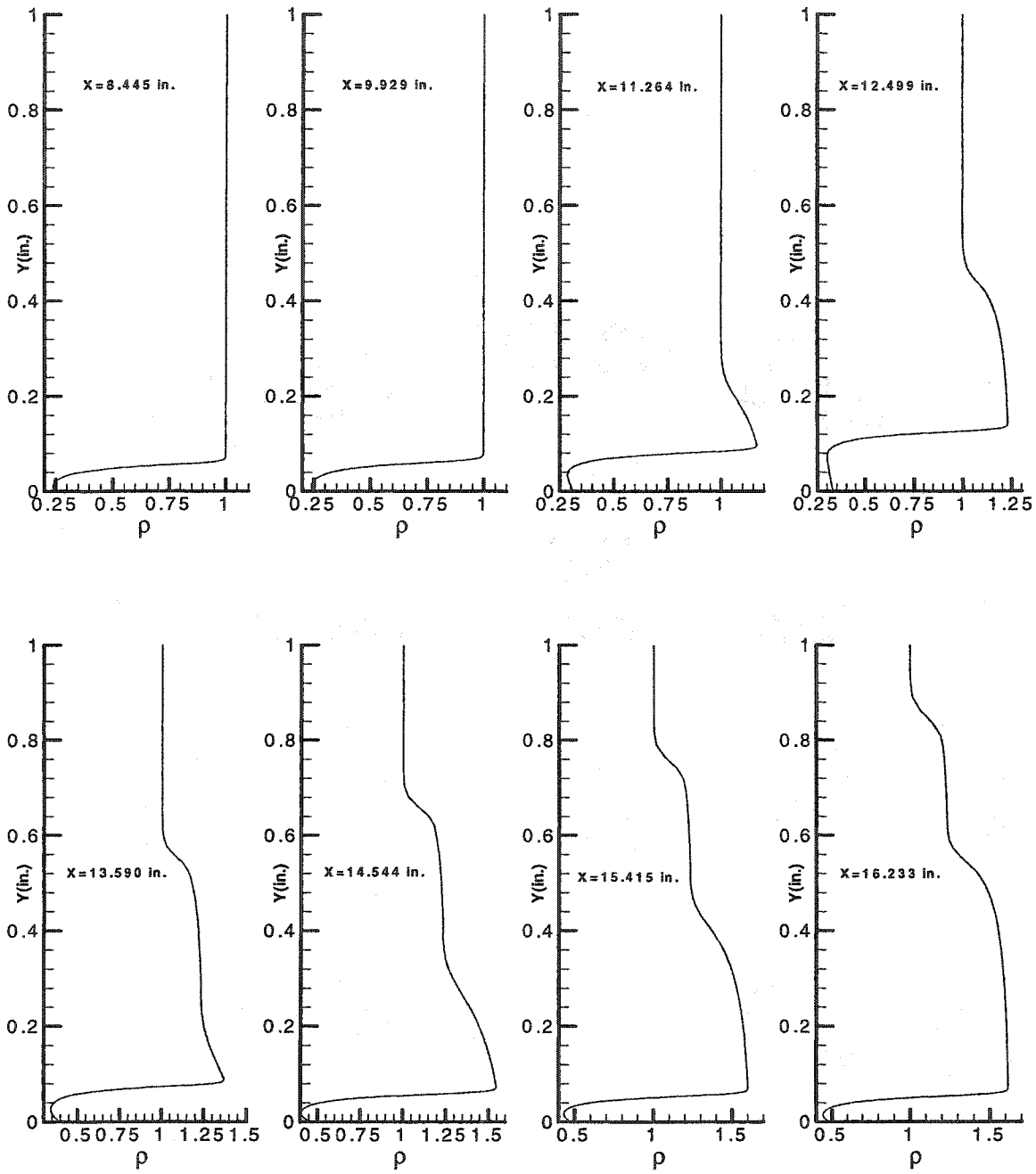

Figure 3.16a Density distributions at different streamwise locations.

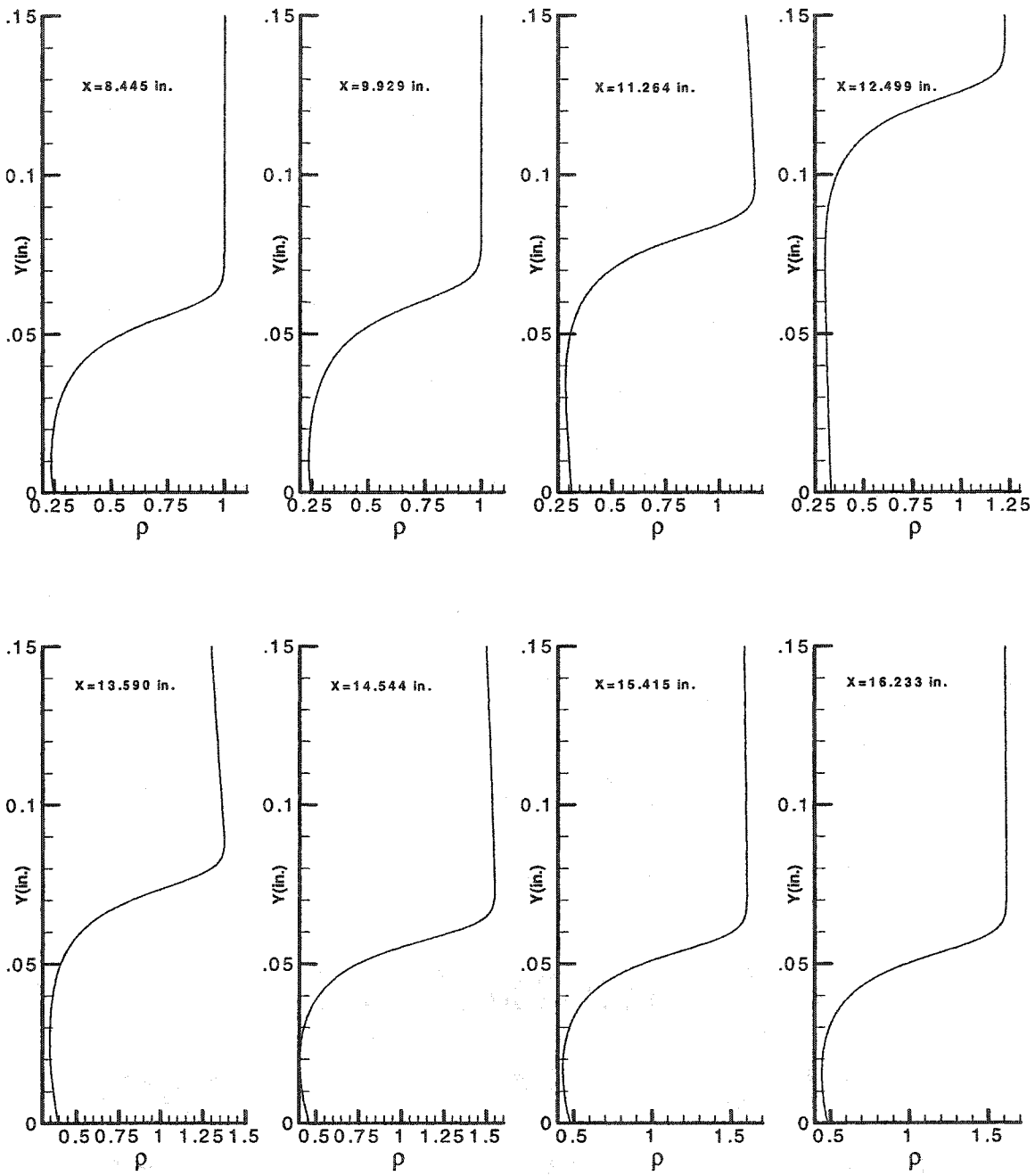

Figure 3.16b Expanded view of the density distributions in the boundary-layer.

Figure 3.13 shows the pressure distributions in the streamwise direction at different normal locations. Where "S" stands for the separation point and "R" stands for the reattachment point. The pressure distribution at the wall surface shows that the pressure starts to increase at X=10 inches which is 0.8 inch upstream of the separation point. This is the free interaction region analyzed by Lighthill[5][6] and Stewartson and Williams[7]. The initial pressure increase saturates in the middle region and then increases again. This shows that near the corner region the flow field is approximately uniform. It is seen that the pressure distributions at Y=0 and Y=0.08 inches which are on the wall and along the edge of the boundary-layer are almost equal. This implies that the compression waves originate from outside of the boundary-layer and do not penetrate inside the boundary-layer. Another important observation is the growth of the boundary-layer which is depicted in the Figure 3.14. Initially, the boundary-layer grows according to the similarity laws along a flat plate and from about X=9.6 inches the boundary-layer thickness remains constant up to the separation point X=10.8 inches. From the separation point, the boundary-layer thickness grows steeply as a wedge and reaches a peak thickness at about 12.8 inches and again decreases very steeply near the reattachment point. It is interesting to note that the boundary-layer thickness reaches a minimum value of 0.068 inches at X=15 inches and this value is smaller than the boundary-layer thickness upstream of separation. Therefore, when the hypersonic flow passes over a compression corner the boundary-layer becomes smaller downstream of the separation region due to compression.

Figures 3.15a and 3.15b show the streamwise velocity profiles at streamwise locations X=8.445, 9.929, 11.264, 12.499, 13.590 14.544, 15.415and 16.233 inches respectively. The locations X=11.264, 12.499 and 13.590 are in the separated region and the others are outside of it. Similarly, Figures 3.16a and 3.16b show the density profiles at these streamwise locations. We clearly see the growth and shrinking of the boundary-layer thickness as discussed earlier. We can also see that the flow reverses in

the separation region. The velocity in the recirculation region is on the order of 200ft/s compared to 3000ft/s at the edge of the boundary-layer. The density is almost constant in the separation bubble and the density gradient inside the boundary-layer is much larger in the downstream region compared to upstream of the corner.

3.7 Summary

In this chapter, we computed the two-dimensional steady mean flow for hypersonic flow (M_∞=5.373) going through a 5.5° compression corner using a fifth-order WENO scheme and a three-stage Runge-Kutta method. The mean flow results show details of the interactions between the shock wave and the boundary-layer. Due to this interaction, the flow separates about 1.6 inches upstream of the corner and reattaches about 1.6 inches downstream of the corner. A circulation flow is created in the separation bubble. Some compression waves appear along the edge of the separation bubble. This mean flow will provide the base flow for the numerical simulation of the hypersonic boundary-layer instability and transition across a 5.5° compression corner, performed in next a few chapters.

CHAPTER IV

LINEAR COMPUTATIONS OF THE DISTURBANCE EVOLUTIONS

The linear eigenvalue computations have been widely used for boundary-layer instability and transition predictions for decades because linear computations are much less costly than DNS. In the present study, before a direct numerical simulation is performed to study the boundary-layer instability and transition across the compression corner, several issues need to be addressed. These issues include how to choose the disturbance frequency and how to introduce the initial disturbances, as well as how to validate the computational results obtained by direct numerical simulation. In order to answer these questions, we first perform some linear computations of both two- and three-dimensional disturbance evolution across the compression corner. The LST analysis will be applied at selected streamwise locations using the local parallel assumption. The linear computation results will give an approximate picture of the linear evolution of disturbances across the compression corner. In addition, due to the existence of the curvature of the streamlines along the edge of the boundary-layer, a Gortler instability will occur at locations with large streamline curvature. In this chapter, the Gortler instability will also be investigated.

4.1 Linear stability analysis

The linear stability theory and its numerical scheme have been discussed in §2.3. In this section, the linear stability theory will be used to compute the spatial amplification rate of both two- and three-dimensional disturbances at selected streamwise locations across the compression corner, using different disturbance frequencies, based on the mean flow profiles obtained in chapter 3.

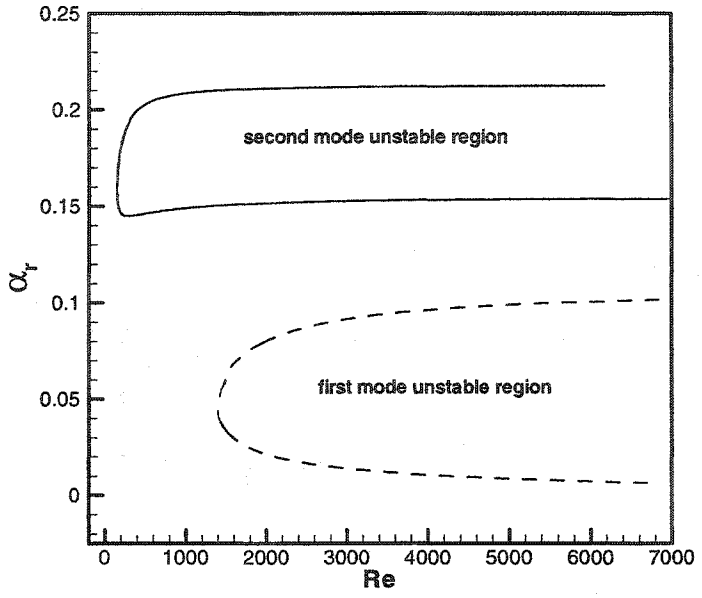

Figure 4.1 The neutral stability curves in (α_r, Re) plane.

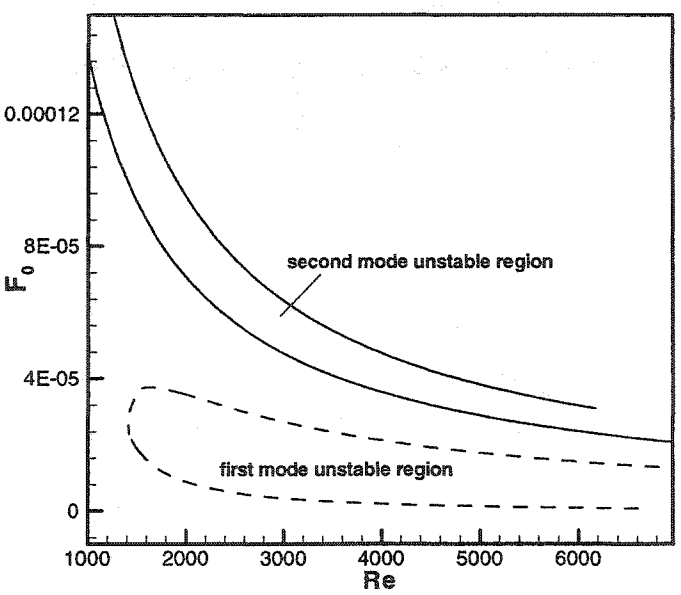

Figure 4.2 The neutral stability curves in (F_0, Re) plane.

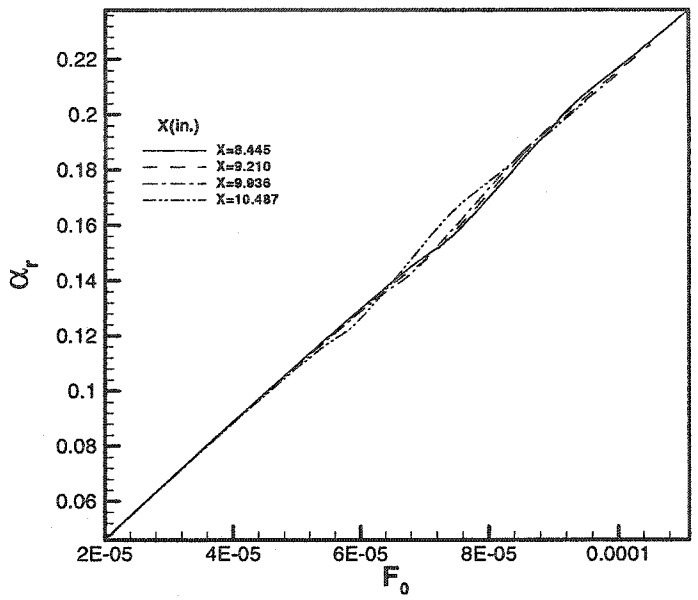

Figure 4.3 The variation of the streamwise wave number with the disturbance frequency.

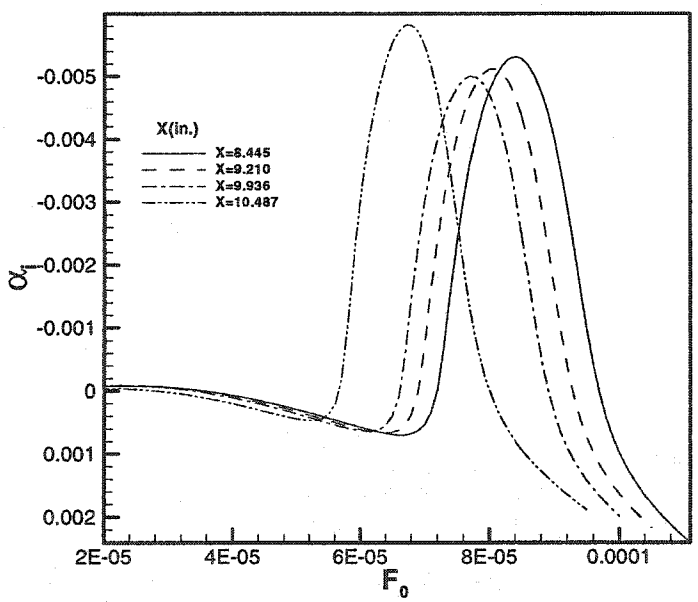

Figure 4.4 The variation of the spatial amplification rate with the disturbance frequency.

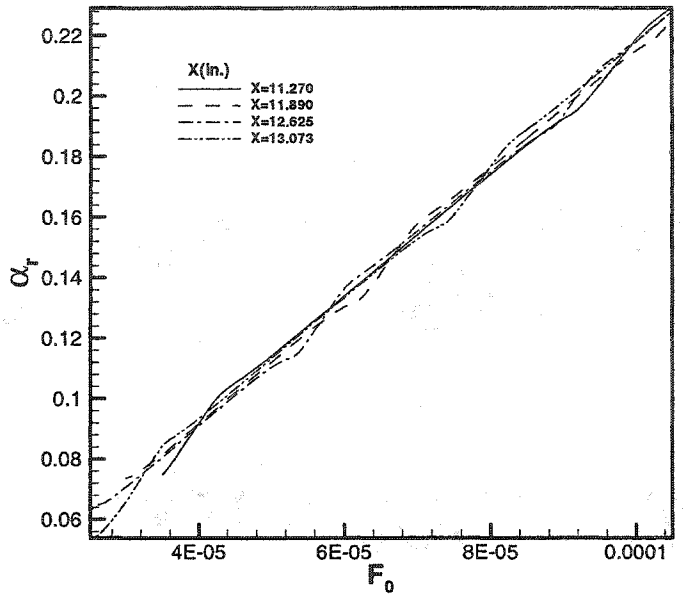

Figure 4.5 The variation of the streamwise wave number with the disturbance frequency.

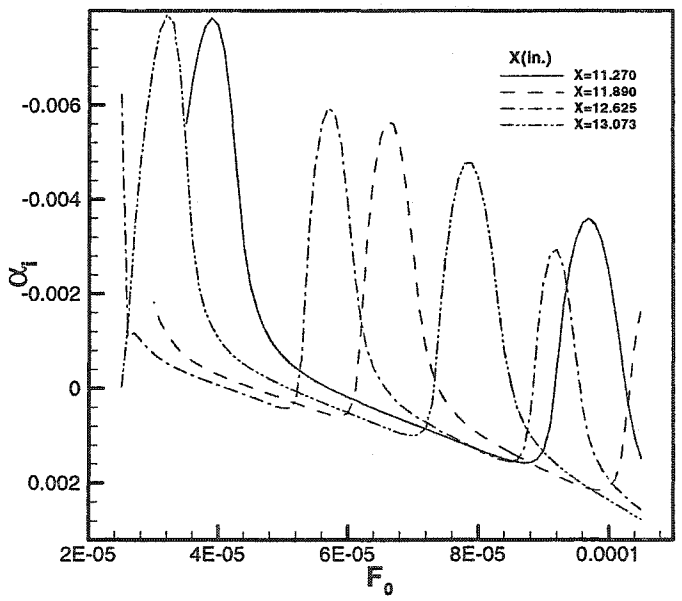

Figure 4.6 The variation of the spatial amplification rate with the disturbance frequency.

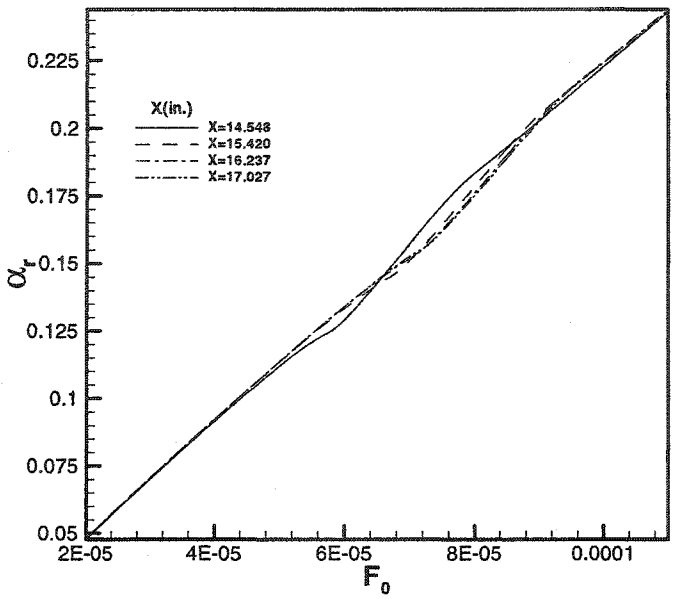

Figure 4.7 The variation of the streamwise wave number with the disturbance frequency.

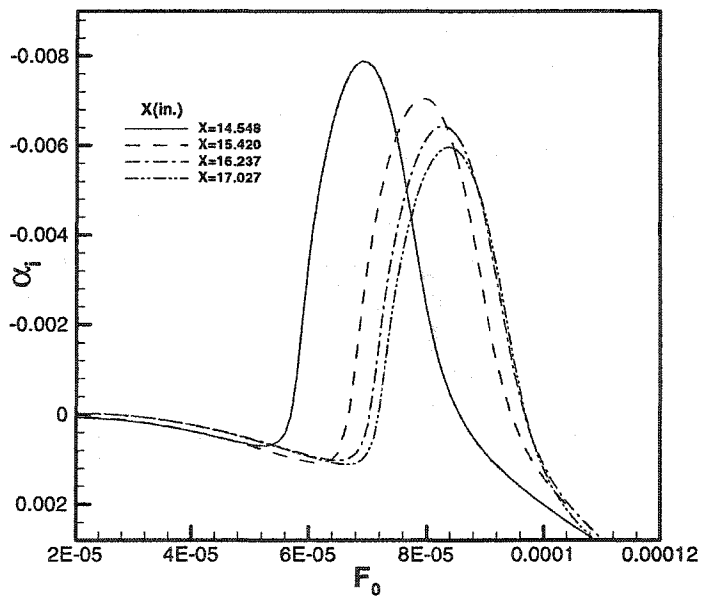

Figure 4.8 The variation of the spatial amplification rate with the disturbance frequency.

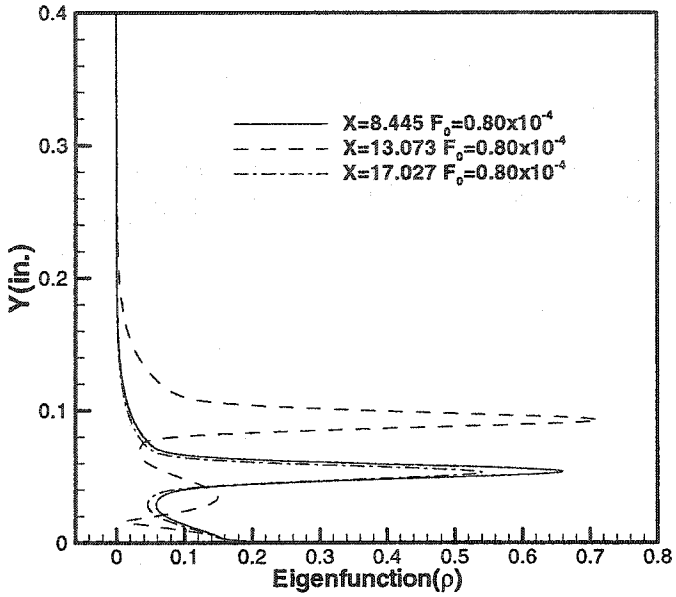

Figure 4.9 The eigenfunctions of the density disturbance at high frequency.

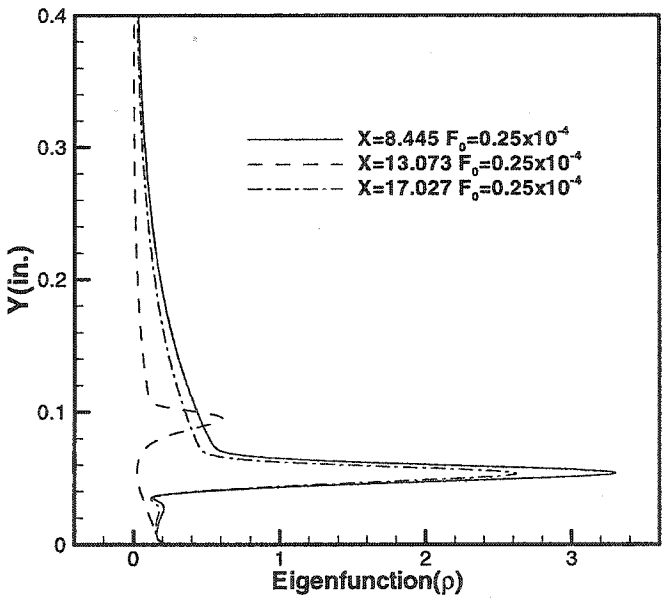

Figure 4.10 The eigenfunctions of the density disturbance at low frequency.

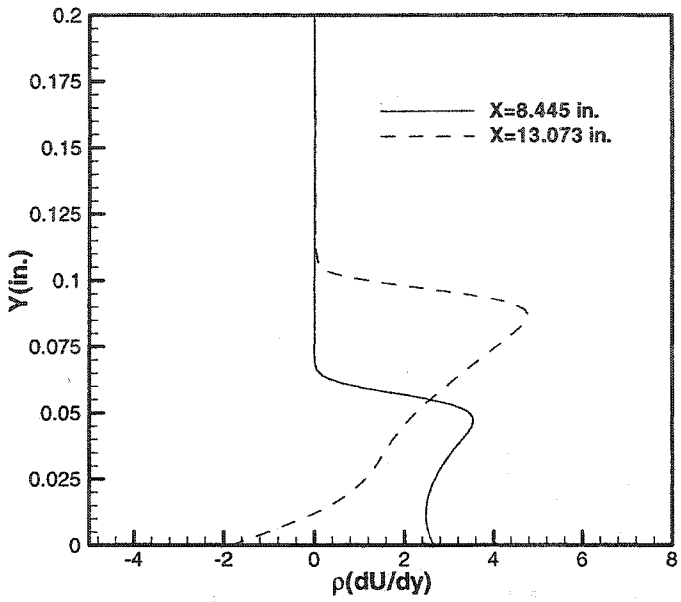

Figure 4.11 The profiles for $\rho \frac{dU}{dy}$ at different streamwise locations.

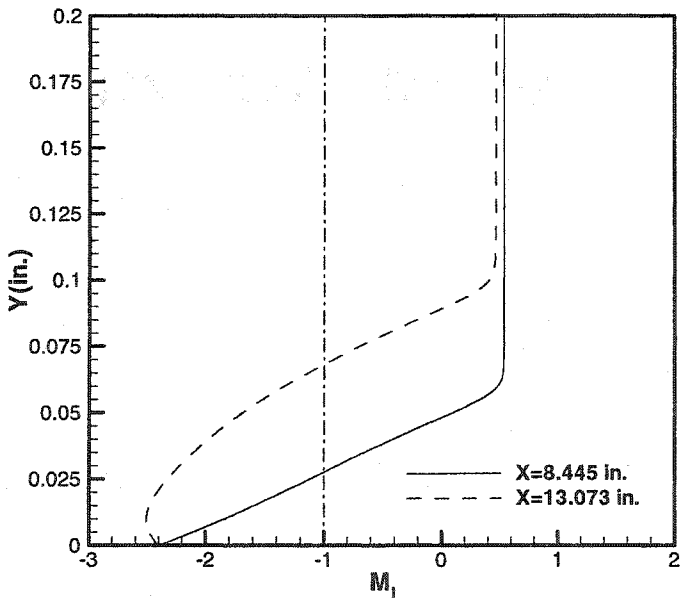

Figure 4.12 The local Mach number relative to the phase velocity.

4.1.1 Linear computation of the evolution of two-dimensional disturbances across the compression corner

Figure 4.1 and Figure 4.2 show the neutral stability curves for both the first mode and the second mode disturbances with the mean flow at the initial streamwise location X=8.445 inches. Figure 4.1 shows the neutral stability curves in (α_r, Re) plane and Figure 4.2 shows the neutral stability curves in (F_0, Re) plane. The neutral stability curves demonstrate that the first mode instability only exists in low frequency regions. No unstable first mode disturbance exists at frequencies above $F_0=0.40\times10^{-4}$. The second mode instability exists in the high frequency regions at low Reynolds numbers and in the low frequency regions at high Reynolds numbers. The second mode disturbance has a much smaller critical Reynold number than the first mode disturbance.

Figures 4.3-4.8 show the computed linear stability results of the streamwise wave number and the spatial amplification rate at different streamwise locations for two-dimensional disturbances. Figure 4.3 and Figure 4.4 show the variations of the streamwise wave number, α_r, and spatial amplification rate, α_i, with frequency respectively at four streamwise locations, X=8.445, 9.210, 9.936, 10.487 inches, upstream of the separation bubble. Figure 4.5 and Figure 4.6 show the variations of α_r and α_i with the frequency at four streamwise locations, X=11.270, 11.890, 12.625, 13.073 inches, in the separation bubble region, while Figure 4.7 and Figure 4.8 show the variation of α_r and α_i with the frequency at four streamwise locations, X=14.548, 15.420, 16.237, 17.027 inches, downstream of the separation bubble. It is observed from these figures that the streamwise wave number almost keeps a linear variation with the disturbance frequency at all streamwise locations. This gives a constant phase velocity of about 0.9. For the same disturbance frequency, the streamwise wave number remains approximately the same at the different streamwise locations. This demonstrates that the streamwise wave number of the disturbance remains approximately constant with the

two-dimensional disturbance propagating downstream in the boundary-layer at a fixed frequency.

One interesting observation from the spatial amplification rate plots is that the spatial amplification rate shows several peaks at different frequencies. From the neutral stability curves, we know that these peaks correspond to the unstable regions for different modes. At the locations upstream of the separation bubble, as shown in Figure 4.4, we obtain the typical high Mach number two-dimensional first and second mode growth rate curves and two peaks for α_i appear. One is located in the low frequency region between F_0=0.2~0.4×10^{-4}, which corresponds to the first mode unstable region. The other peak is located in the high frequency region between F_0=0.7~1.0×10^{-4}, which corresponds to the second mode unstable region. We notice that the two-dimensional first mode is almost neutral and the second mode is very unstable and has a maximal growth rate at a frequency close to F_0=0.8×10^{-4}. The most amplified frequency for the second mode disturbance will move toward the smaller value with the streamwise location moving downstream.

At the locations in the separation region shown in Figure 4.6, the unstable regions for different modes also appear at different frequencies. But now we notice that more peaks have appeared with each unstable region becoming much narrower in frequency band. This demonstrates that the third or higher modes have appeared in the separation region. We also notice that the most unstable region has shifted to the low frequency region between F_0=0.2~0.4×10^{-4}. We will show later that the second peak corresponds to the third mode which is the second acoustic mode. At the locations downstream of the separation region, shown in Figure 4.8, the spatial amplification rate again shows the typical high Mach number two-dimensional first and second mode unstable regions. The first mode unstable region is in the low frequency region between F_0=0.2~0.4×10^{-4} and the second mode unstable region is in the high frequency region between F_0=0.7~1.0×10^{-4}. The first mode is approximately neutral and the second mode is very unstable. The most

amplified frequency for the second mode disturbance moves toward much larger values with the streamwise location moving downstream. Further downstream, the most amplified frequency remains close to $F_0=0.80\times10^{-4}$ and changes little. It is apparent that the disturbance with the frequency $F_0=0.80\times10^{-4}$ will show the greatest amplification when it evolves downstream across the compression corner.

In Figures 4.9 and 4.10, we plot the eigenfunction distributions for the density disturbance with the maximum growth rates at streamwise locations X=8.445, 13.073 and 17.027 inches respectively. Figure 4.9 shows the results at the high frequency $F_0=0.80\times10^{-4}$ while Figure 4.10 shows the results at low frequency $F_0=0.25\times10^{-4}$. At X=8.445 and 17.027 inches, we obtain the eigenfunction distribution for the second mode and the first mode at the high and low frequencies, respectively. The high frequency second mode has a peak near the critical layer and has another peak near the wall. At the streamwise locations X=13.073 inches, at low frequencies we see the same eigenfunction distribution with the peak near the critical layer and another peak near the wall. But at high frequencies, we see that the layer near the wall exhibits two maximums in the distribution. To investigate this further, in Figures 4.11 and 4.12 we plot the distribution of two important boundary-layer functions $\rho dU/dy$ and the local Mach number relative to the phase velocity at the critical point $M_{local}=(U-C_{cr})/\sqrt{\gamma RT}$ respectively. The results are presented for the two stations at X=8.445 and 13.073 inches. As we expected the $\rho dU/dy$ peaks near the edge of the boundary-layer and the phase speed of the disturbances are about 0.9. The interesting observation is the relative supersonic region near the wall, which is the cause for the appearance of the higher acoustic modes in the hypersonic boundary-layers. Since the relative supersonic region is very thick for the boundary-layer in the separation region, multiple high frequency acoustic modes(second, third, ...) are generated. Because the relative supersonic region is thick, the wavelength of these modes are long and hence the frequency of the first high mode or

the second mode will be lower in the separation region than in the region away from the separation region. Hence, in the separation region, the low frequency higher modes that we discussed earlier in F_0=0.2~0.4×10^{-4} are the classical second modes and the higher frequency higher modes in F_0=0.7~1.0×10^{-4} are the third or higher modes. This also explains the reason for the appearance of the multiple oscillations in the eigenfunction distribution near the wall in the separation region. Since away from the corner, the relative supersonic region narrows and the frequencies of the higher modes shift to higher values.

Since transition is caused by the cumulative growth of disturbances, we compute the variation of the growth rate for a fixed frequency in the streamwise direction. Figures 4.13-4.15 show the variation of the local spatial amplification rate and the cumulative growth rate in the streamwise direction for the two-dimensional second mode disturbances in high frequency regions with frequencies F_0=0.85-, 0.70-, and 0.65×10^{-4} respectively. It is observed from these figures that the local spatial amplification rate increases or decreases monotonously upstream and downstream of the separation bubble. However, in the separation bubble region, the local spatial amplification rate keeps oscillating between negative and positive values. The corresponding cumulative growth rates in the streamwise direction at these frequencies can be obtained by the following integral relation.

$$e^N = e^{-\int_{x_0}^{x} \alpha_i(x)dx} \tag{4.1}$$

The cumulative growth rates are plotted using a Log scale so that we can see the disturbance growth characteristics in the separation bubble region more clearly. It is observed that at frequency F_0=0.85×10^{-4}, the disturbance grows monotonously upstream and downstream of the separation region. In the separation region, the disturbance is approximately neutral. For disturbances with frequencies F_0=0.70- and 0.65×10^{-4}, the isolated stable regions have begun to appear upstream and downstream of the separation region. And in the separation region, the disturbances are approximately neutral. The

neutral status of the two-dimensional disturbances in the separation region is due to the oscillation of local spatial amplification rate in this region.

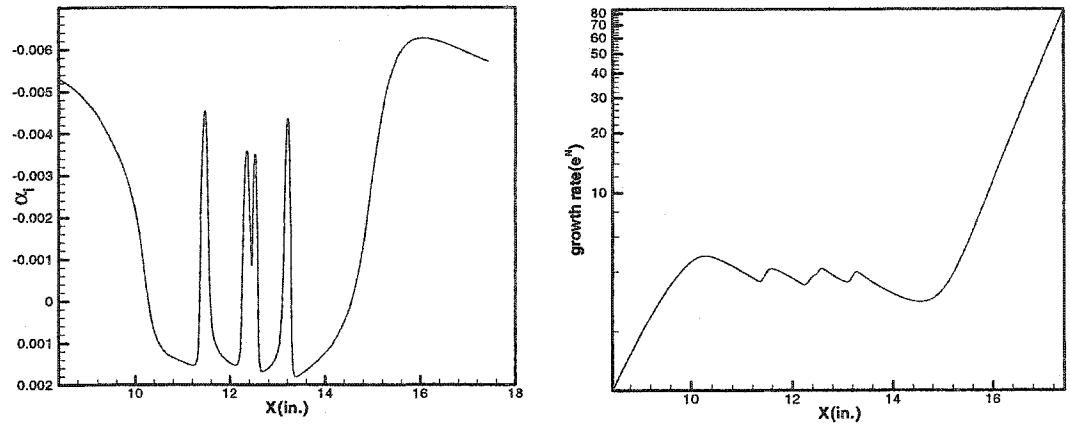

Figure 4.13 Local α_i and cumulative growth rate in the streamwise direction, F_0=0.85x10^{-4}.

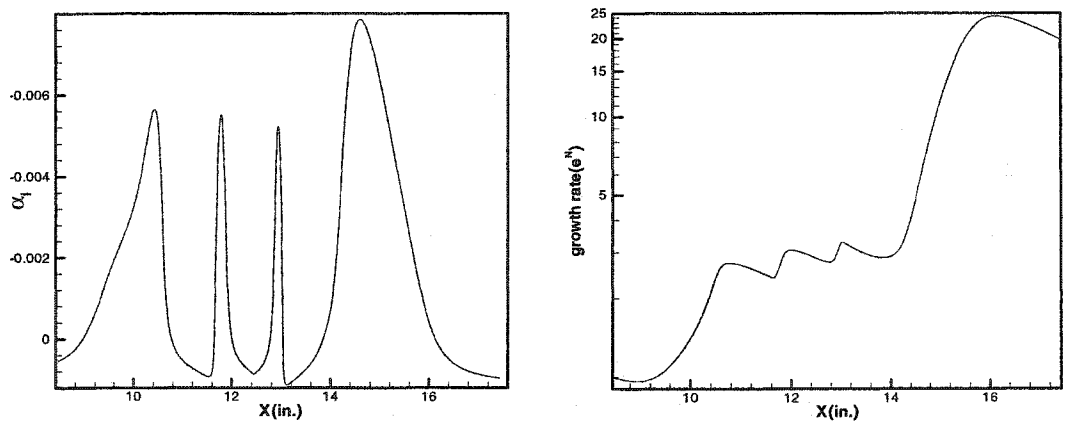

Figure 4.14 Local α_i and cumulative growth rate in the streamwise direction, F_0=0.70x10^{-4}.

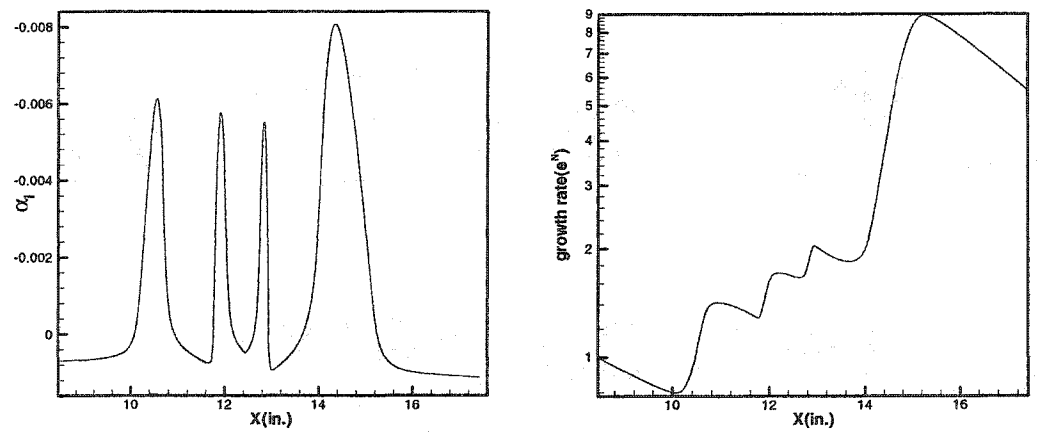

Figure 4.15 Spatial amplification rate and growth rate in the streamwise direction, F_0=0.65x10^{-4}.

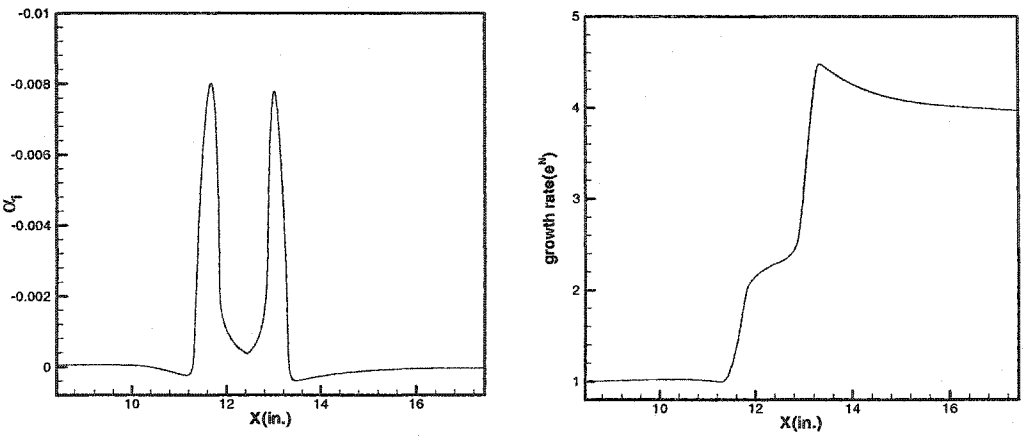

Figure 4.16 Local α_i and cumulative growth rate in the streamwise direction, $F_0=0.30\times10^{-4}$.

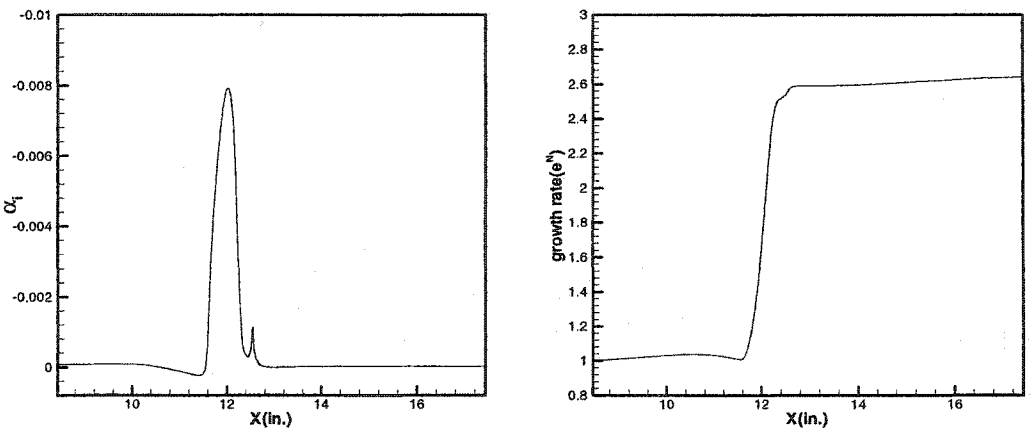

Figure 4.17 Local α_i and cumulative growth rate in the streamwise direction, $F_0=0.25\times10^{-4}$.

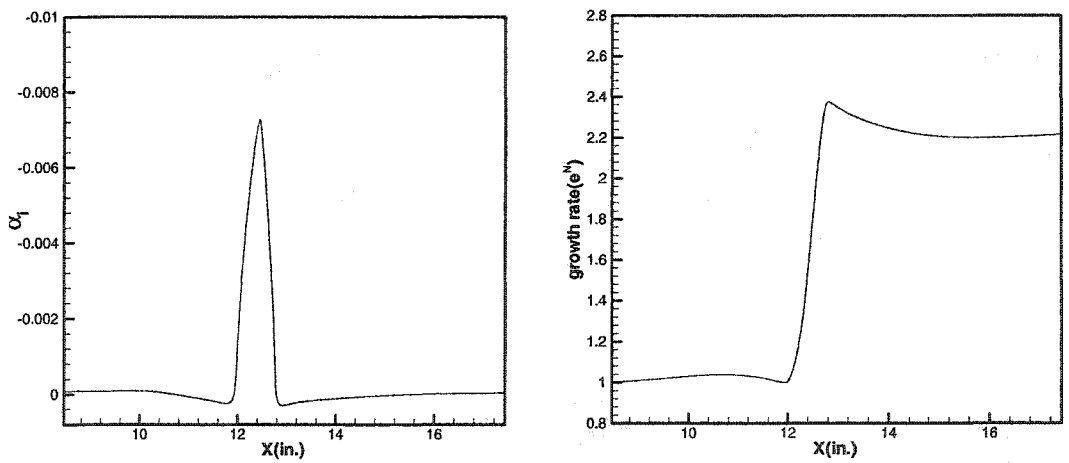

Figure 4.18 Local α_i and cumulative growth rate in the streamwise direction, $F_0=0.20\times10^{-4}$.

Figures 4.16-4.18 show the variation of the local spatial amplification rate and the cumulative growth rate in the streamwise direction for two-dimensional disturbances in the low frequency regions, with the frequencies of F_0=0.30-, 0.25-, and 0.20×10^{-4} respectively. It is observed from these figures that the low frequency two-dimensional disturbances are neutral upstream and downstream of the separation region, but in the separation region, the disturbances show very strong growth tendencies in a very narrow isolated region close to the corner. We have known that the low frequency disturbance growth in the separation region is due to the second mode instability. But because the growing region is very narrow, compared with the high frequency disturbance growth upstream and downstream of the separation region, the cumulative low frequency disturbance growth in the separation region is negligible. So it is the high frequency disturbances that will dominate the boundary-layer instability and transition across the compression corner.

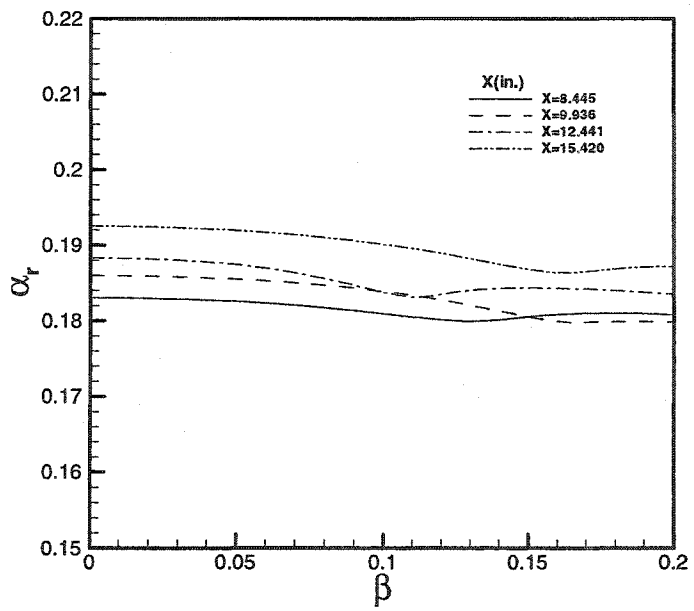

Figure 4.19 The variation of the streamwise wave number with the spanwise wave number, $F_0=0.85\times10^{-4}$.

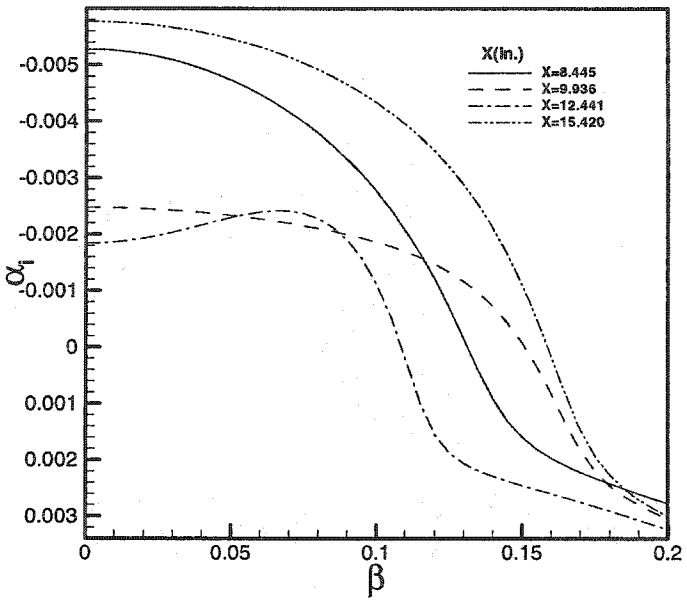

Figure 4.20 The variation of the spatial amplification rate with the spanwise wave number, $F_0=0.85\times10^{-4}$.

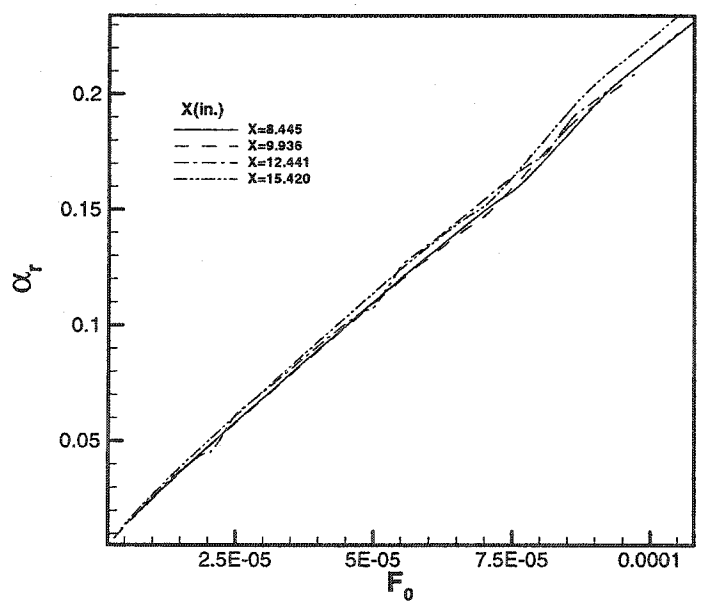

Figure 4.21 The variation of the streamwise wave number with the frequency, β=0.05.

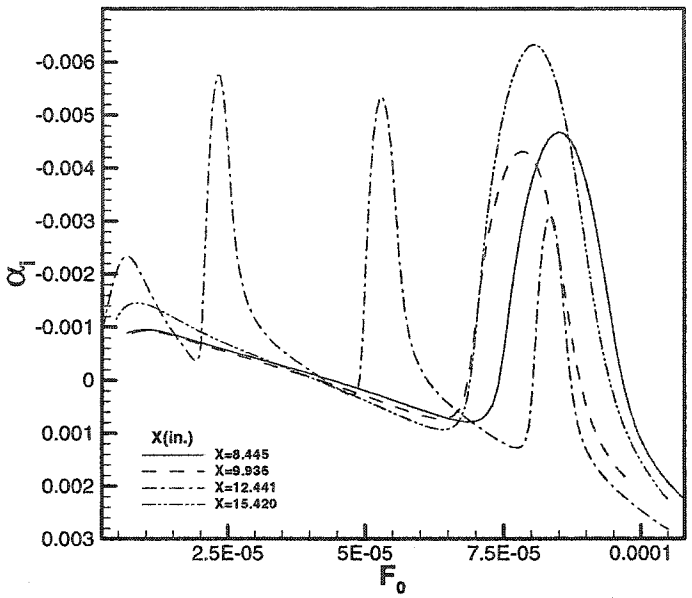

Figure 4.22 The variation of the spatial amplification rate with the frequency, β=0.05.

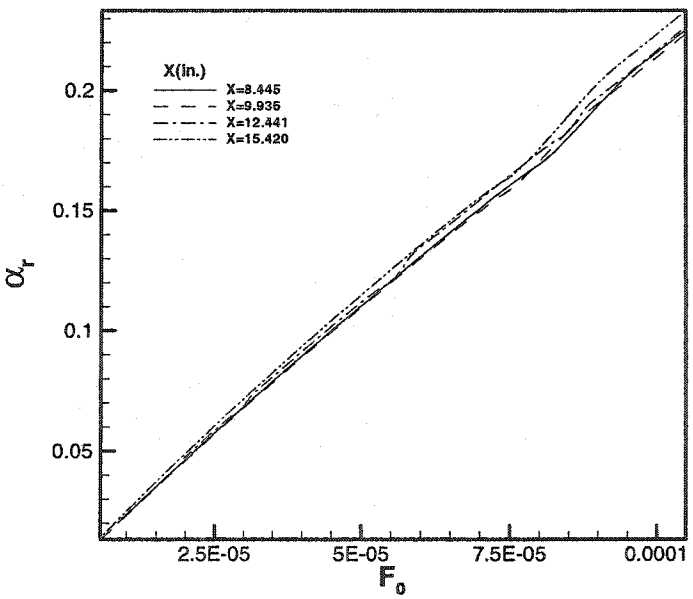

Figure 4.23 The variation of the streamwise wave number with the frequency, β=0.1.

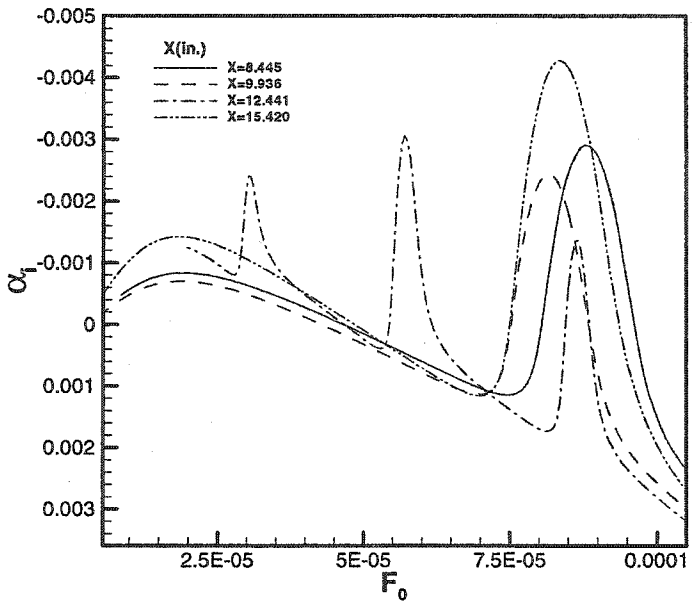

Figure 4.24 The variation of the spatial amplification rate with the frequency, β=0.1.

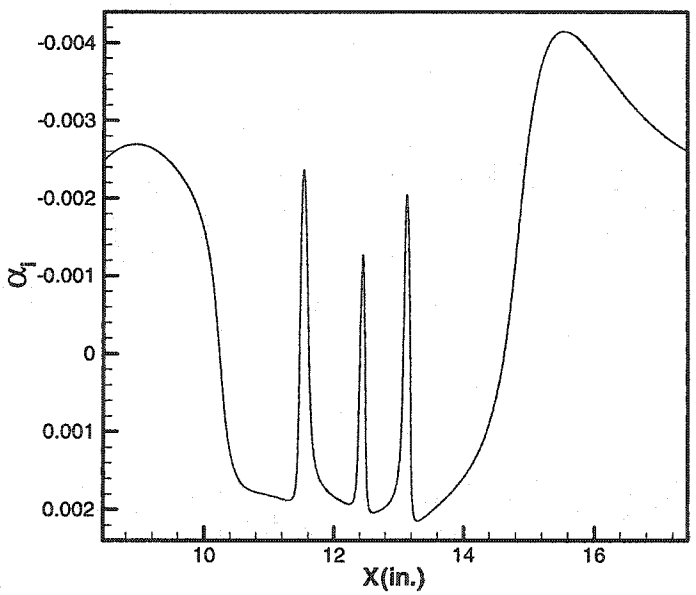

Figure 4.25 The variation of the local spatial amplification rate in streamwise direction, $F_0=0.85\times10^{-4}$, β=0.1.

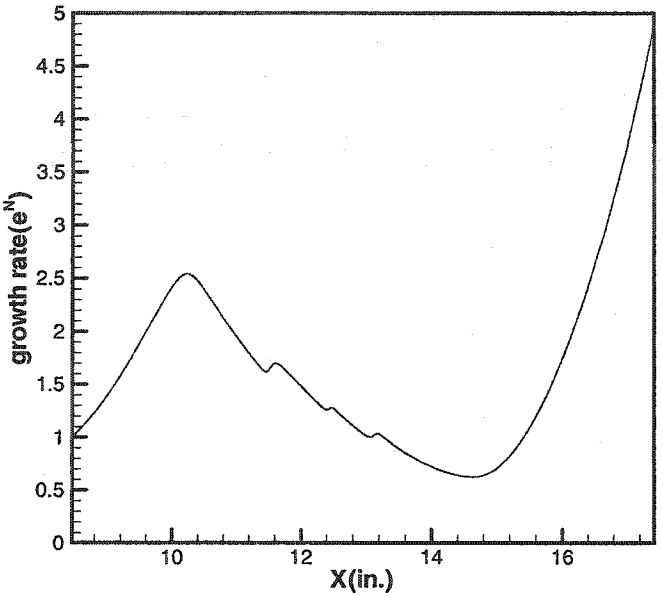

Figure 4.26 The cumulative growth rate in the streamwise direction, $F_0=0.85\times10^{-4}$, $\beta=0.1$.

4.1.2 Linear computation of the evolution of three-dimensional disturbances across the compression corner

Now we will present the linear stability computational results for three-dimensional disturbance evolution across the compression corner. Figure 4.19 and Figure 4.20 show the variation of the streamwise wave number and spatial amplification rate with the spanwise wave number for an oblique disturbance with a fixed disturbance frequency $F_0=0.85\times10^{-4}$ at different streamwise locations X=8.445, 9.936, 12.441 and 15.420 inches respectively. The spanwise wave number $\beta=0$ corresponds to a two-dimensional disturbance. It can be observed in Figure 4.19 that the streamwise wave numbers of three-dimensional disturbances are almost the same as those of the two-dimensional disturbances with the same frequency. We can also see from Figure 4.20 that the spatial amplification rate decreases with increasing spanwise wave number at the locations upstream of the separation bubble (X=8.445, 9.936 inches) and downstream of the separation bubble X=15.420 inches. At these locations, the spatial amplification rate

reaches the maximal value at $\beta = 0$ which corresponds to a two-dimensional disturbance. These results agree well with the theory given by Mack[23] that the second mode disturbance is most unstable in its two-dimensional form. But at the location X=12.441 inches in the separation region, increasing the spanwise wave number from 0, the spatial amplification rate first shows a small increase then begins to decrease. The spatial amplification rate reaches a maximal value at about $\beta = 0.075$. As we have known from the above analysis, in the separation region, the instability for two-dimensional disturbances in the high frequency region is due to the higher acoustic modes(third, fourth, ...). The second mode unstable region has shifted to the low frequency region. We will show that the same is true for three-dimensional disturbances. It is reasonable that the three-dimensional disturbance shows much larger amplification rates than two-dimensional disturbances in the separation region, at the disturbance frequency $F_0=0.85\times10^{-4}$.

Figure 4.21-4.24 show the variation of the streamwise wave number and the spatial amplification rates of three-dimensional disturbances with frequency at different streamwise locations X=8.445, 9.936, 12.441 and 15.420 inches with two different spanwise wave numbers (β=0.05 and β=0.1) respectively. Just like that of the two-dimensional disturbance, the streamwise wave number of the three-dimensional disturbance also varies with frequency in an approximately linear manner and is almost constant at the different streamwise locations at a fixed frequency. At the locations X=8.445, 9.936 inches upstream and X=15.420 inches downstream of the separation region, the three-dimensional disturbances also show two unstable modes, the first mode in the low frequency region between $F_0=0.20\sim0.4\times10^{-4}$ and the second mode in the high frequency region between $F_0=0.70\sim1.0\times10^{-4}$. But unlike the first mode of the two-dimensional disturbance, the first mode of the three-dimensional disturbance achieved quite large spatial amplification rates, comparable to those of the second mode. With increasing spanwise wave number, from 0.05 to 0.1, the spatial amplification rate of

the first mode increases and the spatial amplification rate of the second mode decreases. In the separation region, due to the increased thickness of the boundary-layer, the third or higher acoustic modes will appear, and the second mode unstable region will transfer to the low frequency region between F_0=0.20~0.4×10^{-4}. We also notice that the third acoustic mode has become the most unstable mode at β=0.1 in the separation region.

We need to understand the cumulative growth characteristics of three-dimensional disturbances at a fixed frequency. Figure 4.25 shows the variation of the local spatial amplification rate in streamwise direction for the oblique disturbances at a fixed frequency F_0=0.85×10^{-4} with spanwise wave number $\beta = 0.1$. It is observed that α_i oscillates between negative and positive values in the separation region and exhibits relatively small changes upstream and downstream of the separation region. Figure 4.26 shows the variation of the cumulative growth rate in the streamwise direction, which is obtained by equation (4.1) with the α_i given in Figure 4.25. It is observed that the three-dimensional disturbance grows monotonically in upstream and downstream of the separation region and decays slowly in the separation region. This characteristic of three-dimensional disturbances in the separation region shows some differences from that of the two-dimensional disturbances which maintain an approximately neutral status in the separation region.

4.2 Gortler instability computations

As we can see from the mean flow results shown in chapter 3, the streamlines are curved along the edge of the boundary-layer for hypersonic flow passing through the compression corner. Then the Gortler instability will occur in regions where the large streamline curvature exists. When we simulate the boundary-layer instability and transition across the compression corner, the Gortler instability must also be taken into account.

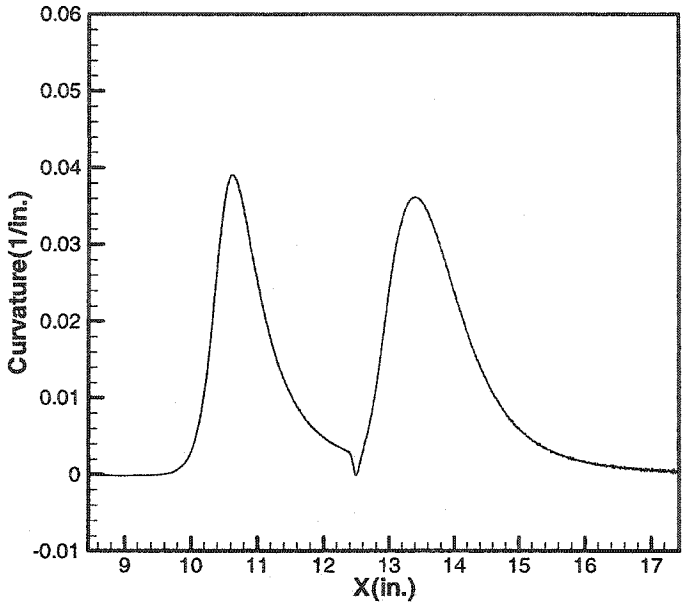

Figure 4.27 The streamline curvature at Y=0.054 inch.

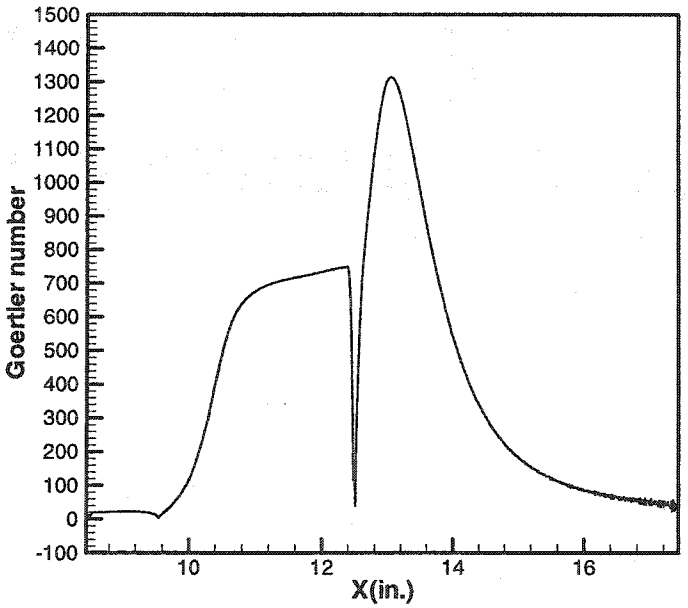

Figure 4.28 The Gortler number distribution along the streamline at Y=0.054 inch.

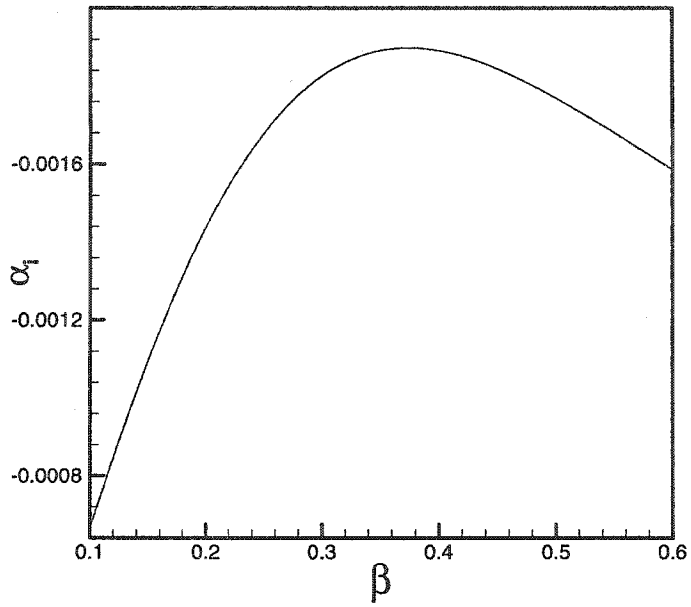

Figure 4.29 The spatial amplification rate of the Gortler vortex at X=10.284in.(κ=50.4in.).

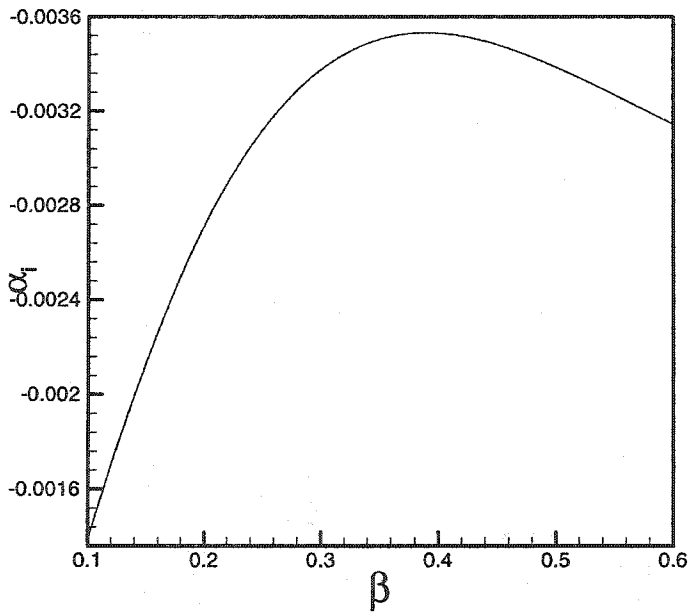

Figure 4.30 The spatial amplification rate of the Gortler vortex at X=10.753in.(κ=25in.).

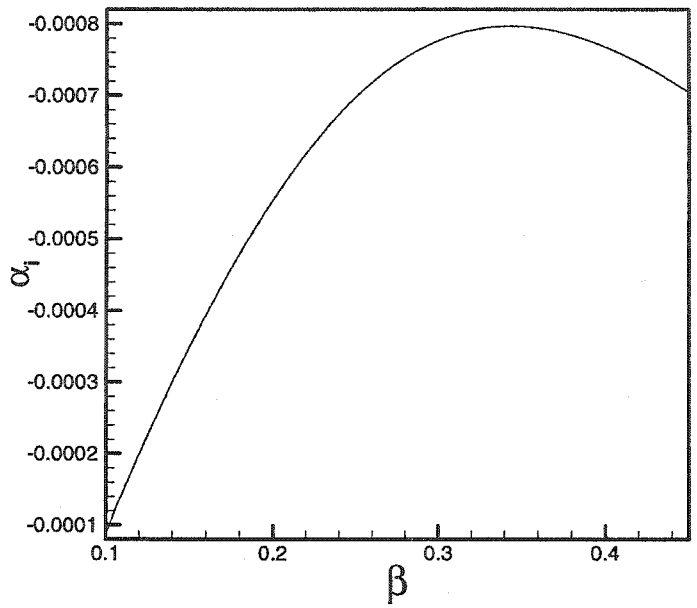

Figure 4.31 The spatial amplification rate of the Gortler vortex at X=11.27in.(κ=66in.).

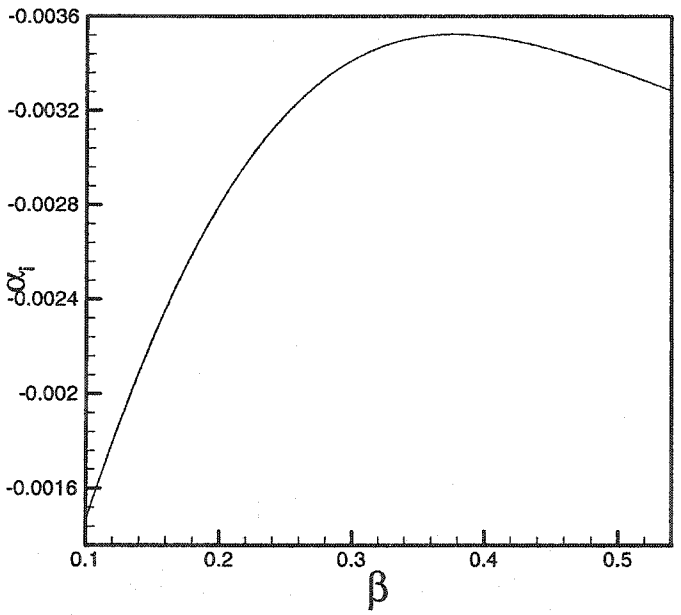

Figure 4.32 The spatial amplification rate of the Gortler vortex at X=13.595in.(κ=27.72in.).

Figure 4.27 shows the curvature distribution of streamlines at the normal location Y=0.054 inch. Figure 4.28 shows the Gortler number distribution along this streamline. The Gortler number is computed using equation $G_r = \frac{U_\infty \delta_d}{\nu}(\delta_d \kappa)^{\frac{1}{2}}$. It is shown that the Gortler number is large at locations where streamline curvatures are large, which occurred at the reattachment point. We will choose several locations with large values of streamline curvature to perform the Gortler instability computations. Figures 4.29 -4.32 show the Gortler instability computation results at four different locations, X=10.284, 10.753, 11.27 and 13.595 inches respectively. These results show the variation of the spatial amplification rate of the Gortler vortices with spanwise wave number.

Figure 4.29 shows the results at the location X=10.284 inches in front of the separation point, where the streamline curvature begins to increase and the radius of curvature is κ=50.4 inches. Because the curvature is relatively small at this location, the spatial amplification rate of Gortler vortices is small. Figure 4.30 shows the spatial amplification rate of Gortler vortices at X=10.753 inches which is close to the separation point. At this location, the streamline curvature is most severe. The radius of curvature is about κ=25 inches. So the Gortler vortices are mostly amplified at this location and show the first large amplification region around this location. Figure 4.31 shows the spatial amplification rate of Gortler vortices at X=11.27 inches which is located in the middle of the separation region. As shown in chapter 3, the boundary-layer edge is almost flat above the separation bubble, so the curvature of the streamlines at these points is very small and the curvature radius is about κ= 66 inches. As a result, the Gortler vortices show only very small amplification at this location. Figure 4.32 shows the spatial amplification rate of Gortler vortices at X=13.595 inches which is close to the reattachment point. At this location, the streamline curvature is the second largest, so the spatial amplification rate of the Gortler vortices becomes big again. The Gortler vortices will show another high amplification region around this location. After this location, the streamline begins to become straight. The Gortler vortices will not be amplified any

further, traveling downstream. In addition, another important observation is that at all these streamwise locations the Gortler vortices show most significant spatial amplification rates at spanwise wave numbers between β=0.3 and 0.4. When we perform the DNS to simulate the boundary-layer instability across the compression corner, the Gortler instability with spanwise wave numbers given in this region should be considered.

4.3 Summary

In this chapter, we performed linear computations for two- and three-dimensional second mode disturbances as well as Gortler vortex evolutions across the compression corner. Two linearized theories have been used for computation: linear stability theory and Gortler instability theory. By LST computations we found that both two- and three-dimensional disturbances are mostly amplified across the compression corner at frequencies close to $F_0=0.80\times10^{-4}$. The two-dimensional high frequency disturbances keep an approximately neutral status in the separation bubble region and the three-dimensional high frequency disturbances decay in this region. The low frequency disturbances show the second mode instability characteristics in the separation region and grow rapidly in a narrow band in this region. The three-dimensional second mode disturbances are less amplified than their two-dimensional counterparts upstream and downstream of the separation region. The Gortler vortex will be mostly amplified at two locations: one is close to the separation point and the other is close to the reattachment point. The Gortler vortex will have a large spatial amplification rate at spanwise wave numbers between β=0.3 and 0.4. All these linear computations provide an approximate picture of the linear two- or three-disturbance evolutions across the compression corner, which will be verified by direct numerical simulations in the next a few chapters. On the other hand, these linear computation results also provide some important information on the selections of the disturbance frequencies and spanwise wave numbers for DNS.

CHAPTER V

DIRECT NUMERICAL SIMULATION OF TWO-DIMENSIONAL DISTURBANCE EVOLUTIONS

Direct numerical simulations of two-dimensional disturbance evolution across the compression corner will be performed in this chapter. Both linear and nonlinear two-dimensional disturbance evolutions will be simulated. We will study the influences of disturbance frequency and initial disturbance amplitude on disturbance evolution. The behavior of different modes during nonlinear interaction will be studied by nonlinear simulation. In this chapter, we will first present computation results for parallel and non-parallel flow along a flat plate and compare these results with those of LST and PSE methods to validate the code for two-dimensional unsteady computation. Next we will show the results for the linear and nonlinear evolution of two-dimensional disturbances across a compression corner. The computational grid for two-dimensional unsteady computation across the compression corner is the same as that employed for of two-dimensional mean flow computations, which was shown in Figure 3.3.

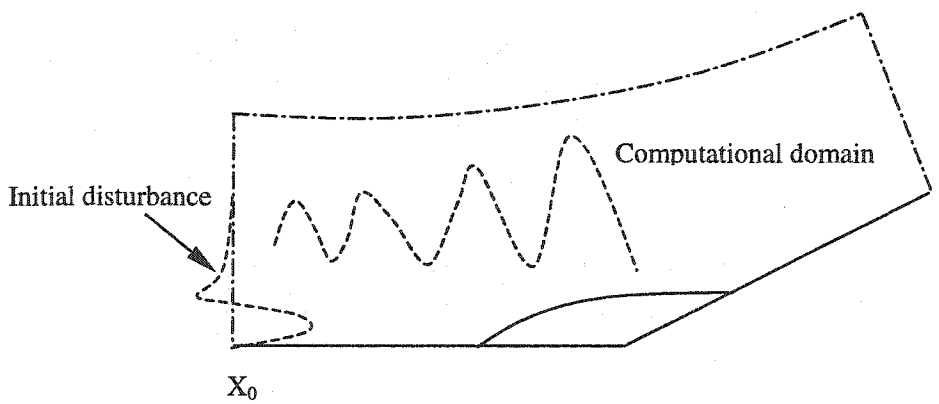

Figure 5.1 Introduction of two-dimensional initial disturbances.

5.1 Introduction of the initial disturbances

The two-dimensional initial disturbances were obtained using two-dimensional PSE computations. They are superposed on the mean flow profile at the beginning of the computational domain, in the streamwise direction according to the following equation.

$$\mathbf{q}(x_0, y, t) = \mathbf{Q}_0(x_0, y) + \varepsilon \,\mathrm{Re}\,al(\hat{\mathbf{q}}(y)e^{-i\omega t}) \tag{5.1}$$

$$\mathbf{q} = [\rho, e_t, u, v]^T;\ \ \mathrm{Q}_0 = [\rho_0, Et_0, U_0, V_0]^T;\ \ \hat{\mathbf{q}} = [\hat{\rho}, \hat{e}_t, \hat{u}, \hat{v}]^T \tag{5.2}$$

where ω is the disturbance frequency, ε is the initial disturbance amplitude, $\hat{\mathbf{q}}$ is the eigenfunction which is obtained by the PSE method and is normalized with the maximum amplitude of the density disturbance so that the maximum amplitude of the density disturbance is unity. $\mathbf{Q_0}$ are the steady mean flow profiles at the initial streamwise location, and x_0 is the streamwise coordinate at the beginning of the computational domain. Figure 5.1 illustrates how the initial disturbances are superimposed on the mean flow.

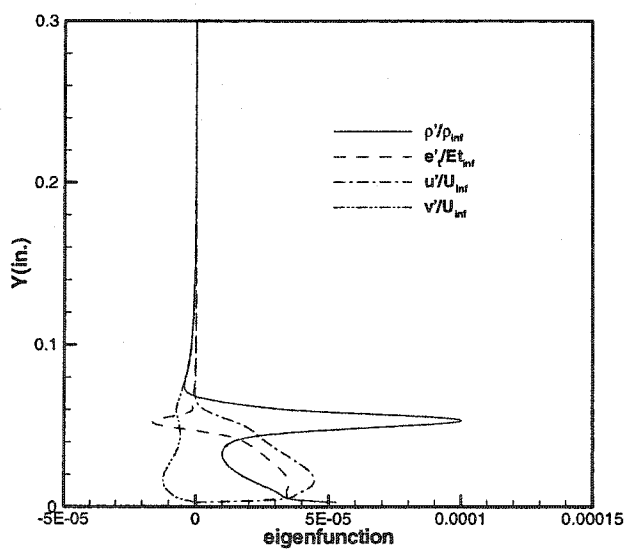

Figure 5.2 The eigenfunctions of the initial disturbance.

Figure 5.2 shows the eigenfunctions of the initial disturbances of density, total energy, streamwise velocity, and normal velocity respectively at the frequency $F_0=0.85\times10^{-4}$ and initial disturbance amplitude $\varepsilon=0.0001$. All these disturbances are normalized by their

corresponding upstream mean flow quantities in upstream infinity. It can be seen that all disturbances concentrate within the boundary-layer. The density disturbance shows the largest relative amplitude among all the disturbance quantities. The density disturbance will dominate the instability and transition of the boundary-layer. In the present study, all numerical analysis of instability and transition will be based on the density disturbance.

5.2 The two-dimensional disturbance evolution across a flat plate

Before we perform the DNS for the evolution of two-dimensional disturbances across the compression corner, we first perform some computations for two-dimensional disturbance evolution across a flat plate using the same code. Both parallel and nonparallel flow computations will be performed. Then the parallel results will be compared with those obtained by linear stability theory computations, and the nonparallel results will be compared with those obtained by PSE computations. The validation of the code for two-dimensional unsteady computation can be checked by these comparisons.

5.2.1 Parallel flow computations

Figures 5.3 and 5.4 show the parallel flow computation results for hypersonic flow over a flat plate with the same incoming flow parameters as those of the compression corner. The dimensionless disturbance frequency is $F_0=0.85\times10^{-4}$. The initial disturbance amplitude is $\varepsilon=0.0001$. Figure 5.3 shows the density disturbance contour and Figure 5.4 shows the streamwise velocity disturbance contours. It can be observed clearly from these contours that the disturbances are constrained in the boundary-layer and maximum disturbances appear in the critical layer. The normal locations of the maximal disturbance in the boundary-layer are constant in the streamwise direction due to the parallel flow assumption.

Figure 5.5 shows the density disturbance evolution in the streamwise direction at the location y=0.0526 inch. The density disturbance amplitude is maximal at this normal location. This figure also shows the comparison between the results in parallel flow and the results for LST computation. It can be seen that the amplitude of the density

disturbance grows exponentially downstream. The results of the parallel flow computation agree very well with the results from the LST computation until about X=10.5 inches. A small difference between these two results begins to appear beyond this location and this difference becomes larger and larger moving downstream. This occurs when the disturbance amplitude becomes large enough relative to the corresponding mean flow quantity, nonlinear influences begin to take effect in parallel flow computation. But the LST computation cannot take into account the nonlinear effects, so the difference between these two results will become large with increasing disturbance amplitude. In addition, the outflow boundary conditions used in DNS may also be responsible for this difference. Figure 5.6 shows a comparison of streamwise velocity disturbance evolutions at y=0.0526 between LST and parallel flow computations. Figure 5.7 shows a comparison of the density disturbance evolution at the wall. From all these comparisons, it can be observed that the parallel flow computation results agree very well with the LST computation results in the linear disturbance evolution region.

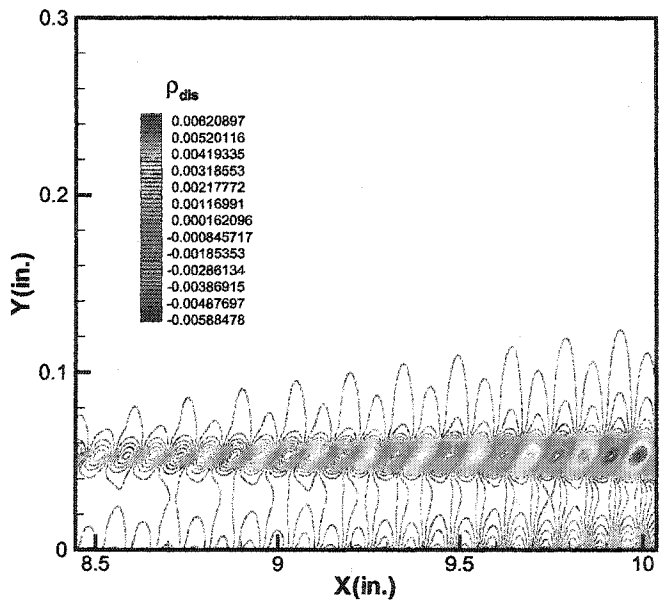

Figure 5.3 Density disturbance contours, $F_0=0.85\times10^{-4}$, $\varepsilon=0.0001$.

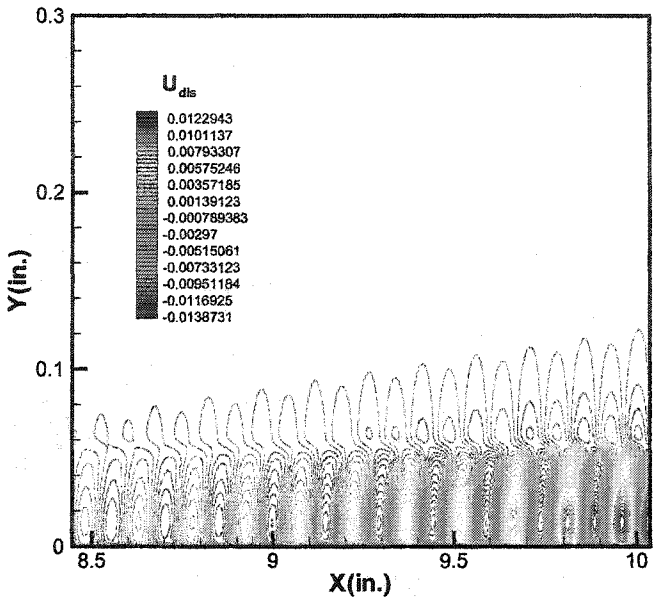

Figure 5.4 Streamwise velocity disturbance contours, $F_0=0.85\times10^{-4}$, $\varepsilon=0.0001$.

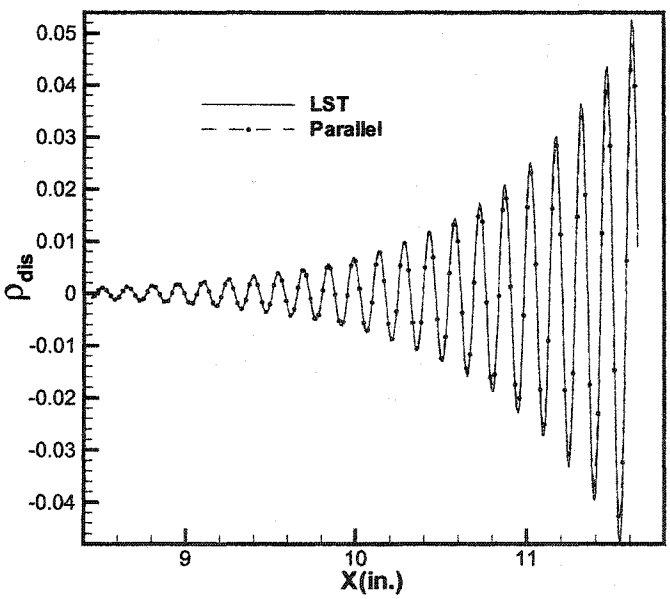

Figure 5.5 Comparison of LST and parallel disturbance density results at y=0.0526 inch.

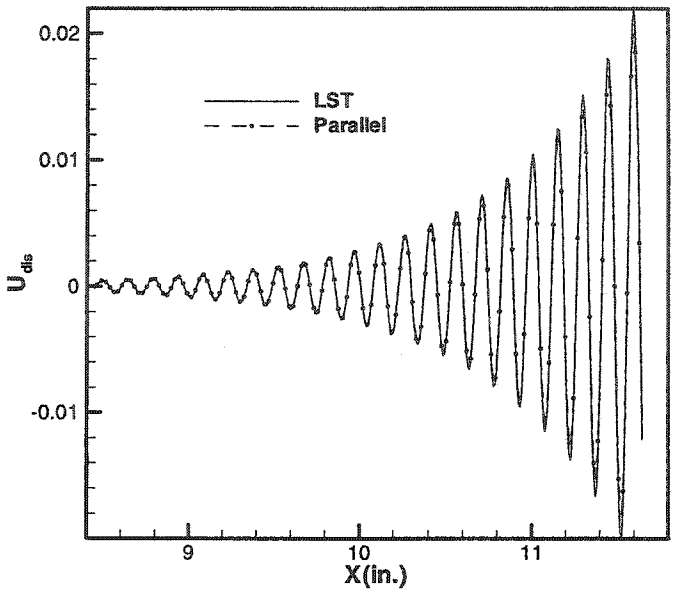

Figure 5.6 Comparison of LST and parallel disturbance velocity results at y=0.0526 inch.

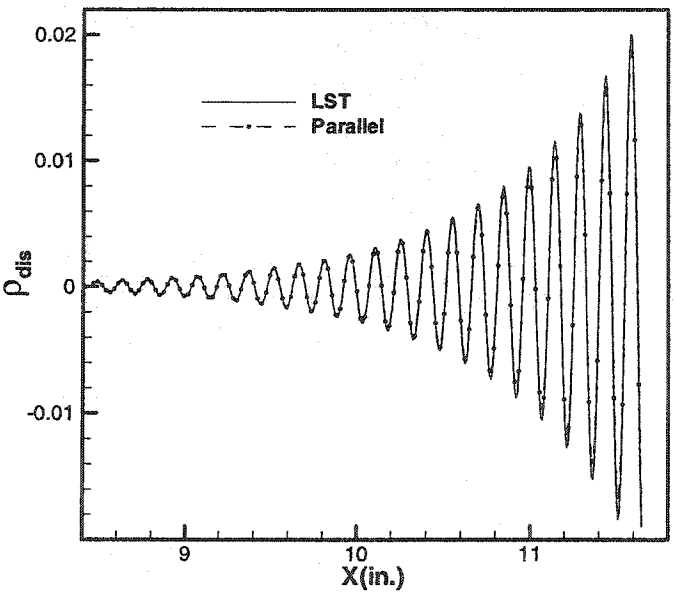

Figure 5.7 Comparison of LST and parallel disturbance density results at the wall.

Next we will make some comparisons for the eigenfunctions of the disturbances at different streamwise locations between LST and parallel flow computations. Figure 5.8(a)

and Figure 5.8(b) show the eigenfunction comparisons for the density disturbance and streamwise velocity disturbance at X=8.837 inches. At this location, nonlinear effects are very small, so the eigenfunctions obtained by these two methods agree with each other very well. Figure 5.9(a) and Figure 5.9(b) show comparisons of the eigenfunctions at X=10.873 inches. At this location, the differences between the eigenfunctions obtained by LST and those obtained by parallel flow computation become large due to nonlinear effects and outflow boundary conditions used in DNS.

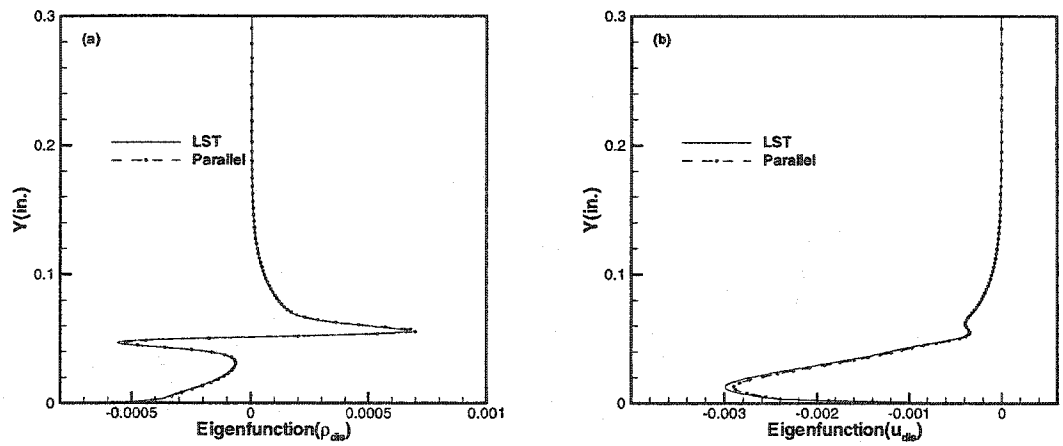

Figure 5.8 Comparisons of eigenfunctions at x=8.837 inches.

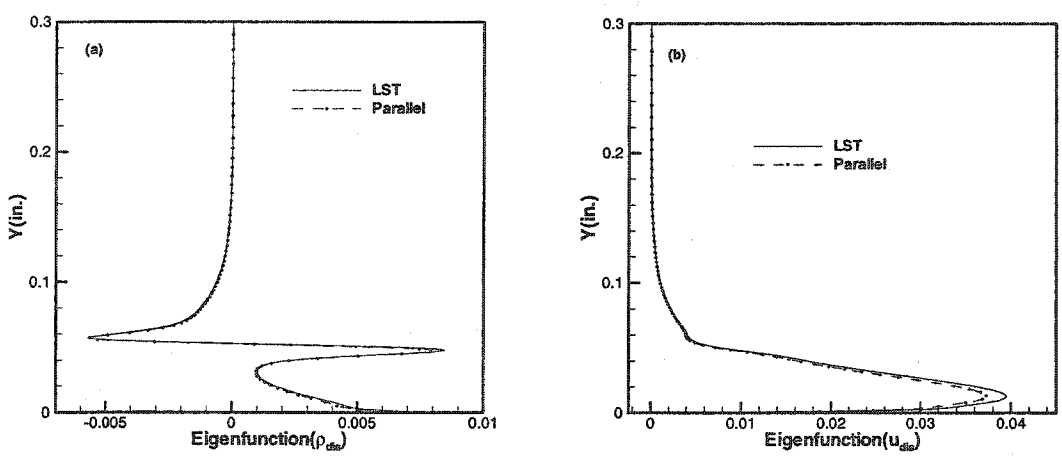

Figure 5.9 Comparisons of eigenfunctions at X=10.837 inches.

5.2.2 Non-parallel flow computations

Due to boundary-layer thickness increases in the streamwise direction, non-parallel effects should be taken into account when we perform the numerical simulations for disturbance evolution along a flat plate. Figure 5.10(a) and Figure 5.10(b) show the non-parallel flow computation results and the comparisons of the results obtained by non-parallel flow computation and PSE computation. Figure 5.10(a) shows the comparison of the maximal density disturbance and Figure 5.10(b) shows the comparison of the maximal streamwise velocity disturbance. It is observed that the results obtained by these two methods agree with each other quite well. Only small differences exist at the end of the streamwise domain. This is due to the nonlinear influence which was neglected in the linear PSE computation and the outflow boundary conditions used in DNS. We also noticed that for non-parallel growth, the spatial amplification rate is no longer constant in the streamwise direction. The disturbances only grow in the second mode unstable region, shown in Figures 4.1 and 4.2, and the growth rate will also be different for different disturbance quantities.

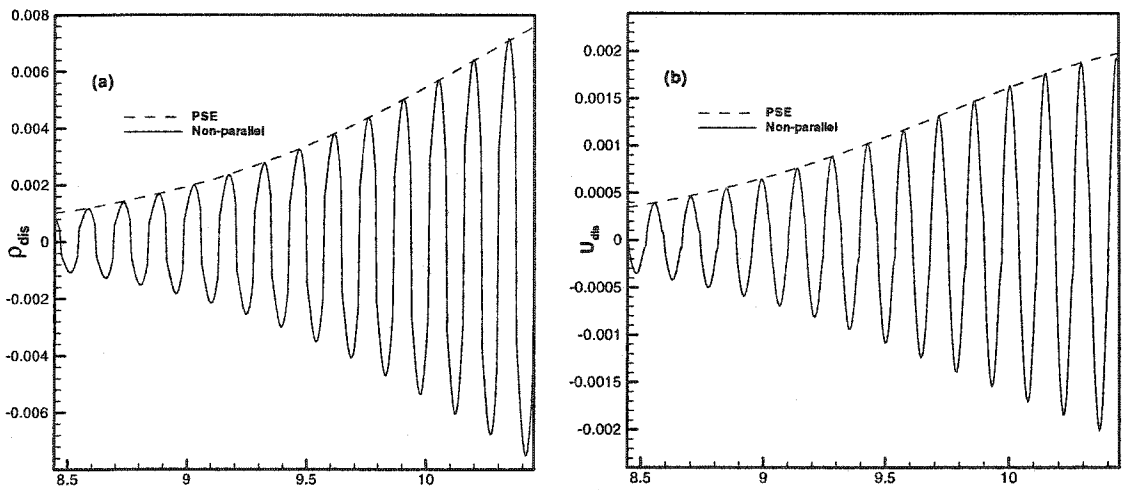

Figure 5.10 Comparisons of the results for non-parallel and PSE disturbance computations.

5.3 The two-dimensional disturbance evolutions across the compression corner

In this section, we will present the DNS results for two-dimensional disturbance

evolution across the compression corner. The simulations are performed with different disturbance frequencies and different initial disturbance amplitudes. According to the linear stability computation results in chapter 4, we know that upstream and downstream of the separation region, the second mode unstable region is in high frequency region between F_0=0.70- and 1.0×10^{-4} and the first mode unstable region is in the low frequency region between F_0=0.20- and 0.40×10^{-4}. But in the separation region, the second mode unstable region transfers to the low frequency region between F_0=0.20- and 0.40×10^{-4}. So in the present computations, we will first run several cases with disturbance frequency values chosen within the high frequency region. Then we will run several other cases with disturbance frequency values chosen from the low frequency region. By these computations, the evolution characteristics of the disturbance with different frequencies in different flow regions will be fully disclosed. Both linear and nonlinear evolution of the disturbances across the compression corner will be simulated.

5.3.1 The linear evolutions of the disturbances

To simulate the linear evolution of the disturbance across the compression corner, the initial disturbance amplitude is required to be small enough to make sure that the primary disturbance amplitude remains below about 5 percent of its corresponding mean flow value in all flow regions. Figure 5.11a shows the density disturbance contour across the compression corner with dimensionless disturbance frequency $F_0=0.85\times10^{-4}$, and initial disturbance amplitude ε=0.0001. With this small initial disturbance amplitude, the linear disturbance evolution across all regions of the compression corner can be guaranteed. Figure 5.11b is an expanded view of the density disturbance contour upstream of the separation bubble. Figure 5.11c is an expanded view of the density disturbance contour in the separation bubble region. Figure 5.11d shows the expanded view of the density disturbance contour downstream of the separation bubble. It can be seen from these contours that the disturbances concentrate in the boundary-layer and propagate downstream along the outer edge of the boundary-layer, and the negative and positive

disturbance zones appear alternatively in the streamwise direction. In the upstream region of the separation bubble, the disturbance evolution is similar to the non-parallel flow result which had been discussed previously. The disturbance evolution in this region conforms to nonparallel theory and can be dealt with by the PSE method. In the separation bubble region, the maximal disturbances reside above the separation bubble and never penetrate into the separation bubble. The disturbances in the separation bubble are very small. Due to the streamline curvature in this region, some outgoing weak compression waves have been produced along the outer edge of the boundary-layer. Downstream of the separation bubble region, due to the reattachment of the boundary-layer and the negligible influence of the shock on the boundary-layer, the boundary-layer in this region can be regarded as the flat plate boundary-layer, so the disturbance evolutions will again approximately conform to the nonparallel theory. Figure 5.12 shows the pressure disturbance contours across the compression corner at disturbance frequency $F_0=0.85\times10^{-4}$ and initial disturbance amplitude $\varepsilon=0.0001$. It is observed that pressure disturbance reaches the maximum at the wall surface.

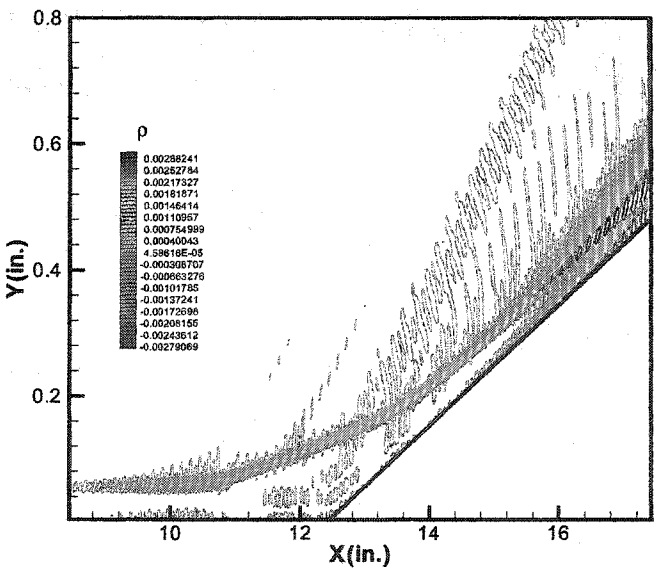

Figure 5.11a Density disturbance contours, $F_0=0.85\times10^{-4}$, $\varepsilon=0.0001$.

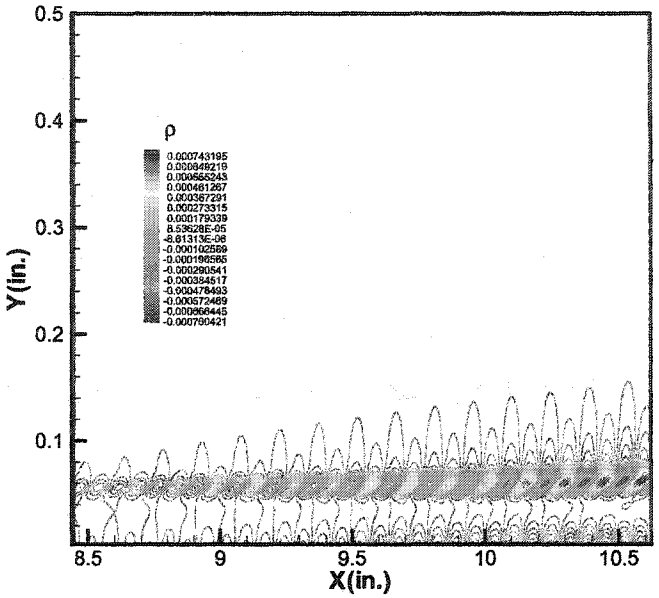

Figure 5.11b Density disturbance contours upstream of the separation region, $F_0=0.85\times10^{-4}$, $\varepsilon=0.0001$.

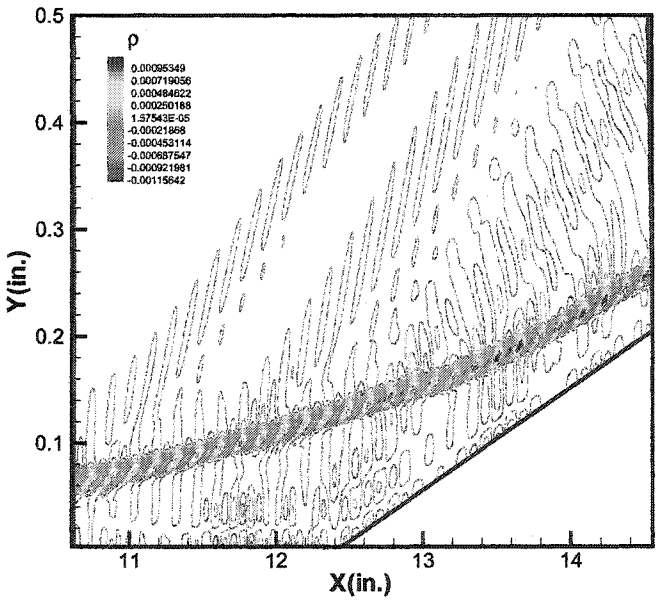

Figure 5.11c Density disturbance contours in the separation region, $F_0=0.85\times10^{-4}$, $\varepsilon=0.0001$.

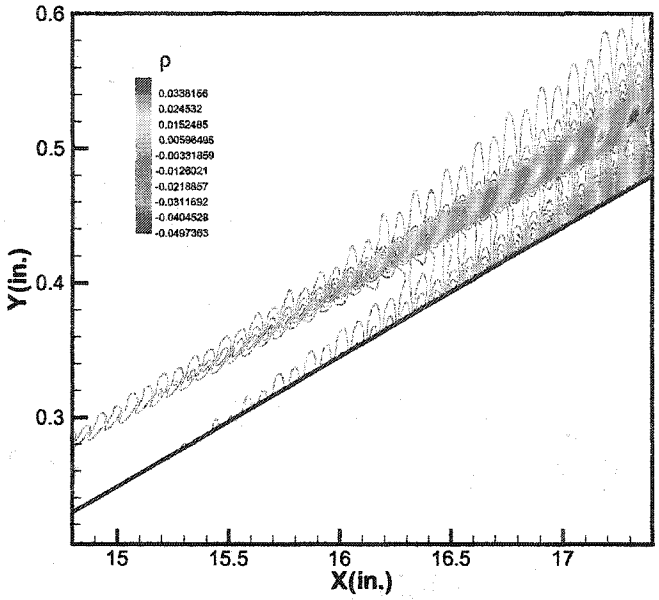

Figure 5.11d Density disturbance contours downstream of the separation region, $F_0=0.85\times10^{-4}$, $\varepsilon=0.0001$.

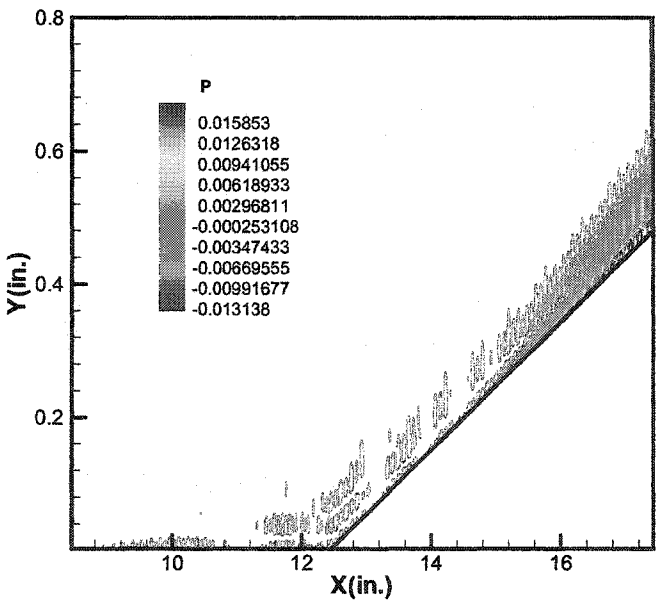

Figure 5.12 Pressure disturbance contours, $F_0=0.85\times10^{-4}$, $\varepsilon=0.0001$.

Figures 5.13-5.18 show the normal maximal density disturbance distributions and the density disturbance distributions at the wall, along the streamwise direction, with different disturbance frequencies F_0=0.85-, 0.80- and 0.75×10^{-4} respectively at a given time step after the disturbances reach a steady periodic status. It is observed from these figures that the normal maximal disturbances oscillate between positive and negative values in the streamwise direction. The maximal disturbance amplitudes show a slow increase upstream of the separation bubble, remaining approximately neutral in the separation region. But downstream of the separation bubble, the maximal disturbance amplitudes begin to show very rapid and continuous growth with the disturbances evolving downstream. At the wall, the disturbance amplitudes are very small in upstream of the separation region and are almost zero inside the separation region. But downstream of the separation region, the disturbance amplitudes at the wall begin to grow sharply and reach a quite large value at the end of the computation domain.

Figures 5.19-5.22 show the normal maximal density disturbance distribution and the density disturbance distribution at the wall in the streamwise direction with the frequencies F_0=0.70- and 0.65×10^{-4} respectively. We know from Figure 4.2 that these two frequency values are located between the first and the second unstable mode region at the initial streamwise location. The disturbances with these two frequencies will decay first from the initial streamwise location, but with increases in Reynolds number downstream, they can again pass through the second mode unstable region and begin to grow again at some specific location. This can be seen from the maximal disturbance amplitude distributions shown in Figure 5.19 and Figure 5.21. Inside the separation region, these two disturbances show very a weak growth tendency. Downstream of the separation region, unlike the higher frequency disturbances, the disturbances with these two frequencies do not continuously grow. Some isolated stable regions have appeared.

Other computations with much lower disturbance frequencies were also performed. Figures 5.23-5.28 show the normal maximal density disturbance distributions and the

density disturbance distributions at the wall in the streamwise direction with the frequencies F_0=0.30-, 0.25- and 0.20×10^{-4} respectively. From the normal maximal disturbance amplitude distributions shown in Figures 5.23, 5.25 and 5.27, we see that disturbances with low frequencies grow in the separation region, but they exhibit neutral growth both upstream and downstream from the separation regions. As we know from chapter 4, in the separation region, the low frequency disturbances show the second mode unstable characteristics, so they will grow in this region. But the growth of the lower frequency disturbances in the separation region is limited to a very short distance in the streamwise direction, and they do not grow much. The low frequency disturbance growth has little influence on the boundary-layer transition in this region.

Figure 5.29 shows the envelope lines of the normal maximal density disturbance wave packet with frequencies F_0=0.85-, 0.80-, 0.75-, 0.70-, and 0.65×10^{-4}. The figures are plotted using a Log scale in the y coordinate so that we can see the disturbance evolution in all three flow regions more clearly. As just discussed, the disturbances with frequencies F_0=0.85-, 0.80- and 0.75×10^{-4} grow monotonously upstream and downstream of the separation region and are neutral in the separation region, but for disturbances with frequencies F_0=0.70- and 0.65×10^{-4}, some isolated stable regions have appeared upstream and downstream of the separation region, so these disturbances show much slower growth tendencies in these two regions compared with the higher frequency disturbances. Comparing the maximal disturbance amplitude distributions for all these frequencies, we observe that the disturbance with the frequency $F_0=0.80\times10^{-4}$ is mostly amplified downstream of the separation region. This result agrees well with the linear stability theory computation result given in chapter 4. At this frequency, the disturbance is amplified approximately 800 times when it reaches the end of the streamwise domain, which corresponds to an N factor of 7. The growth of the disturbance at this frequency is believed to be important to boundary-layer transition across the compression corner. We will pay more attention to the disturbances close to this frequency in our following

computations, including the two-dimensional nonlinear and three-dimensional simulations.

Figure 5.30 show the amplitude envelope lines of the normal maximal density fluctuations with the low frequencies F_0=0.30-, 0.25-, and 0.20×10^{-4} respectively. The plots show that the disturbances are almost neutral upstream and downstream of the separation region and grow exponentially only in the separation region. The total amplification upstream of the separation region to the downstream of the separation region is about 20 times for the most amplified frequency $F_0=0.25\times10^{-4}$. Compared with the amplification of the high frequency disturbance across the compression corner, the amplification of the low frequency disturbance is very small. The low frequency disturbances play a negligible role in hypersonic boundary-layer transition across the compression corner.

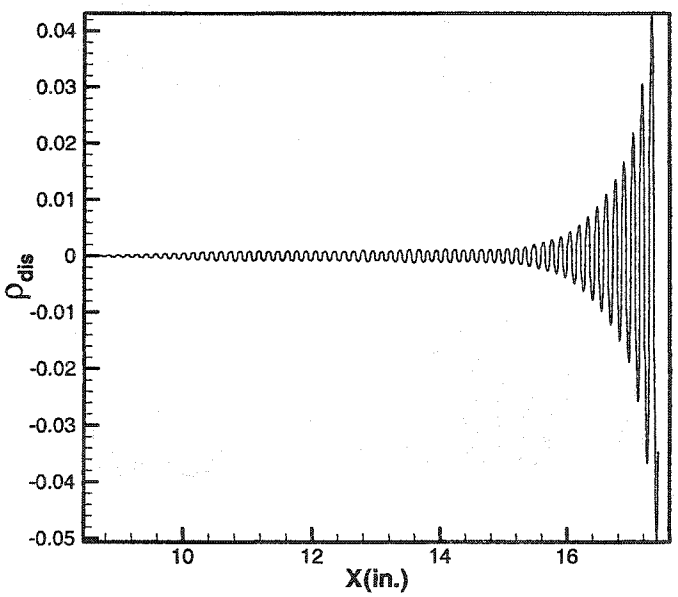

Figure 5.13 The maximal density disturbance distribution in the streamwise direction, $F_0=0.85\times10^{-4}$, ε=0.0001.

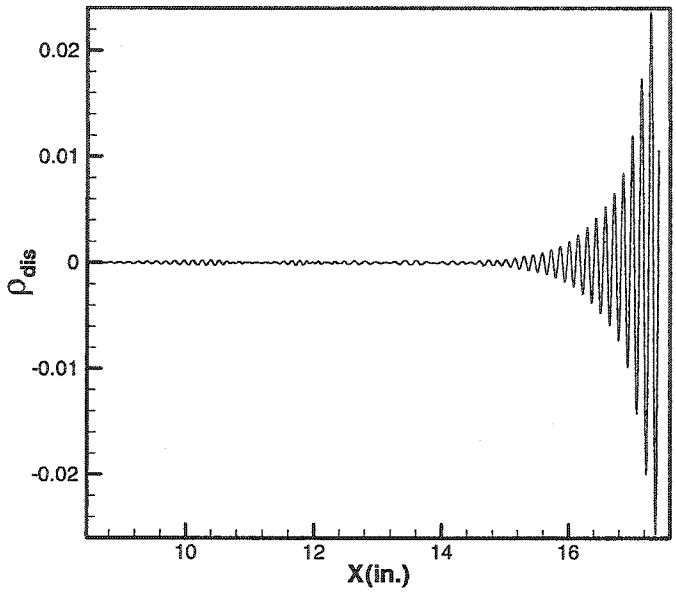

Figure 5.14 Density disturbance distribution at the wall, $F_0=0.85\times10^{-4}$, $\varepsilon=0.0001$.

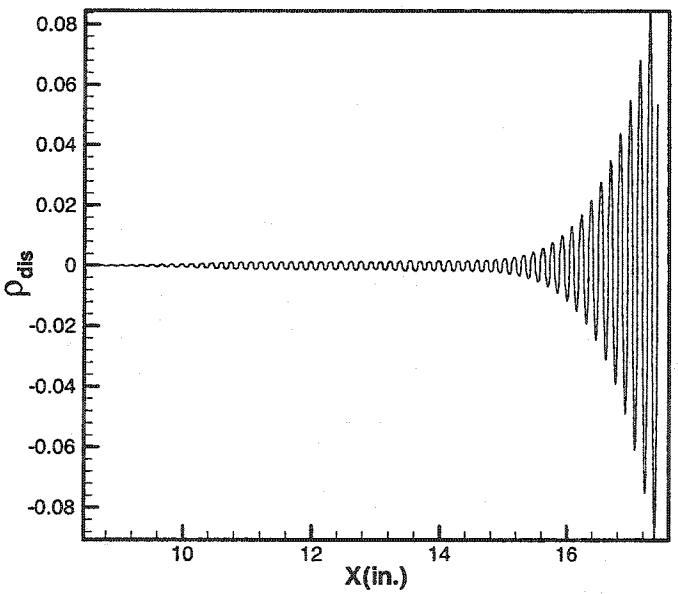

Figure 5.15 The maximal density disturbance distribution in the streamwise direction, $F_0=0.80\times10^{-4}$, $\varepsilon=0.0001$.

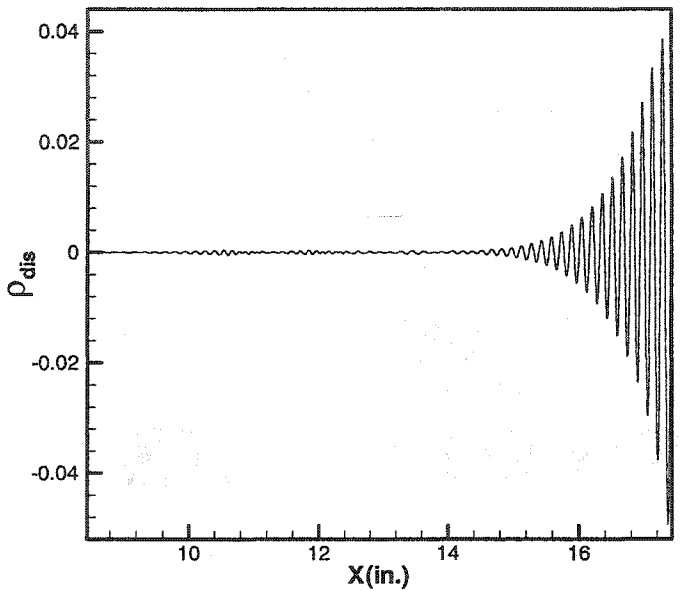

Figure 5.16 Density disturbance distribution at the wall, $F_0=0.80\times10^{-4}$, $\varepsilon=0.0001$.

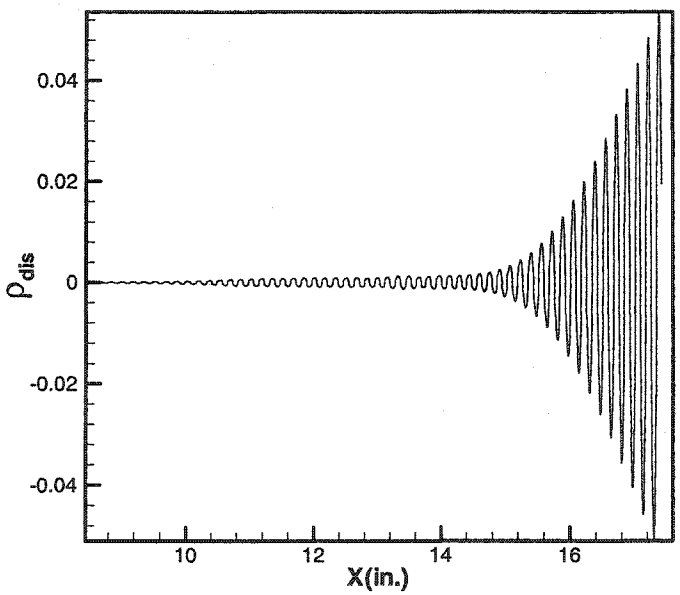

Figure 5.17 The maximal density disturbance distribution in the streamwise direction, $F_0=0.75\times10^{-4}$, $\varepsilon=0.0001$.

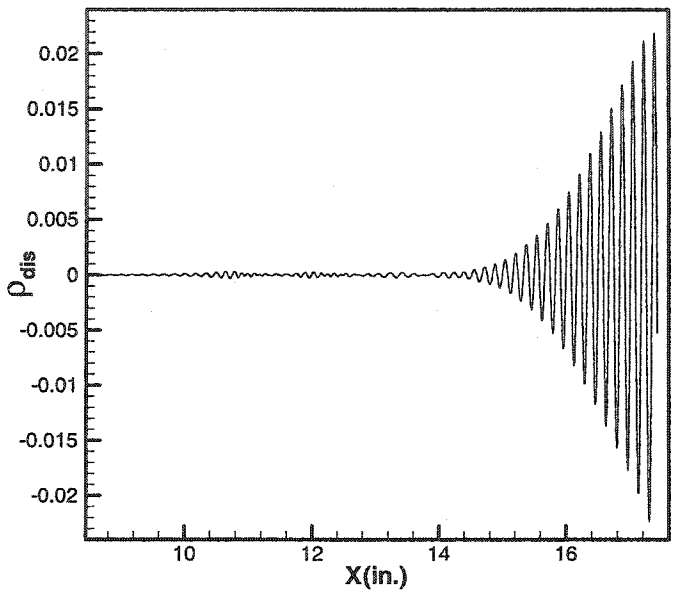

Figure 5.18 Density disturbance distribution at the wall, $F_0=0.75\times10^{-4}$, $\varepsilon=0.0001$.

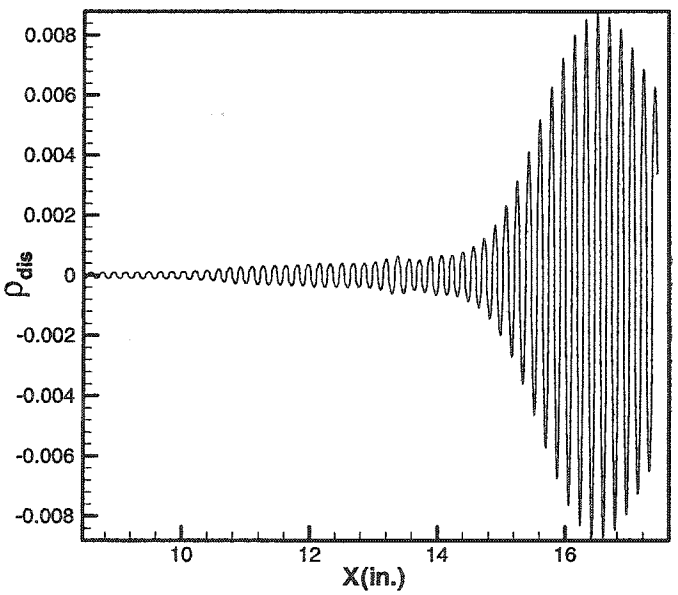

Figure 5.19 The maximal density disturbance distribution in the streamwise direction, $F_0=0.70\times10^{-4}$, $\varepsilon=0.0001$.

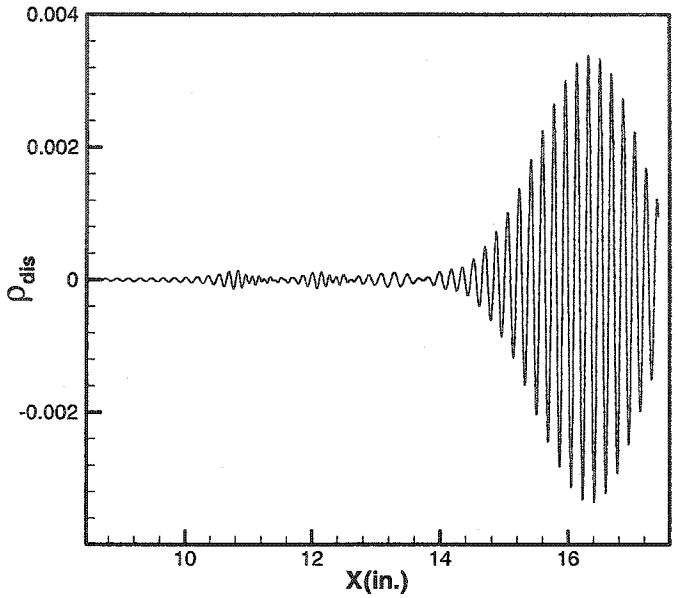

Figure 5.20 Density disturbance distribution at the wall, $F_0=0.70\times10^{-4}$, $\varepsilon=0.0001$.

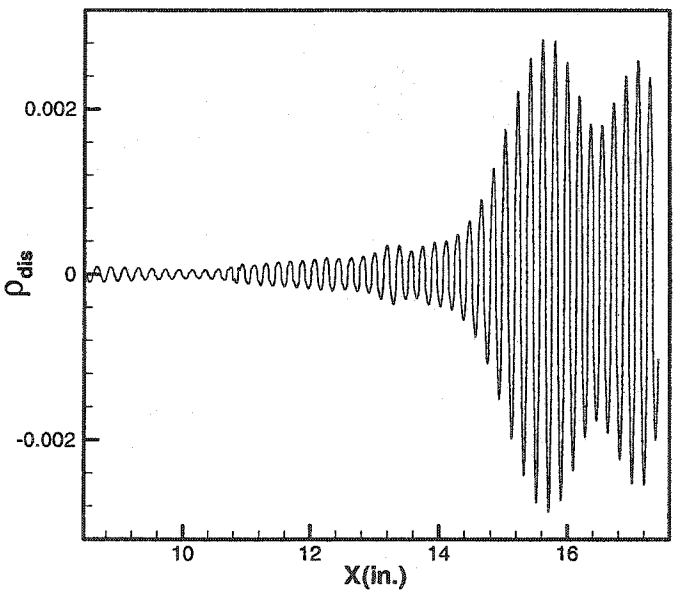

Figure 5.21 The maximal density disturbance distribution in the streamwise direction, $F_0=0.65\times10^{-4}$, $\varepsilon=0.0001$.

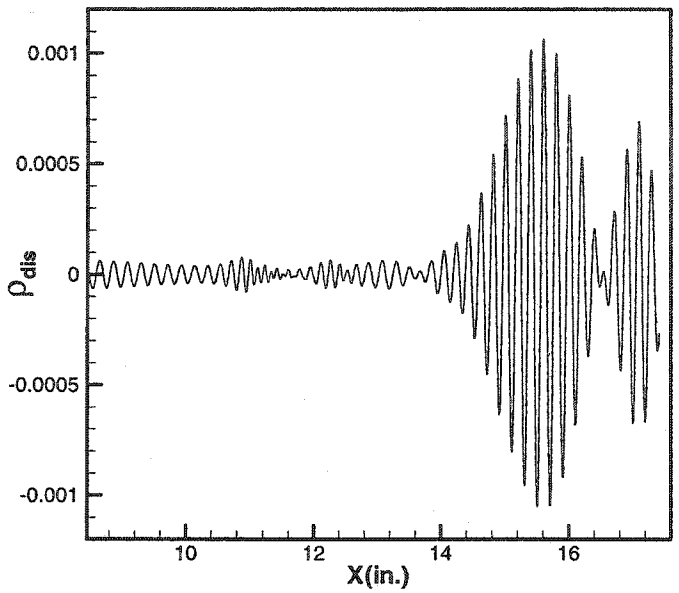

Figure 5.22 Density disturbance distribution at the wall, $F_0=0.65\times10^{-4}$, $\varepsilon=0.0001$.

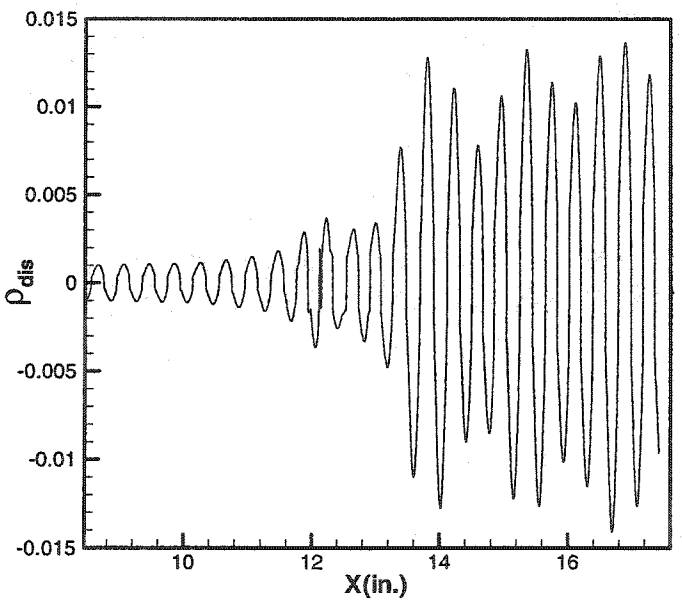

Figure 5.23 The maximal density disturbance distribution in the streamwise direction, $F_0=0.30\times10^{-4}$, $\varepsilon=0.001$.

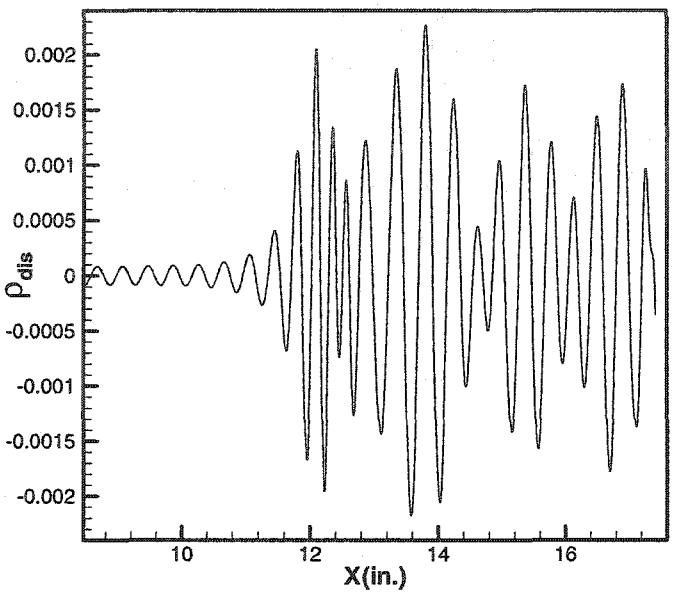

Figure 5.24 Density disturbance distribution at the wall, $F_0=0.30\times10^{-4}$, $\varepsilon=0.001$.

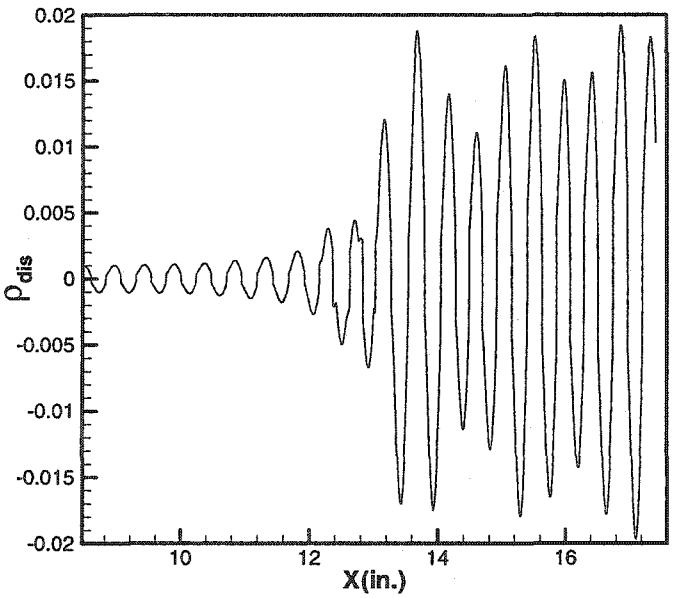

Figure 5.25 The maximal density disturbance distribution in the streamwise direction, $F_0=0.25\times10^{-4}$, $\varepsilon=0.001$.

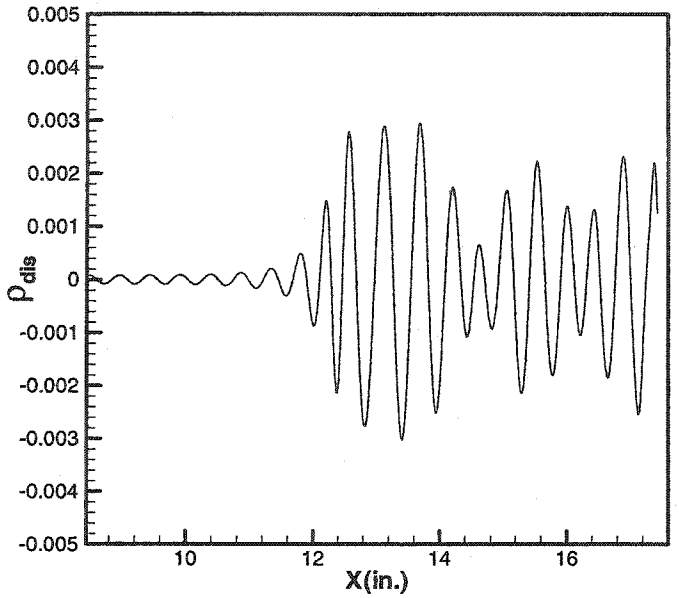

Figure 5.26 Density disturbance distribution at the wall, $F_0=0.25\times10^{-4}$, $\varepsilon=0.001$.

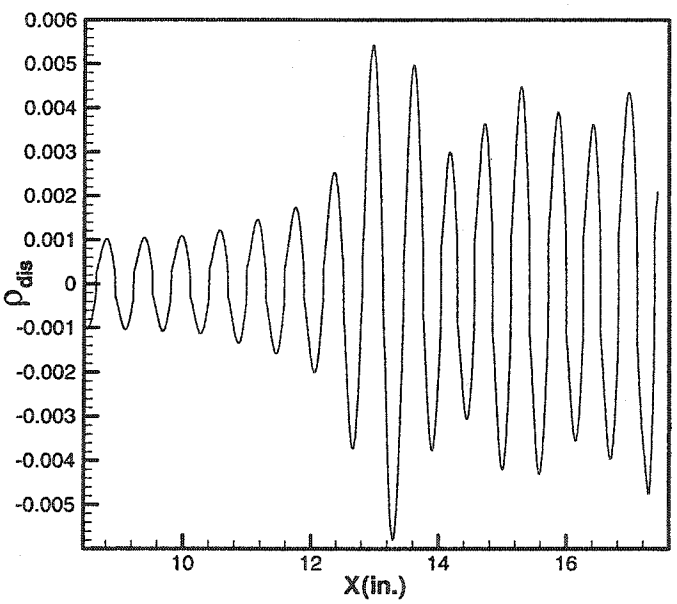

Figure 5.27 The maximal density disturbance distribution in streamwise direction, $F_0=0.20\times10^{-4}$, $\varepsilon=0.001$.

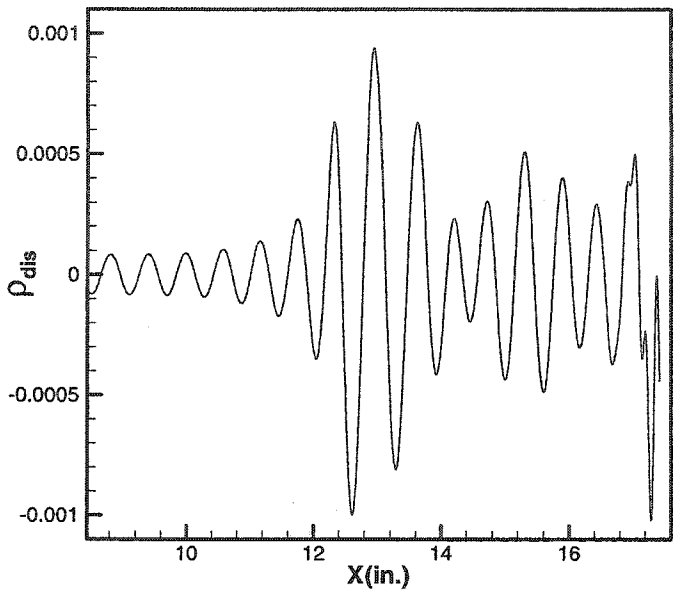

Figure 5.28 Density disturbance distribution at the wall, F_0=0.20×10^{-4}, ε=0.001.

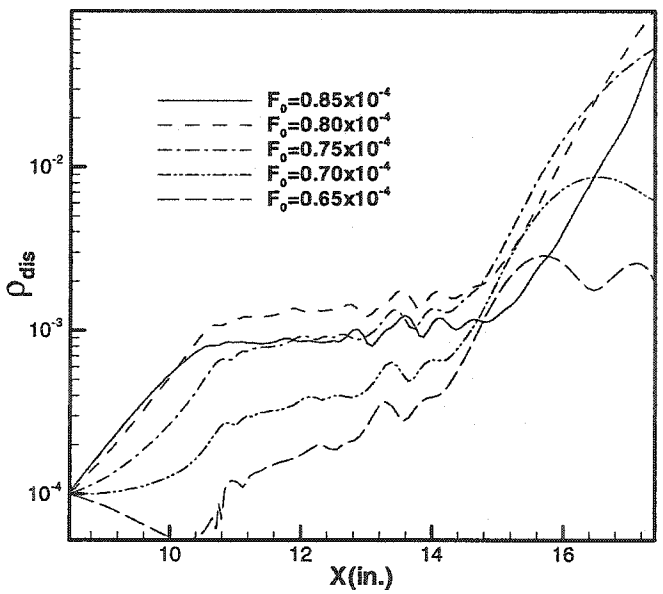

Figure 5.29 Envelope lines of the maximal density disturbance wave packet ε=0.0001.

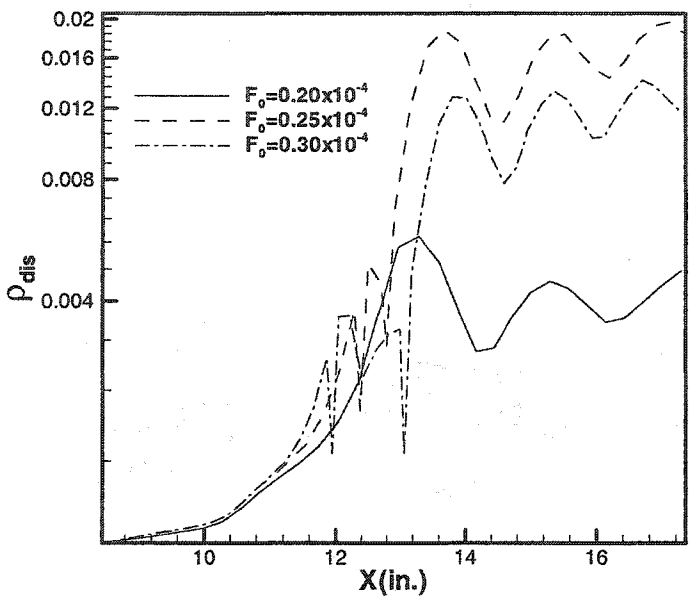

Figure 5.30 Envelope lines of the maximal density disturbance wave packet ε=0.001.

Figures 5.31a-5.31e show the eigenfunctions of the density disturbance at different streamwise locations with the dimensionless frequency $F_0=0.85\times10^{-4}$ and the initial disturbance amplitude ε=0.0001. At the locations upstream of the separation region, the eigenfunctions show the typical characteristics of the second mode disturbance eigenfunction. Two peaks appear within the boundary-layer: one near the wall and the other near the critical layer, but at locations in the separation region, more peaks appear near the wall. This is due to the third or higher acoustic modes existing in the separation regions, which had been discussed in the linear stability computations in chapter 4. At the locations downstream of the separation regions, due to the reattachment of the boundary-layer, the boundary-layer thickness becomes thin again. So the third and higher modes disappear and the eigenfunctions again show the characteristics of the second mode disturbance. The small oscillations of the eigenfunctions outside of the boundary-layer at the locations inside the separation region and downstream of the separation regions are due to the Mach waves produced along the curved boundary-layer edge.

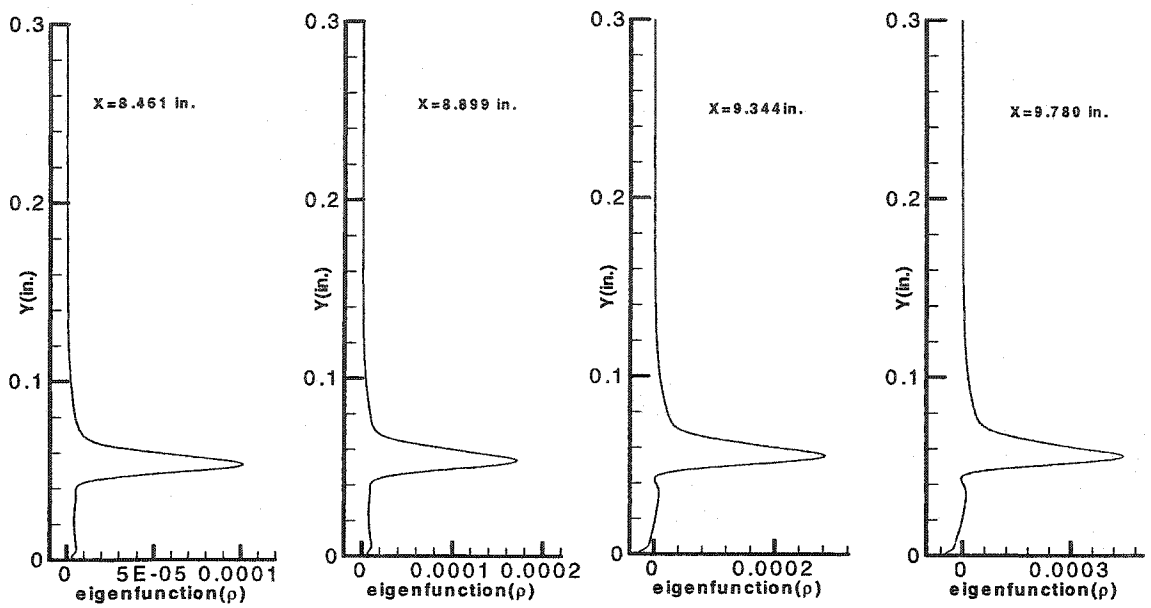

Figure 5.31a Eigenfunctions of the density disturbance, $F_0=0.85\times10^{-4}$, $\varepsilon=0.0001$.

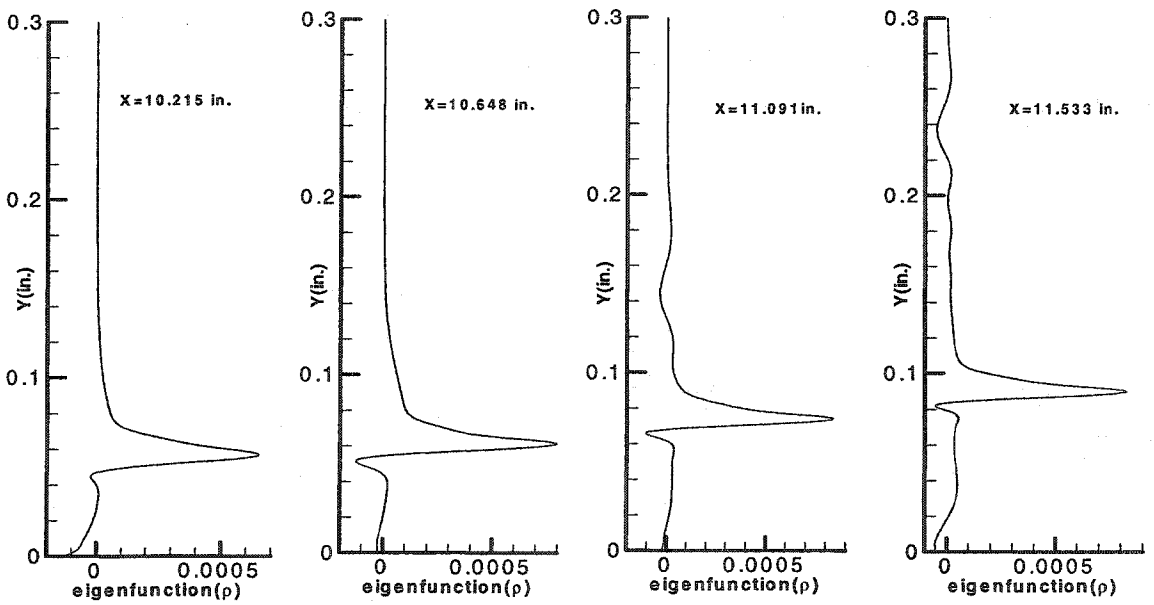

Figure 5.31b Eigenfunctions of the density disturbance, $F_0=0.85\times10^{-4}$, $\varepsilon=0.0001$.

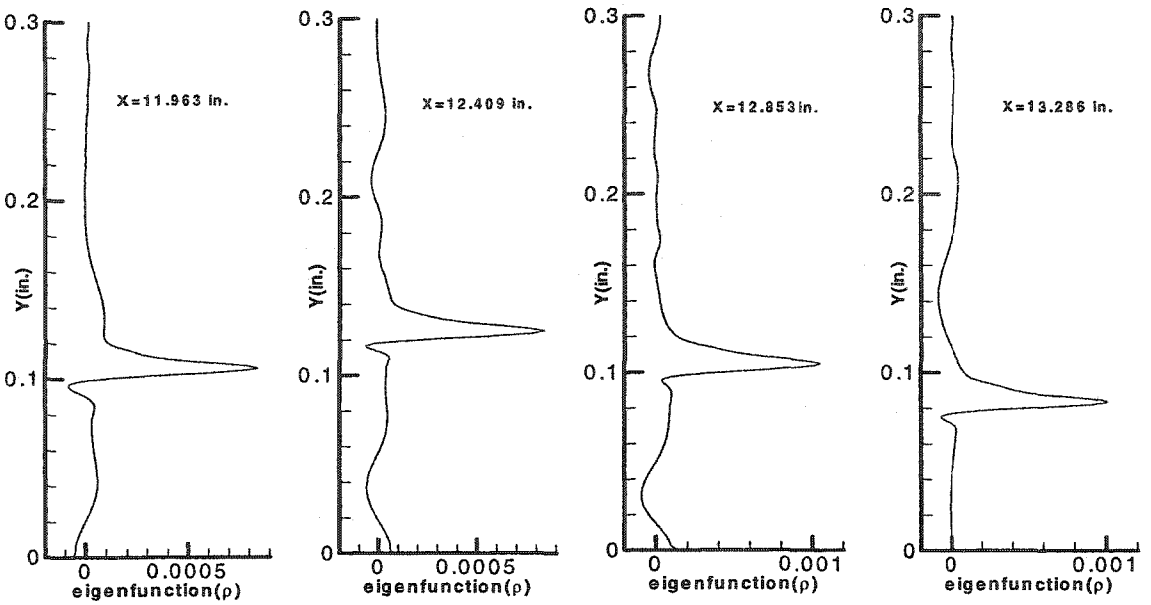

Figure 5.31c Eigenfunctions of the density disturbance, $F_0=0.85\times10^{-4}$, $\varepsilon=0.0001$.

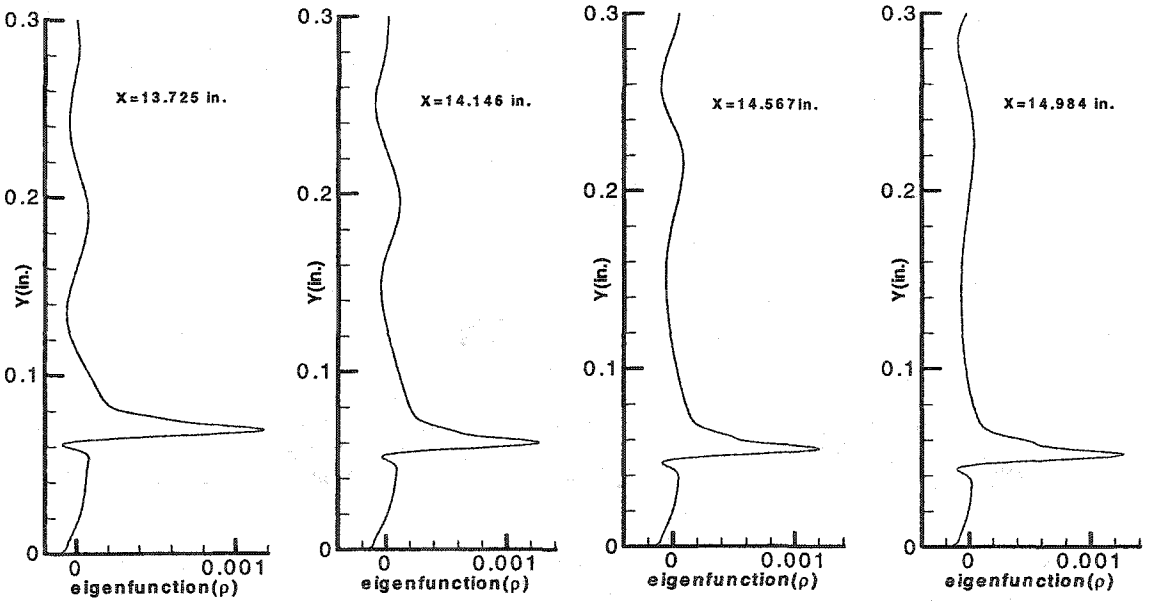

Figure 5.31d Eigenfunctions of the density disturbance, $F_0=0.85\times10^{-4}$, $\varepsilon=0.0001$.

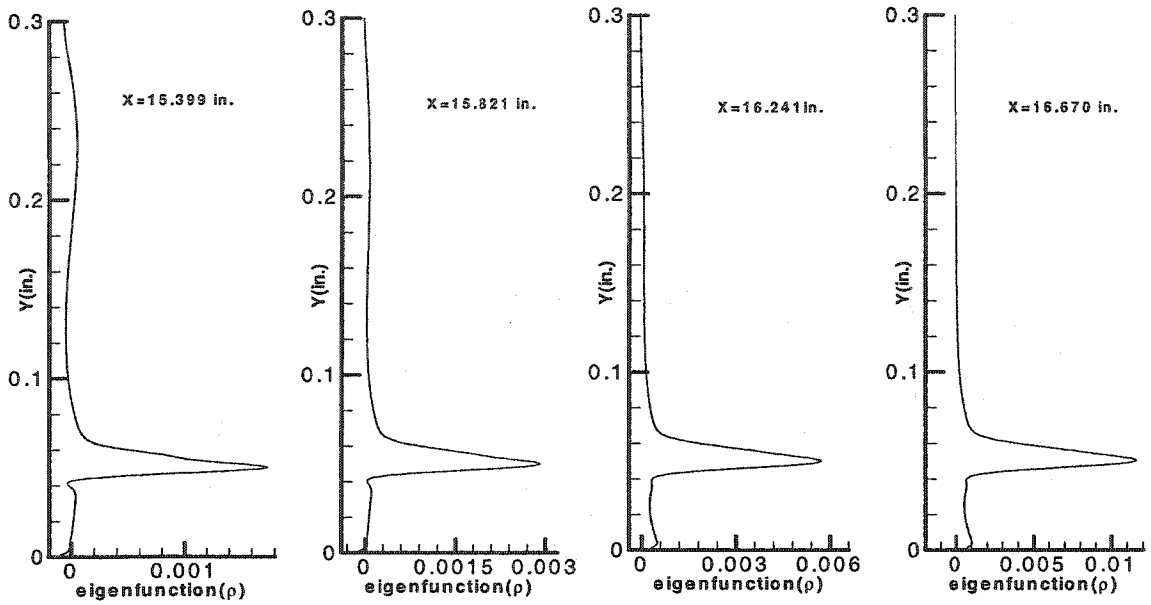

Figure 5.31e Eigenfunctions of the density disturbance, $F_0=0.85\times10^{-4}$, $\varepsilon=0.0001$.

Figure 5.32a and Figure 5.32b show the eigenfunctions of the density disturbance at the low disturbance frequency $F_0=0.25\times10^{-4}$ at the different streamwise locations. As we have discussed in chapter 4, upstream and downstream of the separation region, the low frequency disturbance shows the first mode unstable characteristics, but in the separation region, the low frequency disturbance shows the second mode unstable characteristics. From the density disturbance eigenfunction distributions shown in Figure 5.32a and Figure 5.32b we can observe that at the streamwise locations X=8.649, and 10.372 inches in upstreamwise of the separation region and X=15.542, and 16.882 inches downstream of the separation region, the eigenfunctions don't show the second mode eigenfunction characteristics anymore, and an additional peak appear within the boundary-layer due to the first mode instability. But at the locations X=11.817, 12.700, 13.159 and 13.680 inches in the separation region, the second mode is the most unstable mode, so the eigenfunctions at these locations show the characteristics of the second mode eigenfunction.

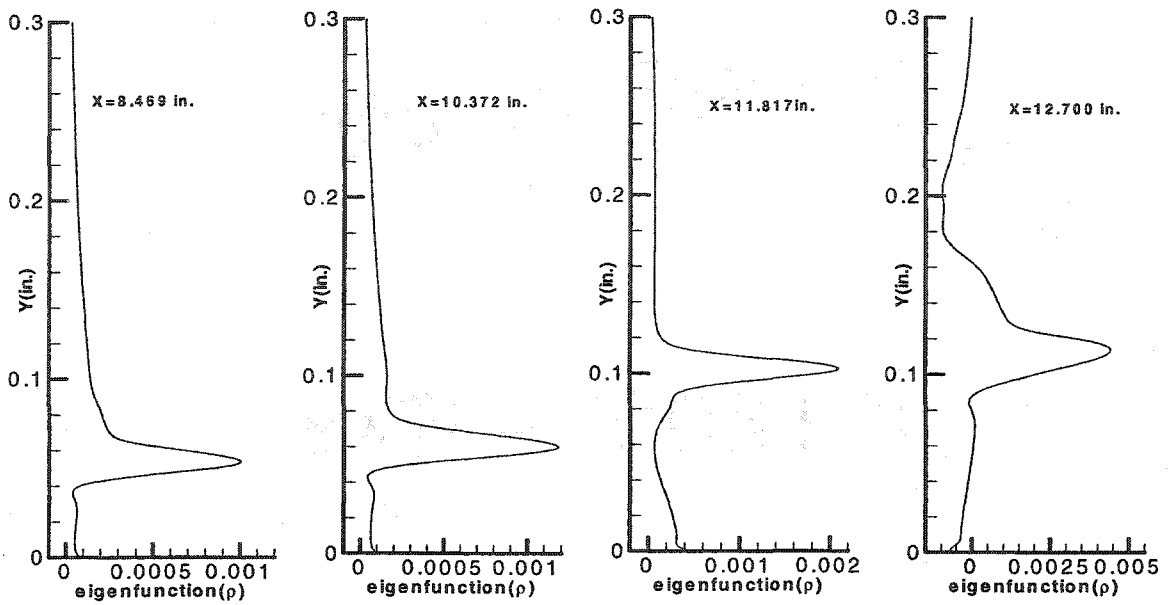

Figure 5.32a Eigenfunctions of the density disturbance, $F_0=0.25\times10^{-4}$, $\varepsilon=0.001$.

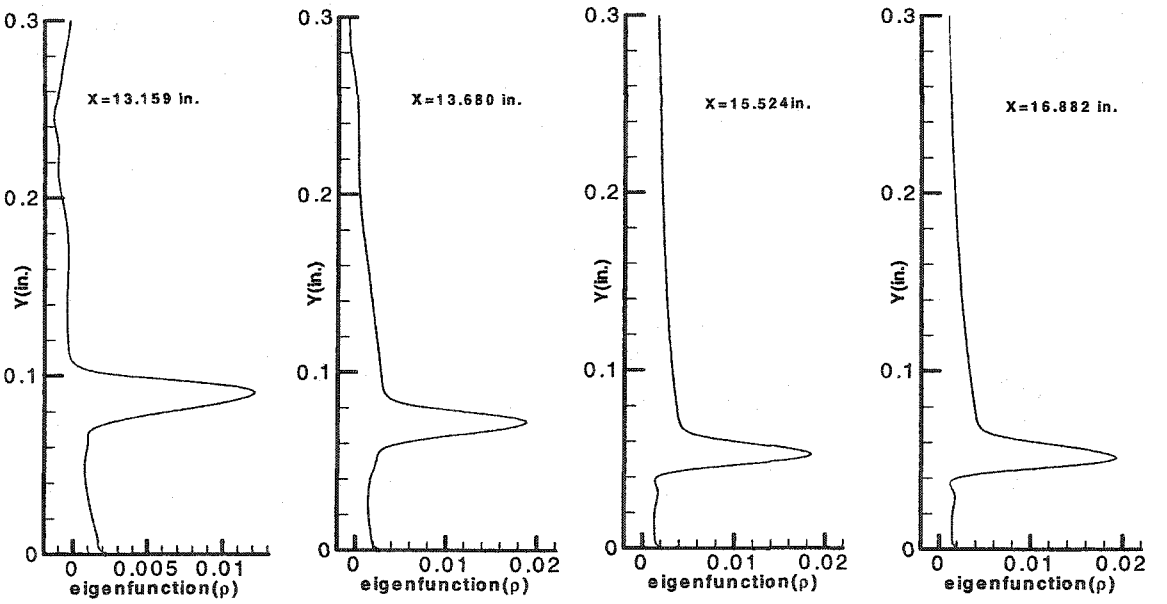

Figure 5.32b Eigenfunctions of the density disturbance, $F_0=0.25\times10^{-4}$, $\varepsilon=0.001$.

5.3.2 The nonlinear evolutions of the disturbances

If a much larger initial disturbance amplitude is specified at the initial streamwise location, the nonlinear interactions of the disturbances will be observed at downstream locations across the compression corner. Figure 5.33a shows the density disturbance contours across the compression corner with disturbance frequency $F_0=0.80\times10^{-4}$ and initial disturbance amplitude $\varepsilon=0.01$. Figure 5.33b shows an expanded view of the density disturbance contour downstream of the separation region. It is observed that, compared with the density disturbance contours of the linear evolution shown in Figure 5.12d, the density disturbance contours for the non-linear evolution show some distortion downstream of the separation region due to nonlinear interactions. This distortion becomes larger and larger when the disturbances evolve further downstream until nonlinear saturation occurs.

Figure 5.34 shows the normal maximal density disturbance amplitude distribution along the streamwise direction at a given time step, when the disturbance reaches a steady periodic condition. Figure 5.35 shows the density disturbance distribution at the wall. The normal maximal disturbance amplitude plot shows that the disturbances evolve linearly upstream of the separation region. When the maximal density disturbance amplitude exceeds 0.05, which is about 5% of its mean flow value, the weak nonlinearity begins to appear. Downstream of the separation region, nonlinear effects become much stronger with the disturbance evolving downstream. When the density disturbance amplitude exceeds about 0.45, the disturbance begins to saturate. It cannot grow further downstream even though the linear disturbance may grow in this region. We can also observe the nonlinear effect according to the density disturbance distribution at the wall. For linear evolution, the disturbance should be symmetric at the wall as shown in Figure 5.16. But when the disturbance evolution becomes nonlinear, the super-harmonics will appear due to the nonlinear interactions of the primary harmonics. These super-harmonics will also grow or decay in the boundary-layer. The superposition of all these harmonics will make the

disturbance at the wall become asymmetric.

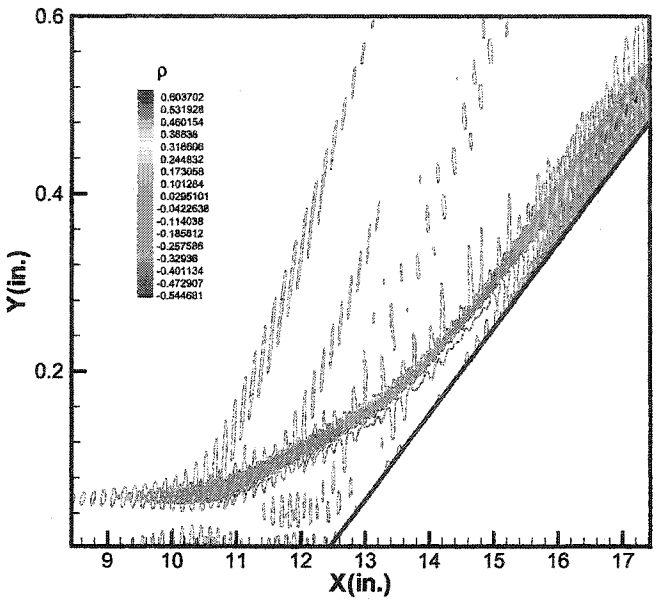

Figure 5.33a The density disturbance contour, $F_0=0.80\times10^{-4}$, $\varepsilon=0.01$.

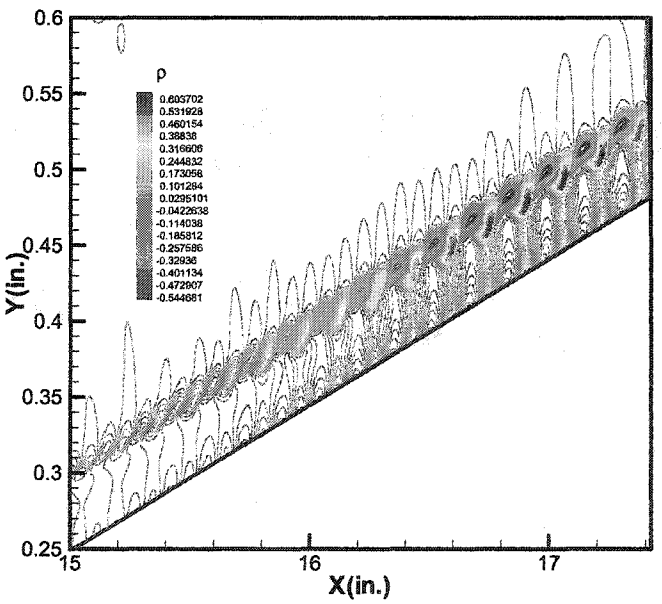

Figure 5.33b The downstream density disturbance contour, $F_0=0.80\times10^{-4}$, $\varepsilon=0.01$.

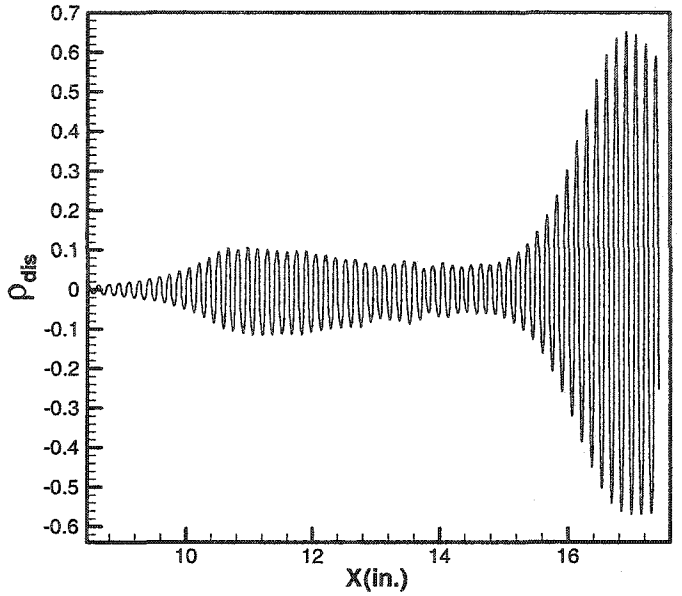

Figure 5.34 The normal maximal density disturbance distribution, $F_0=0.80\times10^{-4}$, $\varepsilon=0.01$.

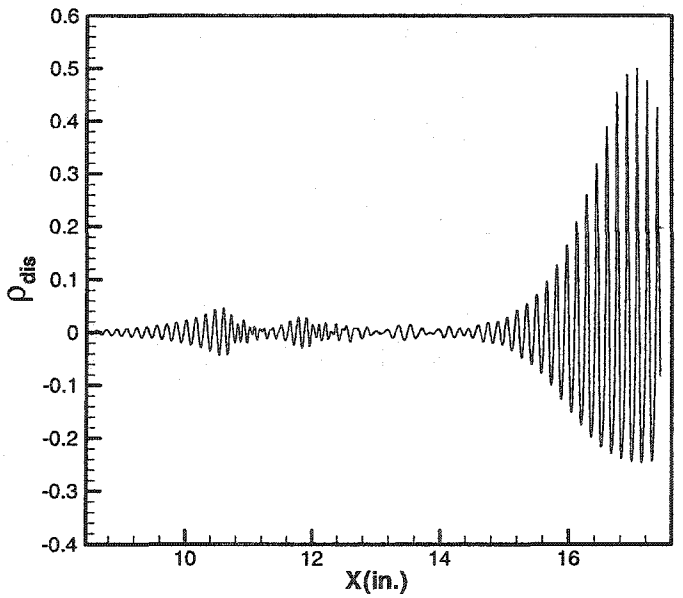

Figure 5.35 The density disturbance distribution at the wall, $F_0=0.80\times10^{-4}$, $\varepsilon=0.01$.

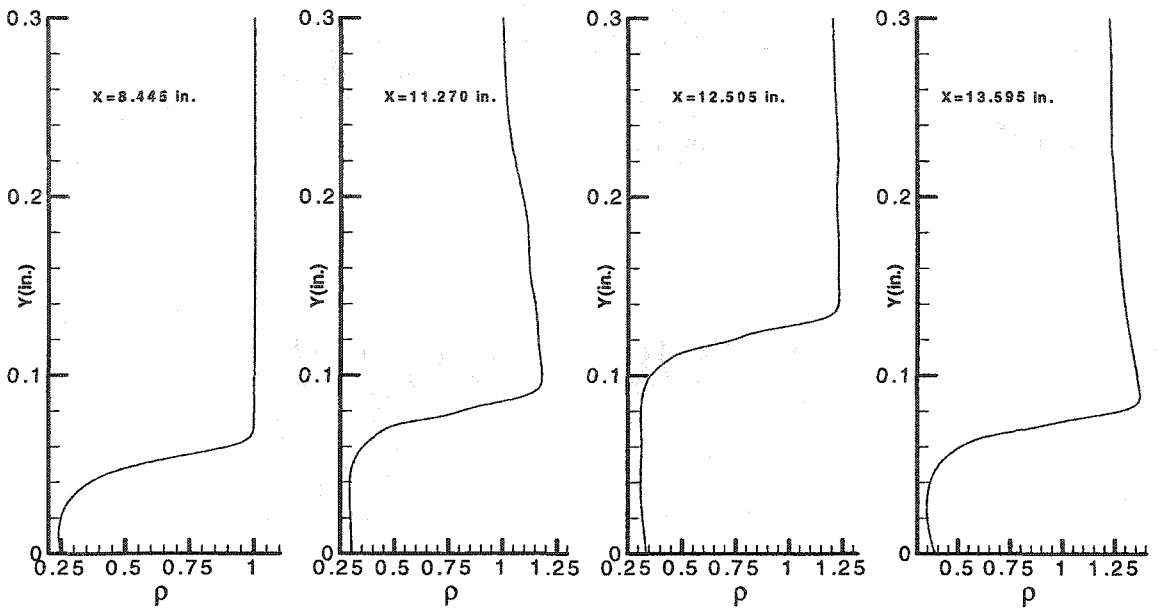

Figure 5.36a The density profiles with distortion.

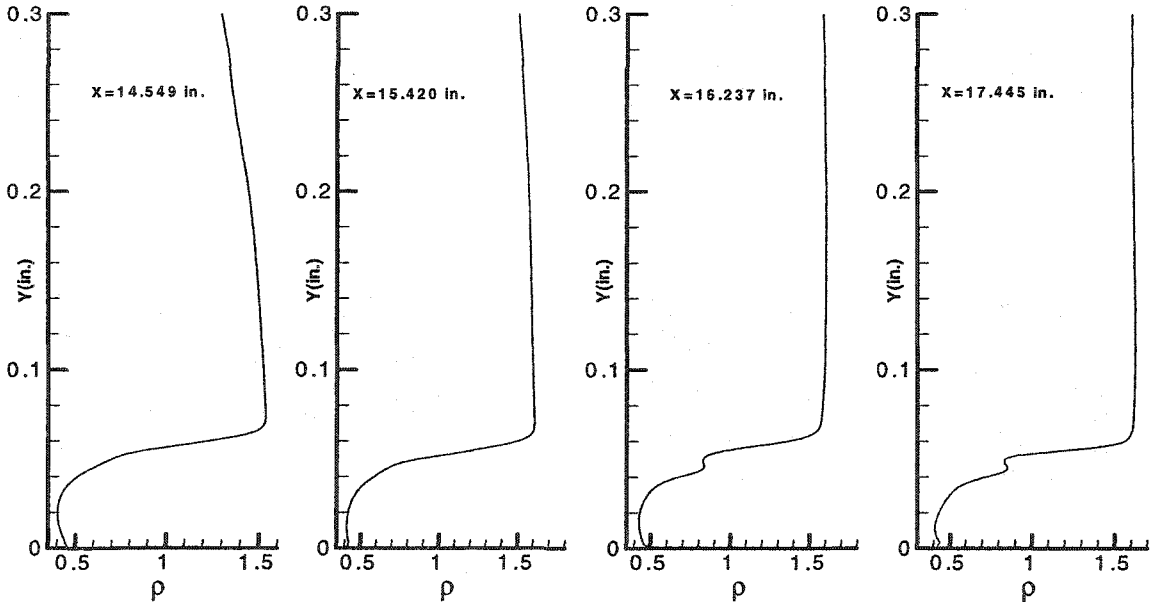

Figure 5.36b The density profiles with distortion.

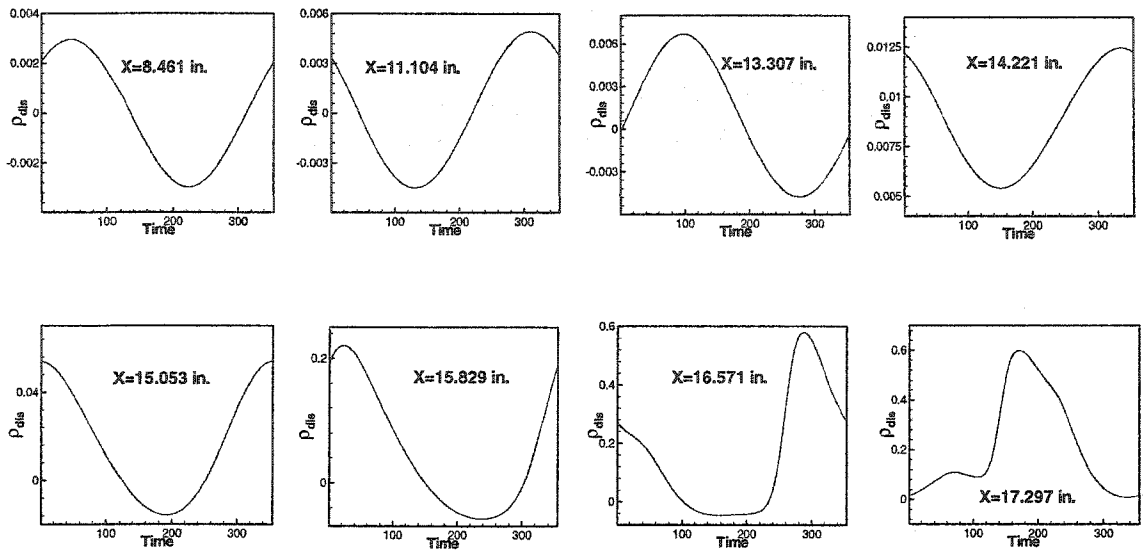

Figure 5.37 The time response of density disturbances at the wall.

Figure 5.36a and Figure 5.36b show the steady density profiles at different streamwise locations. It is observed that the density profiles show little difference from the mean flow profiles at the locations upstream of the separation region and inside the separation region. However, at locations downstream of the separation region, the density profiles begin to show some distortions, and the distortions become much larger in further downstream. This distorted mean flow forms the base flow for the secondary instability. Figure 5.37 shows the time history of the density disturbance on the wall at different streamwise locations. The figures show that upstream of the separation region and inside the separation region, the time response of the density disturbance is pure harmonic. However, the time response begins to show some distortions the locations downstream of the separation region, and the distortions increase in the further downstream.

From the above discussions we know that nonlinear interactions will occur when the disturbances amplitude reaches some specific value and the super-harmonics then appear due to the nonlinear interactions. In addition, some questions need to be addressed such as: Which harmonics will appear? How does each of these harmonics evolve in the boundary-layer? Which harmonic will dominate the instability of the boundary-layer? In order to answer these questions, we need to decompose the total disturbance into different

harmonic components. This can be done by discrete Fourier transformation(DFT) shown as equation (5.3). If we take the data in one temporal cycle at each grid point and perform DFT analysis in time, then we can get the amplitude of each harmonic mode.

$$X(k)=\frac{2}{N_0}\sum_{n=1}^{N_0}x(n)\exp[-2i\pi(k-1)(n-1)/N_0],\ 1\le k\le N_0 \tag{5.3}$$

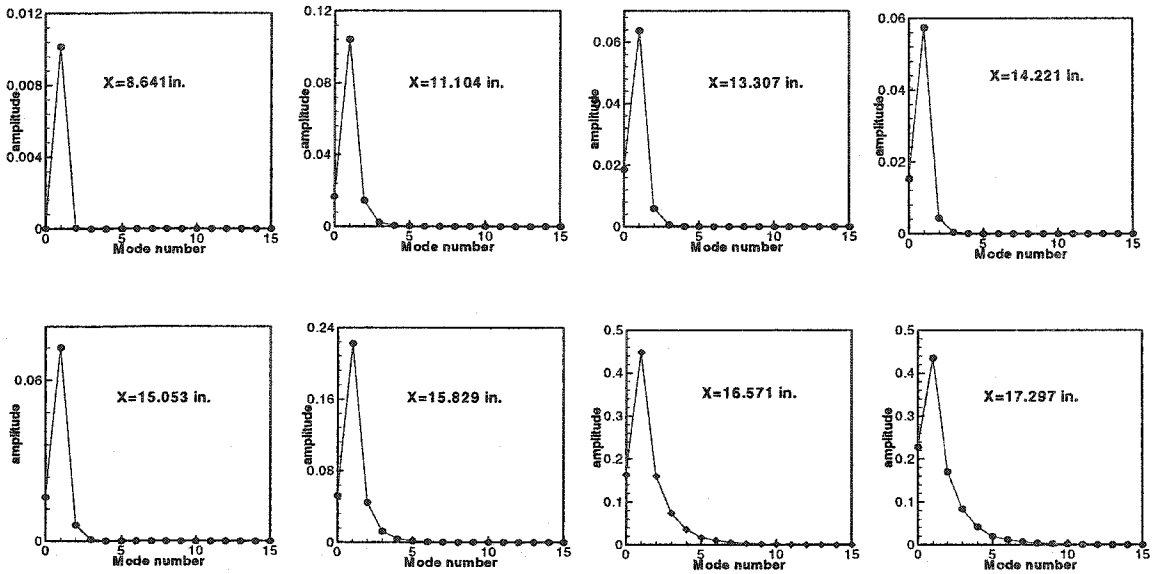

Figure 5.38 The amplitudes of the Fourier modes for the maximal density disturbance.

Figure 5.38 shows the amplitude distributions of each Fourier harmonic component of the normal maximal density disturbance at different streamwise locations. It is observed that very few harmonics appeared at locations upstream of the separation region and inside the separation region, but more and more harmonics appeared at the locations downstream of the separation region. Figure 5.39 shows the normal maximal amplitude distributions of the first five harmonics for density disturbance in the streamwise direction. Figure 5.40 shows the amplitude distributions of the first five harmonics of density disturbance at the wall. It can be seen from these two figures that the nonlinear interactions begin to happen when the amplitude of the primary mode exceeds 0.05 and the super-harmonics begin to appear. The primary mode still keeps an approximately neutral status in the separation region, but grows rapidly after the separation region. It begins to saturate when its amplitude exceeds 0.45. Among all the other harmonic modes,

the 0ω mode, which shows the mean flow distortions decays or grows following the primary mode. Just like the primary mode, all super-harmonics also are nominally neutral in the separation region and grow downstream of the separation region. When the primary mode reaches saturation, these super-harmonic modes also saturate despite their current amplitude. We can also see that only the first three super-harmonics can reach amplitudes which are comparable to those of the primary mode. The influence of the much higher harmonics will be negligible. Figures 5.41-5.45 show the normal distributions of the mean flow distortions and the eigenfunctions of the primary mode as well as the first three super-harmonic modes at different streamwise locations. It is observed that the mean flow show large distortions in the critical layer and all super-harmonics also grow along the outer edge of the boundary-layer. The eigenfunctions of the 1ω mode show the same characteristics as those in linear evolutions in all three flow regions, and we also notice that more peaks appear for the eigenfunctions of the super-harmonic modes 2ω, 3ω and 4ω in all regions. This means that these modes represent the much higher acoustic modes.

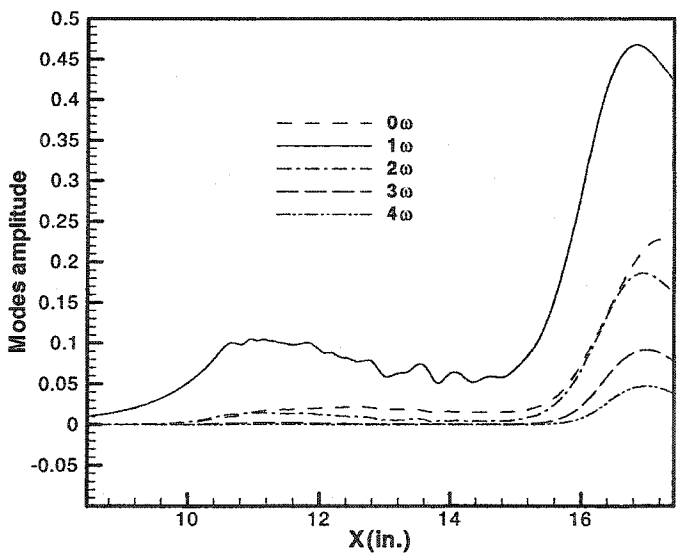

Figure 5.39 DFT analysis results for maximal density disturbance, $F_0=0.80\times10^{-4}$, $\varepsilon=0.01$.

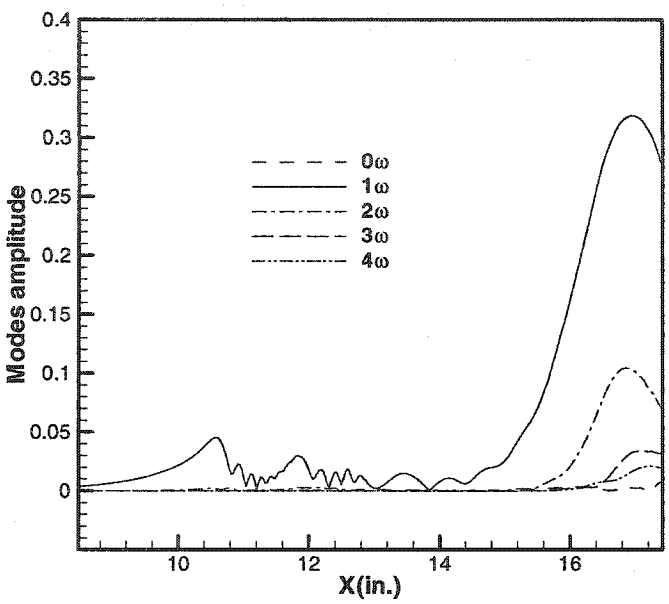

Figure 5.40 DFT analysis results for density disturbance at the wall, $F_0=0.80\times10^{-4}$, $\varepsilon=0.01$.

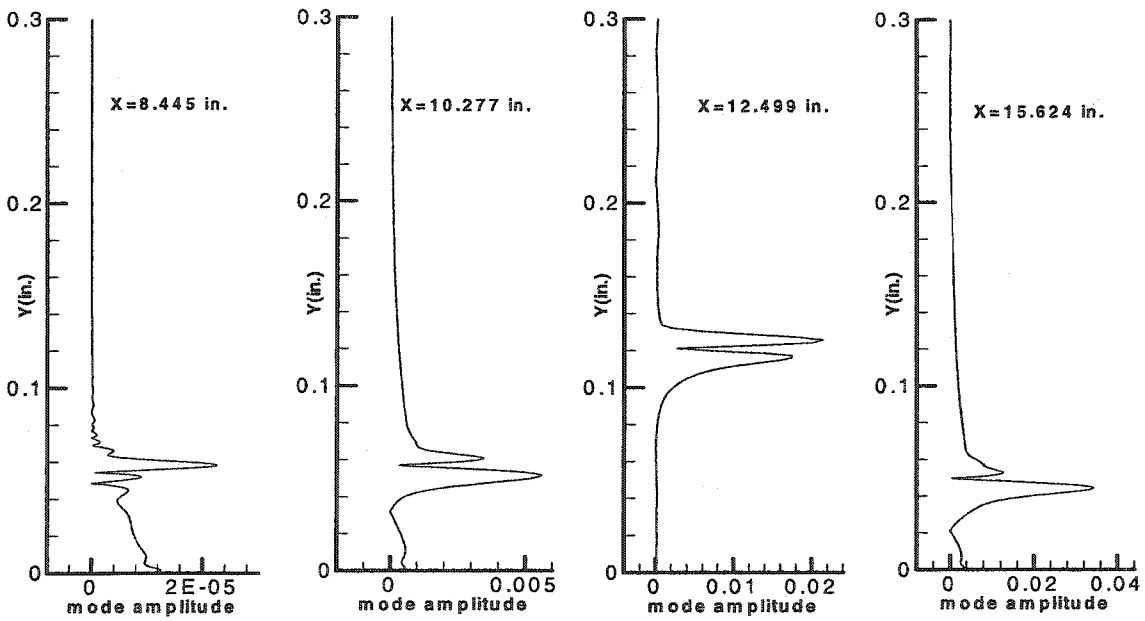

Figure 5.41 Normal distributions for the mean flow distortion.

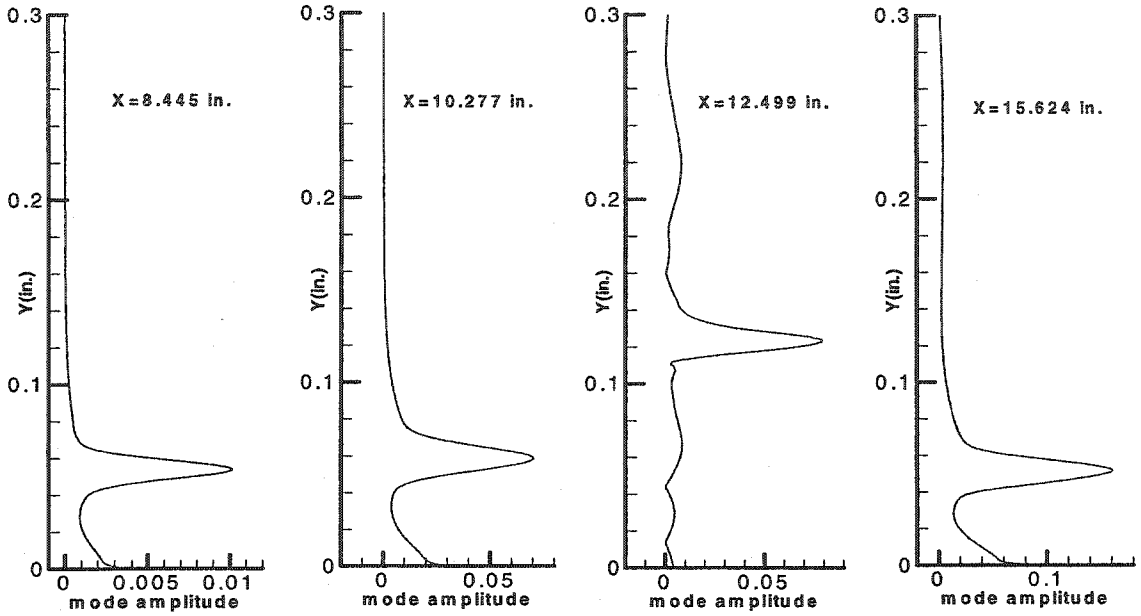

Figure 5.42 The density disturbance eigenfunction for mode 1ω.

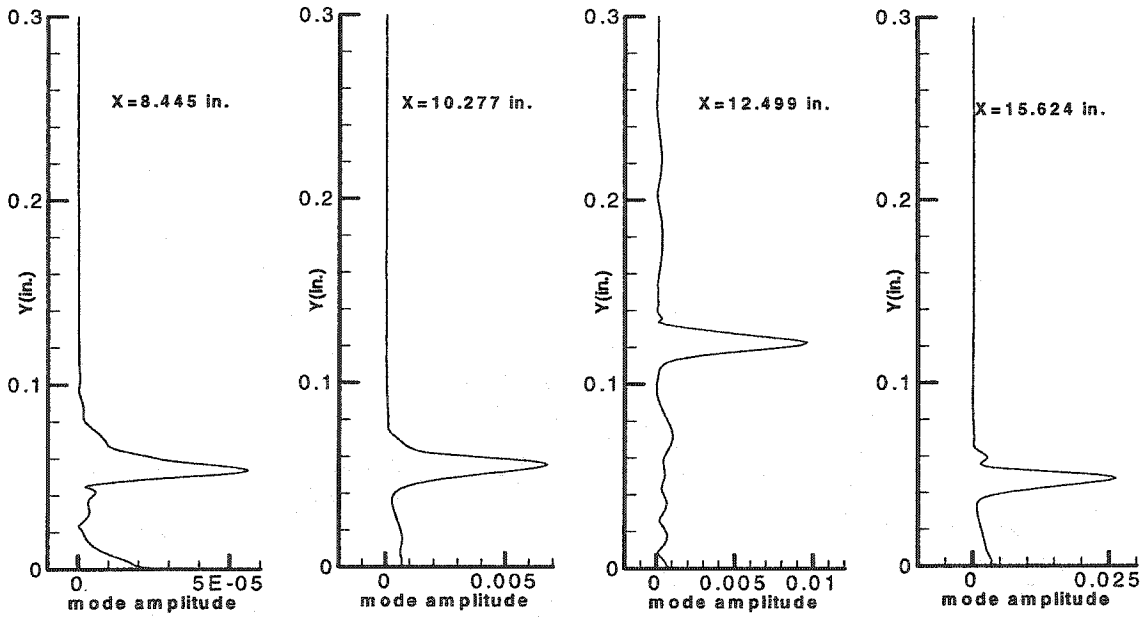

Figure 5.43 The density disturbance eigenfunction for mode 2ω.

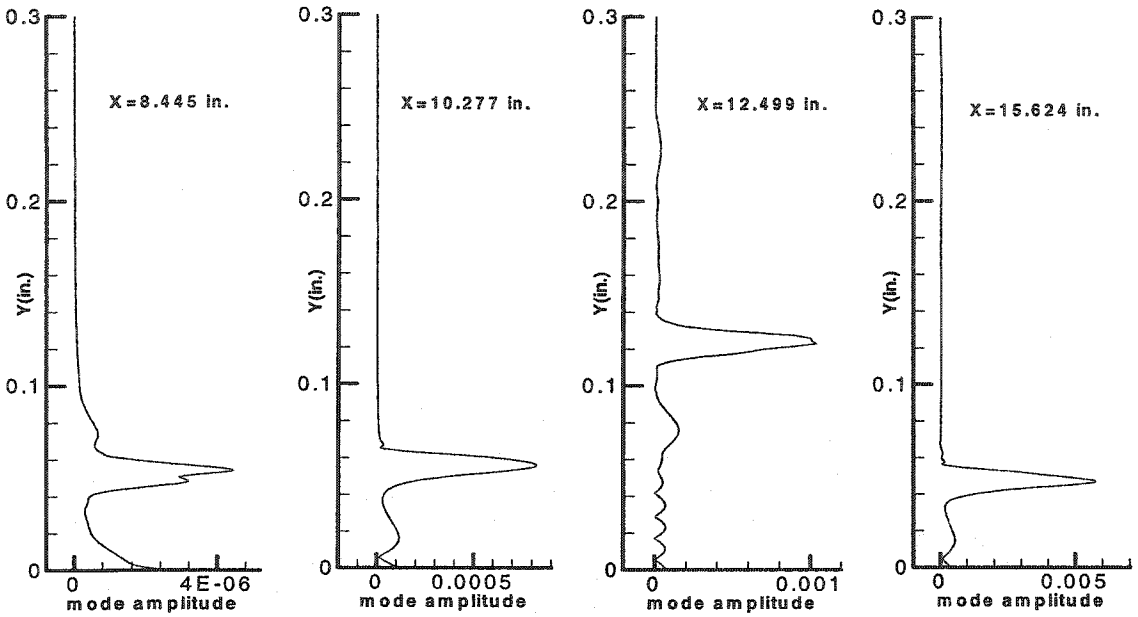

Figure 5.44 The density disturbance eigenfunction for mode 3ω.

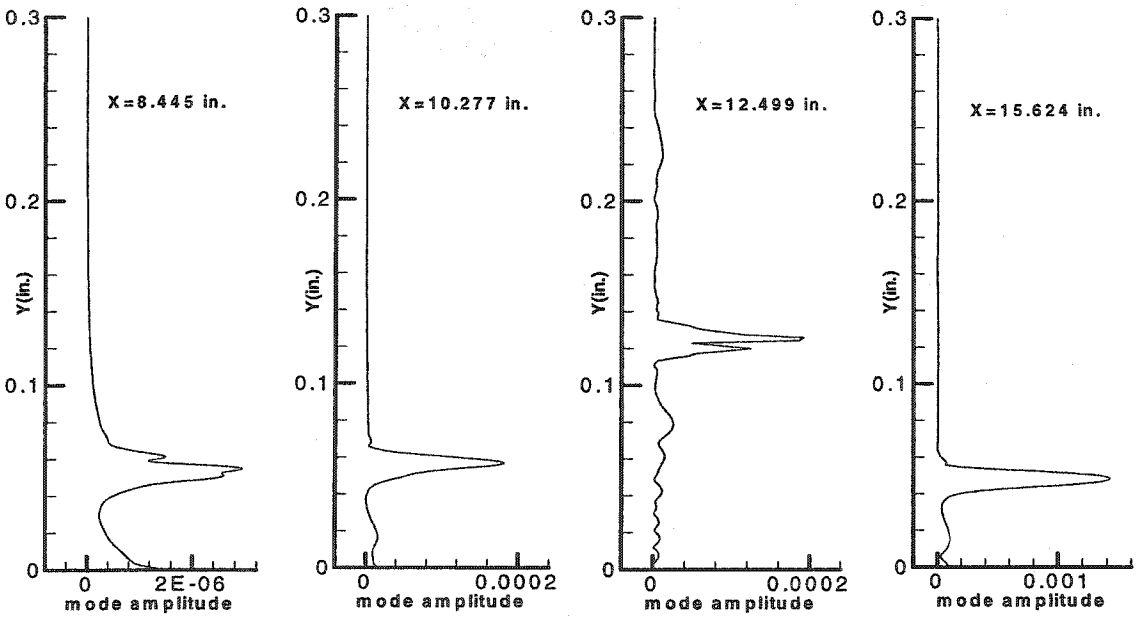

Figure 5.45 The density disturbance eigenfunction for mode 4ω.

§5.4 Summary

In this chapter, we performed the DNS for linear and nonlinear two-dimensional second mode disturbance evolution across the compression corner. The two-dimensional unsteady computational code was validated by the parallel and nonparallel flow computations across a flat plate. The evolution of the second mode disturbance across the compression corner shows that the high frequency disturbances grow exponentially upstream and downstream of the separation region and remains neutral across the separation region; The low frequency disturbances remain neutral upstream and downstream of the separation region, and grow in the separation region. The maximum N-factor up to the second corner region of the Hyper-X wind tunnel model is about 7 and this occurs for a disturbance with a non-dimensional frequency of $F_0=0.80\times10^{-4}$. With larger initial disturbance amplitudes, the disturbance evolution will become non-linear in the downstream of the separation region and the super-harmonics will appear due to the nonlinear interaction. These harmonics will show the same stability characteristics as those of the primary mode in all three regions. The primary mode always dominates all other modes in amplitude. When the amplitude of the primary mode reaches above 45% of its upstream infinity mean flow value, the primary mode and all other harmonic modes will begin nonlinear saturation, and the disturbances do not grow any further. This saturated disturbance along with the distorted mean flow forms the base flow for secondary instability.

CHAPTER VI

DIRECT NUMERICAL SIMULATION OF THREE-DIMENSIONAL DISTURBANCE EVOLUTIONS

In the previous chapter, we performed DNS for two-dimensional second mode disturbance evolution across a compression corner and demonstrated the mechanisms of linear and nonlinear evolutions of the two-dimensional disturbances across the three flow regions of the compression corner. However, considerable quantity of experimental and numerical work have actually demonstrated the three-dimensional nature of transition. The classical experiment conducted by Klebanoff, Tidstrom and Sargent[29] demonstrated that the actual breakdown of the wave motion into turbulence is a consequence of a new instability which arises in the aforementioned three-dimensional wave motion. This instability involves the generation of staggered "Λ" vortices and the transition begins at the peak planes. In order to fully understand the transition mechanism for hypersonic flow going through the compression corner, the three-dimensional disturbance evolution across the compression corner should be investigated. In this chapter, we will study both linear and nonlinear evolution of the three-dimensional second mode disturbance with the mono- and random-frequencies across the compression corner. The transition mechanism for hypersonic flow going through the compression corner will be identified in this chapter.

6.1 Computational model, grid and flow parameters

The computations are performed for the hypersonic flow passing a 5.5° compression corner. The geometry of the computational model is illustrated in Figure 6.1. It is a Hyper-X model with two corners, the computation in the present study only focuses on the disturbance evolution across the first corner. The flow parameters are the same as

those of the two-dimensional computation and are given in Table 3.1. These parameters are selected to simulate the Hyper-X wind tunnel model and the experimental conditions.

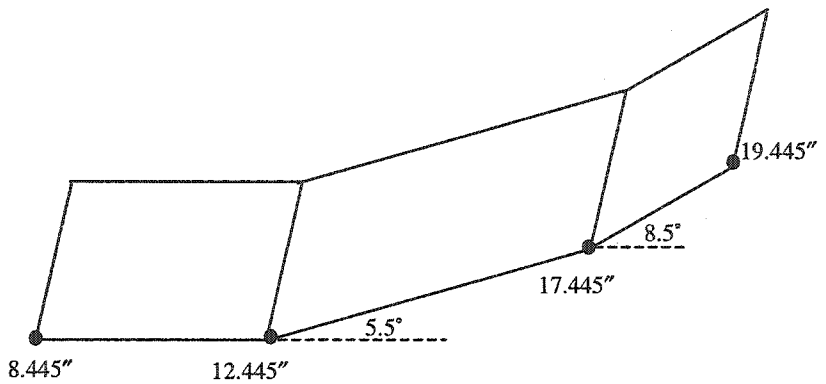

Figure 6.1 The geometry of the computational model.

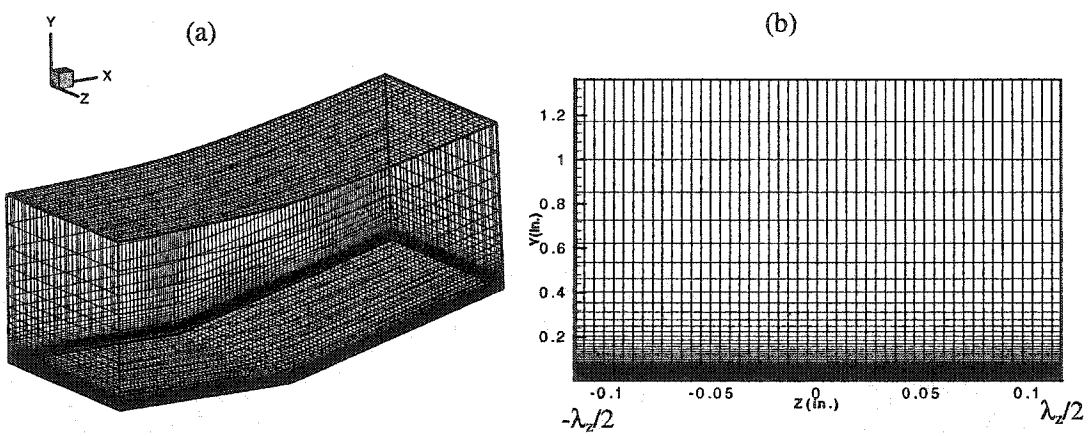

Figure 6.2 The three-dimensional computational grid.

Figure 6.2(a) shows the three-dimensional computational grid. The three-dimensional grid is generated by expanding the two-dimensional grid given in Figure 3.2 evenly, spaced in the spanwise direction. Figure 6.2(b) shows the grid in YZ plane for one wave length in spanwise direction. Because in present computation the symmetric boundary conditions are enforced in spanwise direction, only one half wave length computation domain in spanwise direction needs to be considered. The actual computational domain in spanwise direction locates between Z=0 and Z=λ_z/2. The grid size is 1701×301×30 in the X, Y and Z directions respectively. The mean flow for hypersonic uniform flow going

through the three-dimensional compression corner is still two-dimensional steady mean flow which was obtained in chapter 3. No mean flow variation exists in the spanwise direction. This two-dimensional mean flow will be used as the basic flow for three-dimensional disturbance evolution simulation.

6.2 The introduction of the initial three-dimensional mono-frequency and random disturbances

The three-dimensional mono-frequency initial disturbances are obtained by three-dimensional PSE computation. The three-dimensional initial random disturbances are introduced as random noise together with a two-dimensional mono-frequency primary disturbance. They are superimposed on the mean flow profiles at the beginning of the computational domain, and in the streamwise direction according to the following equations.

$$\mathbf{q}(x_0, y, z, t) = \mathbf{Q}_0(x_0, y) + \varepsilon \, \mathrm{Re}al\left[\hat{\mathbf{q}}(y)(e^{i\beta z - i\omega t} + e^{-i\beta z - i\omega t})\right] \tag{6.1}$$

$$\begin{aligned}\mathbf{q}(x_0, y, z, t) = \mathbf{Q}_0(x_0, y) &+ \varepsilon_{2D} \, \mathrm{Re}al\left[\hat{\mathbf{q}}(y)e^{-i\omega t}\right] \\ &+ \varepsilon_{3D} \sum_n \sum_m \mathrm{Re}al\left[\hat{\mathbf{q}}_{\mathrm{nm}}(y)(e^{i\beta_m z - i\omega_n t} + e^{-i\beta_m z - i\omega_n t})\right]\end{aligned} \tag{6.2}$$

$$\mathbf{q} = [\rho, e_t, u, v, w]^T; \quad \mathbf{Q}_0 = [\rho_0, Et_0, U_0, V_0, W_0]^T; \quad \hat{\mathbf{q}} = [\hat{\rho}, \hat{e}_t, \hat{u}, \hat{v}, \hat{w}]^T \tag{6.3}$$

where ω is the disturbance frequency; ε is the initial disturbance amplitude for mono-frequency, three-dimensional disturbances; ε_{2D} and ε_{3D} are the initial disturbance amplitudes for two-dimensional primary disturbances and three-dimensional random disturbances respectively; $\hat{\mathbf{q}}$ is the eigenfunction which is obtained by the PSE method; $\hat{\mathbf{q}}_{\mathrm{nm}}$ can be simply represented by some random numbers. Q_0 are the steady mean flow profiles at the initial streamwise location; x_0 is the coordinate at the initial streamwise location. Figure 6.3 illustrates how to superimpose the initial three-dimensional disturbances on the mean flow.

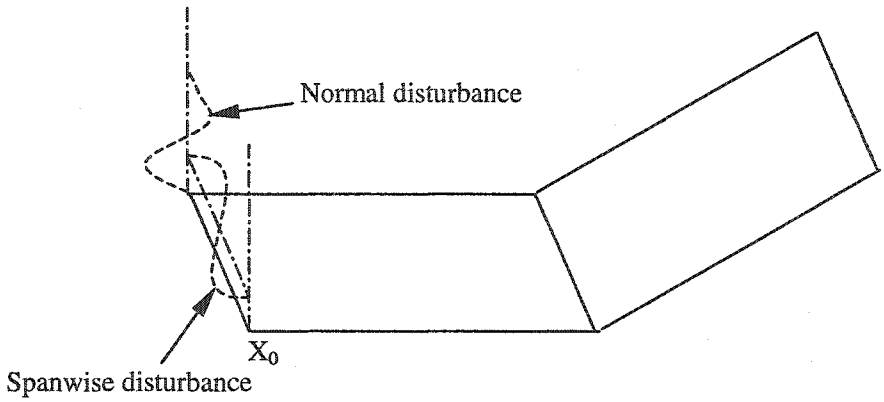

Figure 6.3 The introduction of the initial three-dimensional disturbance.

In the simulation of the three-dimensional disturbance evolutions in this chapter, we chose a dimensionless primary disturbance frequency $F_0=0.85\times10^{-4}$ because both two-dimensional and three-dimensional disturbances are amplified greatly at this frequency based on the linear stability computation results given in chapter 4. The initial three-dimensional mono-frequency disturbances are purely harmonic both in time and in the spanwise direction. Figure 6.4(a) shows the eigenfunctions of the initial three-dimensional mono-frequency disturbances at the spanwise location $Z=2\lambda_z/15$ with the spanwise wave number $\beta=0.1$. Figure 6.4(b) shows the initial disturbance variations in the spanwise direction at the location y=0.0418 inch.

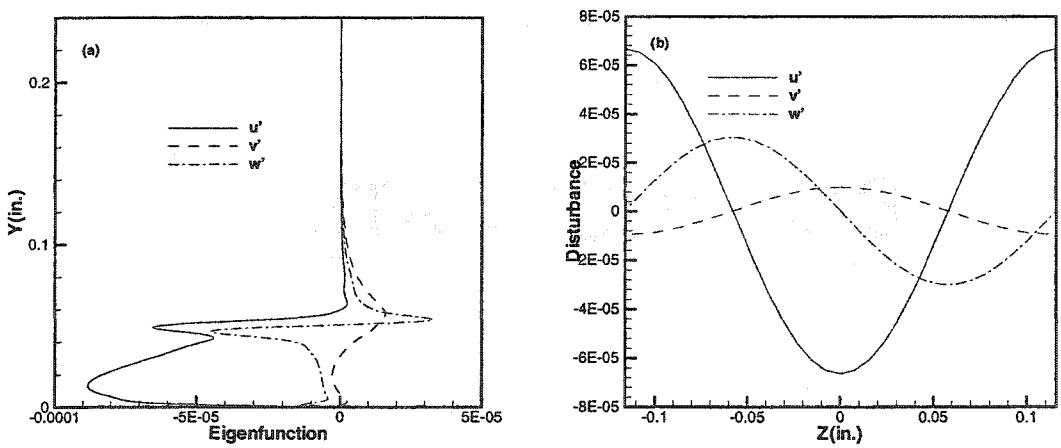

Figure 6.4 The initial three-dimensional disturbance profiles.

6.3 Validation of the code for three-dimensional unsteady computation

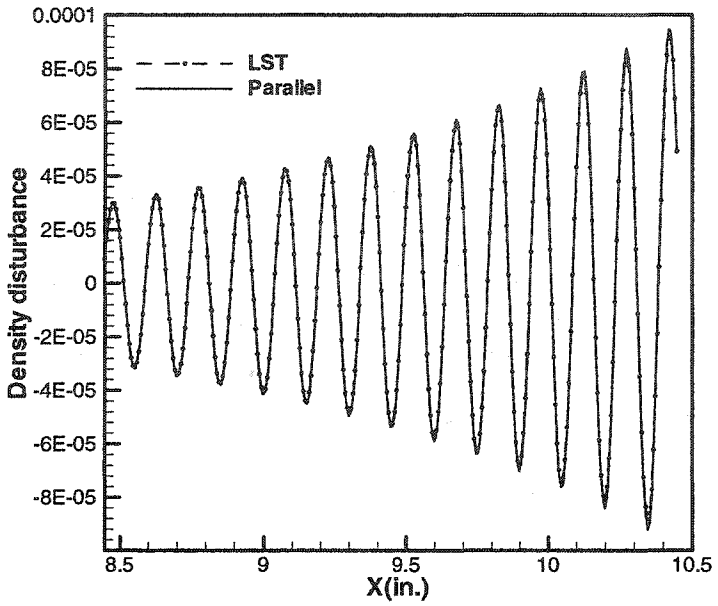

Figure 6.5 Comparison of the LST and parallel result.

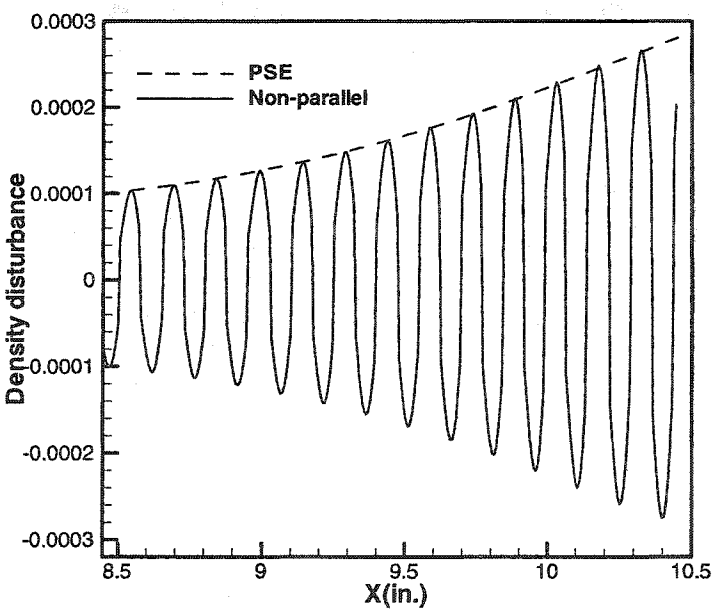

Figure 6.6 Comparison of the PSE and non-parallel result.

To check the validation of the code for unsteady computation, first we perform both parallel and non-parallel flow computations to simulate the three-dimensional disturbance evolutions along a flat plate. Then we compare the parallel results with those obtained by three-dimensional linear stability theory and compare the non-parallel results with those obtained by three-dimensional PSE method. The flow parameters for the flat plate computation are the same as those for the compression corner computation. The mean flow is obtained by solving the similarity equations for a Blasius boundary-layer. The dimensionless disturbance frequency is $F_0=0.85\times10^{-4}$ and the spanwise wave number is $\beta=0.1$. The initial disturbance amplitude was set at $\varepsilon=0.0001$. Figure 6.5 shows the comparison between the results of linear stability theory and those of parallel flow computation for the density disturbances along one streamwise grid line. Figure 6.6 shows a comparison between the results of the PSE method and non-parallel flow computation for the normal maximal density disturbance amplitude along the streamwise direction. The comparisons demonstrate that the direct numerical simulation results of both parallel and non-parallel flow instability agree very well with their corresponding linear computation results. The three-dimensional code is considered to be valid for further computations.

6.4 The linear evolutions of the three-dimensional mono-frequency disturbances across the compression corner

To simulate the linear evolution of the three-dimensional mono-frequency disturbance across the compression corner, we take the disturbance frequency to be $F_0=0.85\times10^{-4}$, the spanwise wave number as $\beta=0.1$ and initial disturbance amplitude $\varepsilon=0.0001$. The spanwise wave length is about 0.232 inches. With this small initial disturbance amplitude, the nonlinear influence can be neglected in the whole flow region across the compression corner. Figure 6.7 shows the density disturbance contours in the X-Y plane at the spanwise location $Z=2\lambda_z/15$. Figure 6.8, Figure 6.9 and Figure 6.10 are the expanded views of these disturbance contour upstream of the separation bubble,

within the separation bubble and downstream of the separation bubble respectively. It is observed that just like the two-dimensional disturbance, the three-dimensional disturbance also evolves downstream along the outer edge of the boundary-layer and the disturbance amplitude reaches a maximum in the critical layer. The maximal disturbance will never penetrate into the separation bubble.

Figures 6.11-6.14 show the density, streamwise velocity, normal velocity and spanwise velocity disturbance contours in the Y-Z plane at three streamwise locations, x=8.445, 12.984 and 17.445 inches respectively. The disturbance contours are shown for one cycle in the spanwise direction. It can be seen from these contours that two peaks appear in the normal direction upstream and downstream of the separation region, and one is in the critical layer, while one is close to the wall. In the separation region, the maximal disturbances reside above the separation bubble. The disturbances are very small in the separation bubble.

Figure 6.15 shows the density disturbance contours in the X-Z plane at three normal locations, y=0.0, 0.0418 and 0.0703 inch respectively. The locations of these three planes are shown for Figure 6.7 as three streamwise grid lines. The disturbance contours are shown in one cycle in the spanwise direction. The contours demonstrate that in all three normal planes, disturbances retain purely harmonic variation in the spanwise direction in all the flow regions. Because these three normal planes pass through the separation bubble and the disturbances are very small in the separation bubble, the contour distributions in these three planes show some blank areas in the separation regions.

Figure 6.16 shows the contour of the normal maximal density disturbance in the X-Z plane which passes through the critical layer across the compression corner. The contour is shown for one cycle in the spanwise direction. It is observed that the normal maximal density disturbance also retains a purely harmonic variation in the spanwise direction and changes sign alternatively in the streamwise direction. No nonlinear influences can be observed from the normal maximal density disturbance contour in all the flow regions.

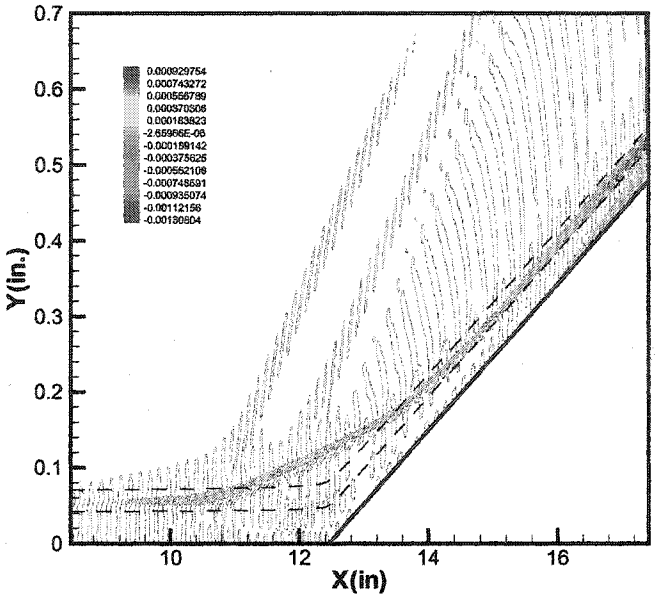

Figure 6.7 Density disturbance contours at the plane $Z=2\lambda_z/15$.

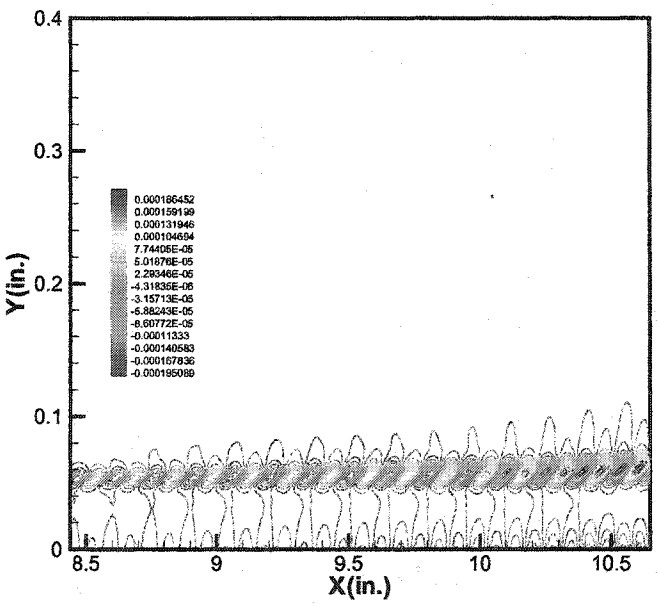

Figure 6.8 Expanded density disturbance contours at the plane $Z=2\lambda_z/15$.

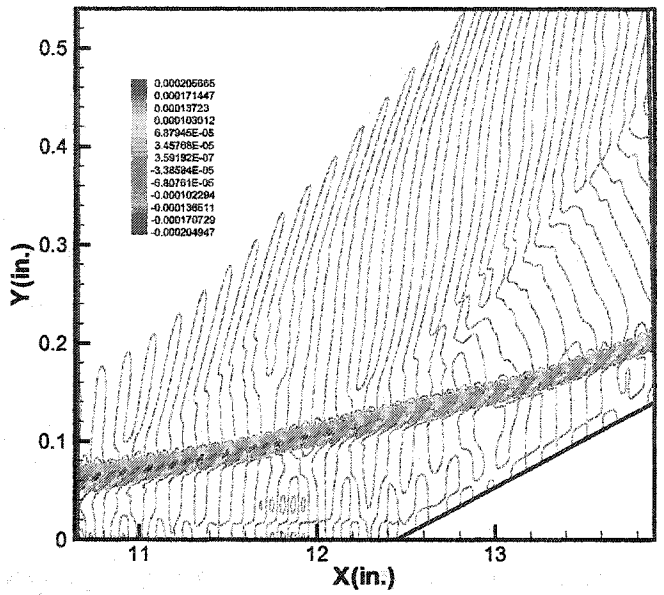

Figure 6.9 Expanded density disturbance contours at the plane $Z=2\lambda_z/15$.

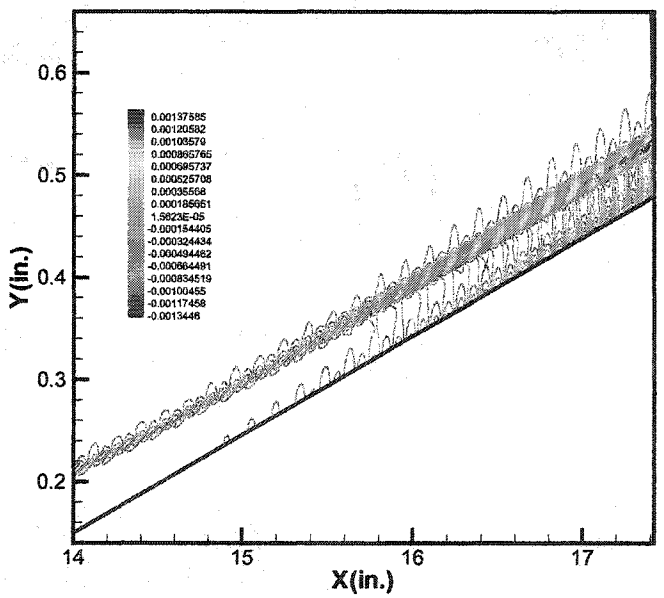

Figure 6.10 Expanded density disturbance contours at the plane $Z=2\lambda_z/15$.

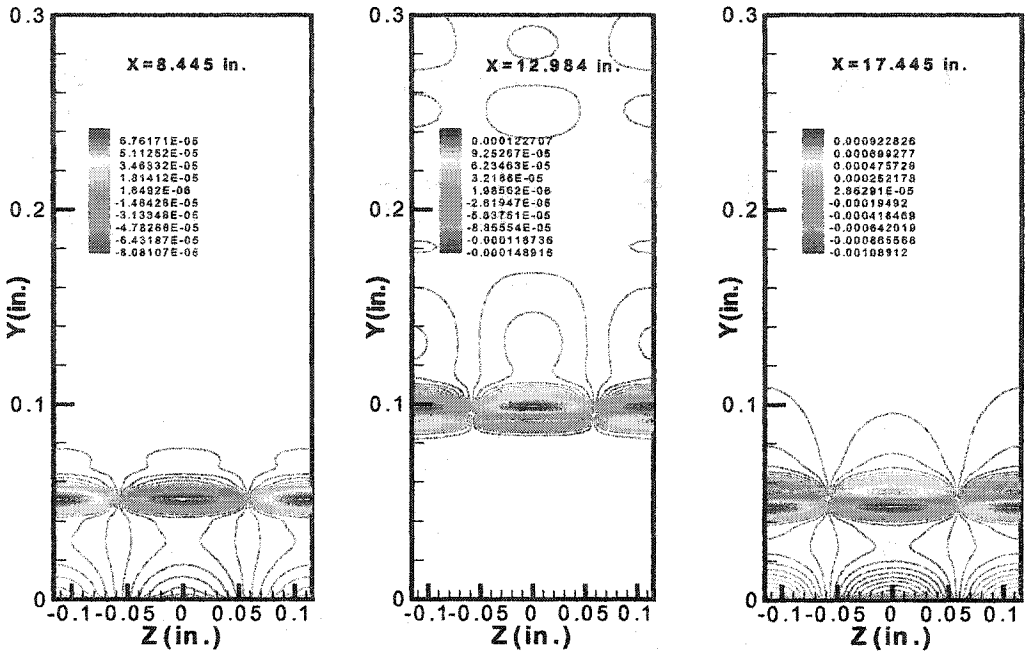

Figure 6.11 Density disturbance contours in the Y-Z plane.

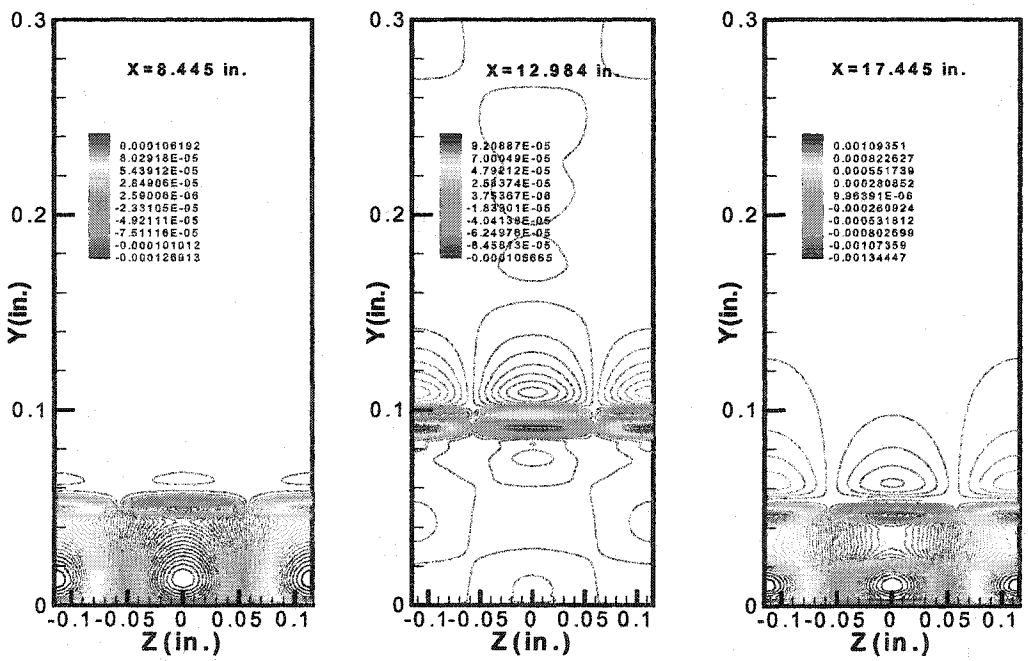

Figure 6.12 Streamwise velocity disturbance contours in the Y-Z plane.

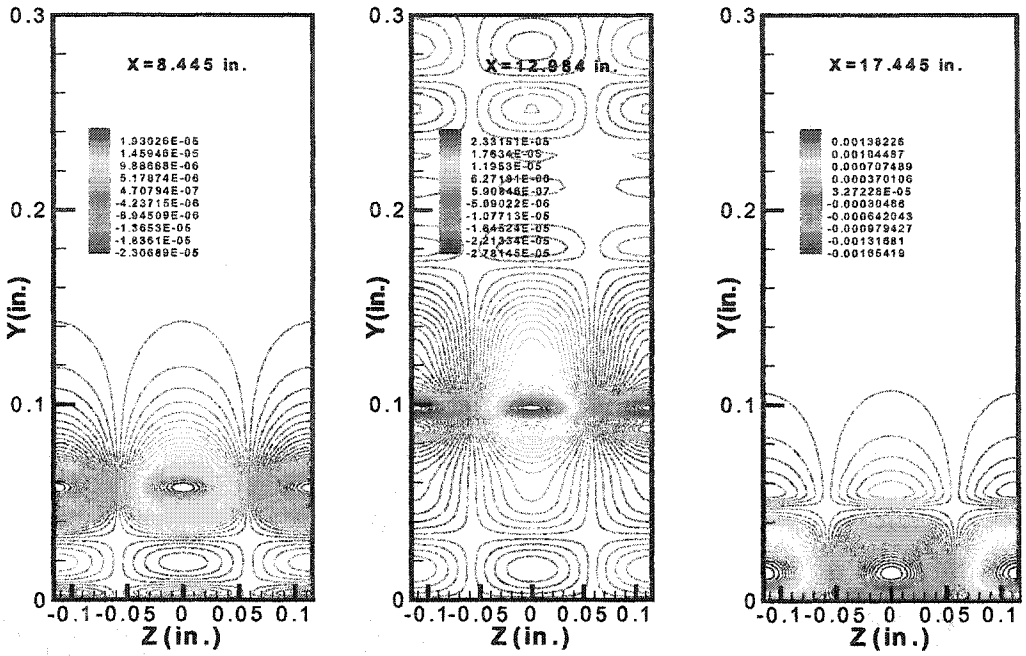

Figure 6.13 Normal velocity disturbance contours in Y-Z plane.

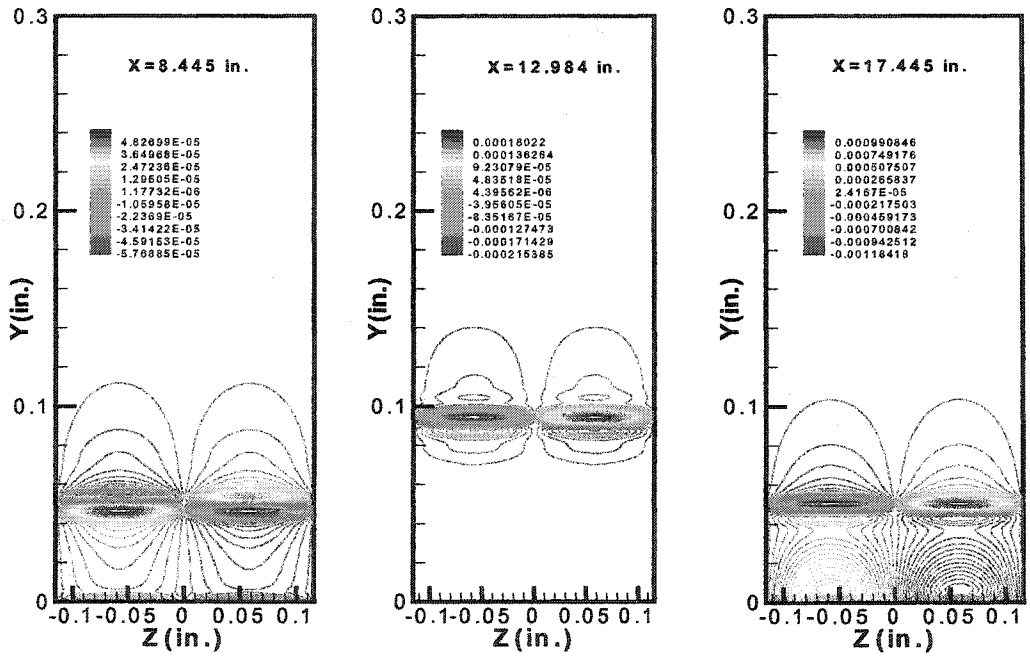

Figure 6.14 Spanwise velocity disturbance contours in Y-Z plane.

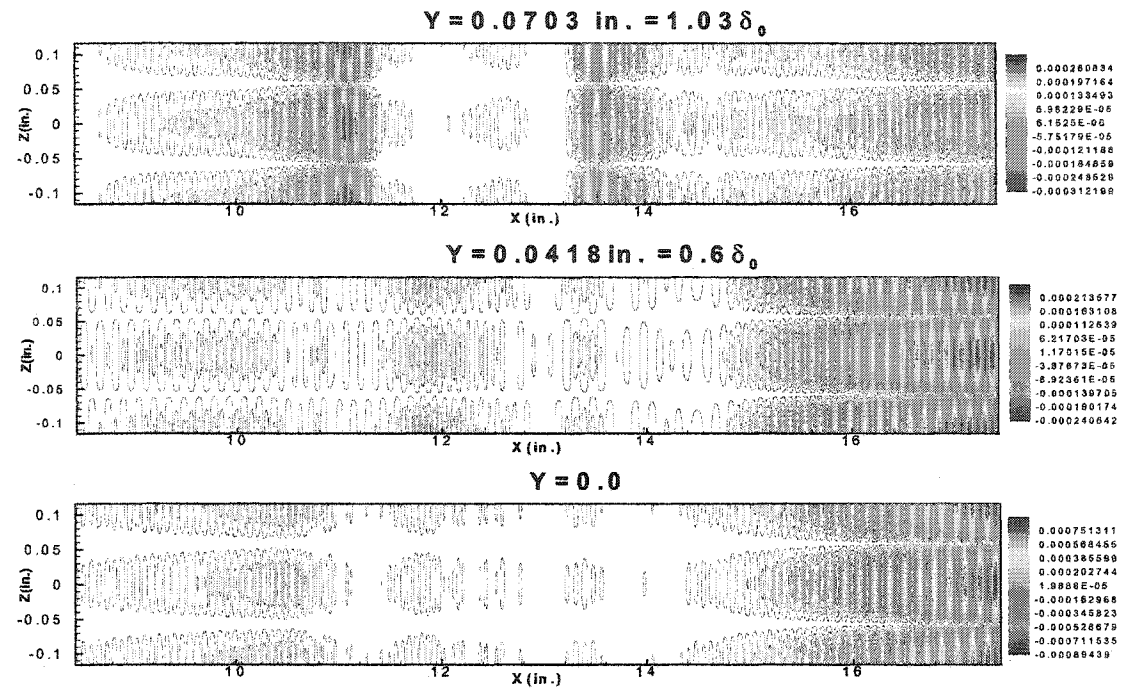

Figure 6.15 Density disturbance contours in the X-Z plane at different heights.

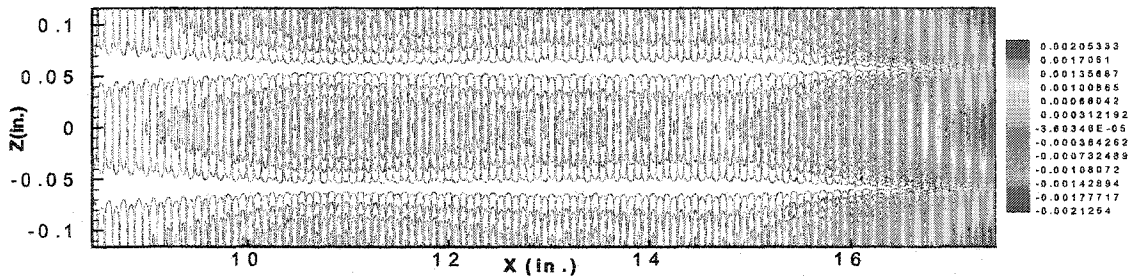

Figure 6.16 Normal maximal density disturbance contours.

Figure 6.17 and Figure 6.18 show the normal maximal density disturbance amplitude distributions in the streamwise direction at two different spanwise sections Z=0.0 and 0.108 inch respectively. It is shown from these two figures that the oblique second mode disturbances keep growing exponentially upstream and downstream of the separation bubble just like the performance of the two-dimensional disturbance in these two regions. Conversely, the oblique disturbance shows a weak decaying tendency in the separation region, and compared with the two dimensional disturbances, the oblique disturbances are much less amplified across the compression corner. The normal maximal density

disturbance at frequency $F_0=0.85\times10^{-4}$ is only amplified about 20 times at the end of the computation domain, whereas the two-dimensional disturbance at the same frequency was amplified almost 400 times. This result agrees well with Mack's conclusion that for supersonic flow, the second mode disturbance is most amplified when it remains two-dimensional. In addition, we also note that the normal maximal density disturbance is symmetric for positive and negative values. This demonstrates that no nonlinear interactions exist across the whole flow region of the compression corner. Figure 6.19 and Figure 6.20 show the density disturbance distributions in the streamwise direction at the wall for two different spanwise planes, Z=0.0 and $7\lambda_z/30$, respectively. It is observed that the disturbance is very small in the separation region. We can also see that for linear evolution of the three-dimensional disturbance, at the different spanwise planes, the disturbance distributions in the streamwise direction have the same shape at the same normal location and only differ in magnitudes.

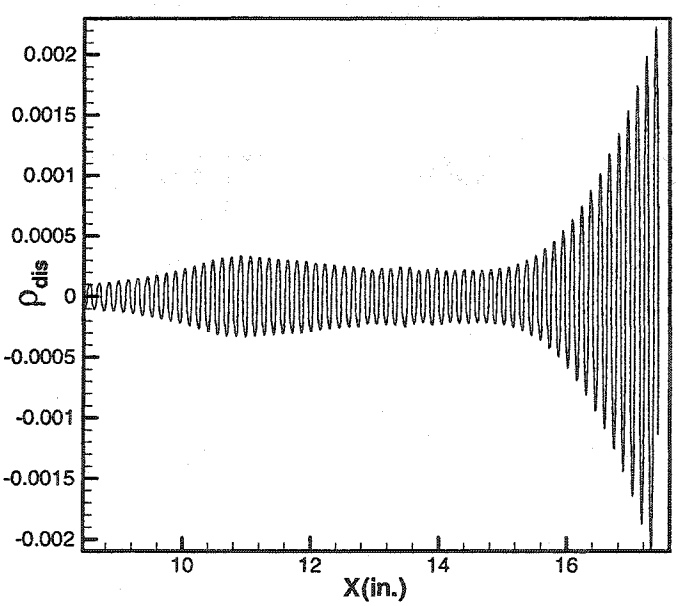

Figure 6.17 Normal maximal density disturbance distribution in the plane Z=0.0.

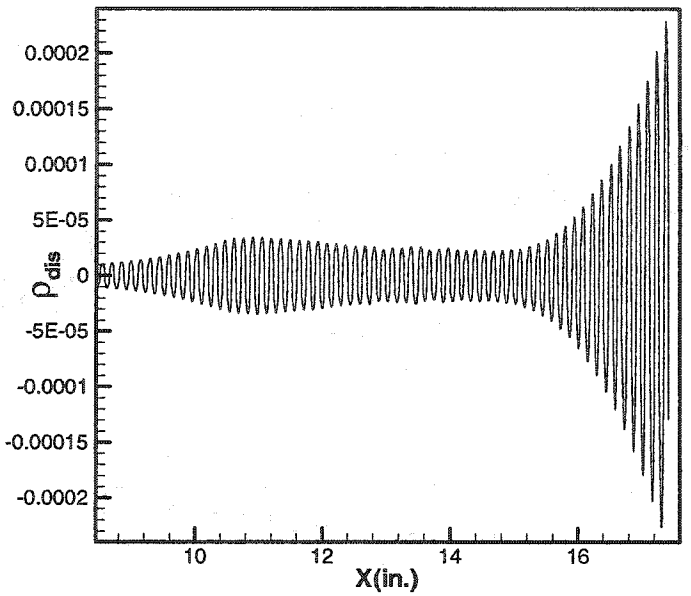

Figure 6.18 Normal maximal density disturbance distribution in the plane $Z=7\lambda_z/30$.

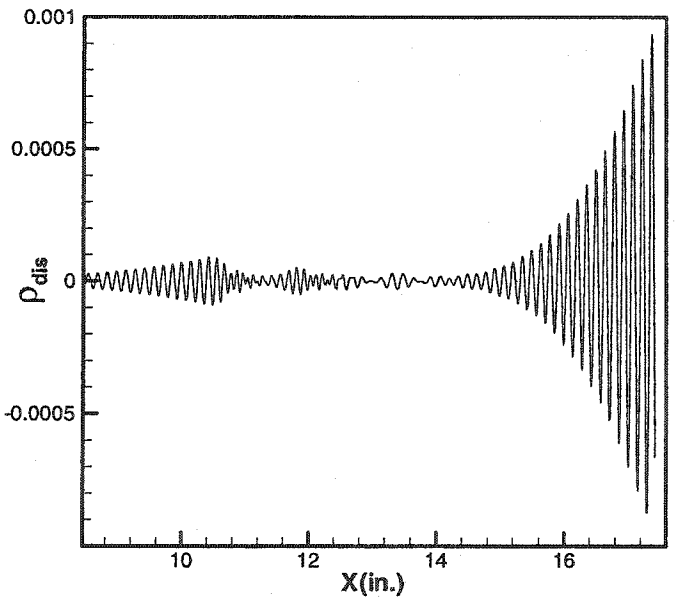

Figure 6.19 Density disturbance distribution at the wall in the plane Z=0.0.

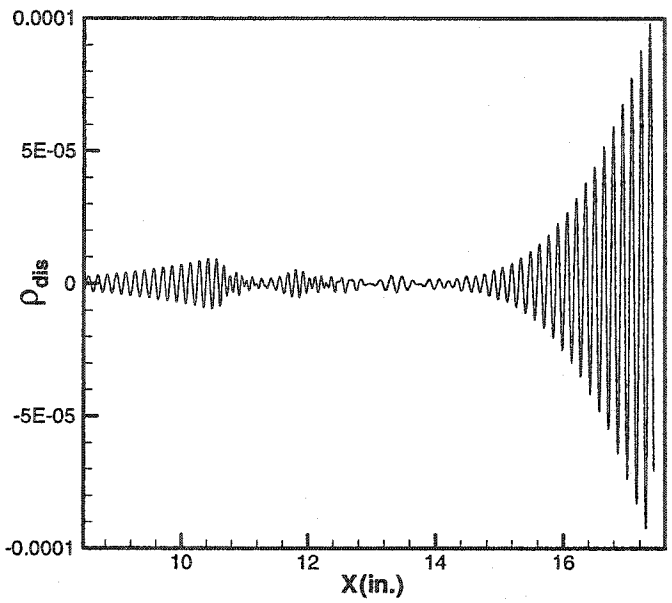

Figure 6.20 Density disturbance distribution at the wall in the plane $Z=7\lambda_z/30$.

Figures 6.21-6.22 show the normal distributions of density disturbance at four different streamwise locations in the spanwise planes Z=0.0 and $Z=7\lambda_z/30$ inch respectively. As we know from the linear computation of the three-dimensional disturbance evolutions, this disturbance frequency still resides in the second mode unstable region upstream and downstream of the separation region, so it is observed that at the location X=8.840 inches and X=16.955 inches, the normal distributions show the second mode characteristics with two peaks, one in the critical layer and another close to the wall. In the separation region, additional peaks appear in the separation bubble due to the existence of the third or higher acoustic modes in this region. In addition, we also noticed that in the different spanwise planes, the normal distributions of the disturbance possess the same shape at the same streamwise location and only differ in their magnitude. This is one of the characteristics of the linear evolution of the three-dimensional disturbance. Figure 6.23 and Figure 6.24 show the spanwise variations of the density disturbance on the wall and in the normal plane Y=0.0418 inch at different streamwise locations. It is seen that at all streamwise locations, the spanwise distributions of the

density disturbance always retain the fundamental pure harmonic forms. This demonstrates again that the disturbance evolutions are linear in all flow regions across the compression corner. The nonlinear interactions are very small and can be neglected.

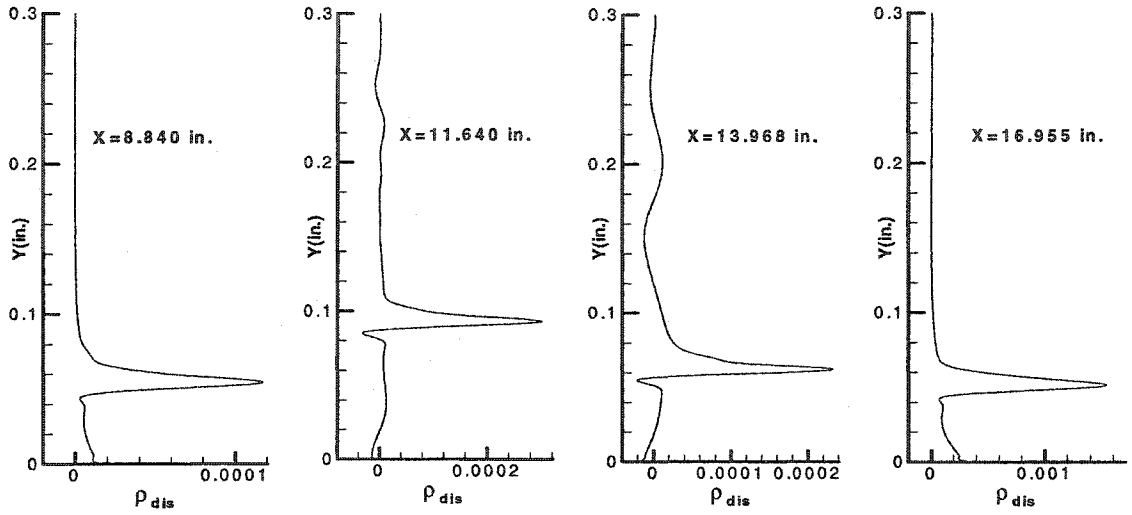

Figure 6.21 Normal distributions of density disturbance in plane Z=0.0.

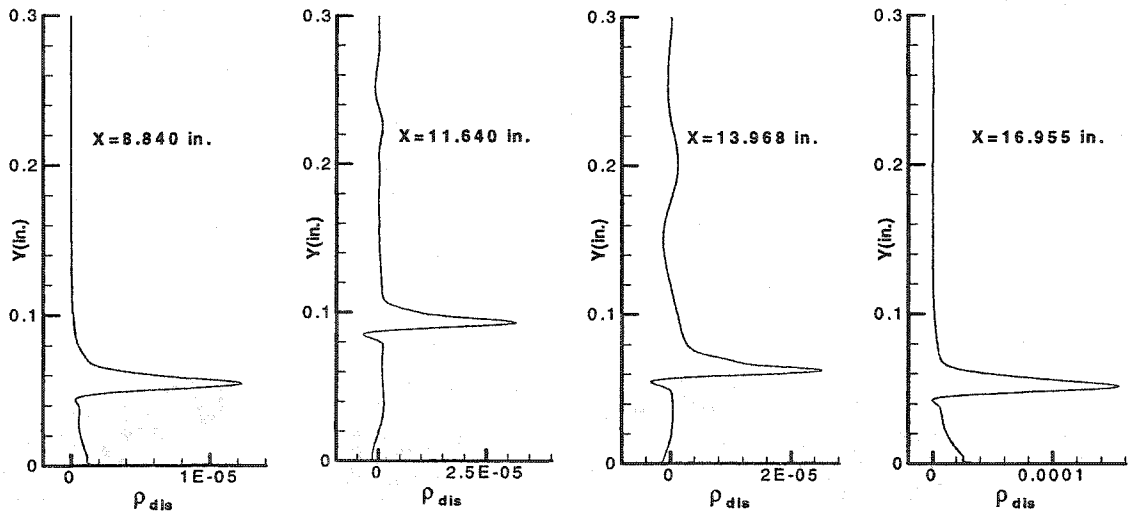

Figure 6.22 Normal distributions of density disturbance in plane Z=7λ_z/30.

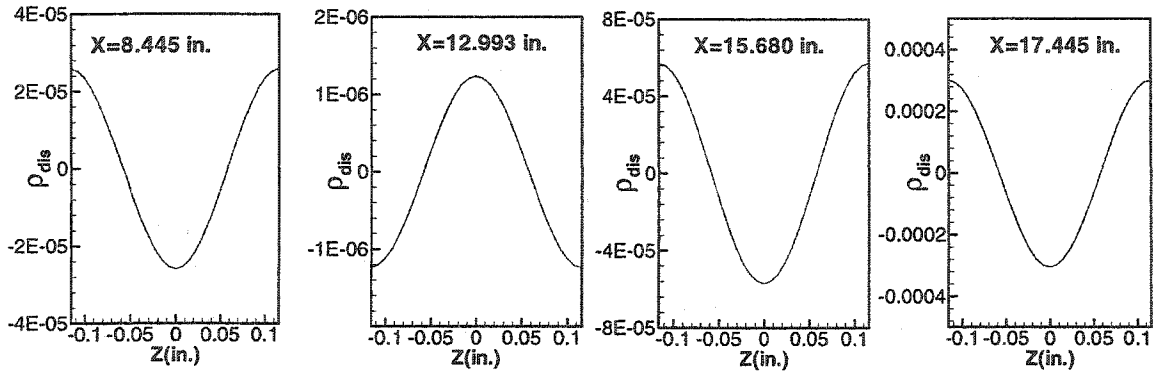

Figure 6.23 Spanwise distribution of the density disturbance at the wall.

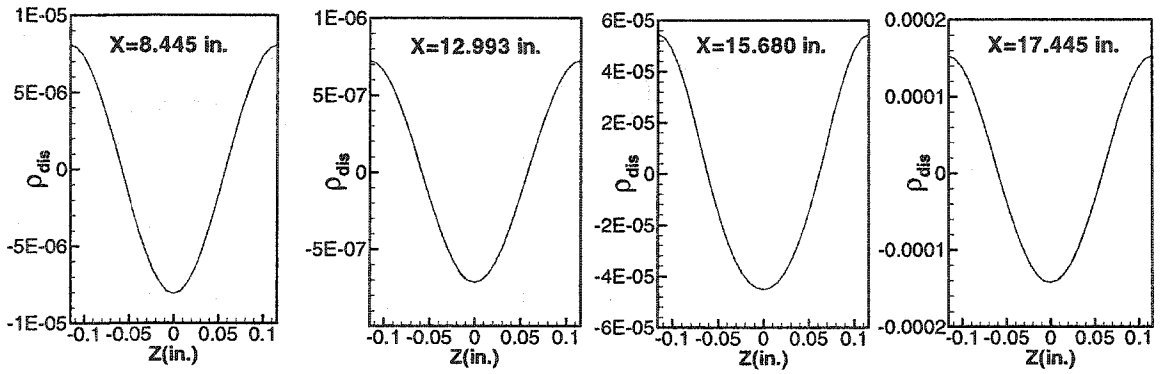

Figure 6.24 Spanwise distribution of the density disturbance in the plane Y=0.0418 inch.

6.5 The nonlinear evolutions of the three-dimensional mono-frequency disturbances across the compression corner

In the simulation of the nonlinear evolution of the three-dimensional mono-frequency disturbance across the compression corner, three computational cases will be investigated. The first two cases will study the oblique breakdown process at different spanwise wave number without the presence of the two-dimensional primary disturbance. The third case will study the secondary instability breakdown process with the presence of the two-dimensional primary disturbance.

Case 1: $F_0=0.85\times10^{-4}$, $\beta=0.1$, $\varepsilon=0.01$

In this case, with the initial disturbance amplitude $\varepsilon=0.01$, the nonlinear interactions will be observed across the compression corner. Figure 6.25 shows the density

disturbance contours in the X-Y plane at the spanwise location Z=0.0. Figure 6.26 shows the density disturbance contours in the X-Y plane at the spanwise location $Z=7\lambda_z/30$. It is observed that unlike the three-dimensional linear disturbance evolution, the three-dimensional nonlinear disturbance evolution exhibits different contour distributions in the X-Y planes at the different spanwise locations due to the nonlinear interactions. The nonlinear interactions begin to appear in the separation region.

Figures 6.27-6.30 show the disturbance contours in the Y-Z plane for density, streamwise velocity, normal velocity, and spanwise velocity at three different streamwise locations X=8.445, 12.984 and 16.545 inches respectively. These three locations are upstream, inside and downstream of the separation region respectively. The contours are shown for one cycle in the spanwise direction. Upstream of separation, the primary disturbance amplitudes are still small and nonlinear interactions can be neglected, so the disturbance contours show the pure fundamental harmonic patterns in the spanwise direction. In the separation region, weak nonlinear interactions begin to appear. Compared with the contours at X=8.445, the contours at X=12.984 show some distortion from the pure harmonic contour patterns which are formed only by the primary disturbances. The maximal contour distortion occurs in the critical layer. Downstream of the separation region, the nonlinear interaction becomes stronger and stronger. With more and more harmonic disturbances added into the primary disturbance, the contours show much more complicated patterns. We can also see that the maximal disturbances evolve closer to the wall downstream of the separation region.

Figure 6.31 shows the streamwise vortex distributions in the X-Z plane at three different normal locations Y=0.0, Y=0.0476 and Y=0.0740 inches respectively. The locations of these three planes are shown in Figure 6.25 as three streamwise grid lines. The contours show the streamwise vortex distributions in one periodic cycle in the spanwise direction. It is observed that at the wall Y=0.0 the nonlinear influence is very small, and the streamwise vortex contours always retain the fundamental pure harmonic pattern in the

spanwise direction for all flow regions. But at the normal plane Y=0.0476 inches, which is close to the critical layer, nonlinear influences become significant. The nonlinear interactions begin to appear in the separation region and become stronger and stronger with the disturbances evolving downstream of the separation region. With more harmonics appeared, the streamwise vortex contours downstream of the separation region begin to deform and show a very different pattern from the pure harmonic disturbance. The steady longitudinal vortex pattern has appeared and becomes more apparent when it evolves downstream. At the plane Y=0.074 inch, which is close to the boundary-layer edge, the nonlinear interaction becomes weak again. The streamwise vortex contours begin to recover to the pure harmonic pattern downstream of the separation region. Because this plane goes through the separation bubble, we can still see some nonlinear influence in critical layer of the separation region.

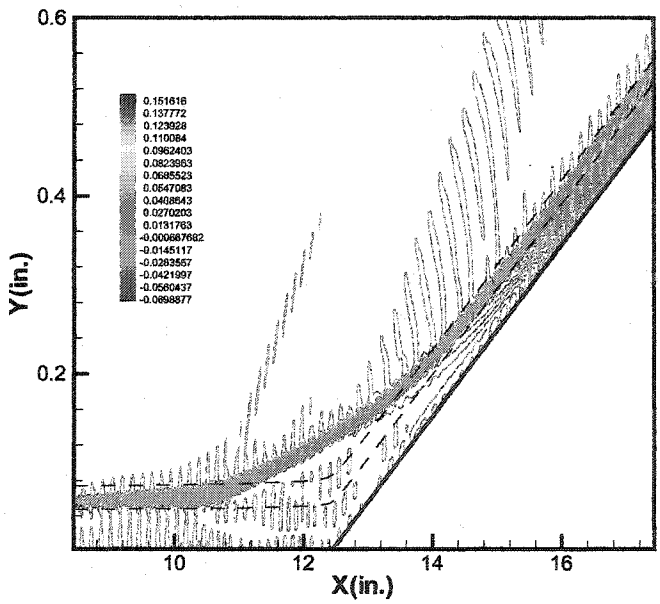

Figure 6.25 Density disturbance contour in plane Z=0.0.

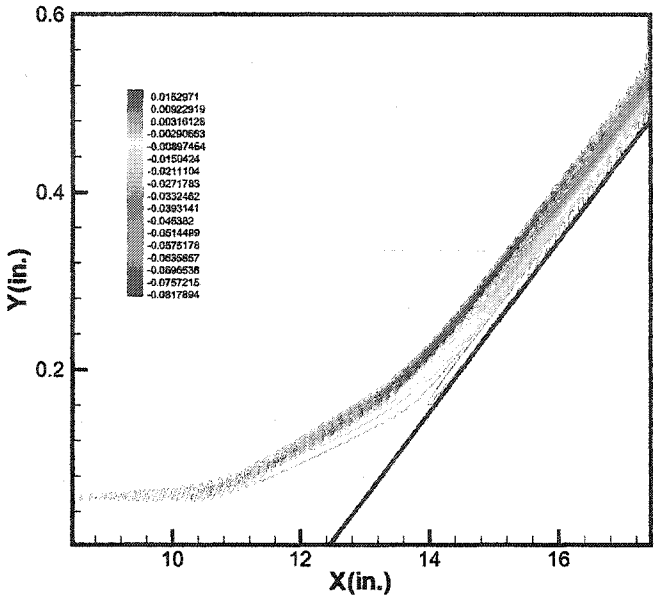

Figure 6.26 Density disturbance contour in the plane $Z=7\lambda_z/30$.

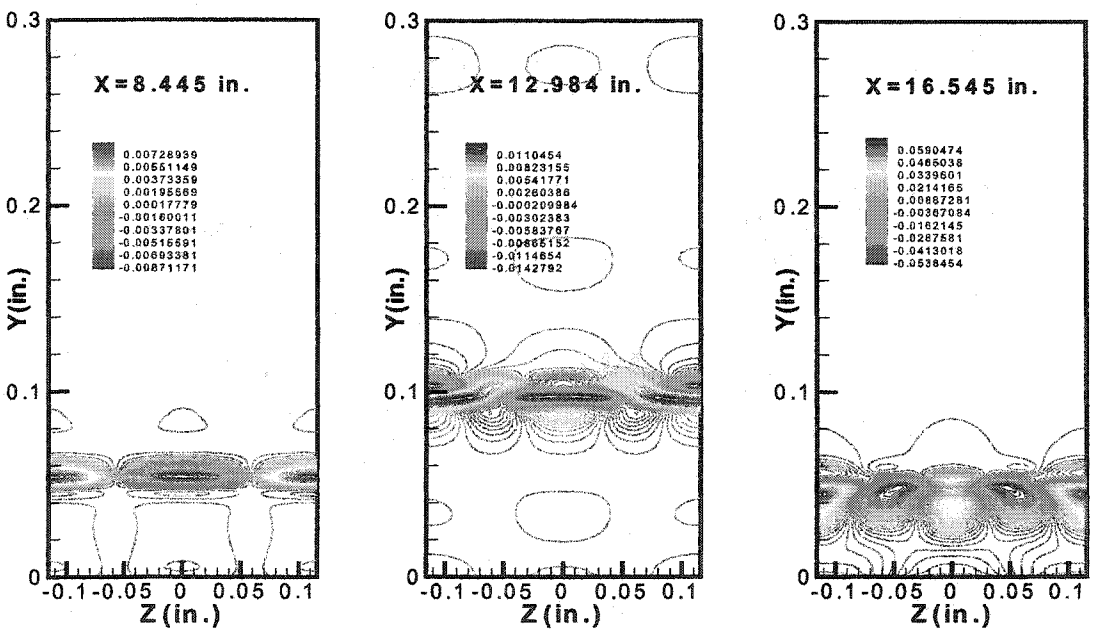

Figure 6.27 Density disturbance contour in the Y-Z plane.

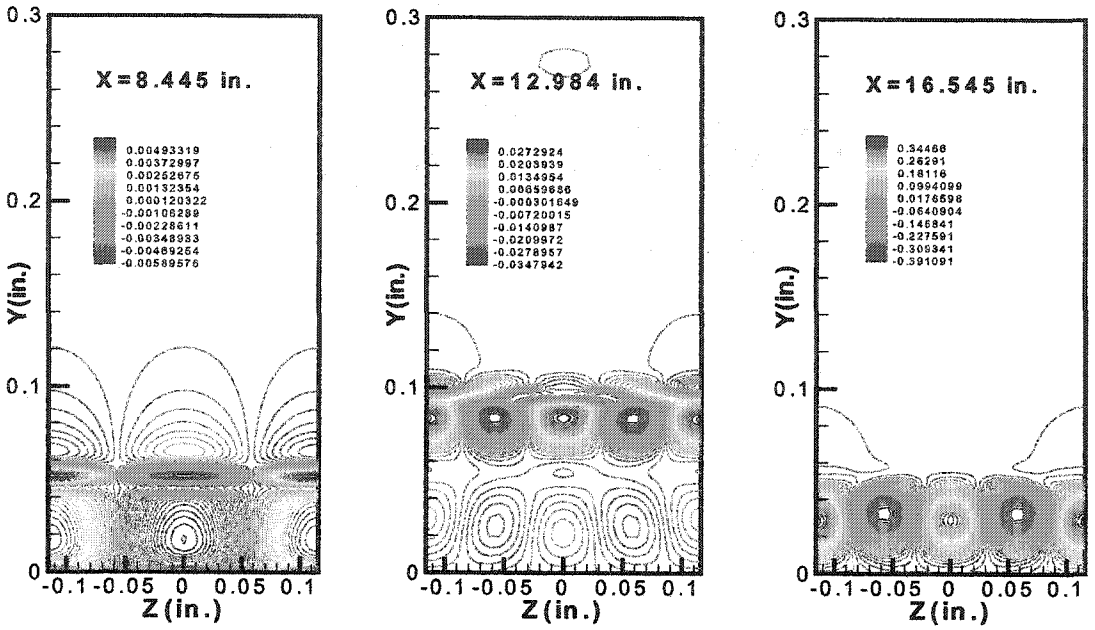

Figure 6.28 Streamwise velocity disturbance contour in the Y-Z plane.

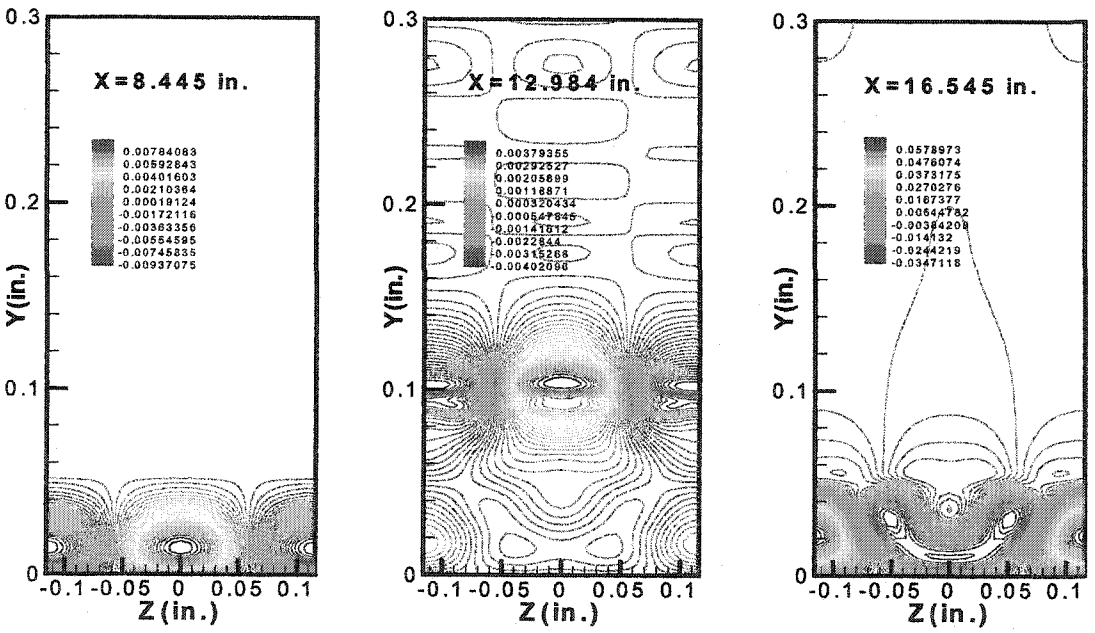

Figure 6.29 Normal velocity disturbance contour in the Y-Z plane.

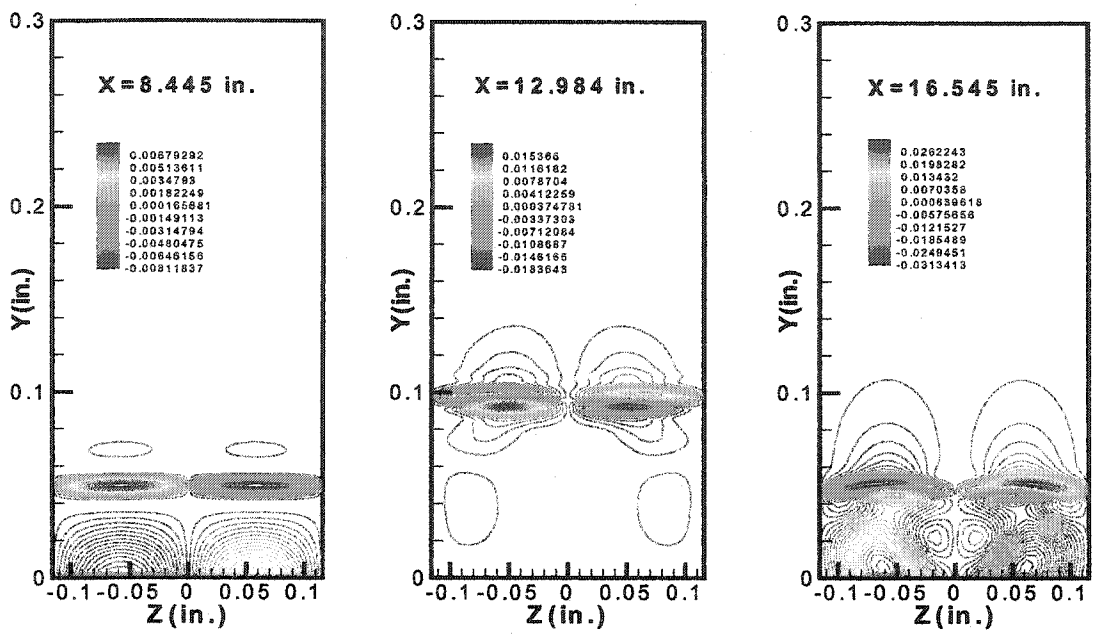

Figure 6.30 Spanwise velocity disturbance contour in the Y-Z plane.

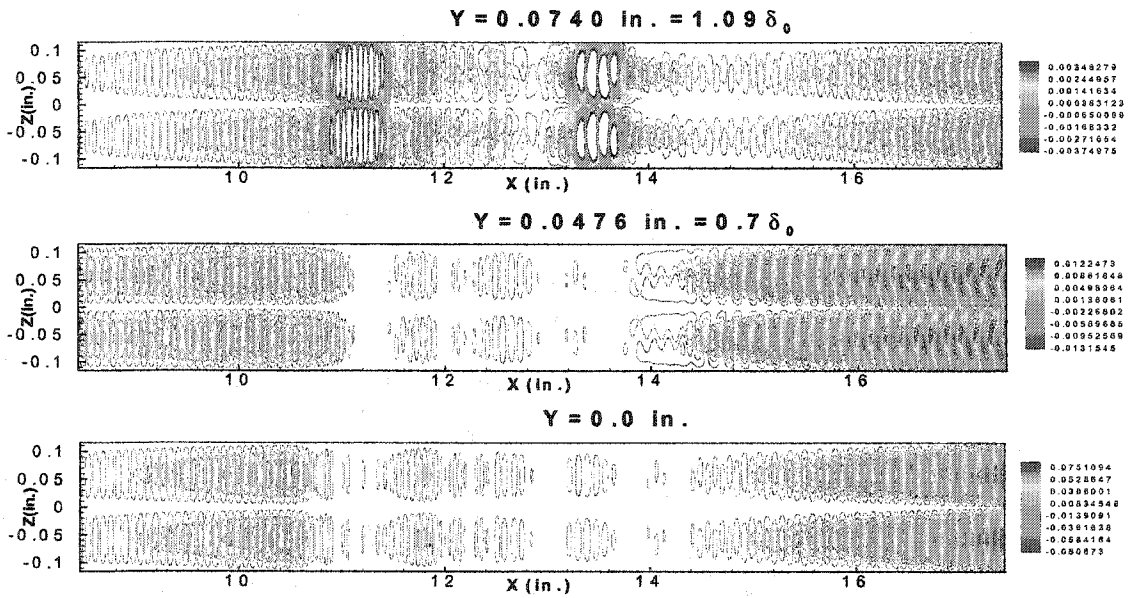

Figure 6.31 Streamwise vortex distributions in the X-Z plane.

Figures 6.32-6.37 show the density disturbance variations along the streamwise direction at three normal locations Y=0.0, 0.0476, 0.074 inch in two spanwise planes Z=0.0, $7\lambda_z/30$ respectively. The plane Z=0.0 corresponds to the maximal value of the primary disturbance amplitude and the plane $Z=7\lambda_z/30$ corresponds to the minimal value

of the primary disturbance amplitude. Figure 6.32 and Figure 6.33 show the density disturbance variations along the wall in these two spanwise planes respectively. It can be seen that the disturbance amplitudes are symmetric for both negative and positive disturbances in both planes. This demonstrates that the nonlinear influences are weak at the wall. Figure 6.34 and Figure 6.35 show the density disturbance variations along the streamwise direction in the critical layer in these two spanwise planes respectively. At this normal location, the nonlinear interactions are very strong, so the density disturbances in downstream of the separation region show significant deviation from the primary disturbance. In the plane Z=0.0, the primary disturbance still dominates over all other harmonic disturbances, but in the plane $Z=7\lambda_z/30$, the higher harmonic disturbance has become dominant. We will show this dominant harmonic disturbance more clearly by discrete Fourier transformation(DFT) later. Figure 6.36 and Figure 6.37 show the density disturbance variations close to the boundary-layer edge. The nonlinear interaction is weak again at this normal location, so the disturbances in both spanwise planes again show the symmetric characteristics upstream and downstream of the separation region.

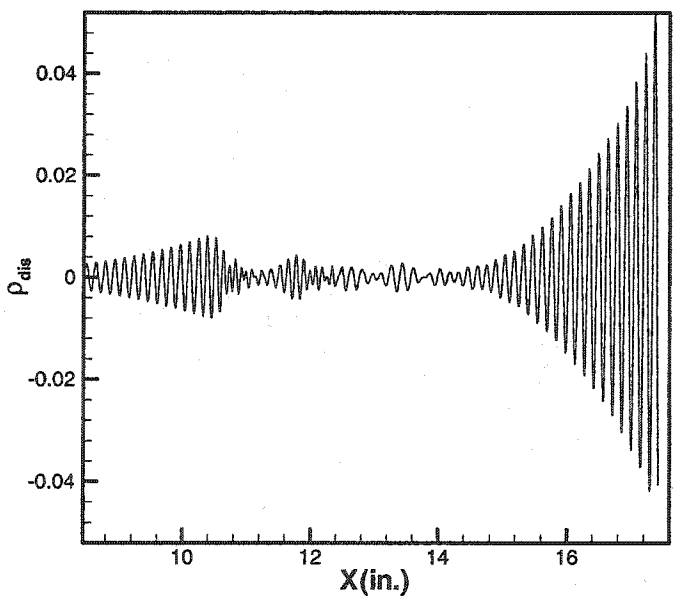

Figure 6.32 Density disturbance distribution at Y=0.0, Z=0.0.

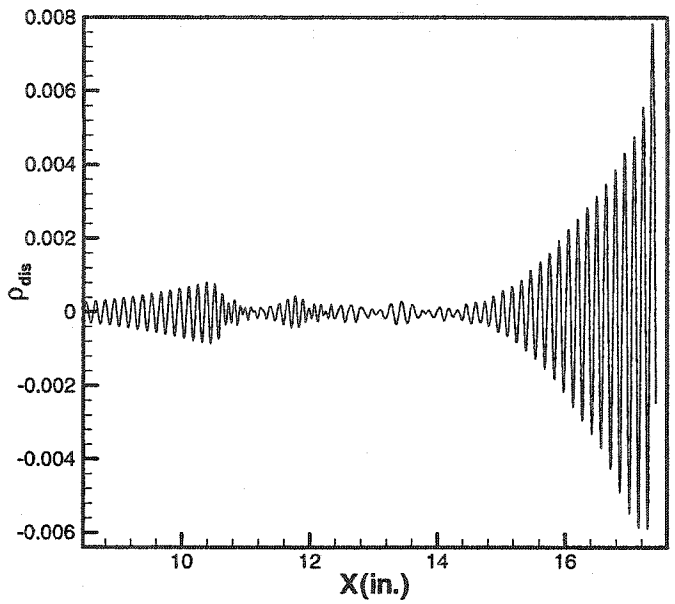

Figure 6.33 Density disturbance distribution at Y=0.0, Z=7λ_z/30.

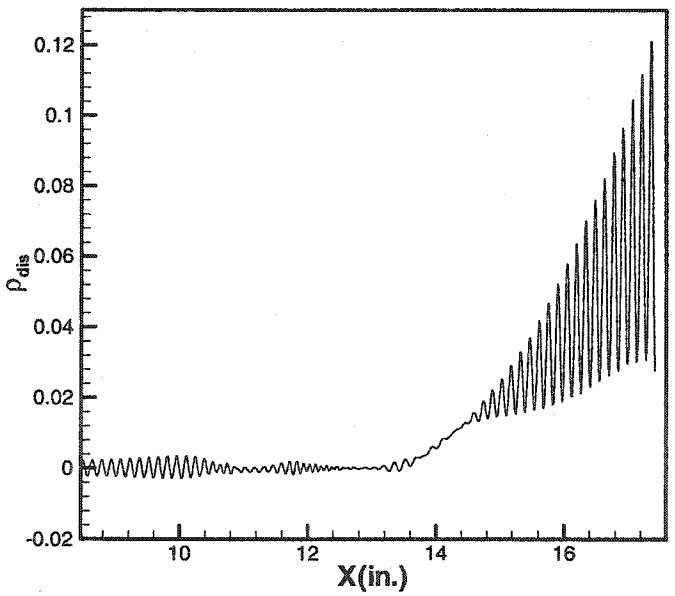

Figure 6.34 Density disturbance distribution at Y=0.0476, Z=0.0.

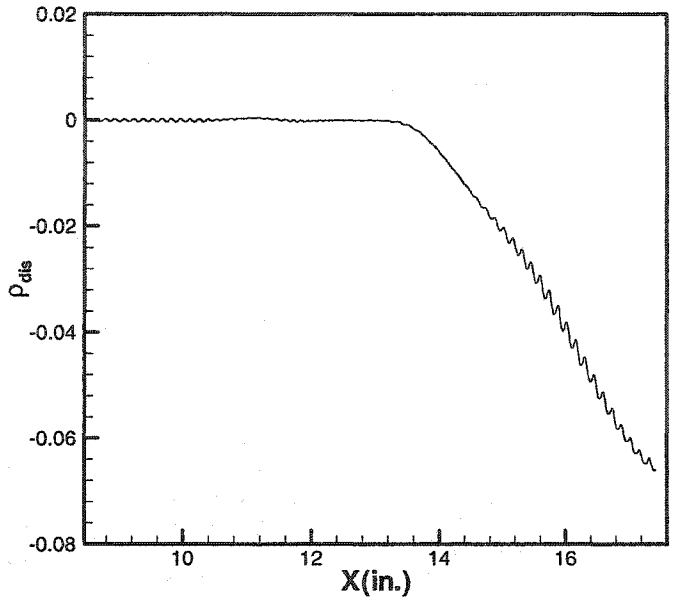

Figure 6.35 Density disturbance distribution at Y=0.0476, Z=7λ_z/30.

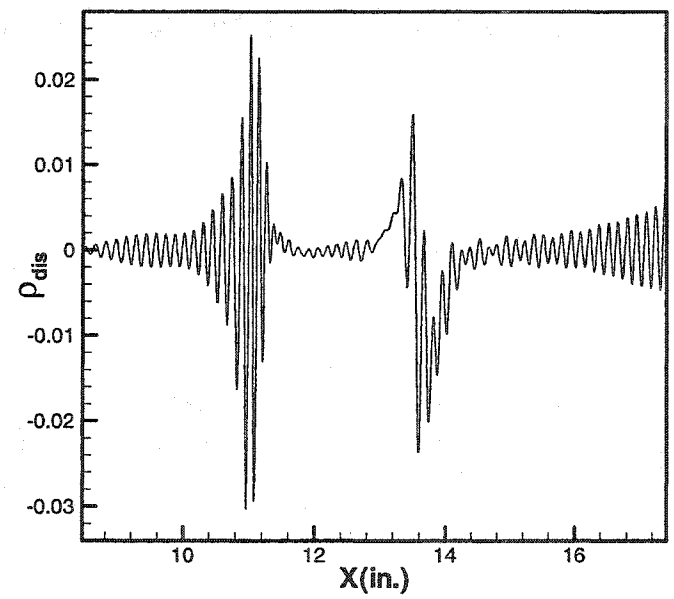

Figure 6.36 Density disturbance distribution at Y=0.074, Z=0.0.

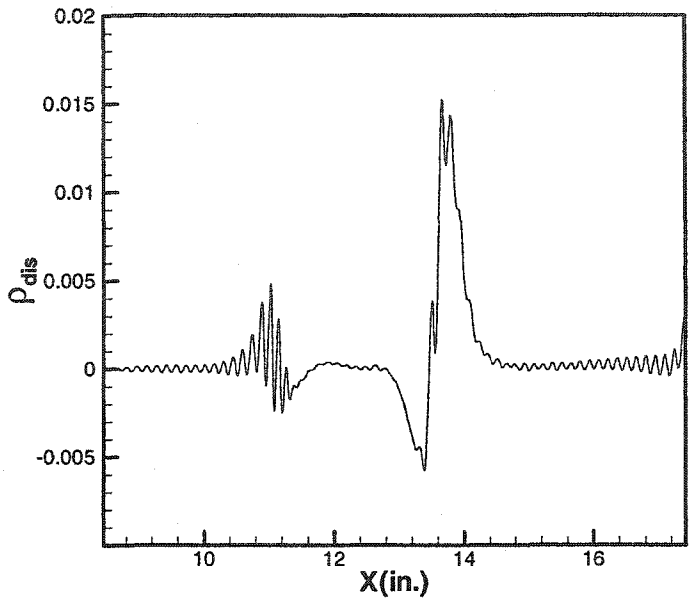

Figure 6.37 Density disturbance distribution at Y=0.074, Z=7λ_z/30.

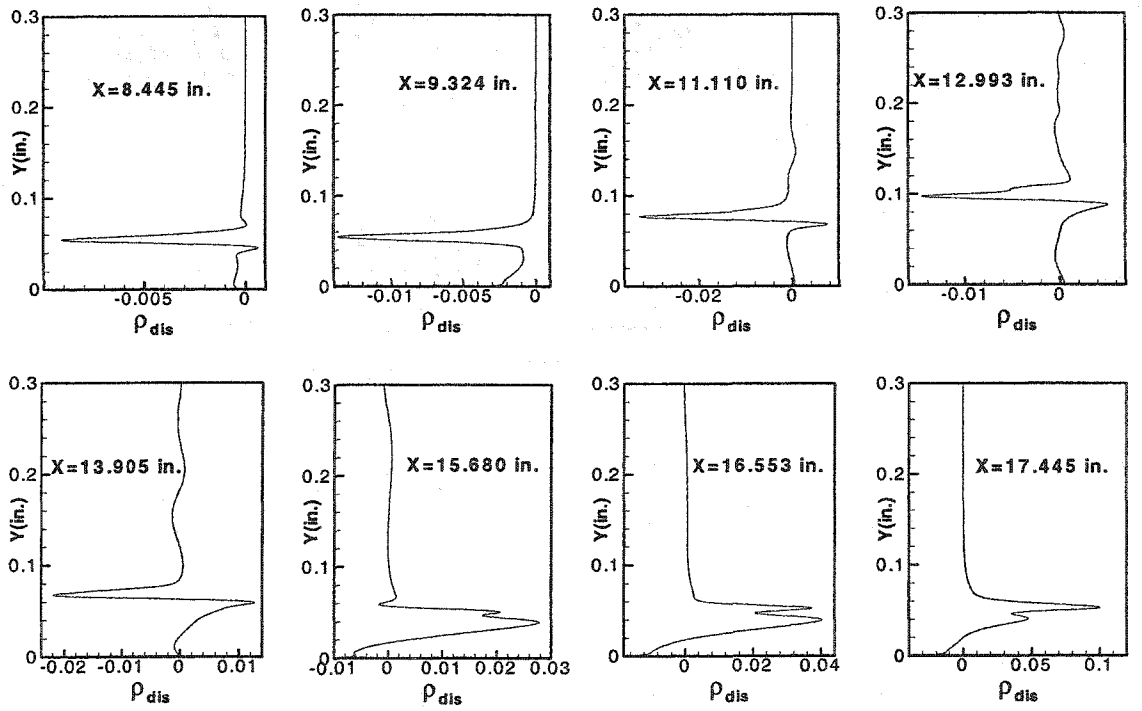

Figure 6.38 Normal distributions of the density disturbance at Z=0.0.

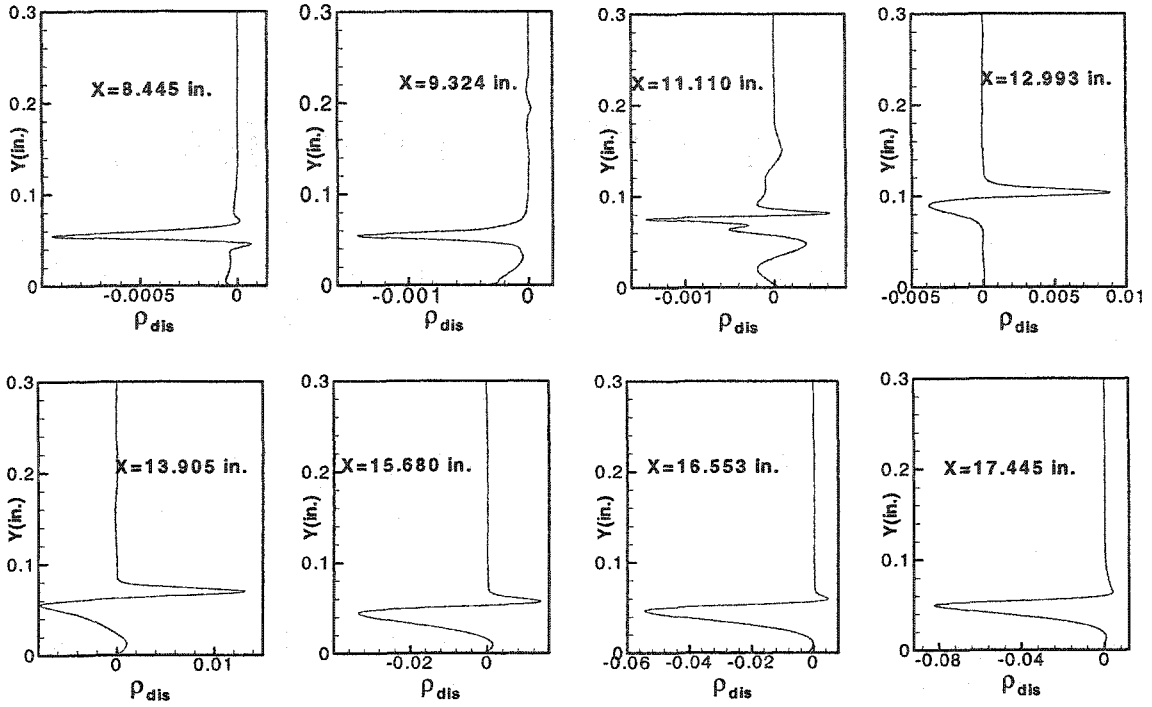

Figure 6.39 Normal distributions of the density disturbance at $Z=7\lambda_z/30$.

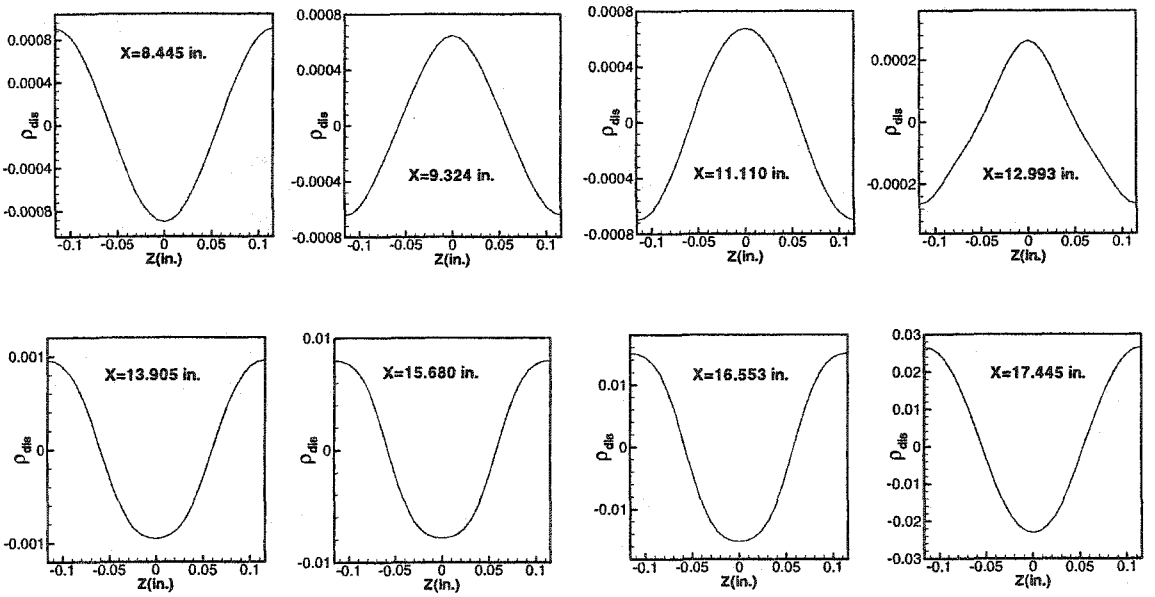

Figure 6.40 Spanwise distributions of the density disturbance at the wall.

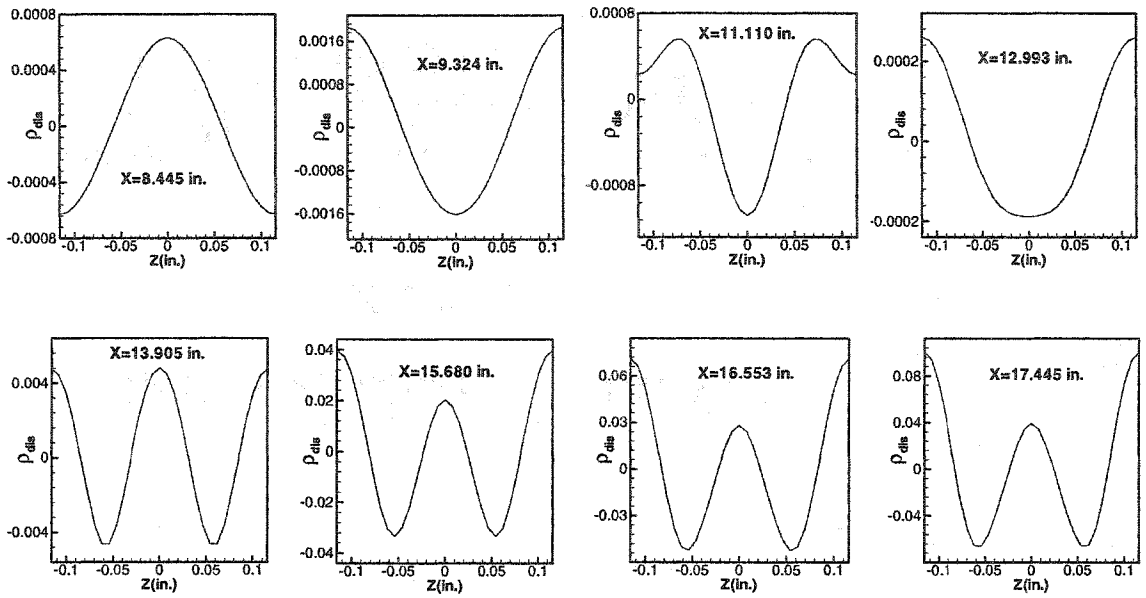

Figure 6.41 Spanwise distributions of the density disturbance at Y=0.0476.

Figure 6.38 and Figure 6.39 show the normal distributions of the density disturbance at different streamwise locations in spanwise planes Z=0.0 and Z=7λ_z/30 respectively. It is observed that the shapes of the normal disturbances in both planes are the same at the same streamwise locations upstream of the separation region. However, they show large differences in the separation region and downstream of the separation region due to nonlinear interactions. At plane Z=0.0, we can clearly see the appearance of the higher harmonic downstream of the separation region and it grows to an amplitude which is large enough to be comparable to the primary disturbance amplitude at the end of the downstream region. In the plane Z=7λ_z/30, the primary disturbance amplitude is very small. We can see the primary mode dominates at X=8.445 inches and X=12.993 inches. But with the disturbance evolving further downstream, the higher harmonic mode becomes dominant. This can be seen clearly at the locations X=15.680 inches and X=17.445 inches. Figure 6.40 and Figure 6.41 show the spanwise variation of the density disturbance at different streamwise location in two normal planes Y=0.0 and Y=0.0476 inch respectively. It is observed again that the disturbances always retain the fundamental pure harmonic in the spanwise direction at the wall and change their spanwise shapes in

the critical layer. This again demonstrates that the nonlinear interaction appears mainly in critical layer.

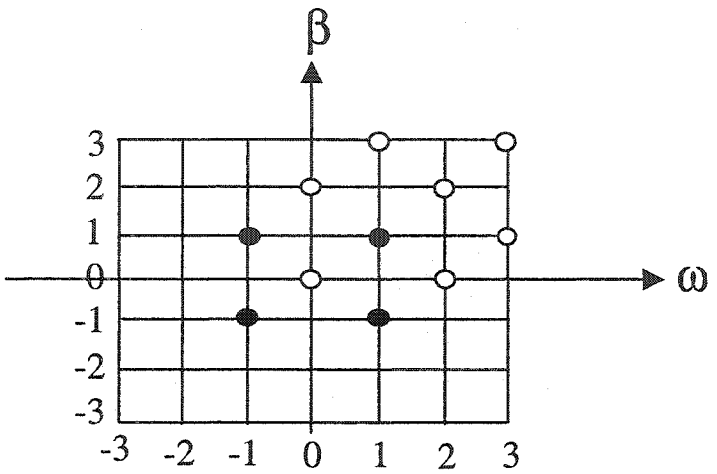

Figure 6.42 The illustration of the harmonic mode distribution.

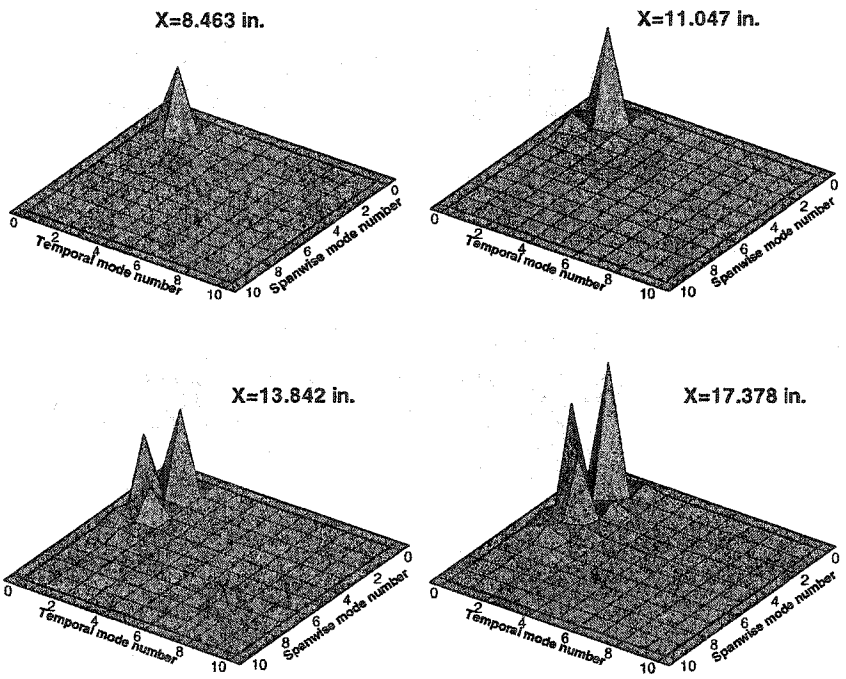

Figure 6.43 The spectral distributions of the disturbances at different streamwise locations.

In order to show which harmonics have appeared during the nonlinear interactions, we take the data in one cycle of both time and in the spanwise direction and perform a two-dimensional DFT given in equation (6.4) to decompose the total disturbance into harmonic modes ($m\omega$, $n\beta$), where m, n stand for the mode number for frequency and spanwise wave number respectively.

$$X(m,n)=\frac{4}{M_0\cdot N_0}\sum_{m_0=1}^{M_0}\sum_{n_0=1}^{N_0}x(m_0,n_0)\exp[-2i\pi(m-1)(m_0-1)/M_0] \cdot\exp[-2i\pi(n-1)(n_0-1)/N_0]\quad 1\le m\le M_0, 1\le n\le N_0 \tag{6.4}$$

Figure 6.42 illustrates all harmonic mode distribution in (ω, β) plane. Where the four solid black dots stand for the initial fundamental harmonic mode (1,1) and its complex conjugates, and all circles stand for the super-harmonics which will be produced by the nonlinear interactions. It is observed that with the initial harmonic mode (1,1) and its complex conjugates, only an isolate harmonic mode distribution can be obtained by the nonlinear interactions.

Figure 6.43 shows the Fourier mode distributions of density disturbances at different streamwise locations. Each mode is shown in its maximal amplitude in normal direction. It can be seen that at X=8.643, nonlinear influences are very small, so only the primary mode (1,1) is present at this location. At X=11.047, which is located at the beginning of the separation region, the nonlinear interactions begin to appear at this location, and the super-harmonics begin to appear. At the location X=13.842, which is close to the end of the separation region, the nonlinear interactions become strong and more harmonics appear, and at the location X=17.378, which is located downstream of the separation region, the nonlinear interactions become even stronger and other harmonics such as the (0,2) and (1,3) modes have reached amplitudes which are large enough to be comparable to that of the primary disturbance.

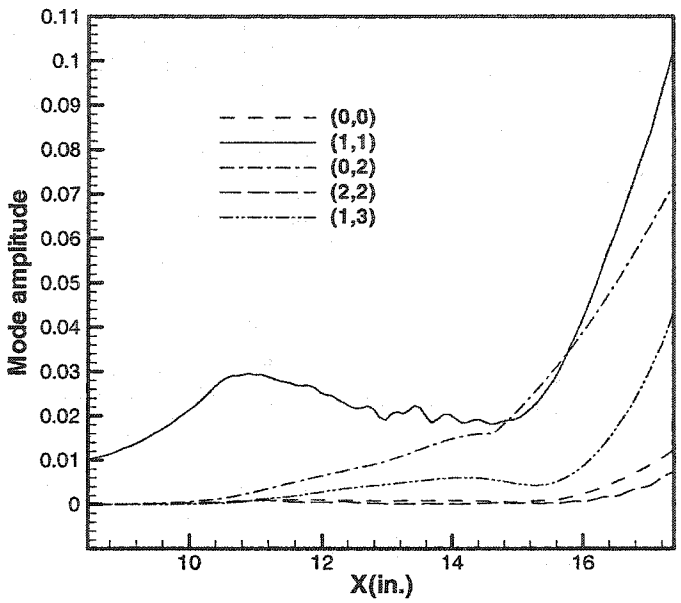

Figure 6.44 Streamwise amplitude distributions for different Fourier modes.

Figure 6.44 shows the maximal amplitude distributions in the streamwise direction for those Fourier modes whose amplitudes can exceed 0.001. It can be seen that the primary mode (1,1) dominates in most parts of the streamwise region. Among all super-harmonic modes produced by nonlinear interactions, the mode (0,2) shows a very distinct characteristic. It grows in the separation region and reaches a very large amplitude in both the separation region and downstream of the separation region. It even surpasses the primary mode in the region close to the reattachment point. This mode is believed to be responsible for the oblique breakdown.

Figures 6.45 and 6.46 show the density disturbance contours of the (1,1) and (0,2) modes in the Y-Z plane at the X=17.378 inches streamwise location. Due to the nature of the DFT analysis, the contours show the maximal value of the disturbance with respect to time for each mode. It is observed that the density disturbance of the (1,1) mode shows an oblique propagation characteristic. And the contours of the (0,2) mode just show the longitudinal stationary vortex pattern.

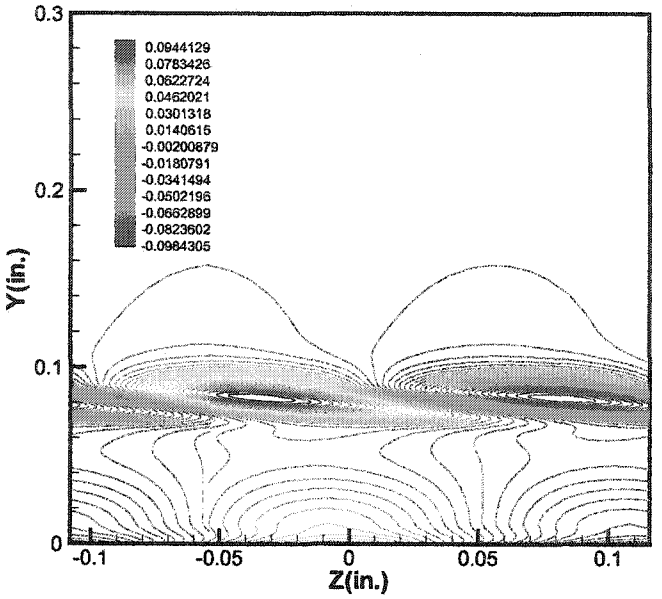

Figure 6.45 Density contours for the (1,1) mode in the Y-Z plane at X=17.378 inches.

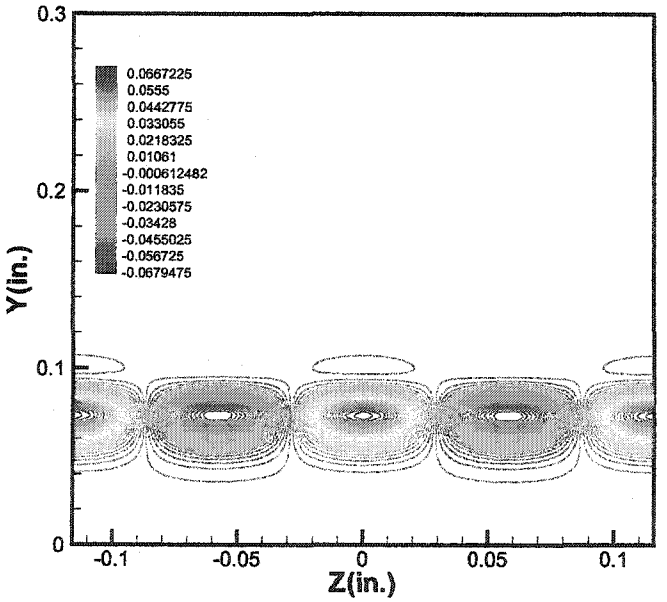

Figure 6.46 Density contours for the (0,2) mode in the Y-Z plane at X=17.378 inches.

Case 2: $F_0=0.85\times10^{-4}$, $\beta=0.2$, $\varepsilon=0.05$

In chapter 4, we determined by the Gortler instability computation that the Gortler vortices have a large amplification rate at spanwise wave numbers between $\beta=0.3\sim0.4$. So we will conduct a computational case for oblique mode evolution with the spanwise wave number $\beta=0.2$ to show the influence of Gortler instability on the evolution of its super-harmonic mode (0,2) across the separation region.

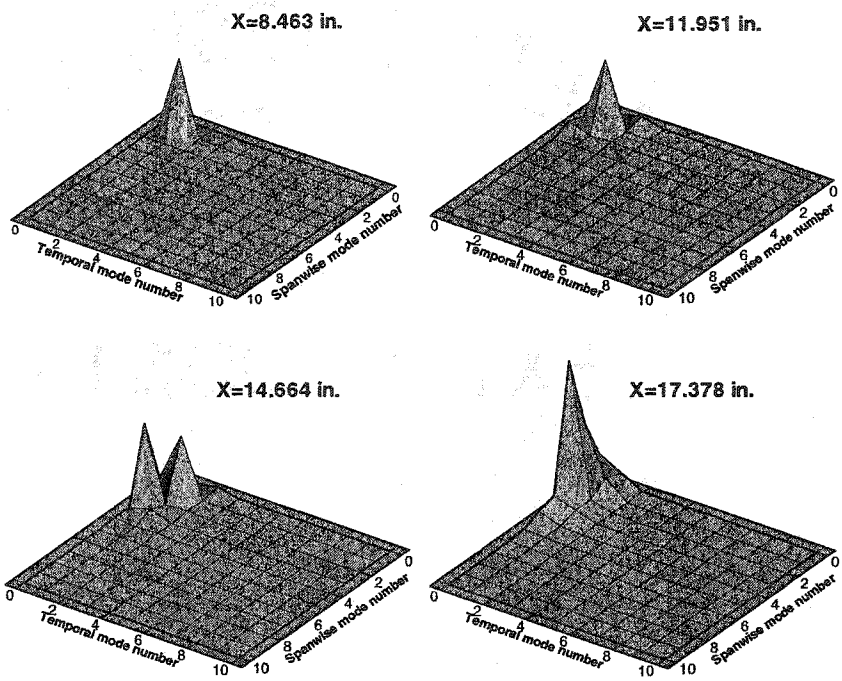

Figure 6.47 The spectral distributions of the disturbances at different streamwise locations.

Figure 6.47 shows the spectral distributions of all Fourier modes which are produced by nonlinear interactions at the different streamwise locations X=8.643, 11.951, 14.664 and 17.378 inches respectively. It is observed that the harmonics begin to appear in the separation region. Further downstream of the separation region, the (0,2) mode dominates all other modes in amplitude. The streamwise distributions of amplitudes for those modes which have relatively large amplitudes downstream of the separation region are plotted in Figure 6.48. It is observed that the fundamental mode (1,1) shows a weak decaying tendency in the streamwise direction at this given spanwise wave number. However, all

other harmonic modes which have appeared due to the nonlinear interactions still keep growing in the streamwise direction. Among them, the stationary mode (0,2) shows the most significant growth rates. At the end of the streamwise domain, mode (0,2) has already reached very large amplitudes. From the growth of the (0,2) mode at this spanwise wave number in the separation region, it can be observed that the Gortler instability can be negligible compared with the instability due to the modal interactions. In this figure, we also noticed that harmonic mode (0,1) has appeared and reached quite big amplitude downstream of the separation region. However, from the harmonic mode distribution shown in Figure 6.42, we find that this mode will never appear by the nonlinear interactions. The only explanation for the appearance of this mode is that this mode was introduced at the initial streamwise location by numerical error. Then it grows downstream of the separation region to reach such large amplitude.

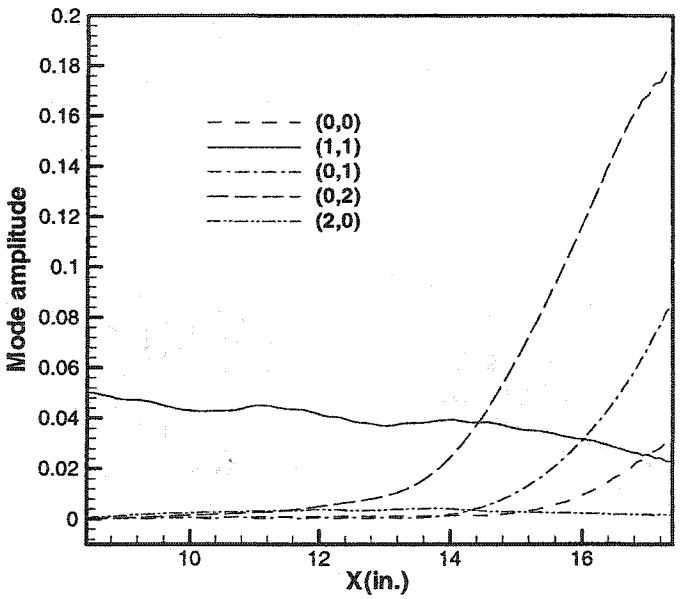

Figure 6.48 The streamwise amplitude distributions for different Fourier modes.

Case 3: $F_0=0.85\times10^{-4}$, $\beta=0.1$, $\varepsilon_{2D}=0.005$, $\varepsilon_{3D}=0.001$

As we know, most transitions are due to the growth of three-dimensional waves by secondary instabilities, in the present study, another computational case was performed to

study the three-dimensional instability across the compression corner in the presence of the two-dimensional instability wave. In order to perform this simulation, a two-dimensional second mode and an oblique mode were introduced at the initial streamwise location. Both the two-dimensional and oblique modes possess the same frequency $F_0=0.85\times10^{-4}$. The spanwise wave number for the oblique mode was $\beta=0.1$. The initial amplitude of the two-dimensional mode is $\varepsilon_{2D}=0.005$ and the initial amplitude of the oblique mode was $\varepsilon_{3D}=0.001$.

Figure 6.49 illustrates all harmonic mode distributions in (ω, β) plane, where the six solid black dots stand for the initial three-dimensional fundamental mode (1,1), the two-dimensional primary mode (1,0) and their complex conjugates. All circles stand for the super-harmonics which will be produced by the nonlinear interactions. It is observed that with the initial harmonic mode (1,1), (1,0) and its complex conjugates, a continuous harmonic mode distributions can be obtained by the nonlinear interactions.

Figure 6.50 shows the spectral distributions of the disturbance at the different streamwise locations. It is observed that at the streamwise location X=8.463 inches upstream of the separation region, only the fundamental two-dimensional mode (1,0) and oblique mode (1,1) are present. At the locations X=11.951 inches, in the separation region, the two-dimensional mode has grown to a quite large amplitude. But the oblique mode shows very little growth and no other harmonics appear in this region. The super-harmonics begin to appear downstream of the separation region. At the location X=17.378 inches, close to the end of the computational domain, many of harmonic modes have already been observed to form a continuous spectrum distribution of disturbances. Figure 6.51 and Figure 6.52 show the spanwise vortex distributions on the wall. It is observed that upstream of and inside the separation region, the instability vortices possess two-dimensional characteristics, but downstream of the separation region, the instability vortices begin to exhibit three-dimensional characteristics. The three-dimensional instability vortices grow continuously further downstream. We also noticed that the

three-dimensional vortices showed an alignment pattern in the spanwise direction. So the growth of the three-dimensional instability vortices will lead to the fundamental laminar breakdown.

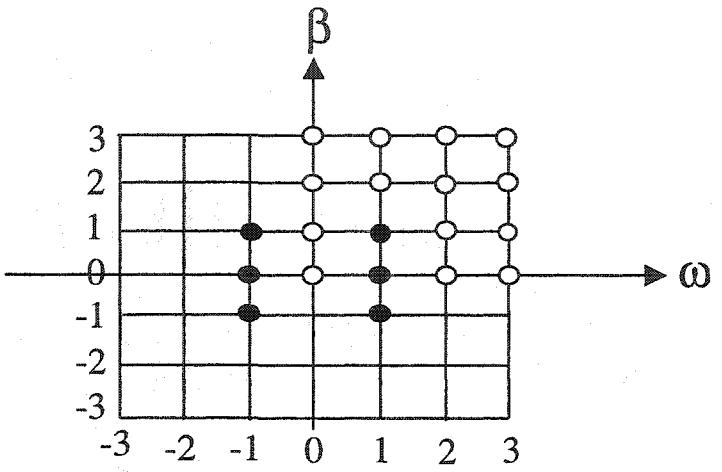

Figure 6.49 The illustration of the harmonic mode distributions.

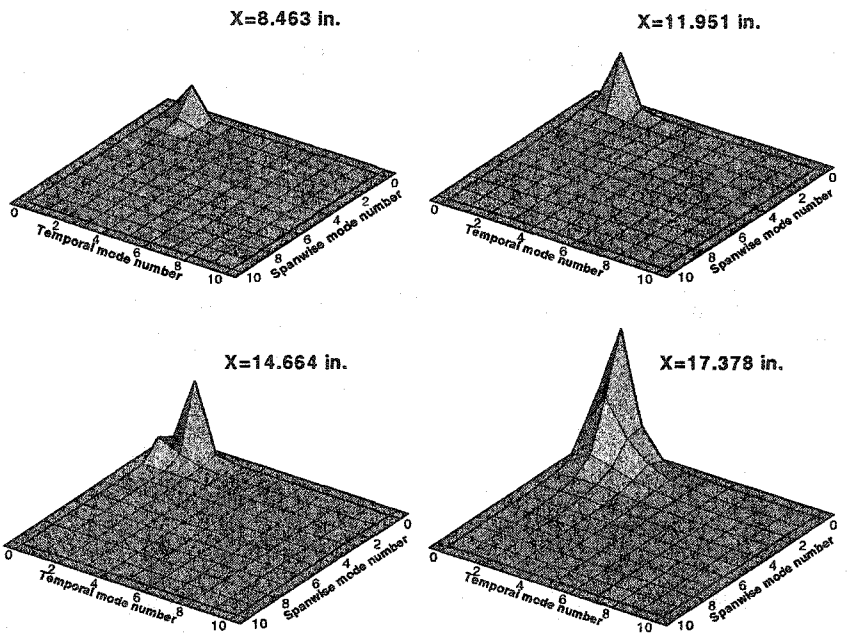

Figure 6.50 The spectral distributions of the disturbances at different streamwise locations.

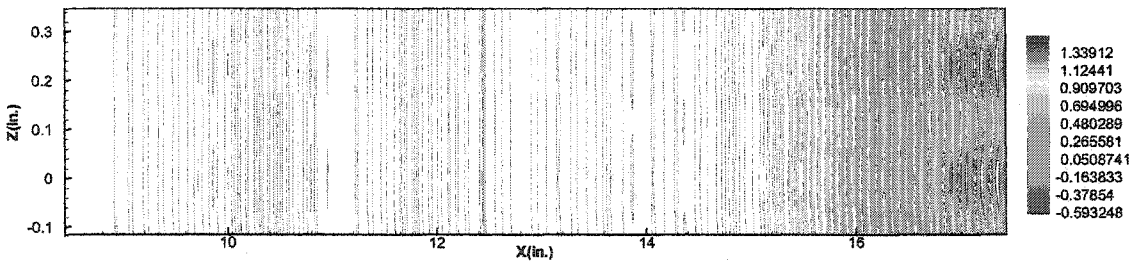

Figure 6.51 Spanwise vortex distributions on the wall.

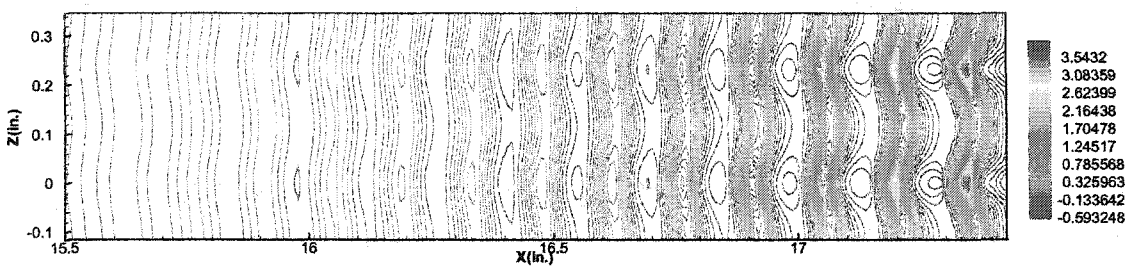

Figure 6.52 Expanded view of spanwise vortex distributions downstream of separation.

Figure 6.53 and Figure 6.54 show the amplitude distributions for each significant Fourier mode downstream of the separation region. It is observed that the two-dimensional fundamental mode (1,0) shows the same nonlinear growth characteristics as those computed in chapter 5, when no oblique mode was present. It grows upstream and downstream of the separation region and is neutral in the separation region. The (1,0) mode begins to saturate near the end of the computational domain, but for the three-dimensional fundamental oblique mode, little growth can be observed either upstream of or inside the separation region. However, it shows significant growth rate downstream of the separation region due to the secondary instability after the saturation of the two-dimensional primary mode. In order to show the influence of the secondary instability more clearly, in Figure 6.55 we compared the growth rate of the mode (1,1) in this case with the growth rate of mode (1,1) in the first case where the two-dimensional primary mode is not present. The growth rate of mode (1,1) in the case 1 is only a factor of 20, but for the growth rate in this case with the presence of the two-dimensional primary mode, an amplification of almost 200 times is observed. This indicates that

three-dimensional disturbances are much more unstable under the secondary instability mechanism. This three-dimensional mode (1,1) continues to grow after the saturation of the two-dimensional primary mode, until it reaches the same amplitude as that of the two-dimensional primary mode.

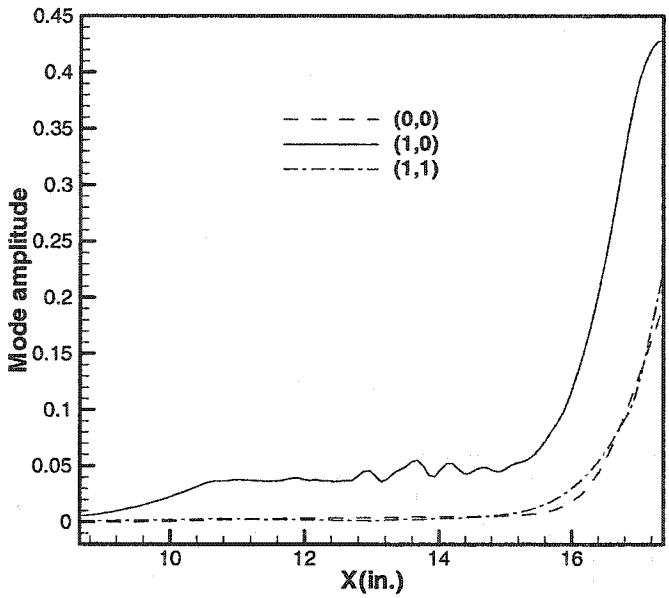

Figure 6.53 The streamwise amplitude distributions for different Fourier modes.

It can also be observed in Figure 6.53 and Figure 6.54 that the harmonics due to the nonlinear interactions begin to appear in the separation region. However, only downstream of the separation region do these harmonics show significant growth rated. Among them, the (0,0) mode which shows the distortion of the mean flow just follows the growth of the fundamental modes (1,0) and (1,1). All other harmonics grow independently. An interesting observation is that all three-dimensional harmonics will grow continuously when the two-dimensional fundamental mode begins to saturate. All two-dimensional harmonics will also saturate with the saturation of the two-dimensional fundamental mode. We also notice that the (0,1) mode which is basically the stationary longitudinal vortex mode shows a remarkable growth characteristic. It grows in the separation region due to the Gortler instability and surpasses all other harmonics in

amplitude at the end of the separation region. Downstream of the separation region, it again shows significant growth rate due to the secondary instability. This mode also plays a very important role in laminar breakdown.

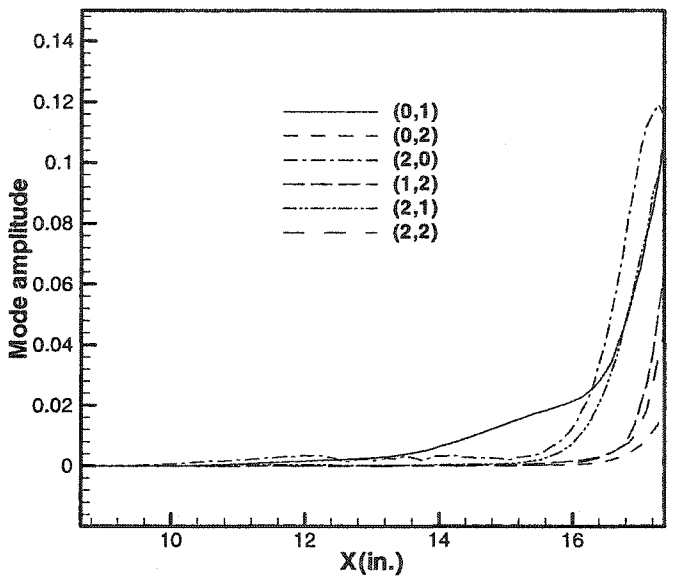

Figure 6.54 The streamwise amplitude distributions for different Fourier modes.

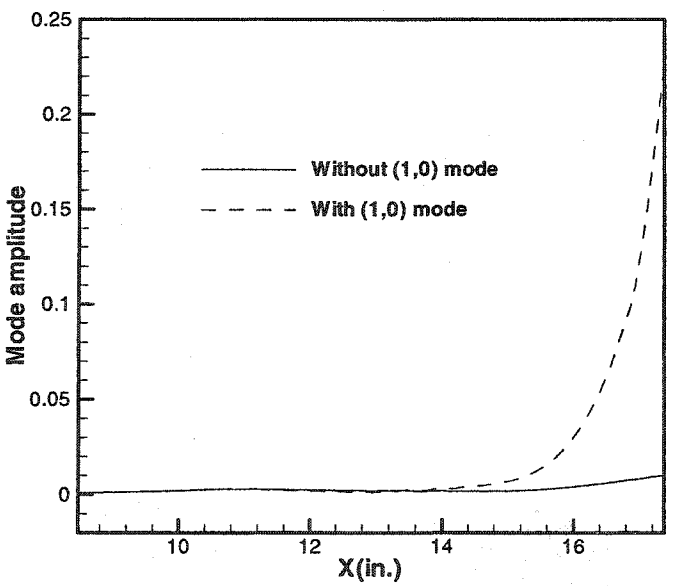

Figure 6.55 Growth rate comparison of (1,1) mode due to different instability mechanism.

6.6 The evolutions of the three-dimensional random frequency disturbances across the compression corner

In this thesis, we also have studied the three-dimensional random frequency disturbance evolutions across the compression corner in the presence of the two-dimensional primary disturbance. The primary disturbance frequency is $F_0=0.85\times10^{-4}$. The initial disturbance amplitude for the two-dimensional primary disturbance is $\varepsilon_{2D}=0.005$ and for three-dimensional random disturbances is $\varepsilon_{3D}=0.0001$.

Figure 6.56 show the random disturbance distribution with time and Figure 6.57 show the spectral distribution of the random disturbance by DFT analysis. It is observed that a continuous spectral distribution is obtained by the random disturbance. Due to the three-dimensional random disturbances which are added at the initial streamwise location, the secondary instability will select the most unstable three-dimensional disturbance frequency automatically. Figure 6.58 shows the spectral distributions of all two-dimensional and three-dimensional disturbances at four different streamwise locations. It is observed that at the location X=8.5 inches which is close to the initial location, a two-dimensional primary mode with high amplitude and many three-dimensional random disturbances with very low amplitudes are present. At the location X=11.355 and X=14.359 inches, the three-dimensional disturbances still are with low amplitudes. But at the location X=17.363 which is close to the end of the computation domain, the three-dimensional disturbances have reached quite large amplitudes, and are comparable to the two-dimensional primary disturbance.

Figure 6.59 and Figure 6.60 show the spanwise vortex distributions on the wall. It is observed that the spanwise vortices always show the two-dimensional characteristics upstream of and inside the separation region. But a three-dimensional pattern begins to appear downstream of the separation region, and this three-dimensional pattern become more and more apparent further downstream. This indicates that the three-dimensional disturbances begin to grow rapidly.

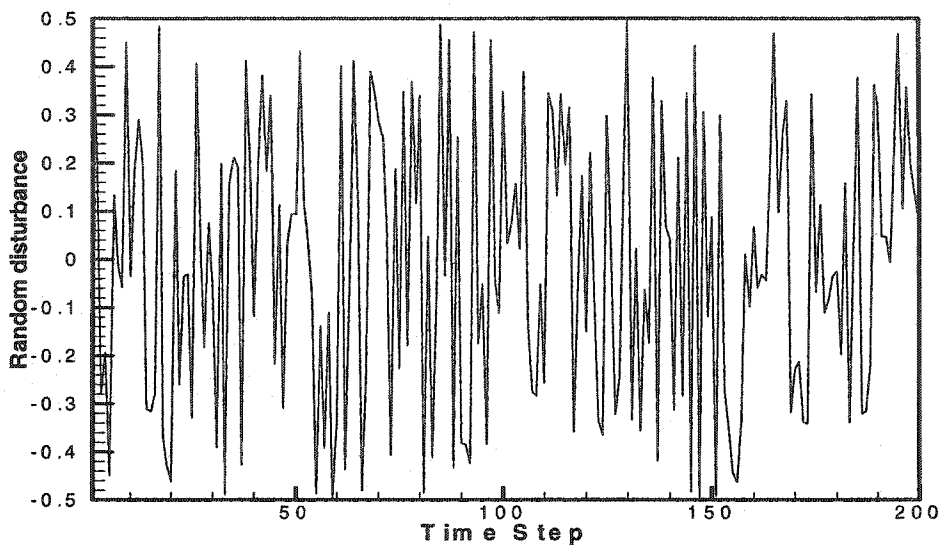

Figure 6.56 Random disturbance distribution with time.

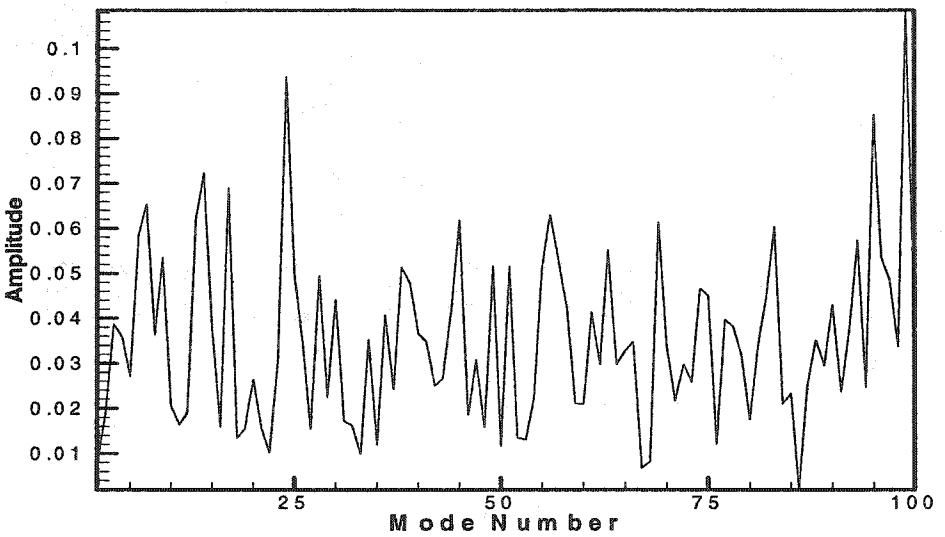

Figure 6.57 The spectral distribution of the random disturbance.

Figure 6.61 shows the streamwise amplitude distributions for two-dimensional primary disturbances and the other two-dimensional harmonics which are produced by nonlinear interactions. It is observed that the two-dimensional primary disturbance and its harmonics show the same growth characteristics as those given in chapter 5 for nonlinear evolution of the two-dimensional disturbances alone. They saturate at the end of the

streamwise computational domain. Figure 6.62 shows the three-dimensional disturbance evolution in the streamwise direction. It is observed that the three-dimensional disturbances are very small and almost neutral upstream of and inside the separation region where the two-dimensional primary disturbance amplitude is still small. However, when the three-dimensional disturbances are downstream of the separation region, with the associated rapid increase of the two-dimensional primary amplitude, they also begin to grow. When the two-dimensional primary disturbance reaches saturation, the three-dimensional disturbances show a very significant growth rate due to the secondary instability. Among all the three-dimensional harmonics, the (1,1) mode shows the largest growth rate and surpasses all other three-dimensional harmonics in amplitude. It will grow continuously further downstream until its amplitude is the same as that of the two-dimensional primary disturbance. Then the Λ vortices will appear and the flow begins to breakdown. So the fundamental or K-type breakdown mechanism will dominate the transition process across the compression corner.

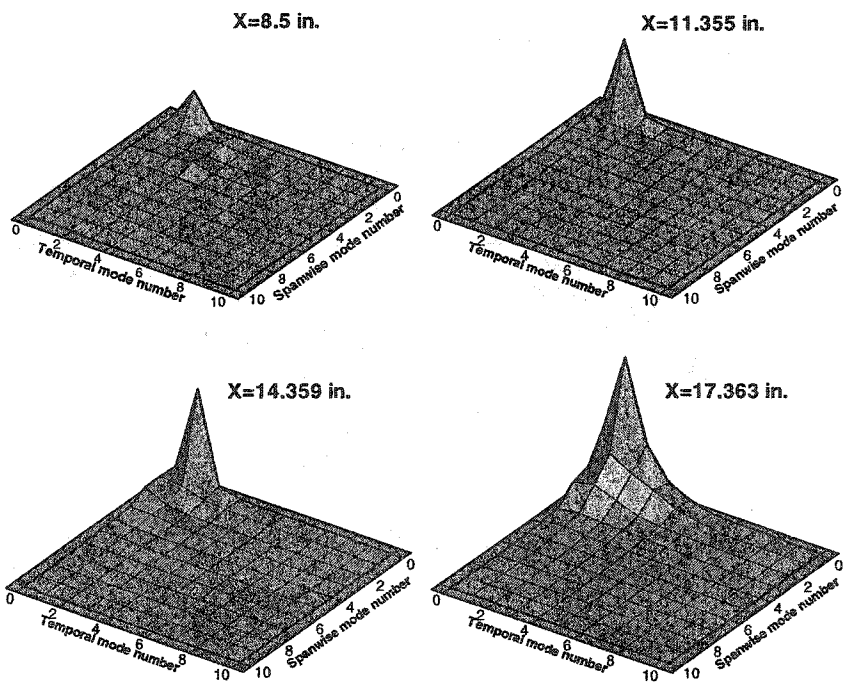

Figure 6.58 The spectral distributions of the disturbances at different streamwise locations.

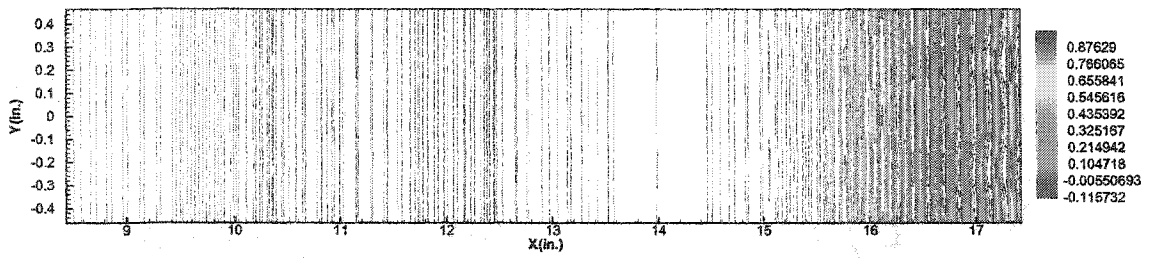

Figure 6.59 Spanwise vortex distributions on the wall.

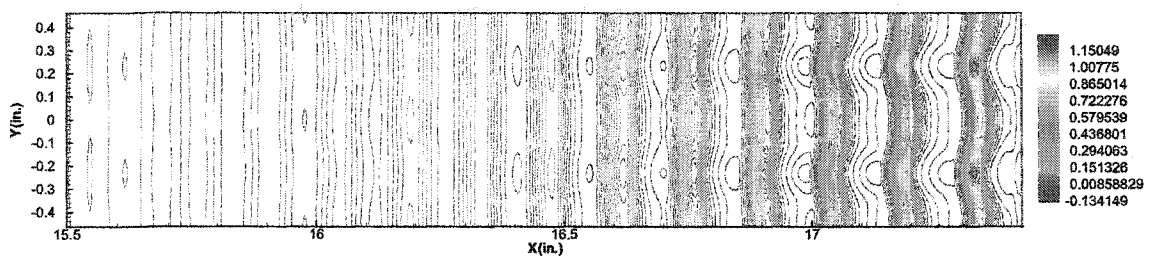

Figure 6.60 Expanded view of spanwise vortex distributions downstream of the separation.

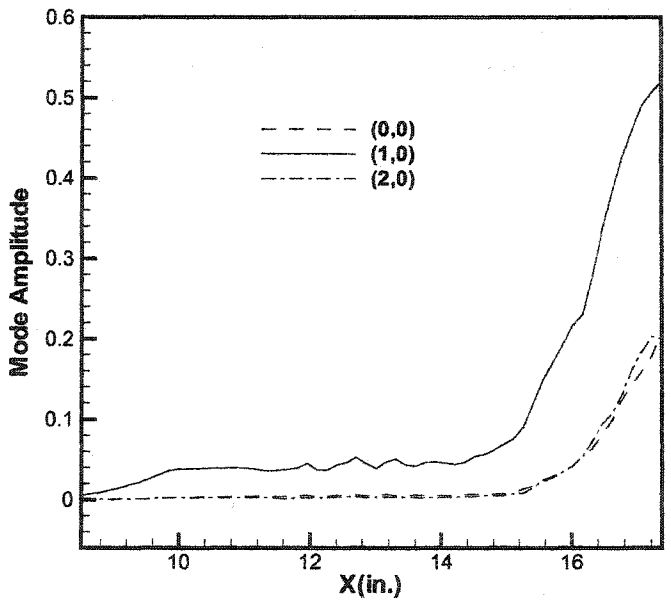

Figure 6.61 Streamwise amplitude distributions of the two-dimensional Fourier modes.

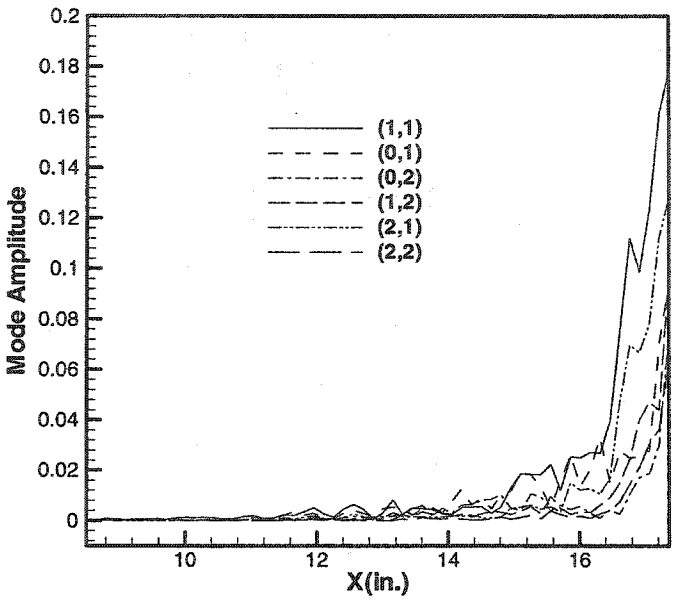

Figure 6.62 Streamwise amplitude distributions of the three-dimensional Fourier modes.

6.7 Summary

In this chapter, the direct numerical simulations were performed to study the linear and nonlinear evolution of the three-dimensional mono-frequency and random-frequency disturbances in a two-dimensional boundary-layer across a compression corner. For the linear evolutions, the three-dimensional mono-frequency disturbances grow monotonically upstream and downstream of the separation region and decay slowly in the separation region. However, the growth rates of the three-dimensional disturbances upstream and downstream of the separation region are much smaller than those of the two-dimensional disturbances with the same frequencies. For the nonlinear evolutions, the super-harmonics begin to appear in the separation region, but most of these harmonics show an apparent growth tendency only downstream of the separation region. Among all these modes, mode (0,2) shows the characteristics of a stationary longitudinal vortex and has its biggest growth rate downstream of the separation region. This mode is responsible for the oblique breakdown. With the presence of the two-dimensional primary mode, the

three-dimensional modes show much greater growth rates due to the secondary instability when the two-dimensional fundamental mode saturates. More and more harmonics begin to appear due to the secondary instability. Among these harmonics, all three-dimensional harmonics grow continuously and all two-dimensional harmonics saturate along with the saturation of the two-dimensional primary mode. The simulations of the three-dimensional random frequency disturbance evolutions in the presence of the two-dimensional primary disturbance show that the secondary instability begins downstream of the separation region. The three-dimensional disturbances will grow rapidly due to the secondary instability. Among all three-dimensional harmonics, the (1,1) mode shows the largest growth rate and finally leads to the fundamental or K-type breakdown.

CHAPTER VII

CONCLUSIONS AND RECOMMENDATIONS

In this thesis, the boundary-layer instability across a compression corner under the hypersonic flow conditions was studied extensively including direct numerical simulations. The linear and nonlinear evolution of both two-dimensional and three-dimensional second mode disturbances have been simulated. In order to perform these simulations, the two-dimensional mean flow was first obtained by solving the two-dimensional compressible Navier-Stokes equations using the WENO scheme. Then the linear stability theory and PSE method were used to validate the code for two- and three-dimensional unsteady computation, and to find the most amplified primary disturbance frequencies. Gortler instability computations were performed to study the influence of the streamline curvature on the Gortler instability. Finally, the direct numerical simulations using the WENO scheme were employed to study the linear and nonlinear evolution of two- and three-dimensional disturbances across the compression corner. Based on all these numerical simulations, several conclusions as well as recommendations for future investigations have been made.

7.1 Conclusions

1. The mean flow results show the detailed pictures of the interaction between the shock wave and the boundary-layers. Due to this interaction, the flow separates at about 1.6 inches upstream of the corner point and reattaches at about 1.6 inches downstream the corner point. A circulation flow is formed within the separation bubble, and compression waves appear along the edge of the separation bubble.
2. By linear stability computation, we found that both two- and three-dimensional disturbances are most amplified across the compression corner at a non-dimensional frequency close to $F_0=0.80\times10^{-4}$. The three-dimensional second mode disturbances

were less amplified than their two-dimensional counterparts upstream and downstream of the separation region. The Gortler instability computations predicted Gortler vortex evolution across the compression corner. The Gortler vortex was most amplified at two locations: close to the separation point and close to the reattachment point. Furthermore, the Gortler vortex experienced significant spatial amplification rates at spanwise wave numbers between β=0.3 and 0.4.

3. By the direct numerical simulation, the evolution of the two-dimensional second mode disturbance across the compression corner shows that the high frequency disturbances grow exponentially upstream and downstream of the separation region, but are neutrally amplified across the separation region. The low frequency disturbances remain neutral upstream and downstream of the separation region, and grow across the separation region. The maximum N-factor up to the second corner region of the Hyper-X wind tunnel model was about 7 and this occured for a disturbance with a non-dimensional frequency of $F_0=0.80\times10^{-4}$. With larger initial disturbance amplitudes, the disturbance evolution became non-linear downstream of the separation region and the super-harmonics appeared due to nonlinear interactions. These harmonics showed the same stability characteristics as those of the primary mode in all three regions. But the primary mode always dominated all other modes in amplitude. When the amplitude of the primary mode reached about 45% of its upstream infinity mean flow quantity, the primary mode and all other harmonic modes began nonlinear saturation.
4. By the direction numerical simulations of the linear evolutions, the three-dimensional mono-frequency disturbances grew monotonically in upstream and downstream of the separation region and decayed slowly in the separation region. But the growth rates of the three-dimensional disturbances upstream and downstream of the separation region are much smaller than those of the two-dimensional disturbances with the same frequencies. For the nonlinear evolutions, the super-harmonics begin to appear in the

separation region, but most of these harmonics show an apparent growth tendency only downstream of the separation region. Among all these modes, mode (0,2) which shows the characteristics of a stationary longitudinal vortex has its largest growth rate downstream of the separation region. This mode is responsible for the oblique break down. In the presence of the two-dimensional primary mode, the three-dimensional modes show much greater growth rates due to the secondary instability when the two-dimensional fundamental mode reaches saturation. More and more harmonics begin to appear due to the secondary instability. Among these harmonics, all three-dimensional harmonics grow continuously and all two-dimensional harmonics will also saturate with the saturation of the two-dimensional primary mode. The simulations of the three-dimensional random frequency disturbance evolutions in the presence of the two-dimensional primary disturbance show that the secondary instability first happens downstream of the separation region. The three-dimensional disturbances will grow sharply due to the secondary instability. Among all three-dimensional harmonics, the (1,1) mode shows the biggest growth rate and finally leads to the fundamental or K-type breakdown.

5. According to the numerical simulations of three-dimensional nonlinear disturbance evolution, we know that an oblique breakdown can be achieved by the growth of (0,2) mode and a fundamental breakdown can be achieved by the growth of (1,1) mode. So for the transition tripping of the boundary-layer at the inlet of Hyper-X vehicle propulsion system, the roughness should be distributed on the forebody surface in such a way that these fast growing modes can be produced easily.

7.2 Recommendations for future researches

1. Due to the limitation of the computational resources, all transition simulations could only reach the nonlinear stage. As a result of all the simulations we have performed, we know that transition will first happen downstream of the separation region. In order to simulate the breakdown process in this region, many more grid points should

be put in this region to capture the additional harmonics that appeared due to the secondary instability. For the spatial simulations, this means that a much more powerful super-computer is needed to perform those simulations.

2. The instability across the compression corner is simulated at a fixed corner angle in this thesis. In order to fully understand the instability mechanism in the separation region, the influence of the corner angle should be considered.
3. The influence of wall roughness at the initial streamwise location should be simulated in order to find the most effective tripping device for boundary-layer transition at the inlet of the Hyper-X propulsion system.
4. The two-corner system should be considered in order to simulate the boundary-layer transition at the inlet of the Hyper-X propulsion system.

REFERENCES

[1] Berry, S., DiFulvio, M., and Kowalkowski, M., "Forced boundary-layer transition on X-43(Hyper-X) in NASA LaRC 20-inch Mach 6 air tunnel," NASA TM-210316

[2] Berry, S. Auslender, A. and Dilley, A., "Hypersonic boundary-layer trip development for Hyper-X," AIAA 2000-4012.

[3] Ackeret, J., Feldmann, F., and Rott, N., "Investigation of compression shocks and boundary-layers in gases moving at high speed," NACA TM-1113, 1947.

[4] Chapman, D., Kuehn, D. and Larson, H., "Investigation of separated flows in supersonic and subsonic streams with emphasis on the effect of transition," NACA TN-3869, 1957.

[5] Lighthill, M. J., "On boundary-layers and upstream influence. I. A comparison between subsonic and supersonic flows," Proc. Roy. Soc. A.217, 1953, pp. 344-357.

[6] Lighthill, M. J., "On boundary-layers and upstream influence. II. Supersonic flows without separation," Proc. Roy. Soc. A.217, 1953, pp. 478-507.

[7] Stewartson, K., F.R.S. and Williams, P., "Self-induced separation," Proc. Roy. Soc. A. 312, 1969, pp. 181-206.

[8] Brown, S., Stewartson, K., and Williams, P., "Hypersonic self-induced separation," The Physics of Fluids, Vol. 18, No. 6, June, 1975, pp. 633-639.

[9] Rizzetta, D., Burggraf, O. and Jenson, R., "Triple-deck solutions for viscous supersonic and hypersonic flow past corners," Journal of Fluid Mechanics, Vol. 89, part 3, 1978, pp. 535-552.

[10] Brown, S., Cheng, H. and Lee, C., "Inviscid-viscous interaction on triple-deck scales in a hypersonic flow with strong well cooling," Journal of Fluid mechanics, Vol. 220, 1990, pp. 309-337.

[11] Lewis, J., Kubota, T. and Lees, L., "Experimental investigation of supersonic laminar, two-dimensional boundary-layer separation in a compression corner with and without cooling," AIAA Journal, Vol. 6, No. 1, January, 1968, pp. 7-14.

[12] Korkegi, R., "Survey of viscous interactions associated with high Mach number flight," AIAA Journal, Vol. 9, No. 5, May, 1971, pp. 771-784.

[13] Andreopoulos, J. and Muck, K., "Some new aspect of the shock-wave/boundary-layer interaction in compression-ramp flows," Journal of Fluid Mechanics, Vol. 180, 1987, pp. 405-428.

[14] Rudy, D., Thomas, J., Kumar, A. and Gnoffo, P., "Computation of laminar hypersonic compression corner flows," AIAA Journal, Vol. 29, No. 7, July, 1991, pp. 1108-1113.

[15] Kerimbekov, R., Ruban, A. and Walker, J., "Hypersonic boundary-layer separation on a cold wall," Journal of Fluid Mechanics, Vol. 274, 1994, pp. 163-195.

[16] Grasso, F. Leone, G. and Delery, J., "Validation procedure for the analysis of shock-wave/boundary-layer interaction problems," AIAA Journal, Vol. 32, No. 9, September, 1994, pp. 1820-1827.

[17] Simeonides, G. Haase, W. and Manna, M., "Experimental, analytical, and computational methods applied to hypersonic compression ramp flows," AIAA Journal, Vol. 32, No. 2, February, 1994, pp. 301-310.

[18] Simeonides, G. and Haase, W., "Experimental and computational investigations of hypersonic flow about compression ramps," Journal of Fluid Mechanics, Vol. 283, 1995, pp. 17-42.

[19] Cassel, K., Ruban, A. and Walker, J., "An instability in supersonic boundary-layer flow over a compression ramp," Journal of Fluid Mechanics, Vol., 300, 1995, pp. 265-285.

[20] Donald, R., Miguel, V. and Datta, G., "Large-Eddy simulation of supersonic compression –ramp flow by high-order method," AIAA Journal, Vol. 39, No. 12, December, 2001, pp. 2283-2292.

[21] Smith, F. and Khorrami, A., "The interactive breakdown in supersonic ramp flow," Journal of Fluid Mechanics, Vol. 224, 1991, pp. 197-215.

[22] Luca, L. and Cardone, G., "Viscous interaction phenomena in hypersonic wedge flow," AIAA Journal, Vol. 33, No. 12, Decemer, 1995, pp. 2293-2298.

[23] Mack, L., "Boundary-Layer stability theory," JPL Report No. 900-277, Nov. 1969.

[24] Kachanov, Y., "Physical mechanism of laminar-boundary-layer transition," Ann. Rev. Fluid mech., Vol. 26, 1994, pp. 411-82.

[25] Kachanov, Y., "On the resonant nature of the breakdown of a laminar

boundary-layer," Journal of Fluid Mechanics, Vol. 184, 1987, pp. 43-74.

[26] Goldstein, M., "The evolution of Tollmien-Schlichting waves near a leading edge," Journal of Fluid Mechanics, Vol. 127, 1983, pp. 59-81.

[27] Goldstein, M. and Hultgren, L., "Boundary-layer receptivity to long-wave free-stream disturbances," Ann. Rev. Fluid Mech., Vol. 21, 1989, pp. 137-166.

[28] Herbert, T., "Secondary instability of boundary-layers," Ann. Rev. Fluid Mech., Vol. 20, 1988, pp. 487-526.

[29] Klebanoff, P., Tidstrom, K. and Sargent, L., "The three-dimensional nature of boundary-layer instability," Ann. Rev. Fluid Mech., vo.12, 1961, pp.1-35.

[30] Herbert, T., "Parabolized stability equations," Ann. Rev. Fluid Mech., Vol. 29, 1997, pp. 245-283.

[31] Piomelli, J., Zang, T., Speziale, C. and Hussaini, M., "On the large-eddy simulation of wall-bounded shear flows," Physics of Fluids A, Vol. 2, 1990, pp. 257-265.

[32] Normand, X. and Lesieur, M., "Direct and Large-Eddy simulation of transition in the compressible boundary-layer," Theoretical Computational Fluid Dynamics, Vol. 3, 1992, pp. 231-252.

[33] Pruett, C. D., Chang, C. L. and Carpenter M. H., "Spatial direct numerical simulation of high-speed boundary-layer flows, Part I: Algorithm considerations and validation," Theoretical computational fluid dynamics, vol.7, 1995, pp49-76.

[34] Pruett, C. D. and Chang, C. L., "Spatial direct numerical simulation of high-speed boundary-layer flows, Part II: Transition on a cone in Mach 8 flow," Theoretical computational fluid dynamics, vol.7, 1995, pp397-424.

[35] Pruett, D. and Chang, C., "A comparison of PSE and DNS for high-speed boundary-layer flows," Transitional and Turbulent Compressible Flows, ASME, Vol. 151, 1993, pp. 57-67.

[36] Pruett, D. and Zang, T., "Direct numerical simulation of laminar breakdown in high-speed, axisymmetric boundary-layers," Theoretical Computational Fluid Dynamics, Vol. 3, 1992, pp. 345-367.

[37] Kleiser, L. and Zang, T., "Numerical simulation of transition in wall-bounded shear flows," Ann. Rev. Fluid Mech., Vol. 23, 1991, pp. 495-537.

[38] Adams, N. and Kleiser, L., "Subharmonic transition to turbulence in a flat-plate boundary-layer at Mach number 4.5," Journal of Fluid Mechanics, Vol. 317, 1996, pp. 301-335.

[39] Laurien, E. and Kleiser, L., "Numerical simulation of boundary-layer transition and transition control," Journal of Fluid Mechanics, Vol. 199, 1989, pp. 403-440.

[40] Joslin, R., "Direct simulation of evolution and control of three-dimensional instabilities in attachment-line boundary-layers," Journal of Fluid Mechanics, Vol. 291, 1995, pp. 369-392.

[41] Hu, S. and Zhong, X., "Hypersonic boundary-layer stability over blunt leading edges with bow-shock effects," AIAA 98-0433.

[42] Zhong, X., "Direct numerical simulation of 3-D hypersonic boundary-layer receptivity to freestream disturbances," AIAA 98-0533.

[43] Zhong, X. and Dong, H., "Hypersonic boundary-layer receptivity to freestream disturbances over an elliptical cross-section cone," AIAA 99-0409.

[44] Guo, Y., Kleiser, L. and Adams, N., "Comparison of temporal and spatial direct numerical simulation of compressible boundary-layer transition," AIAA Journal, Vol. 34, No. 4, April, 1996, pp. 683-690.

[45] Fasel, H., "Numerical investigation of the three-dimensional development in Boundary-Layer Transition," AIAA Journal, Vol. 28, No. 1, January, 1990, pp. 29-37.

[46] Fasel, H., "Numerical Investigation of the interaction of the Klebanoff-mode with a Tollmien-Schlichting wave," Journal of Fluid Mechanics, Vol. 450, 2002, pp. 1-33.

[47] Reshotoko, E., "Boundary-layer stability and transition," Ann. Rev. Fluid Mech. 1976.

[48] Pruett, D., Ng, L. and Erlebacher, G., "On the nonlinear stability of a high-speed, axisymmetric boundary-layer," NASA CR-187538.

[49] Bridges, T. and Morris, P., "Boundary-layer stability calculations," Physics of Fluids, 30(11), November, 1987, pp. 3351-3358.

[50] Bertolotti, F., Herbert, T. and Spalart, P., "Linear and nonlinear stability of Blasius boundary-layer," Journal of Fluid Mechanics, Vol. 242, 1992, pp. 441-474.

[51] Malik, M., Chuang, S. and Hussaini, M., "Accurate numerical solution of

compressible, linear stability equations," Journal of Applied Mathematics and Physics, Vol. 33, No. 2, March, 1982, pp. 189-201.

[52] Balakumar, P. and Reed, H., "Stability of three-dimensional supersonic boundary-layers," Physics of Fluids, A 3(4), April, 1991, pp. 617-632.

[53] Jeyasingham S. and Balakumar, P., "Stability of three-dimensional compressible boundary-layers," AIAA 99-0406.

[54] Malik, M., "Numerical methods for hypersonic boundary-layer stability," Journal of Computational Physics, Vol. 86, No. 2, February, 1990, pp. 376-412.

[55] Hu, S. and Zhong, X., "Nonparallel stability analysis of compressible boundary-layer using 3-D PSE," AIAA 99-0813.

[56] Brogan, T. and Demetriades, A., "Effects of surface heating on instabilities in a supersonic nozzle boundary-layer," AIAA 98-0779.

[57] Kimmel, R. and Poggie, J., "Effect of total temperature on boundary-layer stability at Mach 6," AIAA 99-0816.

[58] Jaffe, N., Okamura, T. and Smith, A., "Determination of spatial amplification factors and their application to predicting transition," AIAA Journal, Vol. 8, No. 2, February, 1970, pp. 301-308.

[59] Gaster, M., "A note on the relation between temporally-increasing and spatially-increasing disturbances in hydrodynamic stability," Journal of Fluid Mechanics, Vol. 14, 1962, pp. 222-224.

[60] Bayliss, A., Maestrello, L., Parikh, P. and Turkel, E., "Wave phenomena in a high Reynolds number compressible boundary-layer," In Stability for Time Dependent and Spatially Varying Flows, Springer-Verlag, New York, 1985, pp. 188-205.

[61] Erlebacher, G. and Hussaini, M., "Numerical experiments in supersonic boundary-layer stability," Physics of Fluids, A 2(1), January, 1990, pp. 94-104.

[62] Maestrello, L., Bayliss, A. and Krishnan, R., "On the interaction between first- and second-mode waves in a supersonic boundary-layer," Physics of Fluids, A 3(12), December, 1991, pp. 3014-3020.

[63] Eissler, W. and Bwstek, H., "Spatial numerical simulations of nonlinear transition phenomena in supersonic boundary-layers," In Transitional and Turbulent

Compressible Flows, ASME, Vol. 151, 1993, pp. 69-76.

[64] Ng, L., and Zang, T., "Secondary instability mechanism in compressible, axisymmetric boundary-layer," AIAA Journal, Vol. 31, No. 9, September, 1993, pp. 1605-1610.

[65] Spalart, P. and Strelets, M., "Mechanisms of transition and heat transfer in a separation bubble," Journal of Fluid Mechanics, Vol. 403, 2000, pp. 329-349.

[66] Yang, Z. and Voke, P., "Large-eddy simulation of boundary-layer separation and transition at a change of surface curvature," Journal of Fluid Mechanics, Vol. 439, 2001, pp. 305-333.

[67] El-Hady, N., "Nonparallel instability of supersonic and hypersonic boundary-layers," Physics of Fluids, A 3(9), September, 1991, pp. 2164-2178.

[68] Gaster, M., "On the effect of boundary-layer growth on flow stability," Journal of Fluid Mechanics, Vol. 66, part 3, 1974, pp. 465-480.

[69] Saric, W. and Nayfeh, A., "Nonparallel stability of boundary-layers with pressure gradients and suction," AGARD Conference Proceedings No. 224, 1977, pp. 1-21.

[70] Fasel, H. and Konzelmann, U., "Non-parallel stability of a flat-plate boundary-layer using the complete Navier-Stokes equations," Journal of Fluid Mechanics, Vol. 221, 1990, pp. 311-347.

[71] Spall, R. and Malik, M., "Gortler Vortices in supersonic and hypersonic boundary-layers," Physics of Fluids, A 1(11), November, 1989, pp. 1822-1835.

[72] Winoto, S. and Low, H., "Transition of boundary-layer flows in the presence of Gortler vortices," Experiments in Fluids, 10, 1991, pp. 281-284.

[73] Benmalek, A. and Saric, W., "Effects of curvature variations on the nonlinear evolution of Gortler vortices," Physics of Fluids, 6(10), October, 1994, pp. 3353-3367.

[74] Whang, C. and Zhong, X., "Direct numerical simulation of Gortler instability in hypersonic boundary-layers," AIAA 99-0291.

[75] Whang, C. and Zhong, X., "Nonlinear interaction of Gortler and second shear modes in hypersonic boundary-layers," AIAA 2000-0536.

[76] Goulpie, P., Klingmann, B. and Bottaro, A., "Gortler vortices in boundary-layers with

streamwise pressure gradient: Linear theory," Physics of Fluid, 8(2), February, 1996, pp. 451-459.

[77] Cunff, C. and Zebib, A., "Nonlinear spatially developing Gortler vortices in curved wall jet flow," Physics of Fluid, 8(9), September, 1996, pp. 2375-2384.

[78] Saric, W., "Gortler Vortices," Annu. Rev. Fluid Mech., Vol. 26, 1994, pp. 379-409.

[79] Bayliss, A., Parikh, P., Maestrello, L., and Turkel, E., "A fourth-order scheme for the unsteady compressible Navier-Stokes equations," ICASE report no. 85-44.

[80] Lele, S., "Direct numerical simulation of compressible free shear layers," AIAA paper 89-0374.

[81] Shu, C., "Essentially Non-Oscillatory and Weighted Essentially Non-Oscillatory Schemes for Hyperbolic Conservation Laws," NASA CR-97-206253.

[82] Atkins, H. L., "High-order ENO methods for the unsteady compressible Navier-Stokes Equations," AIAA paper 91-1557, 1991.

[83] William, G., "Using MPI-1: portable parallel programming with the message-passing interface," MIT press, 1999.

[84] William, G., "Using MPI-2: advanced features of the message-passing interface," MIT press, 1999.

APPENDIX I

THE ELEMENTS OF THE COEFFICIENT MATRIX

FOR LINEAR STABILITY EQUATIONS

$$a_{12} = 1$$

$$a_{21} = \frac{i\,\mathrm{Re}}{\overline{\mu}\overline{T}}(\alpha\overline{U}_1 - \omega) + \alpha^2 + \beta^2$$

$$a_{22} = -\frac{1}{\overline{\mu}}\frac{d\overline{\mu}}{d\overline{T}}\frac{d\overline{T}}{dx_2}$$

$$a_{23} = \frac{1}{\overline{\mu}}\left(\frac{\mathrm{Re}}{\overline{T}}\frac{d\overline{U}}{dx_2} - i\alpha\frac{d\overline{\mu}}{d\overline{T}}\frac{d\overline{T}}{dx_2}\right) - \frac{i\alpha}{3\overline{T}}\frac{d\overline{T}}{dx_2}$$

$$a_{24} = \frac{i\alpha\,\mathrm{Re}}{\overline{\mu}\gamma M_\infty^2} - \frac{\alpha}{3}(\alpha\overline{U}_1 - \omega)$$

$$a_{25} = \frac{\alpha}{3T}(\alpha\overline{U}_1 - \omega) - \frac{1}{\overline{\mu}}\left(\frac{d\overline{\mu}}{d\overline{T}}\frac{d^2\overline{U}_1}{dx_2^2} + \frac{d^2\overline{\mu}}{d\overline{T}^2}\frac{d\overline{T}}{dx_2}\frac{d\overline{U}_1}{dx_2}\right)$$

$$a_{26} = -\frac{1}{\overline{\mu}}\frac{d\overline{\mu}}{d\overline{T}}\frac{d\overline{U}_1}{dx_2^2}$$

$$a_{31} = -i\alpha$$

$$a_{33} = \frac{1}{\overline{T}}\frac{d\overline{T}}{dx_2}$$

$$a_{34} = -i(\alpha\overline{U}_1 - \omega)$$

$$a_{35} = \frac{i}{\overline{T}}(\alpha\overline{U}_1 - \omega)$$

$$a_{37} = -i\beta$$

$$L = \frac{\mathrm{Re}}{\gamma M_\infty^2} + \frac{4}{3}i\overline{\mu}(\alpha\overline{U}_1 - \omega)$$

$$a_{41} = -\frac{i\alpha}{L}\left[\frac{4\overline{\mu}}{3\overline{T}}\frac{d\overline{T}}{dx_2} + 2\frac{d\overline{\mu}}{d\overline{T}}\frac{d\overline{T}}{dx_2}\right]$$

$$a_{42} = -\frac{i\alpha}{L}\overline{\mu}$$

$$a_{43} = \frac{1}{L}\left[\frac{4\overline{\mu}}{3\overline{T}}\frac{d^2\overline{T}}{dx_2^2} + \frac{4}{3\overline{T}}\frac{d\overline{\mu}}{d\overline{T}}\left(\frac{d\overline{T}}{dx_2}\right)^2 - \frac{i\,\mathrm{Re}}{\overline{T}}(\alpha\overline{U}_1 - \omega) - \overline{\mu}(\alpha^2+\beta^2)\right]$$

$$a_{44} = -\frac{4i}{3L}\left[\overline{\mu}\left((\alpha\overline{U}_1 - \omega)\frac{1}{\overline{T}}\frac{d\overline{T}}{dx_2} + \alpha\frac{d\overline{U}_1}{dx_2}\right) + \frac{d\overline{\mu}}{d\overline{T}}\frac{d\overline{T}}{dx_2}(\alpha\overline{U}_1 - \omega)\right]$$

$$a_{45} = \frac{4i}{3L\overline{T}}\left[\alpha\overline{\mu}\frac{d\overline{U}_1}{dx_2} + \frac{d\overline{\mu}}{d\overline{T}}\frac{d\overline{T}}{dx_2}(\alpha\overline{U}_1 - \omega)\right] + \frac{i\alpha}{L}\frac{d\overline{\mu}}{d\overline{T}}\frac{d\overline{U}_1}{dx_2}$$

$$a_{47} = -\frac{i\beta}{L}\left[\frac{4\overline{\mu}}{3\overline{T}} + 2\frac{d\overline{\mu}}{d\overline{T}}\right]\frac{d\overline{T}}{dx_2}$$

$$a_{48} = -\frac{i\beta}{L}\overline{\mu}$$

$$a_{56} = 1$$

$$a_{62} = 2(1-\gamma)M_\infty^2 P_r\frac{d\overline{U}_1}{dx_2}$$

$$a_{63} = \frac{p_r\,\mathrm{Re}}{\overline{\mu}\overline{T}}\frac{d\overline{T}}{dx_2} - 2i(\gamma-1)\alpha M_\infty^2 P_r\frac{d\overline{U}_1}{dx_2}$$

$$a_{64} = \frac{iP_r\,\mathrm{Re}}{\gamma\overline{\mu}}(1-\gamma)(\alpha\overline{U}_1 - \omega)$$

$$a_{65} = \frac{iP_r\,\mathrm{Re}}{\overline{\mu}\overline{T}}(\alpha\overline{U}_1 - \omega) + (\alpha^2+\beta^2) - \frac{1}{\overline{\mu}}\left[\frac{d\overline{\mu}}{d\overline{T}}\frac{d^2\overline{T}}{dx_2^2} + \frac{d^2\overline{\mu}}{d\overline{T}^2}\left(\frac{d\overline{T}}{dx_2}\right)^2\right]$$
$$-\frac{(\gamma-1)P_r M_\infty^2}{\overline{\mu}}\frac{d\overline{\mu}}{d\overline{T}}\left(\frac{d\overline{U}_1}{dx_2}\right)^2$$

$$a_{66} = -\frac{2}{\overline{\mu}}\frac{d\overline{\mu}}{d\overline{T}}\frac{d\overline{T}}{dx_2}$$

$$a_{78} = 1$$

$$a_{83} = -\frac{i\beta}{3\overline{T}}\frac{d\overline{T}}{dx_2} - \frac{i\beta}{\overline{\mu}}\frac{d\overline{\mu}}{d\overline{T}}\frac{d\overline{T}}{dx_2}$$

$$a_{84} = -\frac{\beta}{3}(\alpha\overline{U}_1 - \omega) + \frac{i\beta\,\mathrm{Re}}{\overline{\mu}\gamma M_\infty^2}$$

$$a_{85} = \frac{\beta}{3\overline{T}}(\alpha\overline{U}_1 - \omega)$$

$$a_{87} = \frac{i\,\mathrm{Re}}{\overline{\mu}\overline{T}}(\alpha\overline{U}_1 - \omega) + \alpha^2 + \beta^2$$

$$a_{88} = -\frac{1}{\overline{\mu}}\frac{d\overline{\mu}}{d\overline{T}}\frac{d\overline{T}}{dx_2}$$

APPENDIX II

THE ELEMENTS OF THE COEFFICIENT MATRICES

FOR THE PARABOLIZED STABILITY EQUATIONS

$$A_{21} = \frac{\overline{\mu}}{\mathrm{Re}}$$

$$A_{32} = \frac{4\overline{\mu}}{3\,\mathrm{Re}}$$

$$A_{43} = \frac{\overline{\mu}}{\mathrm{Re}}$$

$$A_{55} = \frac{\overline{\mu}\gamma}{P_r\,\mathrm{Re}}$$

$$B_{11} = \overline{\rho}$$

$$B_{14} = \overline{U}_1$$

$$B_{21} = -\overline{\rho}\overline{U}_1 + \frac{4}{3\,\mathrm{Re}}\frac{\partial\overline{\mu}}{\partial\overline{T}}\frac{\partial\overline{T}}{\partial x_1} + \frac{8}{3}i\overline{\mu}\alpha$$

$$B_{22} = \frac{1}{\mathrm{Re}}\frac{\partial\overline{\mu}}{\partial\overline{T}}\frac{\partial\overline{T}}{\partial x_2}$$

$$B_{23} = \frac{i\beta}{3\,\mathrm{Re}}\overline{\mu}$$

$$B_{24} = -\frac{\overline{T}}{\gamma M_\infty^2}$$

$$B_{25} = -\frac{\overline{\rho}}{\gamma M_\infty^2} + \frac{1}{\mathrm{Re}}\left(\frac{4}{3}\frac{\partial\overline{U}_1}{\partial x_1} - \frac{2}{3}\frac{\partial\overline{U}_2}{\partial x_2}\right)\frac{\partial\overline{\mu}}{\partial\overline{T}}$$

$$B_{31} = -\frac{2}{3\,\mathrm{Re}}\frac{\partial\overline{\mu}}{\partial\overline{T}}\frac{\partial\overline{T}}{\partial\overline{x}_2}$$

$$B_{32} = -\overline{\rho}\overline{U}_1 + \frac{2i\alpha\mu}{\mathrm{Re}} + \frac{1}{\mathrm{Re}}\frac{\partial\overline{\mu}}{\partial\overline{T}}\frac{\partial\overline{T}}{\partial x_1}$$

$$B_{35} = \frac{1}{\mathrm{Re}}\left(\frac{\partial \overline{U}_2}{\partial x_1} + \frac{\partial \overline{U}_1}{\partial x_2}\right)\frac{\partial \overline{\mu}}{\partial \overline{T}}$$

$$B_{41} = \frac{i\beta\overline{\mu}}{3\,\mathrm{Re}}$$

$$B_{43} = -\rho\overline{U}_1 + \frac{1}{\mathrm{Re}}\frac{\partial \overline{\mu}}{\partial \overline{T}}\frac{\partial \overline{T}}{\partial x_1} + \frac{2i\alpha\overline{\mu}}{\mathrm{Re}}$$

$$B_{51} = \frac{4}{3}\overline{\mu}(\gamma-1)\gamma\frac{M_\infty^2}{\mathrm{Re}}\left(4\frac{\partial \overline{U}_1}{\partial x_1} + \frac{\partial \overline{U}_2}{\partial x_2}\right) - \gamma(\gamma-1)M_\infty^2\overline{p}$$

$$B_{52} = 2\gamma(\gamma-1)\frac{M_\infty^2}{\mathrm{Re}}\overline{\mu}\left(\frac{\partial \overline{U}_1}{\partial x_2} + \frac{\partial \overline{U}_2}{\partial x_1}\right)$$

$$B_{55} = -\rho\overline{U}_1 + \frac{2\gamma}{P_r\,\mathrm{Re}}\left(\frac{\partial \overline{\mu}}{\partial \overline{T}}\frac{\partial \overline{T}}{\partial x_1} + i\overline{\mu}\alpha\right)$$

$$C_{12} = \overline{\rho}$$

$$C_{14} = \overline{U}_2$$

$$C_{21} = -\overline{\rho}\overline{U}_2 + \frac{1}{\mathrm{Re}}\frac{\partial \overline{\mu}}{\partial \overline{T}}\frac{\partial \overline{T}}{\partial x_2}$$

$$C_{22} = -\frac{2}{3\,\mathrm{Re}}\frac{\partial \overline{\mu}}{\partial \overline{T}}\frac{\partial \overline{T}}{\partial x_1} + \frac{i\overline{\mu}\alpha}{3\,\mathrm{Re}}$$

$$C_{25} = \frac{1}{\mathrm{Re}}\left(\frac{\partial \overline{U}_1}{\partial x_2} + \frac{\partial \overline{U}_2}{\partial x_1}\right)\frac{\partial \overline{\mu}}{\partial \overline{T}}$$

$$C_{31} = \frac{1}{\mathrm{Re}}\left(\frac{\partial \overline{\mu}}{\partial \overline{T}}\frac{\partial \overline{T}}{\partial x_1} + \frac{i\alpha\overline{\mu}}{3}\right)$$

$$C_{32} = -\overline{\rho}\overline{U}_2 + \frac{4}{3\,\mathrm{Re}}\frac{\partial \overline{\mu}}{\partial \overline{T}}\frac{\partial \overline{T}}{\partial x_2}$$

$$C_{33} = \frac{i\beta\overline{\mu}}{3\,\mathrm{Re}}$$

$$C_{34} = -\frac{\overline{T}}{\gamma M_\infty^2}$$

$$C_{35} = -\frac{\overline{\rho}}{\gamma M_\infty^2} + \frac{1}{\mathrm{Re}}\left(\frac{4}{3}\frac{\partial \overline{U}_2}{\partial x_2} - \frac{2}{3}\frac{\partial \overline{U}_1}{\partial x_1}\right)\frac{\partial \overline{\mu}}{\partial \overline{T}}$$

$$C_{42} = \frac{i\beta}{3\,\mathrm{Re}}\overline{\mu}$$

$$C_{43} = -\overline{\rho}\overline{U}_2 + \frac{1}{\mathrm{Re}}\frac{\partial \overline{\mu}}{\partial \overline{T}}\frac{\partial \overline{T}}{\partial x_2}$$

$$C_{51} = 2\overline{\mu}\gamma(\gamma-1)\frac{M_\infty^2}{\mathrm{Re}}\left(\frac{\partial \overline{U}_1}{\partial x_2} + \frac{\partial \overline{U}_2}{\partial x_1}\right)$$

$$C_{52} = \frac{4}{3}\overline{\mu}\gamma(\gamma-1)\frac{M_\infty^2}{\mathrm{Re}}\left(\frac{\partial \overline{U}_1}{\partial x_1} + 4\frac{\partial \overline{U}_2}{\partial x_2}\right) - \gamma(\gamma-1)M_\infty^2\overline{p}$$

$$C_{55} = -\rho\overline{U}_2 + \frac{2\gamma}{P_r\,\mathrm{Re}}\frac{\partial \overline{\mu}}{\partial \overline{T}}\frac{\partial \overline{T}}{\partial x_2}$$

$$D_{11} = \frac{\partial \overline{\rho}}{\partial x_1} + i\alpha\overline{\rho}$$

$$D_{12} = \frac{\partial \overline{\rho}}{\partial x_2}$$

$$D_{13} = i\beta\overline{\rho}$$

$$D_{14} = \frac{\partial \overline{U}_1}{\partial x_1} + \frac{\partial \overline{U}_2}{\partial x_2} + i(\alpha\overline{U}_1 - \omega)$$

$$D_{21} = i\overline{\rho}(\omega - \alpha\overline{U}_1) - \overline{\rho}\frac{\partial \overline{U}_1}{\partial x_1} + i\frac{4\alpha}{3\,\mathrm{Re}}\frac{\partial \overline{\mu}}{\partial \overline{T}}\frac{\partial \overline{T}}{\partial x_1} - \frac{4\overline{\mu}}{3\,\mathrm{Re}}\alpha^2 + i\frac{4\overline{\mu}}{3\,\mathrm{Re}}\frac{\partial \alpha}{\partial x_1} - \frac{\overline{\mu}}{\mathrm{Re}}\beta^2$$

$$D_{22} = -\overline{\rho}\frac{\partial \overline{U}_1}{\partial x_2} + \frac{i\alpha}{\mathrm{Re}}\frac{\partial \overline{\mu}}{\partial \overline{T}}\frac{\partial \overline{T}}{\partial x_2}$$

$$D_{23} = -i\frac{2\beta}{3\,\mathrm{Re}}\frac{\partial \overline{\mu}}{\partial \overline{T}}\frac{\partial \overline{T}}{\partial x_1} - \frac{1}{3\,\mathrm{Re}}\alpha\beta\overline{\mu}$$

$$D_{24} = -\overline{U}_1\frac{\partial \overline{U}_1}{\partial x_1} - \overline{U}_2\frac{\partial \overline{U}_2}{\partial x_1} - i\alpha\frac{\overline{T}}{\gamma M_\infty^2} - \frac{1}{\gamma M_\infty^2}\frac{\partial \overline{T}}{\partial x_1}$$

$$D_{25} = \frac{1}{\mathrm{Re}}\left(\frac{4}{3}\frac{\partial \overline{U}_1}{\partial x_1} - \frac{2}{3}\frac{\partial \overline{U}_2}{\partial x_2}\right)\left(\frac{\partial^2 \overline{\mu}}{\partial \overline{T}^2}\frac{\partial \overline{T}}{\partial x_1} + i\alpha\frac{\partial \overline{\mu}}{\partial \overline{T}}\right) + \left(\frac{\partial \overline{U}_1}{\partial x_2} + \frac{\partial \overline{U}_2}{\partial x_1}\right)\frac{\partial^2 \overline{\mu}}{\partial \overline{T}^2}\frac{\partial \overline{T}}{\partial x_2}$$
$$-i\alpha\frac{\overline{\rho}}{\gamma M_\infty^2} - \frac{1}{\gamma M_\infty^2}\frac{\partial \overline{\rho}}{\partial x_1} + \frac{1}{\mathrm{Re}}\left(\frac{4}{3}\frac{\partial^2 \overline{U}_1}{\partial x_1^2} + \frac{\partial^2 \overline{U}_1}{\partial x_2^2} + \frac{1}{3}\frac{\partial^2 \overline{U}_2}{\partial x_1 \partial x_2}\right)\frac{\partial \overline{\mu}}{\partial \overline{T}}$$

$$D_{31} = -\overline{\rho}\frac{\partial \overline{U}_2}{\partial x_1} - i\frac{2\alpha}{3\,\mathrm{Re}}\frac{\partial \overline{\mu}}{\partial \overline{T}}\frac{\partial \overline{T}}{\partial x_2}$$

$$D_{32} = i\omega\overline{\rho} - i\alpha\overline{\rho}\overline{U}_1 - \overline{\rho}\frac{\partial \overline{U}_2}{\partial x_2} - \frac{\overline{\mu}\alpha^2}{\mathrm{Re}} + i\frac{\overline{\mu}}{\mathrm{Re}}\frac{\partial \alpha}{\partial x_1} - \frac{\overline{\mu}\beta^2}{\mathrm{Re}} + \frac{i\alpha}{\mathrm{Re}}\frac{\partial \overline{\mu}}{\partial \overline{T}}\frac{\partial \overline{T}}{\partial x_1}$$

$$D_{33} = -i\frac{2\beta}{3\,\mathrm{Re}}\frac{\partial \overline{\mu}}{\partial \overline{T}}\frac{\partial \overline{T}}{\partial x_2}$$

$$D_{34} = -\left(\overline{U}_1\frac{\partial \overline{U}_2}{\partial x_1} + \overline{U}_2\frac{\partial \overline{U}_2}{\partial x_2}\right) - \frac{1}{\gamma M_\infty^2}\frac{\partial \overline{T}}{\partial x_2}$$

$$D_{35} = \frac{1}{\mathrm{Re}}\left(\frac{\partial \overline{U}_2}{\partial x_1} + \frac{\partial \overline{U}_1}{\partial x_2}\right)\left(\frac{\partial^2 \overline{\mu}}{\partial \overline{T}^2}\frac{\partial \overline{T}}{\partial x_1} + i\alpha\frac{\partial \overline{\mu}}{\partial \overline{T}}\right) - \frac{1}{\gamma M_\infty^2}\frac{\partial \overline{\rho}}{\partial x_2}$$
$$+\frac{1}{\mathrm{Re}}\left(\frac{4}{3}\frac{\partial^2 \overline{U}_2}{\partial x_2^2} + \frac{\partial^2 \overline{U}_2}{\partial x_1^2} + \frac{1}{3}\frac{\partial^2 \overline{U}_1}{\partial x_1 \partial x_2}\right)\frac{\partial \overline{\mu}}{\partial \overline{T}} + \frac{1}{\mathrm{Re}}\left(\frac{4}{3}\frac{\partial \overline{U}_2}{\partial x_2} - \frac{2}{3}\frac{\partial \overline{U}_1}{\partial x_1}\right)\frac{\partial^2 \overline{\mu}}{\partial \overline{T}^2}\frac{\partial \overline{T}}{\partial x_2}$$

$$D_{41} = i\frac{\beta}{\mathrm{Re}}\frac{\partial \overline{\mu}}{\partial \overline{T}}\frac{\partial \overline{T}}{\partial x_1} - \frac{\alpha\beta}{3\,\mathrm{Re}}\overline{\mu}$$

$$D_{42} = i\frac{\beta}{\mathrm{Re}}\frac{\partial \overline{\mu}}{\partial \overline{T}}\frac{\partial \overline{T}}{\partial x_2}$$

$$D_{43} = i\omega\rho - i\alpha\overline{\rho}\overline{U}_1 - \frac{4\beta^2\overline{\mu}}{3\,\mathrm{Re}} + \frac{i\alpha}{\mathrm{Re}}\frac{\partial \overline{\mu}}{\partial \overline{T}}\frac{\partial \overline{T}}{\partial x_1} - \frac{\overline{\mu}\alpha^2}{\mathrm{Re}} + \frac{i\overline{\mu}}{\mathrm{Re}}\frac{\partial \alpha}{\partial x_1}$$

$$D_{44} = -i\beta\frac{\overline{T}}{\gamma M_\infty^2}$$

$$D_{45} = -i\beta\frac{\overline{\rho}}{\gamma M_\infty^2} - \frac{i\beta}{\mathrm{Re}}\left(\frac{2}{3}\frac{\partial \overline{U}_1}{\partial x_1} + \frac{2}{3}\frac{\partial \overline{U}_2}{\partial x_2}\right)\frac{\partial \overline{\mu}}{\partial \overline{T}}$$

$$D_{51} = -\overline{\rho}\frac{\partial \overline{T}}{\partial x_1} + \frac{4}{3}\overline{\mu}\gamma(\gamma-1)\frac{M_\infty^2}{\mathrm{Re}}\left(4\frac{\partial \overline{U}_1}{\partial x_1} + \frac{\partial \overline{U}_2}{\partial x_2}\right)i\alpha - i\gamma(\gamma-1)\alpha M_\infty^2\overline{p}$$

$$D_{52} = -\overline{\rho}\frac{\partial \overline{T}}{\partial x_2} + 2\gamma(\gamma-1)\frac{M_\infty^2}{\mathrm{Re}}\left(\frac{\partial \overline{U}_1}{\partial x_2} + \frac{\partial \overline{U}_2}{\partial x_1}\right) i\alpha\overline{\mu}$$

$$D_{53} = \frac{4i\beta}{3}\overline{\mu}\gamma(\gamma-1)\frac{M_\infty^2}{\mathrm{Re}}\left(\frac{\partial \overline{U}_1}{\partial x_1} + \frac{\partial \overline{U}_2}{\partial x_2}\right) - i\gamma(\gamma-1)\beta M_\infty^2 \overline{p}$$

$$D_{54} = -\left(\overline{U}_1\frac{\partial \overline{T}}{\partial x_1} + \overline{U}_2\frac{\partial \overline{T}}{\partial x_2}\right) - \gamma(\gamma-1)M_\infty^2\left(\frac{\partial \overline{U}_1}{\partial x_1} + \frac{\partial \overline{U}_2}{\partial x_2}\right)\frac{\overline{T}}{\gamma M_\infty^2}$$

$$\begin{aligned} D_{55} = {} & i\omega\overline{\rho} - i\alpha\overline{\rho}\overline{U}_1 + i\frac{\gamma}{P_r\,\mathrm{Re}}\left[\alpha\frac{\partial \overline{\mu}}{\partial \overline{T}}\frac{\partial \overline{T}}{\partial x_1} + i\overline{\mu}\frac{\partial \alpha}{\partial x_1} - \overline{\mu}(\alpha^2+\beta^2) + \left(\frac{\partial \overline{T}}{\partial x_1}\right)^2\frac{\partial^2 \overline{\mu}}{\partial \overline{T}^2}\right. \\ & \left. + i\alpha\frac{\partial \overline{\mu}}{\partial \overline{T}}\frac{\partial \overline{T}}{\partial x_1} + \left(\frac{\partial \overline{T}}{\partial x_2}\right)^2\frac{\partial^2 \overline{\mu}}{\partial \overline{T}^2} + \left(\frac{\partial^2 \overline{T}}{\partial x_1^2} + \frac{\partial^2 \overline{T}}{\partial x_2^2}\right)\frac{\partial \overline{\mu}}{\partial \overline{T}}\right] + \gamma(\gamma-1)\frac{M_\infty^2}{\mathrm{Re}}\frac{\partial \overline{\mu}}{\partial \overline{T}} \\ & \cdot\left[2\left(\frac{\partial \overline{U}_1}{\partial x_1}\right)^2 + 2\left(\frac{\partial \overline{U}_2}{\partial x_2}\right)^2 + \frac{2}{3}\left(\frac{\partial \overline{U}_1}{\partial x_1} + \frac{\partial \overline{U}_2}{\partial x_2}\right)^2 + \left(\frac{\partial \overline{U}_1}{\partial x_2} + \frac{\partial \overline{U}_2}{\partial x_1}\right)^2\right] \\ & -\gamma(\gamma-1)M_\infty^2\left(\frac{\partial \overline{U}_1}{\partial x_1} + \frac{\partial \overline{U}_2}{\partial x_2}\right)\frac{\overline{\rho}}{\gamma M_\infty^2} \end{aligned}$$

VITA

Hongwu Zhao
Aerospace Engineering Department
Old Dominion University
Norfolk, VA 23529

Educational Backgound

Ph.D.: August 2003, Old Dominion University, Norfolk VA, USA
Major: Aerospace Engineering
Dissertation: Hypersonic Boundary-layer Stability across a Compression Corner

M.S.: March 1997, Beijing University of Aeronautics and Astronautics, Beijing China.
Major: Aerospace Engineering
Thesis: Active Control of Wall Acoustic Impedance

B.S.: July 1994, Beijing University of Aeronautics and Astronautics, Beijing China.
Major: Aerospace Engineering
Thesis: Design of the Digital Control System for WP-11 engine

Major Publications

1. Balakumar P., Zhao H. and Atkins H., "Stability of hypersonic boundary-layer over a compression corner," AIAA-2002-2848. Presented at the third theoretical fluid mechanics meeting, June, 2002.
2. Zhao H, and Balakumar P., "Direct numerical simulation of the nonlinear disturbance evolution across a hypersonic compression corner," Submitted to 12th AIAA International Space Planes and Hypersonic Systems and Technologies Conference and AIAA Journal.
3. Zhao H. and Sun X., "Active control of wall acoustic impedance," AIAA Journal, Vol. 37, No. 7,1999, pp. 825-831.
4. Sun X., Jing X. and Zhao H., "Control of blade flutter by smart casing treatment," AIAA Journal of Propulsion and Power, Vol. 17, 2001, pp. 248-255.
5. Zhao H. and Sun X., "The design and experimental investigation of control system for acoustic liner with adjustable impedance," Chinese Journal of Acoustics, Vol. 18, No.1, 1999. pp. 70-80.